Karlsruher Institut für Technologie

Search for dark matter with EDELWEISS-III using a multidimensional maximum likelihood method

Zur Erlangung des akademischen Grades eines
DOKTORS DER NATURWISSENSCHAFTEN
der Fakultät für Physik
des Karlsruher Instituts für Technologie
genehmigte
DISSERTATION
von

Dipl.-Phys.

Lukas Hehn

aus Herrenberg

Tag der mündlichen Prüfung:	24.06.2016
Referent:	Prof. Dr. Dr. h.c. J. Blümer
Korreferent:	Prof. Dr. W. de Boer

Abstract

The nature of dark matter is one of the most fundamental questions in modern physics. From measurements of the Cosmic Microwave Background, a dark matter fraction of 27% of the total energy in the Universe can be derived. The known baryonic matter makes up only 5%, while the rest is attributed to an unknown *dark energy*. Evidence from the gravitational effects of this dark matter can be found on all cosmological scales, including our Milky Way. The different observations can be explained in a unified picture with a non-relativistic particle, so-called *Cold Dark Matter* (CDM). Such a particle is not part of the Standard Model (SM) and would require new physics. A generic class of hypothesised candidates are *Weakly Interacting Massive Particles* (WIMPs) with masses m_χ in the GeV–TeV range and interaction cross sections of the order of the weak scale. Such particles can be found e.g. in the proposed SuperSymmetric extension of the SM.

This thesis was performed in the context of the EDELWEISS-III experiment, which is designed to detect the elastic scattering of a WIMP from the galactic dark matter halo in an array of detectors. To shield against the flux of cosmic-ray induced muons, the experiment is located in an underground laboratory with 4800 m w.e.. Multiple layers of active and passive shielding suppress ambient radioactivity. The detectors are 800 g Ge-bolometers, which are cooled down to cryogenic temperatures of 18 mK. A particle interaction in the crystal produces thermal phonons and free charge carriers. They are measured as heat and ionization signals with 2 Ge-NTD sensors and 4 sets of ring electrodes on the detector surfaces. The ratio of ionization over heat energy can be used to discriminate, on an event-by-event basis, between nuclear recoils from a potential signal and electron recoils from backgrounds. Particle interactions on the surface, for which this discrimination can fail due to incomplete charge collection, can be rejected by selecting events from the so-called *fiducial volume*.

In the last years, special interest has risen to explore the physics case of so-called low mass WIMPs with masses $m_\chi = \mathcal{O}(1)\,\mathrm{GeV}/c^2$. The major challenge in the detection of such WIMPs is the discrimination of a small $\mathcal{O}(1)$ keV nuclear recoil from background events and noise fluctuations near the trigger threshold of a detector. This thesis in particular addresses the search for low mass WIMPs by analysing EDELWEISS data with a multidimensional maximum likelihood method. Therefore, a likelihood model based on two observables, the combined heat energy E_c and the fiducial ionization energy E_fid, was constructed in the framework of this thesis. Data from 8 selected detectors, taken during a 10 months long WIMP search run, was analysed in terms of low mass WIMPs. The region of interest (RoI) was defined as $E_\mathrm{c}^\mathrm{min} < E_\mathrm{c} < 15\,\mathrm{keV_{ee}}$ and $0 < E_\mathrm{fid} < 15\,\mathrm{keV_{ee}}$, where $E_\mathrm{c}^\mathrm{min}$ is the energy, for which a detector has a trigger efficiency of at least 80%. This resulted in analysis thresholds between $E_\mathrm{c}^\mathrm{min} = 0.91\,\mathrm{keV_{ee}}$ and $1.46\,\mathrm{keV_{ee}}$, much lower than in standard EDELWEISS WIMP searches before, allowing to search for low mass WIMPs with $m_\chi \in [4, 30]\,\mathrm{GeV}/c^2$ with a signal efficiency up to 60%. A dedicated fiducial cut was developed, to efficiently reject surface events down to these low energies. After all quality cuts, a total of $\approx 5 \cdot 10^4$ events were investigated in the analysis region for a combined exposure of 496 kg·days.

For each detector, a likelihood model was constructed, considering all relevant backgrounds in the RoI: electron recoils from Compton scattered γ's, X-rays and tritium decay in the detector, nuclear recoils from neutrons, ionizationless *heat-only* events and unrejected surface events from the decay chain of ^{210}Pb. The energy spectra of each background were derived from sideband data and a detector response model was used to construct probability density functions (PDFs) in the two observables. The event rate μ of each background was constrained during the fit to the expected rate, including its systematic uncertainties.

The maximum likelihood fit of data from individual detectors resulted in no statistically significant signal component for all probed WIMP masses m_χ. Depending on the mass m_χ of the probed WIMP signal, degeneracies were observed between the signal and different backgrounds from heat-only events and neutrons. Shown for the first time within this thesis, these degeneracies can be efficiently suppressed by combining the likelihood functions of all 8 detectors and performing a combined fit with a common signal signal cross section σ_χ.

For each probed mass m_χ and individual detectors as well as their combination, an upper limit on the WIMP-nucleon scattering cross section σ_χ was derived. For this, a hypothesis test based on the profile likelihood test statistics was performed for different values of σ_χ to find the value which can be excluded with 90% C.L.. The limit was derived with two different methods: with an approximation on the asymptotic distribution of the test statistics and with Monte Carlo generated toy data. A study performed with an extensive number of toy data sets showed that the limit derived with the asymptotic approximation does not provide the correct coverage for a large fraction of the tested likelihood functions, especially for low masses $4\,\mathrm{GeV}/c^2 < m_\chi < 7\,\mathrm{GeV}/c^2$. Based on the proper test statistics, exclusion limits derived with the total exposure of 496 kg·days and all 8 detectors, for the lowest and highest mass evaluated here, are

$$\sigma_\chi^{\mathrm{up}} < 1.6 \times 10^{-39}\,\mathrm{cm}^2 \ (90\%\,\mathrm{C.L.}) \text{ for } m_\chi = 4\,\mathrm{GeV}/c^2 \text{ and}$$
$$\sigma_\chi^{\mathrm{up}} < 6.9 \times 10^{-44}\,\mathrm{cm}^2 \ (90\%\,\mathrm{C.L.}) \text{ for } m_\chi = 30\,\mathrm{GeV}/c^2$$

The limit clearly rules out the existing claims of potential low mass WIMP signals by various other experiments. Thanks to the large signal acceptance and a subtraction of backgrounds, an improvement in the achieved limit by a factor of $\approx$7 is obtained for $m_\chi = 4\,\mathrm{GeV}/c^2$ WIMPs, compared to a Boosted Decision Tree (BDT) based analysis of a similar data set [1]. At higher masses, $m_\chi > 15\,\mathrm{GeV}/c^2$, the limits from both analyses are in good agreement.
This work shows, that an analysis of WIMP search data based on a maximum likelihood method is significantly improving the sensitivity on WIMP parameters over more simplified cut-based count experiments or even a BDT-based analysis. However, such a complex statistical analysis requires excellent knowledge and modelling of all relevant background sources as well as a careful statistical treatment to extract proper statements on confidence levels.

Zusammenfassung

Die Natur der dunklen Materie ist eine der bedeutsamsten ungelösten Fragen der modernen Physik. Aus Messungen der kosmischen Hintergrundstrahlung ist bekannt, dass dunkle Materie einen Anteil von 27% an der Gesamtenergie im Universum hat. Die uns vertraute baryonische Materie ist nur für 5% verantwortlich, während der Rest einer noch gänzlich unbekannten dunklen Energie zugeordnet wird. Hinweise für den gravitativen Einfluss der dunklen Materie finden sich auf allen Größenskalen im Universum, auch in unserer Milchstraße. Diese verschiedenen Beobachtungen lassen sich in einem vereinheitlichten Ansatz durch ein nicht-relativistisches Teilchen erklären, so genannte kalte dunkle Materie. Da solch ein Teilchen nicht Teil des bekannten Standardmodels ist, würde es neue Physik implizieren. Eine generische Klasse von hypothetischen Teilchen sind *Weakly Interacting Massive Particles* (schwach wechselwirkende massive Teilchen, WIMPs), mit Massen im Bereich von GeV bis TeV und Wirkungsquerschnitten im Bereich der schwachen Wechselwirkung. Solche Teilchen sind unter anderem Bestandteil der SuperSymmetrischen (SUSY) Erweiterung des Standardmodels.

Diese Arbeit wurde im Rahmen des EDELWEISS Experiments angefertigt, welches dafür konzipiert ist, die elastische Streuung eines WIMP Teilchens aus dem galaktischen Halo in einem Detektor Array nachzuweisen. Zur Abschirmung von Myonen als Sekundärprodukt der kosmischen Strahlung ist das Experiment in einem Untergrundlabor aufgebaut, wo es von Gestein einer Dicke von 4800 m w.e. abgeschirmt wird. Mehrere aktive und passive Abschirmungen reduzieren die natürliche Strahlung. Die Detektoren sind 800 g Germanium Bolometer, welche auf kryogene Temperaturen von 18 mK gekühlt werden. Eine Teilchenwechselwirkung im Detektorkristall erzeugt thermische Phononen und freie Ladungsträger. Diese werden als Wärme und Ionisationssignal von 2 Ge-NTD Sensoren und 4 Gruppen von Ringelektroden auf den Detektoroberflächen gemessen. Das Verhältnis von Ionisations- zur Wärmeenergie kann genutzt werden, um ereignisbasiert zwischen dem potentiellen Signal von Kernrückstößen und dem Untergrund durch Elektronrückstößen zu diskriminieren. Teilchenwechselwirkungen an der Oberfläche, bei welchen diese Diskriminierung wegen unvollständiger Ladungsauslese stark limitiert ist, können durch die Definition eines sogenannten Vertrauensvolumens (fiducial volume) mithilfe der verschiedenen Elektroden verworfen werden.

In den vergangen Jahren sind WIMPs mit niedrigen Massen von $m_\chi = \mathcal{O}(1)\,\mathrm{GeV}/c^2$ in den Fokus des wissenschaftlichen Interesses gerückt. Die größte Herausforderung für den Nachweis dieser sogenannten *low mass WIMPs* ist die Unterscheidung von niederenergetischen Kernrückstößen mit Energien $\mathcal{O}(1)\,\mathrm{keV}$ von Untergrundereignissen sowie Rauschen nahe der Aufnahmeschwelle der Detektoren. Diese Arbeit behandelt insbesondere die Suche nach low mass WIMPs durch eine Analyse von EDELWEISS-III Daten mittels einer mehrdimensionalen Maximum Likelihood Methode. Dazu wurde ein Likelihood Modell basierend auf den beiden Observablen kombinierte Wärmeenergie E_c und fiducial Ionisationsenergie E_fid erstellt. Daten, welche während einer zehnmonatigen Suche nach WIMPs von 8 nachträglich ausgewählten Detektoren aufgenommen wurden, wurden auf low mass WIMPs hin untersucht. Die Signalregion wurde in einem Energiebereich $E_\mathrm{c}^\mathrm{min} < E_\mathrm{c} < 15\,\mathrm{keV_{ee}}$ und

$0 < E_{\text{fid}} < 15\,\text{keV}_{\text{ee}}$ definiert, wobei $E_{\text{c}}^{\text{min}}$ die Energie ist, für welche die Triggereffizienz eines Detektors mindestens 80% beträgt. Die resultierende Schwellenenergie der Analyse betrug damit zwischen $E_{\text{c}}^{\text{min}} = 0.91\,\text{keV}_{\text{ee}}$ und $1.46\,\text{keV}_{\text{ee}}$. Diese Schwelle ist weit niedriger als die in der bisherigen standard WIMP-Suche verwendete und erlaubte die Suche von low mass WIMPs mit $m_\chi \in [4, 30]\,\text{GeV}/c^2$ mit einer Signaleffizienz von bis zu 60%. Um bei diesen Energien Oberflächenereignisse verwerfen zu können, wurde eine spezielle Auswahl von fiducial Ereignissen entwickelt. Nach allen Qualitätscuts betrug die Gesamtexposition von allen Detektoren 496 kg·Tage. Ca. $5 \cdot 10^4$ Ereignisse verblieben in der Signalregion zur weiteren Analyse.

Unter der Berücksichtigung aller relevanten Untergrundkomponenten wurde für jeden Detektor ein Likelihood-Modell konstruiert. Zu den Untergrundkomponenten zählen Elektronenrückstöße durch γ's nach Compton-Streuung, Röntgenphotonen und β's aus dem Zerfall von Tritium im Detektor, Kernrückstöße von Neutronen, ionisationslose *heat-only* Ereignisse, sowie nicht verworfene Oberflächenereignisse von Teilchen aus der ^{210}Pb-Zerfallskette. Die Energiespektren für jeden Untergrund wurden aus Daten außerhalb der Signalregion extrahiert. Die Wahrscheinlichkeitsdichtefunktionen (PDFs) wurden unter Verwendung der Antwortfunktionen der Detektoren in den beiden Observablen konstruiert. Die Ereignisrate μ für jede Untergrundkomponente wurde während des Fits auf den Erwartungswert unter Berücksichtigung systematischer Unsicherheiten eingeschränkt.

Der Maximum Likelihood Fit der Daten von einzelnen Detektoren resultierte in keiner statistisch relevanten Signalkomponente für alle getesteten WIMP Massen m_χ. Abhängig von der getesteten WIMP Masse m_χ wurde eine Entartung zwischen dem Signal und der Rate von heat-only oder Neutronenereignissen gefunden. In dieser Arbeit wird gezeigt, wie diese Entartungen effektiv unterdrückt werden können, indem die Kombination der Likelihoodfunktionen von allen 8 Detektoren und eines simultanen Fits mit einem gemeinsamen Signalwirkungsquerschnitts σ_χ verlangt wird.

Für jede untersuchte WIMP Masse m_χ, sowohl für einzelne Detektoren wie auch für die Kombination aller Detektoren, wurde eine Obergrenze für den WIMP-Nukleon Streuwirkungsquerschnitt σ_χ abgeleitet. Dafür wurde für verschiedene Werte von σ_χ ein Hypothesentest basierend auf der profile likelihood Teststatistik ausgeführt. Die Obergrenze wurde mit zwei verschiedenen Verfahren ermittelt: Zum einen mit einer Approximation (asymptotische Näherung sehr großer Teststatistik) und zum andern mit Monte Carlo generierten Datensätzen. Eine Untersuchung, welche mit einer großen Anzahl von generierten Datensätzen durchgeführt wurde, erbrachte, dass die asymptotische Approximation nicht in jedem Fall die Vertrauensintervalle korrekt abdeckt. Dies gilt insbesondere für die niedrigsten Massen $4\,\text{GeV}/c^2 < m_\chi < 7\,\text{GeV}/c^2$. Die daraufhin korrigierte Ausschlusskurve für die Gesamtexposition von 496 kg·Tagen und für alle 8 Detektoren hat folgende Ausschlusswerte:

$$\sigma_\chi^{\text{up}} < 1.6 \times 10^{-39}\,\text{cm}^2 \text{ (90\% C.L.) für } m_\chi = 4\,\text{GeV}/c^2 \text{ und}$$
$$\sigma_\chi^{\text{up}} < 6.9 \times 10^{-44}\,\text{cm}^2 \text{ (90\% C.L.) für } m_\chi = 30\,\text{GeV}/c^2$$

für die niedrigste und höchste der untersuchten Massen. Die in dieser Arbeit ermittelte Ausschlusskurve kann die vorhandenen potentiellen Signale von verschiedenen anderen Experimenten mit mehr als 90% Vertrauensinterval ausschließen. Dank der größeren Signalakzeptanz und der Subtraktion von bekanntem Untergrund ist im Vergleich zu einer Analyse eines ähnlichen Datensatzes, welche auf Boosted Decision Trees (BDT) basiert [1], für eine WIMP-Masse von $m_\chi = 4\,\text{GeV}/c^2$ eine Verbesserung der erreichten Sensitivität um einen Faktor 7 erzielt worden. Für höhere Massen mit $m_\chi > 15\,\text{GeV}/c^2$ stimmen die erzielten Ausschlusskurven für beide Analysen gut überein.
Diese Arbeit zeigt, dass eine Analyse von Daten zur WIMP Suche mittels Maximum

Likelihood Methode eine deutliche Sensitivitätssteigerung, im Vergleich zu einer Cut-basierten Analyse oder BDT-Analyse erbringt. Eine statistisch so komplexe Analysemethode verlangt jedoch ausgezeichnete Kenntnisse über alle relevanten Untergrundkomponenten und deren Beschreibung. Dazu gehört auch die korrekte statistische Behandlung der Resultate, um Aussagen mit korrekten statistischen Vertrauensintervallen treffen zu können.
Für die Abschätzung der Sensitivität, wie sie in zukünftigen Messreihen von EDELWEISS erzielt werden soll, sind die Resultate dieser Arbeit eingeflossen, insbesondere die gute Signal-Untergrund-Trennung bei gleichzeitig hoher Signaleffizienz und die genaue, individuelle Detektoreigenschaften berücksichtigende, Modellierung aller relevanten Ereignisklassen in der Analyseregion.

Contents

1. About dark matter

Astronomical observations made over the past century, have lead to the establishment of the standard cosmological ΛCDM (Λ Cold Dark Matter) model. This model is based on Einstein's equations of general relativity which describe the geometry as well as the matter and energy content of the Universe, where Λ denotes the so-called cosmological constant. According to this model, the Universe consists predominantly out of unknown forms of energy and matter. Latest precision measurements of the Cosmic Mircowave Background (CMB) show that the well-known baryonic matter which makes up the stars and interstellar gas[1] sums up to only 5% of the total total energy density in the Universe [2]. Much more, 27%, is in the form of dark matter, while the rest is attributed to an unknown dark energy.

The nature of this dark matter is one of the most fundamental questions in modern physics. Evidence for its existence were already found almost 100 years ago. Already in 1922, J. Jeans [3] used the term "dark matter" to denote an invisible matter which could explain the observed vertical oscillation of stars in our galactic plane. And in 1933, F. Zwicky [4] applied the Virial theorem to the Coma galaxy cluster, and found that it should contain ten times more mass than was deduced from the received light. Today, observations made on all cosmological scales in the Universe allow to infer the existence of a non-luminous type of matter. These observations can be resolved in a unified picture by introducing a new fundamental particle interacting weakly but not electromagnetically. Neutrinos, the only viable candidate for dark matter in the Standard Model (SM), are disfavoured by structure formation. Therefore, the search for dark matter is also a search for new physics. In this context, dark matter search is a textbook example for the field of astroparticle physics as intersection of astronomy, cosmology and particle physics.

In Sec. 1.1, selected evidence on different cosmological scales is given for the existence of dark matter. Further evidence exists but is not discussed in this chapter. Examples which are not mentioned are e.g. the effect of dark matter on the inferred distance of observed type 1a Supernovae or the baryon density from Big Bang Nucleosynthesis, which is affected by the dark matter content as well. Section 1.2 shows that only dark matter in the form of a particle can combine the different observations and a description of three potential particle candidates is given. The different detection methods for WIMP dark matter follow in Sec. 1.3. Naturally, the focus here is on direct detection which is the principle employed by the EDELWEISS experiment. Finally, a short overview over the current field and the status of various direct detection experiments is presented in Sec. 1.4.

[1] In cosmology, the term baryonic matter is used more loosely and e.g. also includes electrons.

1.1. Observational evidence in cosmology

1.1.1. The Cosmic Microwave Background

The largest probe for the dark matter hypothesis is the Cosmic Microwave Backround (CMB), which was predicted by Gamow [5] in 1948 and discovered by Penzias and Wilson [6] in 1965. The origin of this background can be interpreted in the ΛCDM framework: within this model, the Universe was created in the Big Bang as hot dense primordial plasma which rapidly increased in size during the phase of inflation, leading to an isotropy of the distributed matter. In the course of this expansion, the Universe cooled down. Around 380,000 years after the Big Bang the temperature reached $T \approx 3000\,\mathrm{K}$, which allowed the protons and electrons to recombine into neutral hydrogen atoms. Photons, which had scattered off electrons in the hot plasma before with a short mean free path, could thus decouple from the plasma and travel freely. The surface of their last scattering can still be detected today from all directions as cosmic microwave background. Due to the expansion of the Universe, since the recombination at a redshift of $z = 1100$, the wavelength of these photons has increased and consequently the temperature of the radiation has decreased to $T = 2.7\,\mathrm{K}$ in the present Universe ($z = 0$). The CMB arising from these photons is the most perfect black body radiation known in nature. It is almost perfectly isotropic, except for small temperature fluctuations $\mathcal{O}(10^{-5})$ which are thought to be related to the density fluctuations in the early plasma.

The CMB has been measured with increasing angular precision by successive satellite experiments, first COBE [7], then WMAP [8] and more recently Planck [2]. Due to the perfect black body spectrum of the CMB, the measurement of only 5 different frequencies allows to reconstruct the temperature of the CMB radiation under a given angle. Figure 1.1 (top) shows the projection of the CMB in the full sky, more precisely the μK over- and under-fluctuations from the mean temperature. These temperature fluctuations could be explained as density variations in the primordial plasma before the inflation took place. Colder spots arise from overdensities which, due to their higher gravitational potential, reduce the energy of the escaping photons (gravitational red-shift). Imprinted in the CMB are Baryon Acoustic Oscillations (BAO). These density oscillations are sensitive to dark matter: while over-dense baryonic matter heats up and creates phonon pressure, dark matter only acts as a gravitational well and emits no radiation. The CMB fluctuations can therefore be used as a probe for dark matter. For the interpretation of the anisotropies in the CMB, the power spectrum of the spherical harmonics is calculated and is shown in Fig. 1.1 (bottom). The peaks which can be observed in the spectrum represent sound waves (density perturbations) in the primordial plasma. The first peak can be observed for a multipole moment of $l = 200$, which corresponds to an angle of $\approx 1^\circ$ under which fluctuations appear in the sky map. This peak is a probe for the geometry, e.g. the flatness of the Universe. It corresponds to the largest possible standing wave in the primordial plasma, the acoustic horizon. The power spectrum of the CMB temperature fluctuations can be fitted to derive values for the 6 parameters of the ΛCDM model. The most recent results found by Planck are [2]:

$$\begin{aligned} \theta &= (1.04103 \pm 0.00046) \cdot 10^{-2} \\ \Omega_\mathrm{b} h^2 &= 0.02226 \pm 0.00023 \\ \Omega_\mathrm{cdm} h^2 &= 0.1186 \pm 0.0020 \\ n_\mathrm{s} &= 0.9677 \pm 0.0060 \\ H_0 &= 67.8 \pm 0.9\,\mathrm{km/s/Mpc} \\ \Omega_\mathrm{m} &= 0.308 \pm 0.012 \end{aligned} \tag{1.1}$$

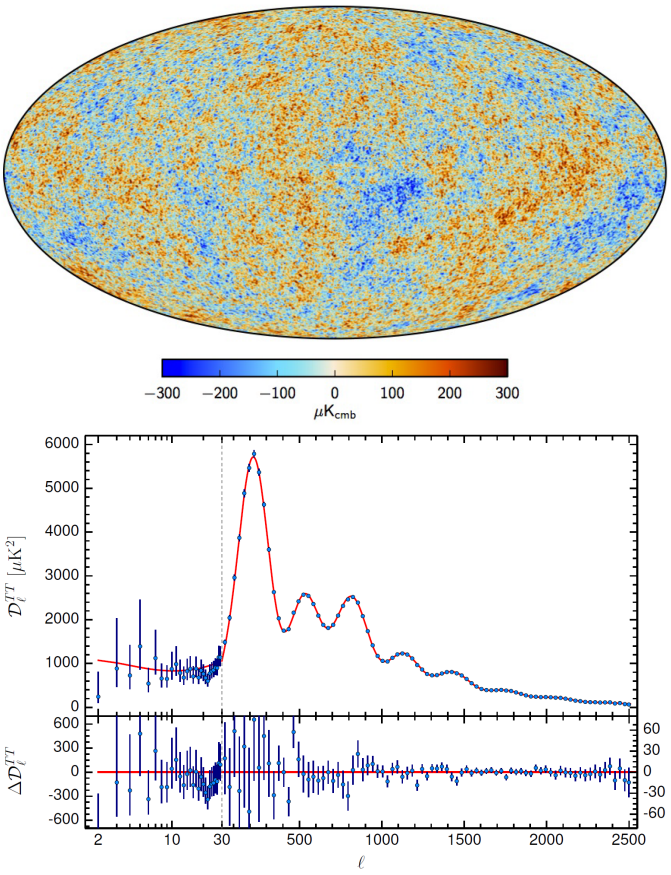

Figure 1.1.: *Top*: Intensity map of CMB temperature fluctuations with 5' angular resolution and combined data from Planck, WMAP, and 408 MHz observations after subtraction of all (galactic) foregrounds. *Bottom*: Planck 2015 temperature power spectrum with 1σ errorbars and best fit ΛCDM model (red curve). Shown below are the residuals with respect to the model. Figures extracted from [2].

where θ is the angular scale of the acoustic horizon, Ω_b the baryon density relative to the critical density, Ω_cdm the cold dark matter density, n_s the scalar spectral index, H_0 the Hubble constant and Ω_m the matter density. By introducing the dimensionless Hubble parameter h defined as $H = h \cdot 100\,\mathrm{km/s/Mpc}$, the fraction of dark matter of the total energy density in the Universe can be calculated as $\Omega_\mathrm{cdm} \approx 27\%$ and the age of the Universe derived as $13.799 \pm 0.038\,\mathrm{Gyr}$.

1.1.2. Galaxy clusters

On of the first indications of dark matter was found on the scale of galaxy clusters. In 1933, F. Zwicky studied the Coma galaxy cluster and found clear evidence for missing mass [4]. Assuming that the cluster was old enough to reach a stable state, the relationship between the total average kinetic energy E_kin and the potential energy E_pot can be described by the Virial theorem:

$$\langle E_\mathrm{kin} \rangle = -\frac{1}{2} \langle E_\mathrm{pot} \rangle \tag{1.2}$$

Zwicky determined the velocity distribution of galaxies in the cluster by determining their Doppler red-shift. Equation 1.2 can be reordered to calculate the total mass as a function of the (measured) average velocity and the typical length scale of the gravitational potentials in the cluster. Comparing the derived mass with the luminosity from the galaxy

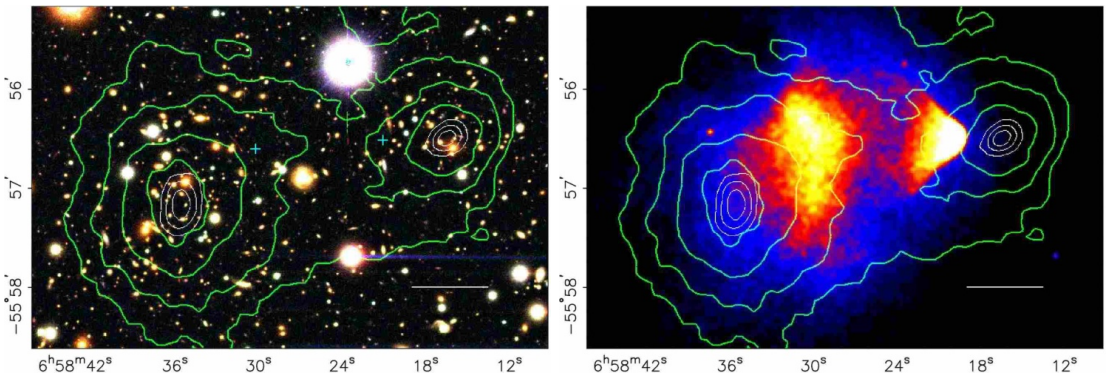

Figure 1.2.: *Left*: Optical image of two collinding galacy clusters which form the Bullet cluster. Green contours denote the mass distribution found from optical lensing studies, with the 1, 2 and 3σ error of the center of mass given in white contours. A clear separation is visible between the total mass an the center of mass of the hot interstellar gas (small green crosses). *Right*: X-ray image taken with the Chandra telescope showing the distribution of the shocked gas. Figure extracted from [9].

cluster, Zwicky found that the ratio between gravitational mass and luminous mass is ≈400. Although uncertainties in the application of the Virial theorem for this system may reduce this discrepancy by a factor of 2, the measurement gave clear evidence for a dominating non-luminous fraction of matter in galaxy clusters.

A more recent example and a compelling piece of evidence for the existence of dark matter on the scale of galaxy clusters is the so-called *Bullet Cluster* [9], which has been analysed with multiple wavelength techniques. Figure 1.2 (left) shows a picture of this cluster merger taken in the optical wavelength. Approximately 150 million years ago, in a distance of 1.1 Gpc, two galaxy clusters collided. The galaxies and stars passed through each other without significant disturbance. The interstellar gas of each cluster, however, was shocked and heated up as can be seen in the false color image taken with the Chandra X-ray telescope in the right panel of Fig. 1.2. The distribution of the total galaxy cluster mass can be deduced from weak lensing studies, where the distortion of light sources in the background is analysed statistically to derive the distribution of matter in the galaxy cluster. It is depicted in green contours in both panels of the figure. A separation of the center of mass for the hot gas and the center of mass derived from optical lensing for both clusters is found with a confidence level of 8σ. As the interstellar gas outweighs the stars in a galaxy cluster, this can be well understood by assuming that the dominant matter component is dark matter, which does not interact electromagnetically.

1.1.3. Galactic rotation curves

Single spiral galaxies, such as the Milky Way, are the smallest cosmological objects for which evidence of a dark matter component has been found. In these galaxies, the rotational speed v of stars (assuming approximately circular orbits and Newtonian dynamics), can be described as a function of distance r to the galactic center as:

$$v(r) = \sqrt{\frac{GM(r)}{r}} \tag{1.3}$$

where G is the gravitational constant and $M(r)$ the attracting mass within a sphere of the same radius r. Under the assumption that the main fraction of the mass of a galaxy is within the galactic bulge, $M(r)$ can be regarded as constant for large r and consequently,

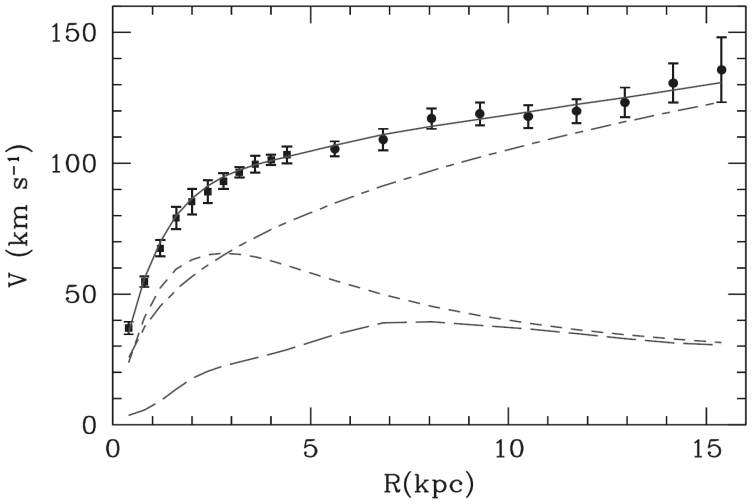

Figure 1.3.: Rotation curve of the galaxy M33 (points) compared with the best fit model (continuous line). Also shown the halo contribution (dasheddotted line), the stellar disk (short dashed line) and the gas contribution (long dashed line). Adapted from [13]

one expects to find $v(r) \propto r^{-1/2}$.
However, first measurements of the rotational velocity of stars performed by Vera Rubin [10] via the Doppler shift of the hydrogen absorption lines, showed that the velocity was approximately constant or even increasing for larger r. An example for such a measurement for the galaxy M33 is given in Fig. 1.3. The data clearly shows that an additional matter component is needed to explain the rotation curves of stars around the galactic center, which can be parametrized in the form of a dark matter halo. Based on N-body simulations of dark matter in galaxies, Navarro, Frenck and White derived a parametrization regarding the dark matter halo density, the so-called NFW-profile [11]:

$$\rho(r) = \frac{\rho_{\mathrm{crit}}\delta_{\mathrm{c}}}{(r/r_{\mathrm{s}})(1+r/r_{\mathrm{s}})^2} \tag{1.4}$$

where ρ_{crit} is the critical density for a flat Universe, $r_{\mathrm{s}} = r_{200}/c$ with r_{200}, the radius for which the density is $\rho(r_{200}) = 200\rho_{\mathrm{crit}}$, c a dimensionless parameter and δ_{c} parametrizing the characteristic overdensity of the halo.
By applying the NFW profile to the galactic rotation curve of the Milky Way, local dark matter density at the distance of the sun of $\rho(R_\odot) = 0.235 \pm 0.030\,\mathrm{GeV}/c^2\mathrm{cm}^3$ has been derived [12]. While estimations based on a different principle have obtained higher densities, the canonical value which is used in direct detection experiments is $\rho(R_\odot) = 0.3\,\mathrm{GeV}/c^2\mathrm{cm}^3$.

1.2. Dark matter candidates

Over the years, various theories have been made to explain the observations related to the dark matter problem. One purely phenomenological theory is *MOdified Newtonian Dynamics* (MOND), which was proposed by M. Milgrom in 1983 [14]. A more recent account is given in [15]. MOND theory can well explain the observed flattening of the galactic rotation curves by altering the Newtonian laws at large scales. However, it cannot account for the observation of dark matter on other scales, e.g. in the Bullet Cluster (see Sec. 1.1.2). It would also imply that the theory of general relativity, from which Newtonian dynamics can be derived, is incomplete.
Another explanation for the observation of non-luminous matter at galactic scales could

arise from so-called *MAssive Compact Halo Objects* (MACHOs). This class includes objects made of baryonic matter such as black holes, neutron stars, brown dwarfs, white dwarves and so-called *rogue planets* which have been ejected from their solar orbit. Dedicated searches using the microlensing effect as a detection method have been conducted to search for these objects and the existence of a significant fraction of MACHOs in the galactic halo, which would explain the measured rotation curves, can be excluded [16]. As for the MOND theory, MACHOs cannot account for dark matter observation on all scales. In particular, they are incompatible with the observed baryonic fraction obtained from CMB (see Sec. 1.1.1).

After this short description of alternative theories and their deficiencies, we now come to a discussion of the canonical solution for the dark matter problem: a new, fundamental particle. To satisfy all of the different observations which are considered as evidence for dark matter, the following particle properties are required:

- It has to be stable on the time scale of the Universe, otherwise it would have decayed and no gravitational effects could be observed today.
- It must have no electro-magnetic interaction, i.e. must not couple to photons in order to be invisible and not emit any type of radiation. This is also an underlying assumption about dark matter in the description of the density fluctuations of the CMB: only baryonic matter contributes to the density oscillations due to its radiation, while dark matter only acts as a gravitational well.
- It must be non-relativistic to explain the observed density power spectrum in the Universe.
- It must account for the right relic density observed in the CMB, i.e. $\Omega_{\mathrm{cdm}}h^2 = 0.1186 \pm 0.0020$.

While it is not mandatory for dark matter to interacts weakly, this property arises naturally from many dark matter models and would be required for a possible detection in laboratory experiments. Various particle candidates have been suggested over the past decades. In the following, the three of them which are of relevance for the EDELWEISS experiment will be introduced.

1.2.1. Axions

The axion is a hypothetitcal particle which was postulated already in 1977 by Peccei and Quinn [17, 18], and Wilczek and Weinberg in 1978 [19], to solve the strong CP-problem in quantum chromodynamics (QCD) as well as the missing dipole moment of the neutron[2].

Axions are also a viable dark matter candidate. Their mass is predicted as

$$m_{\mathrm{a}} \approx 10^{-6}\,\mathrm{eV}\left(\frac{10^{12}\,\mathrm{GeV}}{f_{\mathrm{A}}}\right) \tag{1.5}$$

where f_{A} is their decay constant. Despite their small mass, axions could account for cold dark matter as they are produced non-thermally. Their density relative to the critical density of the Universe is given as [20]

$$\Omega_{\mathrm{a}} \approx \left(\frac{6\,\mu\mathrm{eV}}{m_{\mathrm{a}}}\right)^{\frac{7}{6}} \tag{1.6}$$

[2]The neutron, consisting of 3 charged quarks (uud), is expected to have an electric dipole moment of $d_{\mathrm{theor.}} \approx 10^{-16}\,\mathrm{e}\cdot\mathrm{cm}$, whereas measurements have obtained upper limits of $d_{\mathrm{meas.}} < 10^{-25}\,\mathrm{e}\cdot\mathrm{cm}$

requiring an axion mass of $m_a \approx 20\,\mu$eV to account for the entire dark matter component in the Universe. A possible production mechanism is the Primakoff effect, where the interaction of a photon in an electric field, e.g. the Coulomb field of an atom, creates an electrically neutral axion. Searches for axions are ongoing and we can distinguish between three different types: dark matter axion searches such as ADMX [21], searches for solar axions as with CAST [22] and last, so-called "Light Shining through Walls" (LSW) experiments like ALPS [23], which try to produce axions with a laser in a strong magnetic field and detect the light produced by the inverse Primakoff-effect. Using low energy electron recoil data, the EDELWEISS-II experiment also looked for axions and axion like particles [24]. A detailled review of axions is given in [20].

1.2.2. SUSY WIMPs

A favourite dark matter candidate are Weakly Interacting Massive Particles (WIMPs), a generic class of heavy particles which interact gravitationally and via the weak interaction, but not electromagnetically. They will be denoted with the symbol χ in the following.
The intriguing property of WIMPs is that they arise naturally from a thermal freeze out process in the early Universe after the big bang, with cross sections on the order of the weak scale, masses in the GeV to TeV range and a relic density compatible with dark matter. The principle behind this freeze out process is that WIMPs were produced and annihilated into standard matter (anti)particles (denoted P in the following):

$$\chi + \chi \Leftrightarrow P + \bar{P} \tag{1.7}$$

It is assumed here that WIMPs are Majorana particles. In the early Universe, at high temperature, this process was in thermodynamic equilibrium, i.e. the production rate Γ_{prod} and annihilation rate Γ_{ann} were equal:

$$\begin{aligned} &\Gamma_{\text{prod}} = \Gamma_{\text{ann}} && \text{where} \\ &\Gamma_{\text{ann}} \propto \langle \sigma_{\text{ann}} v_\chi \rangle \cdot n && \text{and} \\ &\Gamma_{\text{prod}} \propto n_{\text{eq.}} \end{aligned} \tag{1.8}$$

where n (n_{eq}) is the particle density of WIMPs (in equilibrium), σ_{ann} the annihilation cross section of the process in Eq. 1.7 and v_χ the WIMP velocity, where the product $\langle \sigma_{\text{ann}} v_\chi \rangle$ is thermally averaged. Taking into account the dilution of the Universe due to the Hubble expansion H, the time evolution of the particle density n can be described by the Boltzmann equation as

$$\frac{dn}{dt} = -3Hn - \langle \sigma_{\text{ann}} \cdot v_\chi \rangle \left[n^2 - n_{\text{eq}}^2 \right] \tag{1.9}$$

As the Universe expands, the particle density n in a co-moving volume decreases proportional to the Boltzmann factor, i.e. $n \propto e^{-m_\chi/T}$, where T is the temperature. At some point, the annihilation rate becomes smaller than the Hubble expansion rate: WIMPs decouple from the thermal equilibrium. Equation 1.9 can be solved numerically to determine the relic density of WIMPs after this freeze-out. The process is illustrated in Fig. 1.4 for a WIMP mass $m_\chi = 100\,\text{GeV}/c^2$. The freeze-out temperature T_{freeze} for this process is remarkably model independent and is $T_{\text{freeze}} \approx \frac{1}{20} m_\chi$, which directly implies that WIMPs are non-relativistic. By this production mechanism, WIMPs are a suitable *cold* dark matter

candidate. It can be shown that the abundance of WIMPs today, which depends on the decoupling temperature and therefore on the annihilation rate, can be approximated as [25]:

$$\Omega_\chi h^2 \approx \frac{3 \cdot 10^{-27}\,\mathrm{cm^3 s^{-1}}}{\langle \sigma_{\mathrm{ann}} \cdot v_\chi \rangle}\,\mathrm{GeV}/c^2 \tag{1.10}$$

where Ω_χ is the fraction of WIMPs to the critical mass and h the Hubble parameter defined in Sec. 1.1.1. The fact, that the relic density of dark matter arises from annihilation cross sections and masses of the order of the weak interaction is called *WIMP miracle*.

A possible WIMP candidate can be found in theoretical extensions of the standard model (SM), such as SuperSymmetry (SUSY) [26]. In SUSY a symmetry between fermions and bosons is introduced. For each fermion (boson) a supersymmetric partner boson (fermion) exists. As superpartners have been detected experimentally so far, the symmetry must be broken. In the frame of the Minimal Supersymmetric Standard Model (MSSM), a new symmetry called R-parity is introduced as

$$R = (-1)^{3B+L+2S} \tag{1.11}$$

with S being the spin and $R = 1$ for standard particles and $R = -1$ for sparticles. Standard particles have a positive R-parity whereas superpartners have a negative R-parity. As only decays and interactions which conserve R-parity are allowed, a supersymmetric particle cannot decay into supersymmetric particles. With this definition, the lightest supersymmetric particle (LSP) is stable and, if it is electrically neutral, would make an ideal candidate for WIMPs. As the mass hirarchy of SUSY is unknown, the LSP is not defined and several candidates are possible, e.g. the sneutrino as the SUSY partner of the neutrino. A favourite LSP is the lightest of the 4 neutralinos, which are the mass eigenstates of the 4 gauginos, which are the spin $S = 1/2$ gauge bosons bino, wino and two higgsinos [25]. The lightest neutralino can be expressed as a linear combination of these 4 gauginos, with unknown amplitudes c_i:

$$\tilde{\chi}_1^0 = c_1\tilde{B}^0 + c_2\tilde{W}^0 + c_3\tilde{H}_u^0 + c_4\tilde{H}_d^0 \tag{1.12}$$

Depending on the value of these amplitudes, the mass of $\tilde{\chi}_1^0$ varies between $10\,\mathrm{GeV}/c^2$ and $10\,\mathrm{TeV}/c^2$, making it an ideal candidate for standard WIMP dark matter.
However, searches of SUSY at the LHC so far have given no indication of its existence. The most simple SUSY models, the MSSM and the constrained MSSM model called *CMSSM* have already been partially ruled out by the combination of results from direct and indirect dark matter experiments and production at the LHC.

1.2.3. Others (Asymmetric dark matter and low mass WIMPs)

Several observations in recent years have arisen interest in low mass dark matter with masses $\mathcal{O}(1)\,\mathrm{GeV}/c^2$. These observations include excess of events observed by direct detection experiments (see following Sec. 1.4) and a possible signal of dark matter annihilation from the galactic center [28].
While typical WIMPs as described in Sec. 1.2.2 would have masses in the $100\,\mathrm{GeV}/c^2$ to $1\,\mathrm{TeV}c^2$ range, their mass is also allowed to be as low as $m_\chi = 2\,\mathrm{GeV}/c^2$. This lower limit is set by the so-called Lee-Weinberg bound [29] from the freeze-out process depicted in Fig. 1.4: as the annihilation cross section σ_{ann} is $\mathcal{O}(m_{\mathrm{cdm}}^2/M^4)$ with m_{cdm} the dark matter particle mass and $M = 91\,\mathrm{GeV}/c^2$ the Z-boson mass, lighter particles have a lower

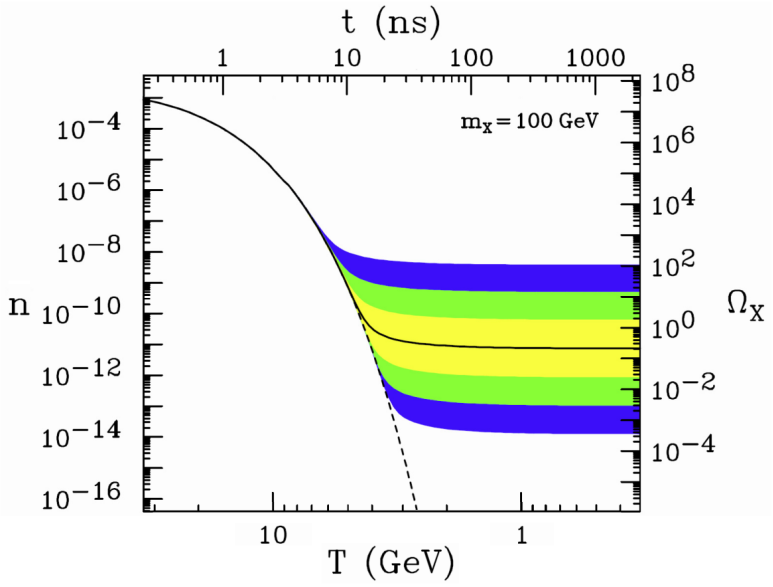

Figure 1.4.: Freeze-out process for a WIMP with mass $m_\chi = 100\,\mathrm{GeV}/c^2$ showing the co-moving number density n as a function of temperature T and age of the Universe t. Depending on the deviation from the weak interaction cross section by a factor of 10, 10^2 or 10^3 (yellow, green and blue shaded areas, respectively), a deviation of the resulting relic density is obtained. Figure adapted from [27].

interaction rate and therefore freeze out earlier. This would lead to a higher relic density which is incompatible with observations.

In contrast to the production of (low mass) WIMP dark matter in a freeze-out process is so-called *Asymmetric Dark Matter* (ADM). From the temperature fluctuations of the CMB (see Sec. 1.1.1) the overall density of dark matter in the Universe is derived to be approximately a factor of five higher than than the density of visible, baryonic matter, i.e. $\Omega_{\mathrm{cdm}} \simeq 5\,\Omega_{\mathrm{b}}$, suggesting a possible common origin of the two particle species. The principle idea behind ADM is that it was produced similarly to baryonic matter with an asymmetry of particles of their antiparticles of 10^{-10}, i.e. as an asymmetry between the DM particles and their antiparticles. The total density of ADM could then be described by

$$\Omega_{\mathrm{cdm}} \approx \frac{m_{\mathrm{cdm}}}{m_{\mathrm{b}}} \cdot \Omega_{\mathrm{b}} \tag{1.13}$$

where m_{b} is the mass of a baryon which is $\approx 1\,\mathrm{GeV}/c^2$, leading to a dark matter mass of $m_{\mathrm{cdm}} \approx 5\,\mathrm{GeV}/c^2$. The similarity between the origin of baryonic matter and ADM would also indicate that the dark sector could be as complex as the visible sector, i.e. that dark matter could have more than one constituent. For an extended review of ADM we refer to [30].

1.3. Detection methods for WIMP dark matter

The three fundamental detection methods for dark matter particles are depicted schematically in Fig. 1.5. In the production channel, the annihilation of standard model particles (denoted P in the figure) can create pairs of dark matter particles (denoted χ in the figure). Indirect detection is based on the opposite principle: to search for standard model particles as a product of dark matter annihilation. The third channel is direct detection, which is

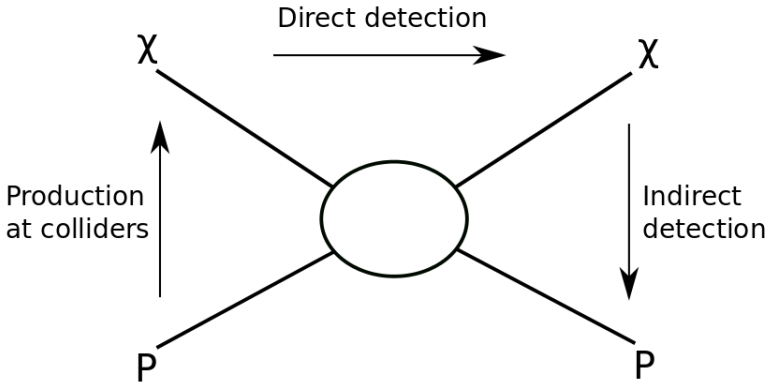

Figure 1.5.: Schematics of the three possible detection channels for dark matter particles (χ) via their interaction with standard model particles (P). Figure extracted from [31].

the principle employed in the EDELWEISS experiment. The principle here is to search for the (in)elastic scattering of a dark matter particle off a nucleus[3] of a detector.

1.3.1. Production at colliders

The principle of detecting dark matter at e.g. the Large Hadron Collider (LHC) at CERN is to produce a pair of dark matter particle and antiparticle in a collision of standard model particles in the detectors ATLAS or CMS. A requirement for this is the sufficient center-of-mass energy necessary to produce a pair of dark matter particles, which at the current stage of the LHC is 13 TeV. The LHC was not solely designed to search for the Higgs-Boson, but also to probe a parameter space of new physics which could be relevant for SUSY-particles, including the neutralino dark matter candidate for WIMPs. As WIMPs, by definition, interact only weakly in the LHC detectors, they can not be measured directly. Similar to neutrinos, they could only be found via the missing transverse energy and momentum of a reconstructed event. Both the experiments ATLAS and CMS therefore perform so-called *monojet* searches. While a pair of WIMP particles alone cannot be measured with the detector, the possible initial or final state radiation of a standard model particle during that pair production can be detected. The principle is therefore to search for events with a single, well-reconstructed jet which has a large transverse momentum and a large missing transverse energy. However, several background processes exist with similar properties. The main background arises from the production of a Z-boson and a single jet, where the boson decays into a pair of undetected neutrinos.

Monojet searches performed at the LHC [32] have shown no significant event excess above background hinting at dark matter. In a model-independent approach, an Effective Field Theory (EFT) can be used to compare the obtained results with those of direct detection experiments. Within the EFT, the mediating particles between the produced WIMPs and the standard model particles are too heavy to be produced directly at the collider, but can be integrated out. The limits obtained on the suppression scale of the EFT can be converted into exclusion limits on the WIMP-nucleon scattering cross section for a direct comparison with direct detection experiments. Opposite to those, the highest sensitivity for dark matter is achieved for low WIMP masses $m_\chi < 10\,\mathrm{GeV}/c^2$, while for higher masses the sensitivity decreases due to the required collision energy.

A fundamental drawback of this detection method is that it is model dependent. And even the discovery of a possible particle is not equal to solving the dark matter puzzle. A priori,

[3] Although for e.g. axion dark matter, the interaction is with the electrons.

no link exists between to the observed dark matter in a possible detected particle. The search for dark matter via collider production can therefore only complement other efforts to search for dark matter.

1.3.2. Indirect detection

Indirect detection dark matter experiments are sensitive to the annihilation cross section of WIMP dark matter. The detection principle is based on the assumption that (WIMP) dark matter is of Majorana type and thus its own antiparticle. Consequently, WIMPs can annihilate with each other producing standard model particles. The annihilation rate would be larger in over-densities of WIMPs, which one expects in gravitational wells of galaxies. The most significant gravitational well would be the galactic center, but possible sources of annihilation are also other stellar bodies, including the Sun and Earth, yet with much lower density and therefore lower annihilation rate. The decay products of this annihilation could be standard model particles and antiparticles such as electrons, positrons, photons and neutrinos. Earth- or space-based experiments search for an excess of these particles in the direction of an expected DM annihilation source. The great challenge is to discriminate a possible signal from the background of unknown astrophysical sources. Another difficulty is that charged particles are deflected by the magnetic field in our galaxy and therefore do not directly point to the source of their production. Strategies to address all these challenges are the modelling of astrophysical sources, simulations of the propagation of cosmic rays in the galaxy and a so-called *multi-messenger* approach: the detection of different types of particles is combined to suppress uncertainties in one channel.

Several possible signal hints have been found by indirect detection dark matter experiments. A selected one is a rise in the positron fraction, defined as $e^+/(e^+ + e^-)$, in the energy range from $10\,\mathrm{GeV}/c^2$ to $100\,\mathrm{GeV}/c^2$ which was first indicated by PAMELA [33] and later confirmed by Fermi LAT [34] and AMS-02 [35]. This rise contradicts with the expectation of a falling spectrum above this energy from known astrophysical sources. However, dark matter annihilation is not the only possible explanation and models exist in which the excess is caused by nearby Pulsars. An overview of the current status of indirect detection is e.g. given in [36].

1.3.3. Direct detection

The principle of direct dark matter detection, which is employed in the EDELWEISS experiment, is based on the hypothetical elastic scattering of a non-relativistic galactic halo WIMP on a nucleus of a target material, in the case of EDELWEISS a germanium atom. Although the interaction cross section of WIMPs is expected to be of the order of the weak scale, the high flux on Earth $\Phi_\chi \approx \mathcal{O}(10^5)\,\mathrm{cm}^{-2}\mathrm{s}^{-1}$ should be sufficiently large to detect a rare scattering process. To reduce the background induced by cosmic rays, in particular the one from cosmogenic muons which produce neutrons with similar interaction properties as WIMPs, direct detection experiments are located in underground laboratories where they are shielded by the rock overburden. Additional shielding of the detectors against ambient β- and γ-radiation as well as radiogenic and cosmogenic neutrons is also necessary. The kinematics of the non-relativistic scattering process lead to a differential energy spectrum for the recoil energy of the interaction, the shape of which depends on various astrophysical and experimental parameters, on the properties of the WIMP and on the target material. A first detailed calculation of this recoil spectrum was performed by Lewin and Smith [37] and later modified by Savage [38]. Here, we closely follow the description in [38] and summarize the equations which are relevant for the analysis performed within this thesis.

The elastic scattering of a WIMP with mass m_χ off a nucleus of mass M deposits a recoil energy E_{rec}, which can be calculated as

$$E_{\mathrm{rec}} = \frac{\mu^2 v^2}{M}(1 - \cos\theta) \tag{1.14}$$

where $\mu = \frac{m_\chi M}{m_\chi + M}$ is the reduced mass, v the relative velocity between WIMP and nucleus and θ the scattering angle in the center of mass frame.

The differential event rate normalized to a detector mass of 1 kg and given in units of dru = counts/kg/day/keV can be written as

$$\frac{dR}{dE_{\mathrm{rec}}} = \frac{\sigma(q)}{2m_\chi \mu^2}\rho_\chi \eta(E_{\mathrm{rec}}, t) \tag{1.15}$$

where $q = \sqrt{2ME_{\mathrm{rec}}}$ is the recoil momentum transfer of the nucleus, $\sigma(q)$ the WIMP-nucleus cross section and ρ_χ the local dark matter density, which for the purpose of comparing experiments is usually set to $\rho_\chi = 0.3\,\mathrm{GeV/c^2/cm^3}$. The mean inverse speed $\eta(E_{\mathrm{rec}}, t)$ is defined as

$$\eta(E_{\mathrm{rec}}, t) = \int_{u > v_{\mathrm{min}}} \frac{f(\vec{u}, t)}{u} d^3u \tag{1.16}$$

with the minimum WIMP velocity $v_{\mathrm{min}} = \sqrt{ME_{\mathrm{rec}}/2\mu^2}$ which results in a recoil energy E_{rec}. The velocity $\vec{u}$ of WIMPs relative to the detector can be described with the time-dependent distribution $f(\vec{u}, t)$, which will be described at a later point.

The WIMP-nucleus cross section $\sigma(q)$ can be written as

$$\sigma(q) = \sigma_0 F^2(q) \tag{1.17}$$

where σ_0 is the cross section for zero-momentum transfer and $F^2(q)$ the nuclear form factor, which is normalized to $F(0) = 1$. This form factor accounts for the fact that, as the momentum transfer q increases, the scattering amplitudes of the individual nucleons no longer add up in phase i.e. the coherence is lost. For this analysis a Woods-Saxon/Helm form factor was used, for which a parametrization can e.g. be found in the original publication of [37]. The interaction between WIMPs and the nucleus can have both scalar and spin-dependent contributions. Results given in the context of this work are based on a purely scalar interactions, for which the zero-momentum cross section can be written as

$$\sigma_0 = \frac{4\mu^2}{\pi}\left[Zf_{\mathrm{p}} + (A - Z)f_{\mathrm{n}}\right]^2 \tag{1.18}$$

with Z being the number of protons, A the atomic mass of the target and thus $A - Z$ the number of neutrons, and f_{p} and f_{n} are the respective couplings between WIMPs and protons or neutrons. The simple assumption is that $f_{\mathrm{p}} \approx f_{\mathrm{n}}$, but a variation of these couplings can be considered to increase the agreement with the findings of different target type experiments, due to their different proton and neutron fractions [39]. For the work performed here, the equality of both couplings was assumed, leading to a simplification of Eq. 1.18 to

$$\sigma_0 = \sigma_\chi \left(\frac{\mu}{\mu_\chi}\right)^2 A^2 \tag{1.19}$$

where we introduce the WIMP-nucleon cross section σ_χ which is defined via the equal interaction of a WIMP with either a proton or a neutron. Consequently, μ_n is the WIMP-nucleon reduced mass. To compare the results of different direct detection experiments, it is not only common to employ the same astrophysical parameters of the WIMP halo, but also to express the interaction in terms of WIMP-nucleon scattering instead of an interaction with the entire nucleus.

To fully calculate the recoil energy spectrum given in Eq. 1.15, the velocity distribution $f(\vec{u}, t)$ used in Eq. 1.16 is needed. In the standard halo model, WIMPs have a Maxwellian velocity distribution, which can be written as

$$\tilde{f}(\vec{v}) = \begin{cases} \frac{1}{N_\mathrm{esc}} \left(\frac{3}{2\pi\sigma_\mathrm{v}^2}\right)^{3/2} e^{-3\vec{v}^2/2\sigma_\mathrm{v}^2}, & \text{for } |\vec{v}| < v_\mathrm{esc} \\ 0 & \text{otherwise.} \end{cases} \tag{1.20}$$

and is described by the velocity dispersion σ_v, the truncating escape velocity v_esc for which WIMPs can leave the galaxy and N_esc is a normalization factor. It can be written as

$$N_\mathrm{esc} = \mathrm{erf}(z) - 2z\exp(-z^2)/\pi^{1/2} \tag{1.21}$$

where $z = v_\mathrm{esc}/\bar{v}_0$ is a unitless parameters with $\bar{v}_0 = \sqrt{2/3}\sigma_\mathrm{v}$ defined as the most probable speed. The description of the velocity distribution given in [38] takes into account that the Maxwellian distribution of either the galactic WIMP halo or a stream of dark matter flowing into our galaxy can have a bulk motion v_obs relative to the detector (the observer), i.e.

$$f(\vec{u}) = \tilde{f}(\vec{v}_\mathrm{obs} + \vec{u}) \tag{1.22}$$

With these definitions one can finally construct the mean inverse speed $\eta(E_\mathrm{rec}, t)$ given in Eq. 1.16 as

$$\eta(E_\mathrm{rec}, t) = \begin{cases} \frac{1}{\bar{v}_0 y}, & \text{for } z < y, x < |y - z| \\ \frac{1}{2N_\mathrm{esc}\bar{v}_0 y}\left[\mathrm{erf}(x+y) - \mathrm{erf}(x-y) - \frac{4}{\sqrt{\pi}} y e^{-x^2}\right], & \text{for } z > y, x < |y - z| \\ \frac{1}{2N_\mathrm{esc}\bar{v}_0 y}\left[\mathrm{erf}(z) - \mathrm{erf}(x-y) - \frac{2}{\sqrt{\pi}}(y + z - x)e^{-x^2}\right], & \text{for } |y - z| < x < y + z \\ 0, & \text{for } y + z < x \end{cases} \tag{1.23}$$

with the dimensionless parameters $x \equiv v_\mathrm{min}/\bar{v}_\mathrm{o}$, $y \equiv v_\mathrm{obs}/\bar{v}_\mathrm{o}$ and, as introduced above, $z \equiv v_\mathrm{esc}/\bar{v}_\mathrm{o}$.

For calculations of the interaction rate, one typically considers the values of the Standard Halo Model (SHM), which is a simplified model of a non-rotating isothermal sphere describing our Milky Way dark matter halo. Canonical values are $v_\mathrm{esc} = 544\,\mathrm{km/s}$ for the escape velocity and $\sigma_\mathrm{v} = 270\,\mathrm{km/s}$ for the velocity dispersion. Including the definition of the WIMP-nucleon cross section given in Eq. 1.19, we can write the differential rate in a detector given in Eq. 1.15 as

$$\frac{dR}{dE_\mathrm{rec}} = \frac{F(q)^2 \sigma_\chi \rho_\chi}{2 m_\chi \mu^2} \left(\frac{\mu}{\mu_\chi}\right)^2 A^2 \eta(E_\mathrm{rec}, t) \tag{1.24}$$

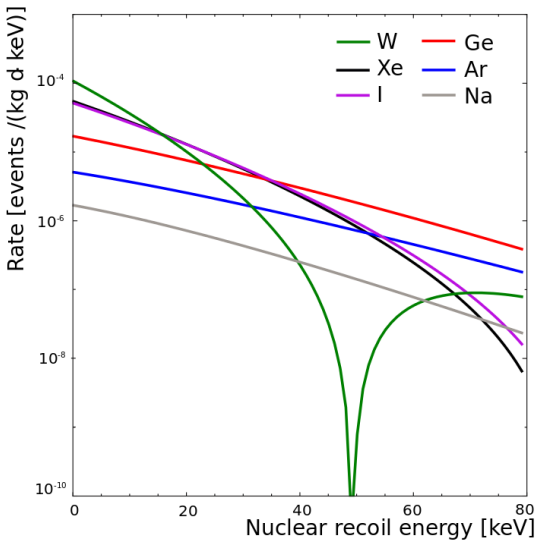

Figure 1.6.: Differential event rate for a WIMP of mass $m_\chi = 100\,\mathrm{GeV}/c^2$ and a scattering cross section with nucleons of $\sigma_\chi = 10^{-45}\,\mathrm{cm}^2$ for different target materials: tungsten (green), xenon (black), iodine (magenta), germanium (red), argon (blue) and sodium (grey). The "dip" in the event rate for tungsten is related to form factor corrections. Extracted from [31].

with the mean inverse speed $\eta(E_{\mathrm{rec}}, t)$ given in Eq. 1.23 and $F(q)$ the Woods-Saxon/Helms form factor given in [37]. We will use this formula later to derive the nuclear recoil energy spectra of the WIMP interaction in the EDELWEISS detectors. Figure 1.6 shows the expected event rate for a WIMP of mass $m_\chi = 100\,\mathrm{GeV}/c^2$ and WIMP-nucleon cross section $\sigma_\chi = 10^{-45}\,\mathrm{cm}^2$ in different detector materials and thus different A^2 and form factors. The influence of the WIMP mass m_χ on the recoil energy spectrum will be shown in Sec. 4.3.1 in the context of the analysis performed in this thesis.

Due to the motion of the Earth around the Sun, the rate given in Eq. 1.24 has an annual modulation, with an amplitude $\mathcal{O}(10\%)$ depending on the WIMP mass m_χ and a phase peaking on June 2$^{\mathrm{nd}}$. As will be shown in Sec. 1.4, several direct detection experiments use this annual modulation as a possible mean of discriminating a WIMP induced signal from backgrounds, such as DAMA/LIBRA and CoGeNT.

1.4. The current status of direct dark matter detection

As shown in Sec. 1.3.3, the direct detection of WIMP dark matter is based on the measurement of a nuclear recoil induced by a galactic halo WIMP. The recoil energy spectrum of the interaction depends on the WIMP mass m_χ, the atomic number A and the form factor F of the target nucleus, and the astrophysical parameters of the WIMP halo such as the escape velocity v_{esc}. Over the last decades, different detector technologies have emerged which make use of various target materials and detection principles, thus being most sensitive to specific WIMP mass ranges or also to spin-dependent scattering processes (in case the target material contains elements with unpaired nucleons). To separate a potential WIMP induced signal from background, various discrimination techniques have been developed. Most commonly used is a multi-channel readout of the detector: measuring two parameters of a particle interaction in the detector allows to discriminate between electron recoils related to background processes and nuclear recoils of a potential WIMP signal (or neutron). Figure 1.7 depicts the different readout channels which are used in current experiments. The three main detection channels of an energy deposit are phonons/heat, ionization in the

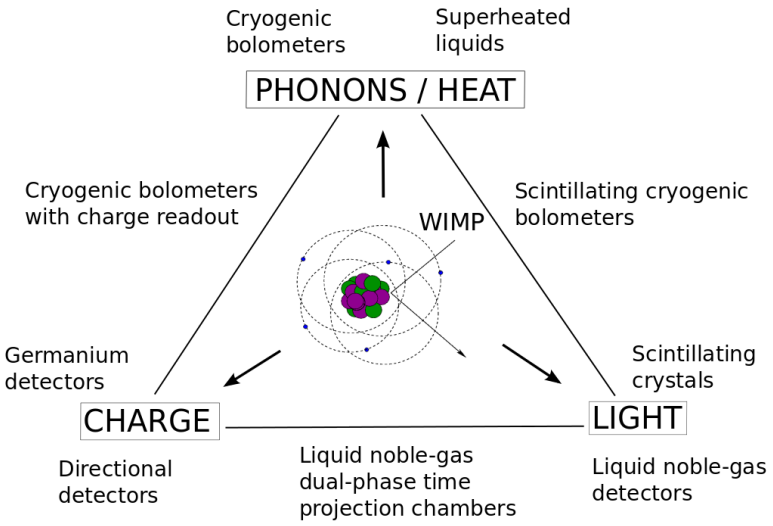

Figure 1.7.: Schematics of the possible readout channels of direct detection experiments. The combination of multiple channels allows to separate between the scattering of a WIMP on the nucleus and the scattering of other particles on the electron shell (not depicted here). Extracted from [31].

form of free charge carriers and scintillation light. Combining two of these channels results in powerful discrimination techniques. However, experiments can also use only a single readout channel. In that case, other principles for event discrimination have to be employed. Among them are pulse shape discrimination, directionality of the incoming particle or the time variation of the measured event rate in order to search for the annual modulation of a WIMP signal. In the following, we give an overview of the various experiments and their detection principle, closely based on the review given in [31].

Scintillator crystals at room temperature

Direct detection experiments based on scintillators measure the emission of light which is produced by the excitation and subsequent de-excitations of the target electrons due to through-going particles. These experiments are relatively simple to operate and allow large detector masses. However, no particle discrimination is possible and the only detection method is based on the annual modulation of a potential signal in addition to the measured background rate. The most prominent example for a scintillator based experiment is DAMA/LIBRA at the Gran Sasso underground laboratory, which employs ultra low-radioactive NaI(TI) crystals. Over the past 14 years it has collected a combined dataset of 1.33 ton·yr exposure showing a clear annual modulation of the low energy bin with 9.3σ confidence level. If interpreted as a WIMP signal, the reconstructed WIMP mass depends on the target nucleus on which the WIMP scatters: for sodium a WIMP of $m_\chi = 10 - 15\,\mathrm{GeV}/c^2$ is favoured, for iodine a WIMP with mass $m_\chi = 60 - 100\,\mathrm{GeV}/c^2$. These results are controversial, as they have been in strong tension with results by various other experiments. Other source for the annual modulation are considered such as a modulation due to atmospheric muons, neutrinos or neutrons. Other experiments such as Anais [40] in Spain, DM-Ice [41] at the south-pole and KIMs in South Korea [42] try to confirm or discard the signal with similar technologies.

Germanium detectors

Detectors made out of high-purity germanium, doped p- or n-type, can be operated at liquid nitrogen temperatue $T = 77\,\mathrm{K}$. They achieve low threshold of $\approx 0.5\,\mathrm{keV_{ee}}$ and an

excellent energy resolution due to the operation with an ionization channel only. P-type semiconductors have a dead layer around the detector which shields against α and β radiation. Otherwise, the rejection of surface events is based on pulse shape analysis. Indeed, with only a single ionization readout channel, no discrimination is possible between electron recoil and nuclear recoil events. An example is the CoGeNT experiment at Soudan Underground Laboratory. In a 3.4 year dataset it measured an annual modulation of the low energy event rate [43], although with an amplitude 4-7 times larger than expected from WIMPs. If interpreted as a signal, the corresponding WIMP mass is $m_\chi = 8\,\mathrm{GeV}/c^2$ and the cross section $\sigma_\chi = 2.5 \times 10^{-41}\,\mathrm{cm}^2$, which is however excluded by various other direct detection experiments. Similar type experiments are MALBEK [44] and CDEX-1 [45].

Cryogenic bolometers

Cryogenic bolometers measure a phonon signal from a particle interaction and either an additional scintillation or charge signal which is quenched and can be used to discriminate between nuclear and electronic recoils. The working principle of such a detector used in EDELWEISS-III is described in more detail in Sec. 2.2. While these detectors reach low threshold and excellent energy resolution, the disadvantage is the limited crystal size, which required a large array of detectors, complicating the analysis. Besides the EDELWEISS experiment, cryogenic bolometers are e.g. also used by CDMS II [46]. CDMS is located in the Soudan Underground Laboratory and uses a mix of 19 Ge and 11 Si detectors. A fiducialization of the detector volume is performed with the athermal phonon component which is read out with Transition Edge Sensors (TES). In the analysis of Si-crystal data, an excess of events was observed [47] which can be interpreted as a WIMP with $m_\chi = 8.6\,\mathrm{GeV}/c^2$ and $\sigma_\chi = 1.9 \cdot 10^{-41}\,\mathrm{cm}^2$. This excess was not found in the successor experiment SuperCDMS, which uses an improved detector design with better surface event rejection [48]. In CDMSlite, a single detector is operated in a special mode, in which low energy signals are boosted (Neganov-Luke amplification) to achieve a lower threshold, leading to the best sensitivity in parts of the low mass region [49]. Another experiment ist CRESST-II, which uses $CaWO_4$ crystals with a phonon and scintillation light readout via TES. CRESST-II observed an excess of events [50] corresponding to a WIMP mass of $m_\chi = 11.6\,\mathrm{GeV}/c^2$ or $m_\chi = 25.3\,\mathrm{GeV}/c^2$ depending on the interaction element. An improved detector layout lead to a significant decrease of the achievable energy threshold down to $600\,\mathrm{eV_{nr}}$ and a reduction of backgrounds from ^{210}Po decay in the detector holders, which might have caused the excess. With a detector module with the best energy threshold, CRESST-II reached for the first time a sensitivity to sub-GeV WIMPs [51].

Liquid noble-gas detectors

The advantage of liquid noble-gas detectors is their large target mass and the excellent self-shielding effect due to the high density of the target. These detectors are designed as time-projection chambers, in which the ionizing radiation produces ionization and scintillation light in the liquid. The scintillation light is measured with photomultipliers (PMTs) and the charges are extracted with a drift field. A discrimination between electron recoil backgrounds and nuclear recoil signals is performed with either pulse shape discrimination or the ratio of charge-to-light. Well known experiments using the latter principel are DarkSide, XENON100 [52] and LUX [53], which is the currently leading sensitivity experiment for both intermediate and high WIMP masses. An example for a single phase experiment is XMASS [54]. The next generation of liquid noble gas experiments will employ masses of several tons. The XENON1T [52] experiment is under construction and is expected to take data within the next year.

The field of direct dark matter detection has grown large and there are many experiments which have not been listed here, e.g. Bubble-chamber and directional experiments. For

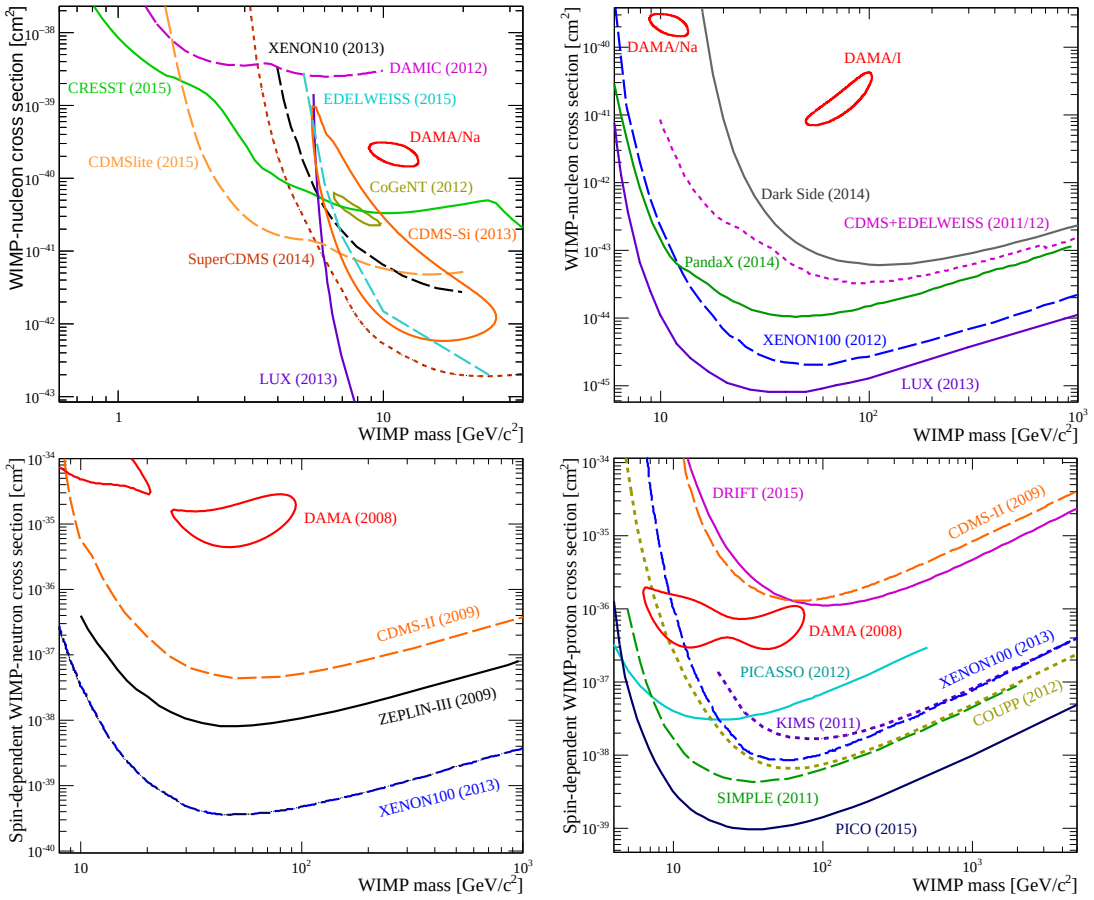

Figure 1.8.: Overview of exclusion limits and potential signal indications of direct detection dark matter experiments from Sep. 2015. *Top*: Spin-independent parameter space for low mass (left panel) and high mass WIMPs (right panel). For an update exclusion limit for LUX, see Fig. 4.35. *Bottom*: Spin-dependent paramter space for interaction with neutrons (left panel) and protons (right panel). Figures extracted from [31].

a full review, we refer to [31]. An overview of the current exclusion limits for both spin-independent and spin-dependent interactions is shown in Fig. 1.8. For spin-independent interactions, the current best limits are set by CRESST and CDMSLite at low masses and LUX at all higher masses (see also updated limit from LUX in Fig. 4.35). In the spin-dependent case, the best limit is set by XENON100 (for coupling to neutrons) and PICO (for coupling to protons). The future of direct detection dark matter search is outlined with projections of sensitivity in Fig. 1.9: standard mass WIMPs can be most effectively explored by large scalable liquid noble gas experiment such as XENON1T and LZ. The direction for cryogenic bolometer experiments is to make use of their low energy threshold and good resolution and to explore new parameter space for low mass WIMPs. A projection of the future for EDELWEISS can also be found in Fig. 4.37. The next frontier is the so-called neutrino floor, were detectors become sensitive to the coherent nucleon scattering of atmospheric and solar neutrinos [55].

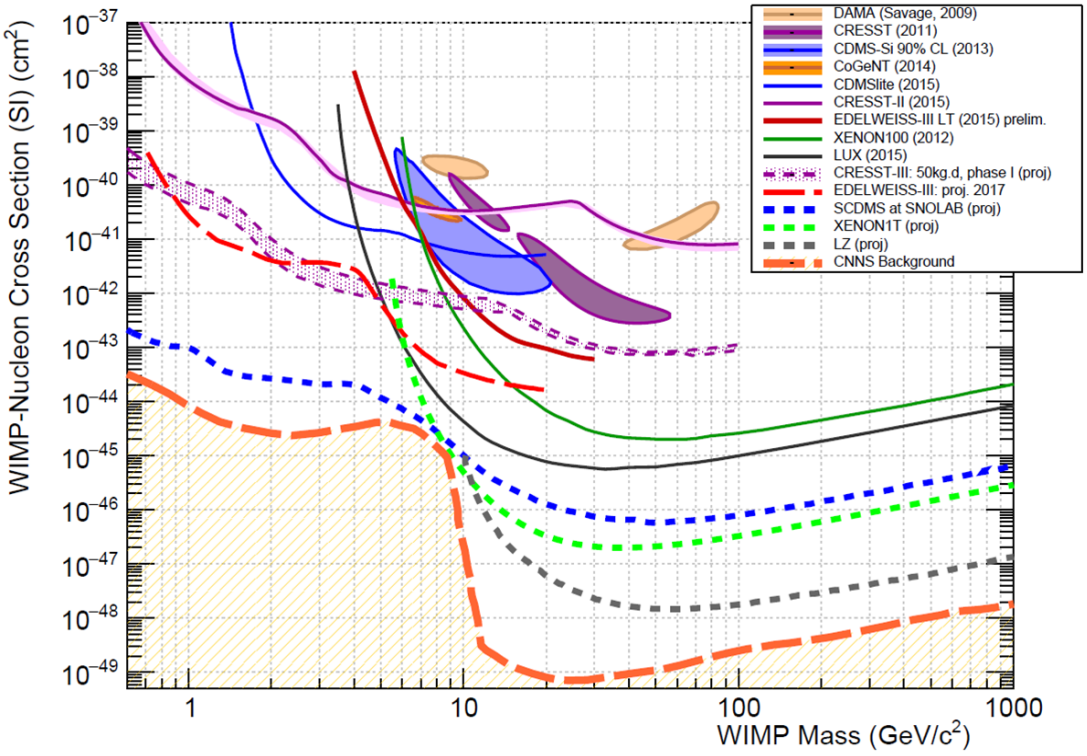

Figure 1.9.: Current status and prospects of the direct detection WIMP search. Plotted are existing signal claims (contours) and upper exclusion limits (lines) in the parameter space of WIMP-nucleon scattering cross section σ_χ and WIMP mass m_χ. Solid limits represent obtained limits while dashed lines show the projected sensitivity of future experiments. The so-called *neutrino-floor*, which is depicted as yellow shaded area, marks the parameter space for which a detectors are sensitive to the predicted coherent scattering of solar and atmospheric neutrinos. To detector dark matter with particle properties below this barrier, new detection techniques such as directional detection would have to be employed. For current result of the EDELWEISS experiment, including the low WIMP mass region, see also figures 3.4,3.10 and 4.35, while Fig. 4.37 shows the projected sensitivity.

2. The EDELWEISS-III experiment

The data which were analysed in the framework of this thesis were recorded with the EDELWEISS-III experiment. EDELWEISS is a direct detection experiment primarily designed to search for WIMP dark matter. Its goal is the detection of nuclear recoils from galactic halo WIMPs in an array of germanium bolometer detectors which are cooled down to 18 mK. As all rare event search experiments, it is located in an underground laboratory to signifiantly reduce of cosmic radiation. The acronym EDELWEISS stands for *Expérience pour Détecter les WIMPs en Site Souterrain* and the experiment was established in 1990 by French groups from Lyon, Paris and Grenoble. Since then, the collaboration grew and now includes several institutes from CNRS and CEA (France), Dubna (Russia), Oxford and Sheffield (UK) as well as KIT (Germany). Both the EDELWEISS-I [56] and EDELWEISS-II [57],[58] stages of the experiment published exclusion limits on the scattering cross section of galactic halo WIMPs. In 2012 construction for the improved EDELWEISS-III setup started with better shielding, improved electronics and DAQ-system, and new detectors.

The EDELWEISS-III experiment will be explained in detail in this chapter. First, the setup, from the shielding concept to the cryogenic system, will be introduced in Sec. 2.1. The following Sec. 2.2 is dedicated to the working principle of the detectors and explains how nuclear recoils from possible WIMP signal interactions can be discriminated from the dominating electron recoils and from background originating from interactions on the detector surface. Section 2.3 gives a short overview of how the recorded data is processed, from the initial pulse reconstruction, the energy calibration and the storage of data files. Also described in this context is the data transfer from the underground laboratory to the Tier-2 computer cluster at INPL, Lyon, and the backup to a long term storage. Both processes use a dedicated database system and were monitored and maintained in the framework of this thesis. Last, the residual background in the experiment related the to interactions of particles is detailed in Sec. 2.4. The focus here is clearly on the low energy background, which is relevant for the maximum likelihood analysis detailed in Ch. 4. The results obtained from EDELWEISS-III data for both standard and low mass WIMPs, using different analysis methods, are described in the following Ch. 3.

2.1. Experimental setup

2.1.1. Underground installation and shielding concept

To shield the experiment from cosmic ray induced radiation, in particular muons, the EDELWEISS setup is installed in the deepest underground laboratory in Europe, the *Labo-*

ratoire Souterrain de Modane (LSM) together with other experiments such as NEMO [59]. The LSM is located in the south-western Alps, in the middle of the 13 km-long car tunnel connecting the town of Modane in France to Bardonecchia in Italy, as it is shown in Fig. 2.1. The maximum rock overburden of 1800 m (4800 m w.e.) reduces the flux of atmospheric muons down to 5 muons/m^2/day [60], which is a factor 10^6 lower compared to the muon flux at sea level. Muons are relevant for dark matter search as they can induce neutrons in materials surrounding the detectors or in the vicinity of the experiment which are, a priori, indistinguishable from a possible WIMP signal. To tag the residual muons and reject all events which are in coincidence with a through-going muon, the setup is surrounded by an active muon veto system as it is shown in Fig. 2.2. It consists of a total of 46 plastic scintillator modules and has a combined surface area of 100 m^2. These modules surround the experiment almost hermetically with an effective geometric coverage of $\simeq$98% for through-going muons, with only small gaps remaining on the sides due to the support structure and the electrical and cryogenic supply lines. To cover a gap between the two halves of the veto due to the cryogenic supply line, four modules are installed on the top center. The efficiency of the whole system for the EDELWEISS-III configuration has been determined as $\epsilon_{\mu-\text{veto}} > 93\%$ (90% C.L.) [61].The active muon veto system surrounds several layers of further passive shielding. The first consists of 50 cm of polyethylene (PE) which moderates or captures neutrons from ambient radioactivity in the surrounding rock or other materials. Within the PE-shield is a layer of 20 cm thick lead which has a total weight of 40 tons and suppresses the gamma background to less than 1% of its intensity outside the experiment. The two innermost centimetres of this lead shield are made of *Roman lead* which comes from a sunken galley [62]. After having been protected from cosmic rays by the water shield for a long time, Roman lead has a reduced activity and the radioactive isotope ^{210}Pb which has a half-life of $T_{1/2} = 22.3$ years is reduced by two orders of magnitude to below 120 mBq/kg. The high neutron yield from cosmic ray muons in the lead shield can be compensated by the active rejection of muon-induced events. Located within the lead shield is the cryostat housing the detectors (see following Sec. 2.1.2). Its thermal screens are made out of ultra-pure copper and act as further shield to reduce ambient gamma radiation. Installed within the cryostat at the 1 K stage are additional pieces of PE (10 cm) and roman lead (15 cm), as it is shown in Fig. 2.3.

The entire shielding structure around the cryostat consists of two halves which are mounted on rails. Both parts can slide apart to allow accessing the cryostat as well as the electronics located next to it. The whole upper part of the setup (see Fig. 2.2), including the muon-veto system, is housed in a clean room of class 10000. Within the clean room the radon level is reduced down to 10 Bq/m^3 compared to 20 Bq/m^3 in the rest of LSM. The radon isotope ^{222}Rn which has a half-live of $T_{1/2} = 3.8$ days is a radioactive noble gas and a product of the natural decay chain of ^{238}U. It is a particularly difficult background for rare event search due to its high mobility and high absorption on surfaces. In its decay chain are several charged particles which constitute the surface background of the detectors (see Sec. 2.4.5). For this reason, the small remaining space between cryostat and inner lead shielding which has a total volume of $\approx$0.1 m^3 is continously flushed with deradonized air with an activity of less than 20 mBq/m^3 [64]. The activity of radon in this volume is continously measured with a dedicated detector. As it has been shown in [65] for the EDELWEISS-II configuration, the measured rate of electron recoil events within the detector is correlated with the radon level around the cryostat. Periods during which the supply with radon depleted air was interrupted and the level increased up to the clean room level, resulted in an increase of up to 50% in the rate of electron recoil events.

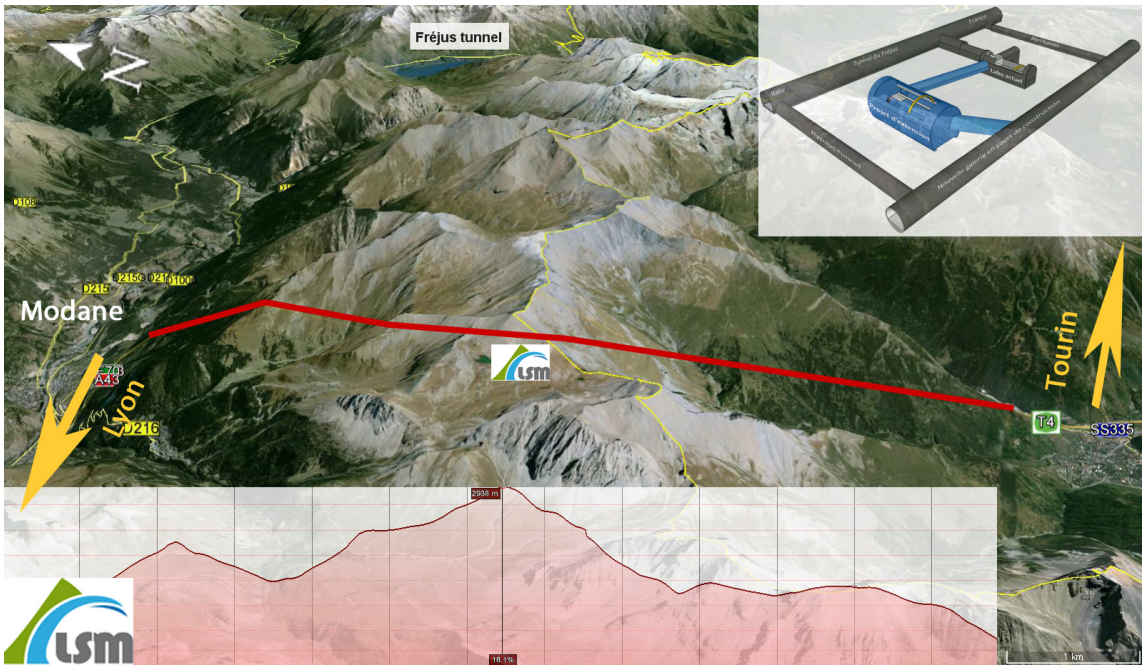

Figure 2.1.: Location of the LSM underground laboratory hosting the EDELWEISS experiment in the middle of the car tunnel under the Fréjus mountain. *Bottom*: Mountain profile showing the maximum rock overburden of 1800 m (4800 m w.e.). *Top right*: location of the LSM laboratory (smaller gray hall) with respect to the car tunnel (left tube) and the safety gallery (right tube). A planned larger extension of LSM is shown in blue. Figure from [63].

2.1.2. Cryostat and cold electronics

The EDELWEISS-III detectors are mounted in a custom designed dilution cryostat which was also used in the previous EDELWEISS-II phase of the experiment. The cryostat has an inverted geometry to reduce vibrations and allow for easier access to the experimental chamber on the top, as it is shown in Fig. 2.3. It has a volume of 50 l and was designed to host up to 40 detectors. The detectors are mounted on four copper plates in an arrangement which was optimized for maximum self-shielding. They are organised in 12 towers which are connected to the cold electronics in the 100 K volume with Kapton cables which were developed in-house [66]. Each detector is installed with Teflon clamps in a copper casing to shield against infra-red radiation. The working principle of the cryostat is based on the enthalpy coming from the mixing of liquid ^{3}He and ^{4}He isotopes. The consumption of helium is reduced by a helium reliquifier. While the cryostat allows to reach temperatures down to 10 mK with a stability of $\pm 10\,\mu$K, the normal operating temperature of the bolometers is 18 mK and can be kept stable for months even when fully equipped with $\approx$40 kg of detectors. A total of 5 consecutive thermal screens surround the experimental chamber and are at temperatures of 10 mK, 1 K, 4 K, 40 K and 300 K. They are made out of extremely pure copper. An approximately 2 m long cryoline connects the thermal machines, which are in the clean room outside the EDELWEISS shielding, with the cryostat. While this decoupling reduces vibration noise and microphonics it resulted in a small gap in the muon-veto system which is partly compensated by the 4 extra top modules seen in Fig. 2.2. Installed within the 100 K volume are capacitances, relays and *field effect transistor* (FET) electronics. They produce radiation from which the detectors are shielded by an additional lead plate within the cryostat. The guiding principle behind the design of the readout electronics was to maximize the distance to the detectors in order to reduce the background coming from the electrical components, while improving the baseline resolution for heat and ionization signals [67].

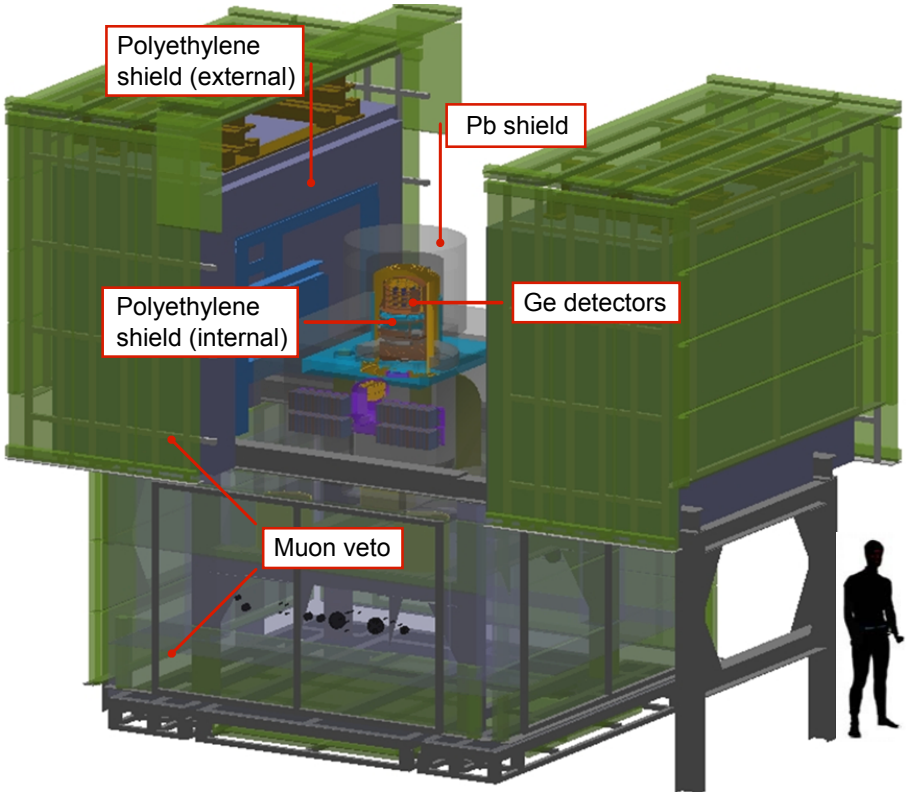

Figure 2.2.: Setup of the EDELWEISS-III experiment. The cryostat housing the detectors in the center is surrounded by a passive shielding of 20 cm lead and 50 cm of polyethylene. Outermost is the active muon-veto system to tag through-going muons. Only the upper part of the setup is installed in a clean room. The two halves of the shielding are mounted on rails to gain access to the cryostat and electronics.

2.2. Germanium detectors

The detectors employed in EDELWEISS-III are HPGe crystals with a cylindrical shape of 70 mm diameter and 40 mm height. They are of type *FID800*, where FID stands for *Fully Inter Digitized* and refers to the design of the readout electrodes and 800 is the typical detector mass in grams. Actual measured detector masses, however, range from 801 g to 890 g. Each detector is a high-purity germanium mono-crystal which, at the operating temperature of typically 18 mK, acts as a bolometer. A particle interaction in the detector produces phonons, which are measured by two Ge *Neutron Transmutation Doped* (NTD) sensors, glued on top and bottom of the detector. As germanium is a semi-conductor, with a lower band gap energy of 0.67 eV at 300 K, every particle recoil also produces free charges in the crystal. For Ge, the energy required to produce a single electron-hole pair (e^-/h^+) is $\epsilon = 2.96\,\text{eV}$ [68], which means that for an electron recoil of 1 keV more than 300 e^-/h^+-pairs are produced. These charges are collected by aluminium electrodes, which are evaporated on the surface, and biased with different voltages to create an electric field in the crystal, as it is shown in Fig. 2.4. To minimize charge trapping, which reduces the number of collected charges and thus the energy resolution, the crystals are made of high-purity purity Ge and the number of charged impurities is less than $10^{10}\,\text{cm}^{-3}$. In the following section, the principle of the energy measurement of the heat and ionization channels of a detector will be described in more detail. In section 2.2.2 the discrimination between different particle recoil types based on the fraction of ionization energy will be discussed. Last, the rejection of surface events with the electrode configuration of the FID800 detectors will be introduced in Sec. 2.2.3.

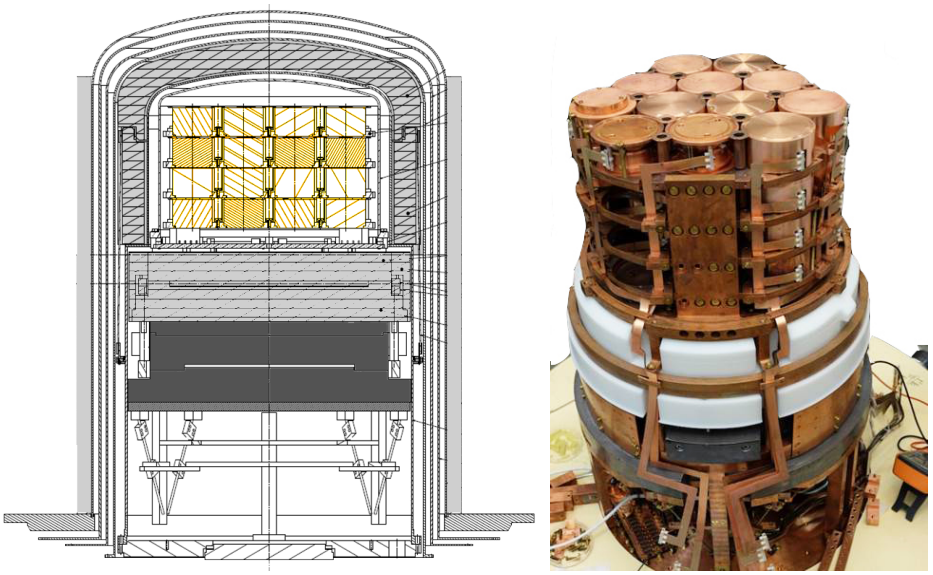

Figure 2.3.: *Left*: Technical drawing of the EDELWEISS-III cryostat with the additional polyethylene (light gray) and roman lead shielding (dark gray) around and under the detector array (yellow). *Right*: Picture of the opened cryostat revealing the detector array. All detectors are hosted in a copper casing and installed on four levels and read out as 12 towers connected with Cu-Kapton cables.

2.2.1. Measurement of heat and ionization energy

The interaction of a particle in the Ge-crystal creates lattice vibrations, so-called *phonons*, which are measured as a heat signal. The Ge-NTD sensors employed in EDELWEISS are designed to measure the thermalized phonon signal, although it has been shown, that in principle they are also sensitive to *athermal* phonons [69]. Such athermal (non-equilibrium) phonons can, for example, be used to determine the location of an interaction within the detector, as it is done in the CDMS-experiment [70] or for pulse shape discrimination. In the bolometers, an energy deposit E_{rec} causes a temperature rise ΔT, which depends on the combined heat capacity $C(T)$ of the system bolometer, NTD sensors and parasitic heat capacitances:

$$\Delta T = \frac{E_{\mathrm{rec}}}{C(T)} \tag{2.1}$$

Each bolometer is weakly coupled to the thermal bath of the cryostat via a gold wire. After a temperature increase, the temperature slowly returns to the equilibrium state, with a time constant of 100 to 500 ms. To measure even the smallest energy deposits as a temperature increase, the heat capacity has to be as low as possible. At low temperatures, this capacity can be described by the Debye law as

$$C(T) \propto \left(\frac{T}{T_{\mathrm{D}}}\right)^3 \tag{2.2}$$

where $T_{\mathrm{D}} \approx 360\,\mathrm{K}$ is the Debye temperature for germanium. It must be noted, that the heat capacity of the small NTD sensors is of the same order as the capacity of the 800 g bolometers. Each of the two NTD sensors works as a thermistor and is operated in the resistive transition, which allows to measure a temperature increase through a change in

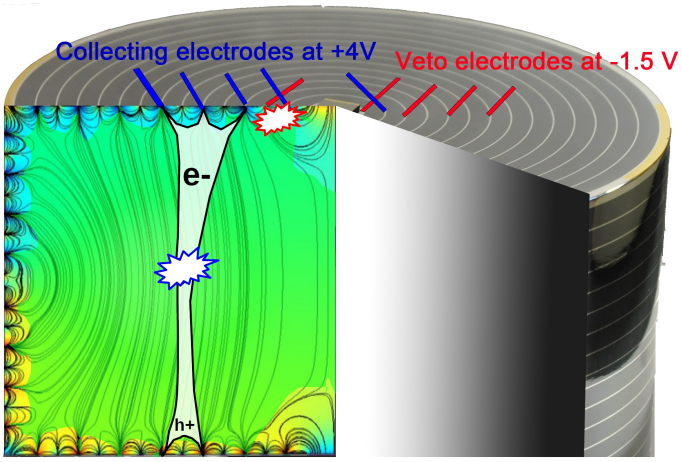

Figure 2.4.: Map of the rationally symmetric electric field in an FID800 detector with standard voltage configuration used in EDELWEISS-III. The green shaded area marks the fiducial volume which, while the blue (yellow) shaded area is the surface volume of the upper (lower) side of the detector. Bulk events (blue) have charges drifted to the set of collecting electrodes with higher potential, while surface events (red) have their charges drifted to both collectin and veto electrodes of one side. A selection of events from either volume can be achieved with a combination of cuts on the signals of the collecting and veto electrodes. Modified from [63].

resistance R:

$$R = R_0 \exp \sqrt{\frac{T_0}{T}} \tag{2.3}$$

where the two constants R_0 and T_0 are sensor dependent properties, and of order of Ω and K. The resulting resistance R for an operating temperature of the bolometer of $T = 18\,mK$ is $\mathcal{O}(\mathrm{M}\Omega)$. It is read out by biasing the sensor with a constant current and measuring the voltage. The change ΔR in resistance due to the temperature increase ΔT of a particle interaction, leads to a typical change in voltage of $\mathcal{O}(\mathrm{nV})$ which can be measured.
In the normal operating mode of the FID800 detectors, with voltages applied on all electrodes, the measurement of the heat energy does not directly give the initial recoil energy E_{rec} of a particle. It includes an additional energy E_{Luke}, which increases the total measured heat signal to:

$$E_{\mathrm{tot}} = E_{\mathrm{rec}} + E_{\mathrm{Luke}} \tag{2.4}$$

The effect is known as Luke-Neganov amplification [71, 72], and the additional energy contribution E_{Luke} is caused by the drift of the e^-/h^+-pairs in the electric field:

$$E_{\mathrm{Luke}} = N \cdot e \cdot V \tag{2.5}$$

where N is the number of produced charge carriers, e the elementary charge and V the applied voltage between electrodes[1]. The number of charge carriers N which are produced is proportional to the recoil energy E_{rec}:

$$N = \frac{E_{\mathrm{rec}}}{\epsilon_p} \tag{2.6}$$

[1] As will be shown in the following Sec. 2.2.3 the 4 sets of electrodes are biased with different voltages. As a result, the E_{Luke} is different for bulk and for surface events.

The energy ϵ_p, which is needed to produce one e^-/h^+-pair depends on the recoil type in the detector and therefore on the particle type p. For γ's and β's, which scatter off the electron shell of the germanium atoms, an average energy of $\epsilon_\gamma \approx 3\,\mathrm{eV}$ is needed to produce an e^-/h^+-pair. WIMPs are expected to scatter off the Ge-nucleus and produce a nuclear recoil as neutrons. Due to the different energy losses of the ionizing particles in Ge, a larger average energy of $\epsilon_n = 9\,\mathrm{eV}$ is required for nuclear recoils and the ionization signal is quenched.
The ionization energy E_{ion} which is measured on one of the electrodes of an FID800 detector, is directly proportional to the number of charged particles N and therefore, with Eq. 2.6, can be written as

$$E^p_{\mathrm{ion}} = c_{\mathrm{ion}} \frac{E_{\mathrm{rec}}}{\epsilon_p} = Q^p E_{\mathrm{rec}} \tag{2.7}$$

where c_{ion} is a calibration coefficient and Q_p is the so-called ionization yield for a particle of type p. In EDELWEISS, the energy scale of all readout channels (ionization and heat) is calibrated with bulk electron recoils, and therefore in units of $\mathrm{keV_{ee}}$. A ^{133}Ba source is used for the calibration, which produces a 356 keV photopeak in the measured energy spectrum. The calibration coefficient c_{ion} is chosen such, that this initial recoil energy $E_{\mathrm{rec}} = 356\,\mathrm{keV}$ corresponds to $E_{\mathrm{ion}} = 356\,\mathrm{keV_{ee}}$. Effectively, the ionization yield Q_γ for electron recoils is normalized to $\langle Q_\gamma \rangle = 1$. This can be observed, for example, in the ^{133}Ba calibration measurement shown in Fig. 2.6b, where the population of electron recoils is centred around $Q_\gamma = 1$ for all recoil energies E_{rec}. As a result of this calibration, the average ionization yield for neutrons (and WIMPs) is

$$\langle Q_n \rangle = \epsilon_\gamma/\epsilon_n = {}^{3\,\mathrm{eV}}/_{9\,\mathrm{eV}} \approx 0.3 \tag{2.8}$$

In practice, Q_n is energy dependent and a semi-empirical parametrization of $Q_n(E_{\mathrm{rec}})$ was derived by Lindhard [73]. An example of the Lindhard parametrization for germanium with measurements by different experiments is given in Fig. 2.5. For the EDELWEISS detectors, the energy dependence of the nuclear recoil ionization yield Q_{n} has been measured with neutron calibration data to [74]

$$Q_{\mathrm{n}}(E_{\mathrm{rec}}) = 0.16 E^{0.18}_{\mathrm{rec}} \tag{2.9}$$

which is in good agreement with the Lindhard parametrization.

With the introduction of the principle of the ionization yield Q, the calibration of the total heat signal E_{tot} can be discussed. By combining Eq. 2.5 and Eq. 2.6, the total heat energy given in Eq. 2.4 can be expressed as a function of recoil energy only:

$$E^p_{\mathrm{tot}} = E_{\mathrm{rec}} \left(1 + Q_p \frac{V}{\epsilon_\gamma} \right) \tag{2.10}$$

The total heat energy therefore depends on the initial recoil energy E_{rec} and the additional Luke energy, which is proportional to the number of created charges and thus a function of the ionization yield Q_p of a particle. In EDELWEISS, the heat signal of each of the two NTD sensors, is constructed as

$$E_{\mathrm{heat}} = c_{\mathrm{heat}} E_{\mathrm{tot}} \tag{2.11}$$

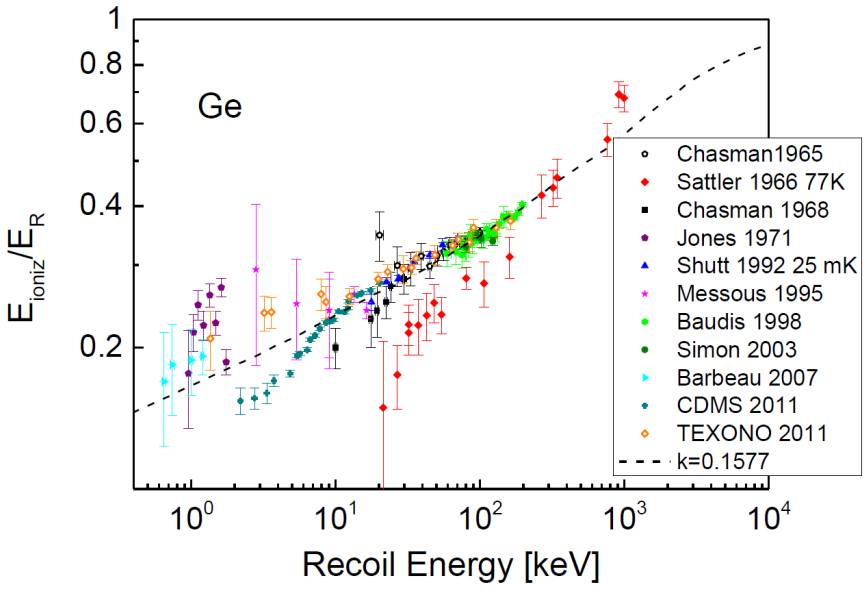

Figure 2.5.: Ratio of ionization energy E_{ion} over recoil energy E_{rec} for germanium as parametrized by lindhard (dashed line). The parametrization has been tested down to low energies of $\mathcal{O}$(keV). Extracted from [75].

The calibration factor c_{heat} is chosen such, that for electron recoils, the measured heat energy is equivalent to the recoil energy, i.e. $E^{\gamma}_{\mathrm{heat}} = E_{\mathrm{rec}}$. As a result, the heat energy of any particle p is given as

$$E^{p}_{\mathrm{heat}} = E_{\mathrm{rec}} \left(\frac{1 + Q_{\mathrm{p}} V/\epsilon_{\gamma}}{1 + V/\epsilon_{\gamma}} \right) \tag{2.12}$$

were p can either be a neutron/WIMP producing a nuclear recoil, or a surface event from e.g. γ's, β's , which has a reduced effective ionization yield.

2.2.2. Discrimination of nuclear and electron recoils

As it was discussed in Sec. 1.3.3, many direct detection experiments use the simultaneous measurement of multiple readout channels to discriminate between a potential WIMP signal and the background. In EDELWEISS, the discrimination is based on the different ionization signals, which are produced by electron and nuclear recoils. The discrimination is performed on an event-by-event basis with a variable called ionization yield Q, which is defined as

$$Q = \frac{E_{\mathrm{ion}}}{E_{\mathrm{rec}}} \tag{2.13}$$

By combining Eq. 2.7 and Eq. 2.12, the true recoil energy E_{rec} of any scattered particle p can be determined thanks to the simultaneous measurement of heat and ionization energy as:

$$E_{\mathrm{rec}} = E_{\mathrm{heat}} \left(1 + \frac{V}{\epsilon_{\gamma}} \right) - E_{\mathrm{ion}} \frac{V}{\epsilon_{\gamma}} \tag{2.14}$$

It was shown in Eq. 2.9, that the energy dependent ionization yield $Q_{\mathrm{n}}(E_{\mathrm{rec}})$ for nuclear recoils can be parametrized in EDELWEISS, while electron recoils by definition have an

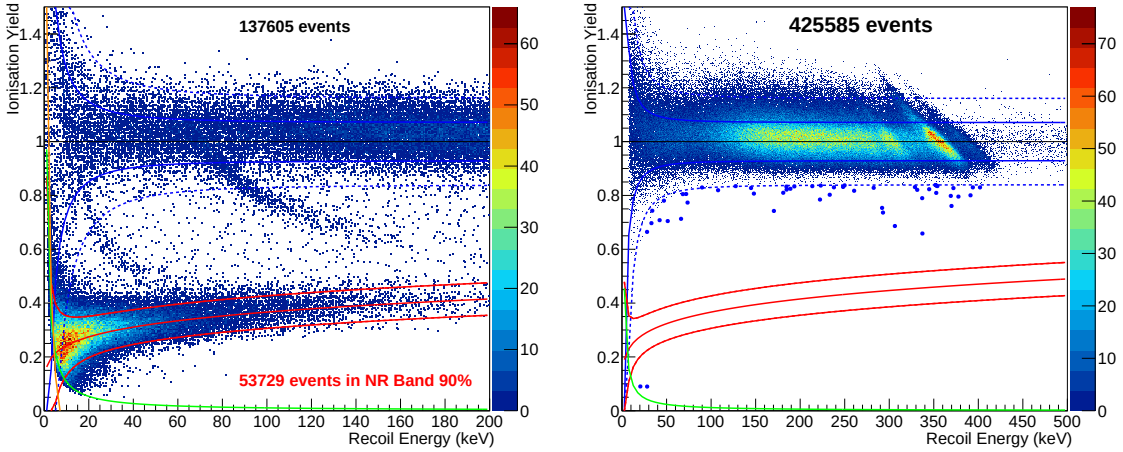

(a) ^{241}AmBe neutron-calibration **(b)** ^{133}Ba γ-calibration

Figure 2.6.: Results of large statistics calibration measurements with two different sources. Plotted is the ionization yield of the event density as a function of recoil energy E_{rec}. (a) The calibration with a neutron source not only shows nuclear recoils which fall into the 90% C.L. NR-band (red) but also additional γ-events from Compton scattering and short-lived excited states which fall out of the 90% and 99% C.L. ER-band (blue solid and dashed curves, respectively). See text for more details. (b) The calibration with a γ-source shows the excellent discrimination power between electron recoils and nuclear recoils.

ionization yield of $Q = 1$. This is illustrated in Fig. 2.6, which shows the results of two measurements with different calibration sources. Plotted in both subfigures is the ionization yield Q of events as a function of true recoil energy E_{rec}.

The events shown in Fig. 2.6a have been measured during a calibration with a ^{241}AmBe source. This source produces neutrons with energies up to 11 MeV, but with a branching ratio of 60% also additional high energy γ's with 4.4 MeV. While the neutrons induce nuclear recoils in the Ge-crystal, the gammas lose energy via Compton scattering and produce lower energy electron recoils. The neutrons can also inelastically scatter on the isotope ^{73}Ge, bringing it to the short lived excited states with $E = 13.3\,\mathrm{keV}$ ($T_{1/2} = 2.95\,\mu\mathrm{s}$) or $E = 66.8\,\mathrm{keV}$ ($T_{1/2} = 0.49\,\mathrm{s}$). In the decay, a γ of the same energy is produced that can be measured as an electron recoil in coincidence with the initial neutron. All three interactions can be observed in the Fig. 2.6a: nuclear recoils from the neutron follow the ionization yield $Q_{\mathrm{n}}(E_{\mathrm{rec}})$ given in Eq. 2.9 and their spread is proportional to the energy resolution. The Compton scattered gammas, on the other hand, are distributed in a band around $Q = 1$, while in between there are events from the inelastic scattering of neutrons. For those, the ionization yield is averaged over neutron and γ.

In order to search for a standard mass WIMP signal, the candidate events are typically single-scatter events falling in the 90% C.L. band of nuclear recoils (NR-band). The dominating electron recoil background is separated thanks to to the ionization yield. Single events can however leak into the NR band, especially if their charge is not fully collected and E_{ion} therefore underestimated. This is particularly the case for surface events, as it is discussed in the following Sec. 2.2.3. The discrimination power of the ionization yield Q for bulk events has been measured with a ^{133}Ba source. ^{133}Ba decays with a half-life of $T_{1/2} = 10.5\,\mathrm{years}$ producing γ's with energies between 53.2 keV and 383.9 keV. These gammas can interact in the bolometers via the photoeffect or lose energy via compton scattering. In both cases they induce an electron recoil which can be measured. Fig. 2.6b

shows the energy independent (by calibration) ionization yield of a calibration measurement. The rejection factor, i.e. the number of γ's misidentified as nuclear recoils was measured [76] to be:

$$R_\gamma < 6 \times 10^{-6} \text{ nuclear recoils}/\gamma \tag{2.15}$$

2.2.3. Rejection of surface events

The discrimination between electron and nuclear recoils via the ionization yield Q relies on the full measurement of the heat and ionization signals. A misreconstruction of either of them leads to a false determination of Q and thus possible "leakage" of events into the signal region of the nuclear recoil band. Due to the trapping of charges or their recombination, electron recoil events in the first 100μm below the detector surface suffer from incomplete charge collection [77]. And for particles hitting one of the electrodes on the detector surface, no charge signal is measured at all.

To reject surface events, FID800 detectors make use of their particular electrode design [78]. As shown in Fig. 2.4, all sides of the detector are covered with ring electrodes with 2 mm spacing. These are Al-electrodes of 200 μm width and 250 nm thickness, which have been evaporated on the detector with a shadow mask. Interleaved electrodes are connected by ultra-sonic bonding into 4 different groups, 2 on each top and bottom half, which are biased with different voltages. To address the issue of leakage currents between the electrodes, the detectors have undergone a XeF_2 dry-etching procedure [79]. In standard operating conditions, the so-called *fiducial* (or collecting) electrodes on top and bottom are biased with +4 V and -4 V, while the so-called *veto* electrodes in between are biased with a lower opposite sign voltage of -1.5 V and +1.5 V. A simulation of the resulting electric field lines is shown in Fig. 2.4. The green shaded area indicates the so-called *fiducial volume*, which constitutes approximately 75% of the total volume of a detector (≈600 g). In a simplified picutre, charges produced by a particle interaction within this volume are drifted along the field lines[2] to the corresponding fiducial electrodes on each side which have a total voltage of 8 V in between them. For these events only baseline noise is measured on the veto electrodes. For a particle interaction within a small region below the surface, the created charges follow the field lines which are almost parallel to the surface and are collected by the fiducial and veto electrode of the respective detector side. By rejecting events with a signal on one of the two veto electrodes in the offline analysis, a selection of fiducial events can be achieved. As will be shown in Sec. 4.1.4, the power of this rejection depends on the ionization energy of the event, as low energy events cannot be distinguished from baseline fluctuations of the veto electrode.

The rejection power of this fiducialization has been measured with calibration data from a ^{210}Pb-source. The source is implanted in a copper foil which is installed within the casing of a selected detector, facing its surface. As will be discussed in Sec. 2.4.5, the decay chain of ^{210}Pb includes α-particles, multiple low energy β's and a recoiling ^{206}Pb-nucleus. Figure 2.7 shows data recorded with a detector equipped with a ^{210}Pb-source, with a total of $\mathcal{O}(10^5)$ accumulated events for each particle type. After the application of the fiducial cut to reject surface events, only one event above $E_{\text{rec}} = 15$ keV is observed in the 90% C.L. nuclear recoil band, leading to a rejection factor [76] of

$$R_{\text{surf}} < 4 \times 10^{-5} \text{ events/alpha (90\% C.L.)} \tag{2.16}$$

A discussion of the surface background during normal operating conditions follows in Sec. 2.4.5.

[2] Due to scattering processes, the trajectories of the charges are more complicated, see also [80].

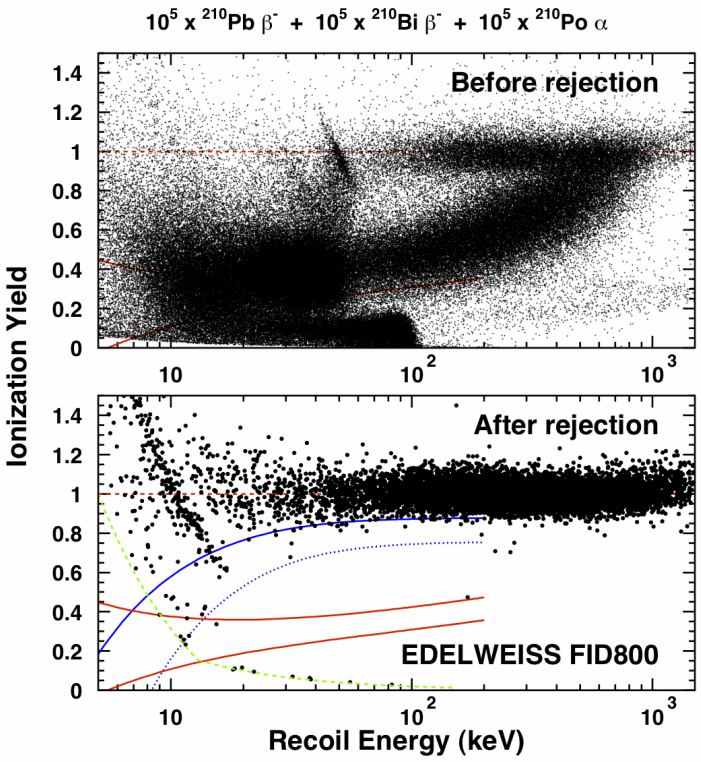

Figure 2.7.: Ionization yield as a function of recoil energy in keV for a ^{210}Pb calibration. *Top*: Events passing standard quality cuts. *Bottom*: events passing the standard quality cuts and the fiducial cut to reject surface events. Only 1 event above 15 keV is within the 90% C.L. band for nuclear recoils (red lines). The 99.99% (99%) gamma rejection is shown as blue dashed (solid) line. Extracted from [76].

To further improve the rejection of surface events, R&D efforts are ongoing to use a 40 MHz sampling frequency readout of the two fiducial electrodes [81], allowing the discrimination of fiducial events due to the rise time of the associated pulse.

2.3. Data acquisition and management

2.3.1. DAQ system and signal processing

The heat and ionization signals from the FET pre-amplifiers at 100 K are digitized outside the cryostat in dedicated electronic boxes at the 300 K stage. These so-called *bolometer boxes* are an in-house developement and, besides the digitization, fulfil multiple other functions: they control the cold electronics and relays, supply the voltage which is applied on the detector electrodes, reset the ionization *Digital Analog Conveter* (DAC), and generate the modulation pattern for the heat channels. Different versions of these bolometer boxes have been designed in EDELWEISS. The current version in use can digitize all 4 ionization and 1 of the 2 heat channels of a detector, which means that two bolometer boxes are needed to read out a single detector. In the typical configuration, the unused DACs of the second bolometer box, which only reads one heat channel, are used for the control of the ionization relays. The signals for all channels are digitized with a sampling frequency of 100 kHz and 16 bit precision and then guided via optical fibers to a crate system which was developed at the IPE institute of KIT [82]. The crate system is a scalable solution, which can be extended to handle a much larger number of detectors than installed in EDELWEISS-III. Adapted versions of the crate system are also used in the Auger experiment [83] and the KATRIN experiment [84]. The system uses multiple electronic components called *First Level Trigger*

(FLT) cards based on FPGAs (Field-programmable gate array) to perform signal shaping and triggering operations. In EDELWEISS-III, the capability to trigger on events was used to evaluate the time resolved readout with 40 MHz for the two fiducial electrodes of a single test detector with the goal of discriminating events based on pulse shape analysis of the ionization signal [81]. However, the general triggering of EDELWEISS-III detectors is not performed with this system. Instead, the data of all readout channels is streamed at a slower sampling rate of 100 kHz via standard Gigabit Ethernet to 3 standard Mac computers of the DAQ system.

Running on each Mac is an in-house developed software called SAMBA. It is used to control the electronics and to perform intensive signal processing such as event triggering as well as storing the data to disk. The triggering of an event is performed on the two heat channels of a detector. Nuclear recoils, which are the potential WIMP signal, have a lower ionization yield than electron recoils and therefore a larger heat than ionization signal for the same recoil energy. An additional advantage of triggering on the heat channel compared to the ionization channel is its lower baseline noise, which allows a lower trigger threshold energy before triggering on noise events. Before applying the trigger condition, the heat signal is first demodulated to an effective sampling frequency of 500 Hz to remove the square wave shape coming from the alternating polarisation of the NTD sensor. Low frequency noise is then removed by applying a high-pass Butterworth filter [85], while high-frequency noise is removed by convolution of the pulse with a signal template. The pulse shape of the heat pulse depends on the temperature of the NTD sensor. Therefore, the template has to be updated whenever the operating temperature of the bolometers change, which is only necessary during the cool-down of the cryostat. A trigger decision is then performed on the cross-correlation of heat pulse and template and with an variable amplitude threshold. This threshold is adapted in the time-frame of minutes to the baseline noise fluctuations of the heat channel which is used for triggering to keep a constant trigger rate of ≈10 mHz. The design of the trigger algorithm is to record the lowest possible event energies events without recording mostly noise fluctuations. For each triggered event, the signals of all 6 readout channels of the triggering detector, as well as all channels of the two nearest neighbours within its tower, are stored on disk for offline analysis. This allows to detect coincidence events where the same particle deposits energy in neighbouring detectors, but it can also be used to validate the trigger efficiency, by providing random triggers for a detector. For each of the two heat channels of a detector the demodulated trace of 1024 points centred around the trigger is stored, while for each of ionization channels two different traces are kept: the full trace, labelled "slow ionization", which is down-sampled to 1 kHz and uses a window of 2048 samples for each event and a smaller subsample of the event with 100 kHz sampling frequency which is labelled "fast ionization" and can be used for the precise time determination of the event. An example of the heat and (slow) ionization trace of a low energy event is given in Fig. 2.8.

All further signal processing is performed offline. The first step includes baseline subtraction and a slope correction. Following that, a filtering of the recorded pulse and the fit with a template pulse is performed. While optimal filtering is used for the heat pulse, this has not been implemented yet for the step-function ionization pulse, and a Butterworth filter is used instead. Both filtering methods give the estimated uncalibrated amplitude of the pulse as well as the χ^2-value of the goodness-of-fit, which can be used to reject events having pulse shapes different from the template, such as NTD-events or pile-up events. Before the calibration of the absolute energy scale, a cross-talk correction between different ionization channels needs to be performed. Cross-talk can occur between cables or within a bolometer box due to electromagnetic interferences. The cross-talk between any two of the ionization channels can be described by a linear coefficient between the (uncalibrated) energies of the two channels. It can therefore be fitted and corrected for.

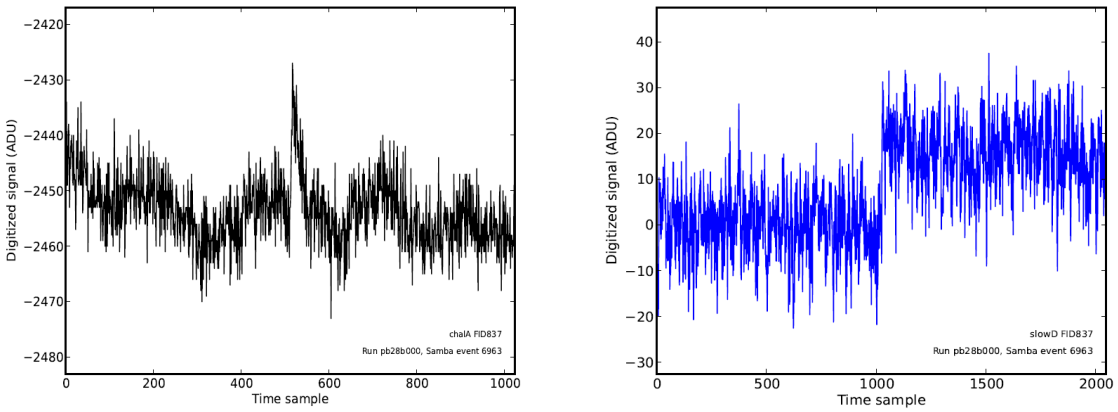

Figure 2.8.: Pre-processed pulse traces for a low energy event of ≈3 keV, recorded with detector FID837 during physics Run308 of the EDELWEISS-III experiment. *Left*: Pulse trace of the top NTD sensor in uncalibrated units of ADU for 1024 sample points. The small signal is centred in the window at 512 samples. *Right*: 1 kHz pulse trace ("slow ionization") of the bottom fiducial electrode which is a step function centred in the 2048 sample window of the event. Extracted from [86].

The energy calibration of the ionization channels of a detector, after cross-talk correction, is performed using data taken with an external ^{133}Ba source. With a probability of 62% a γ with 356 keV is produced, which can be observed in the measured data as a large photopeak next to the typical spectrum from Compton scattering. By fitting this peak for each of the ionization channels, the corresponding calibration factor from ADU to keV can be determined. Due to their high energy, the 356 keV γ dominantly scatter within the fiducial volume of the detectors and only a small fraction interacts in the surface volume. The photopeak is therefore much smaller for the two veto electrodes which makes it more difficult to calibrate them. Also more difficult to calibrate are the detectors located in the innermost towers of the detector array, due to the shielding effect from surrounding detectors and the external source position. Calibration measurements with a ^{133}Ba are performed regularly during a run.

The calibration of the heat channels relies on the previously calibrated ionization channels and is done differently. It is performed with a selection of clear fiducial events with energies $E \in [100, 200]$ keV. As the gain of a heat channel can change over time, the ratio of uncalibrated heat amplitude over calibrated ionization energy for these events is plotted as a function of time and fitted to extract the heat calibrated factor. Additionally, non-linearities in the heat channel, due to the temperature dependence of the heat capacity of the detectors, are corrected from the observed dispersion of this ratio as a function heat amplitude.

2.3.2. Data handling and storage

Only minor analysis tasks are performed directly on the Mac computers, which are installed in the LSM underground laboratory. The main part of the data processing, from the pulse fitting to the energy calibration, is performed on the *Centre de Calcul de l'IN2P3* (CC-IN2P3) in Lyon, which is a LHC Tier-2 computing cluster [87]. CC-IN2P3 has a high-speed connection to LSM, which allows for a fast transfer of recorded data with a speed of $\mathcal{O}(10)$ MiB/s. The data transfer from LSM to CC-IN2P3 is automatized and performed by a process management system which is part of the *KData* framework [88]. KData is a powerful analysis framework that was designed for the processing and analysis of data from a large detector array, such as the proposed EURECA experiment [89]. Both

the application of KData for analysis purposes and the data transfer management, are described in detail in [63]. Based on that, a summary is given in the following of the data transfer management, which was monitored and maintained in the framework of this thesis.

The automatic data transfer is managed using a CouchDB database [90]. CouchDB stores information as JSON-documents (Java Script Object Notation) and is *schema-free*, i.e. the type of information in the database is not fixed and can change from document to document, making it extremely flexible. Several CouchDB databases are in use within the EDELWEISS experiment, each for a different purpose: to store information coming from different slow control systems, for example the Radon monitor which measures the Radon level in the vicinity of the cryostat, and temperature and pressure measurements from the cryogenic system or the high voltage values of the muon-veto system. For a high availability and flexibility, all databases are hosted with a commercial provider, IBM Cloudant [91]. As backup, in case of network problems from the underground laboratory to the outside, the databases are also hosted on one of the Mac computer at LSM. Any changes to these database are automatically replicated to the versions hosted at IBM Cloudant. There are several convenient ways to access the stored data. The most tangible one is a web interface, which can be used to both read and change any database document manually. More convenient for the processing of multiple database documents are the different existing programming libraries to access CouchDB. Most commonly used in the scripts which control the data management is the python library Couchdbkit [92]. A third possibility is mainly used for slow control data: with the use of small web applications, so-called CouchApps, it is possible to directly visualize database information on a website. This feature is used for example to monitor the cryostat conditions and the Radon level.

The DAQ software SAMBA introduced in the previous section, is running in parallel on multiple Mac computers. Each of them reads out several detectors, triggers on events, and stores the recorded data into a single data partition file per hour. These files are a combination of ascii text and raw binary data and contain system configuration information and the raw digitized signals. File sizes range from a few MiB to several GiB, depending on the number of detectors and the type of run (WIMP search or calibration). For every one-day SAMBA run, which consists of several data partitions, additional log- and metafiles are also stored on disk: files are then copied by automated scripts to a separate Mac computer, which is used for monitoring and processing and referred to in the following as ”monitoring Mac”. Using this dedicated monitoring Mac ensures that the DAQ software running on the other acquisition Macs has sufficient computing resources to perform the time-critical task of event triggering. Running on the monitoring Mac are a set of python scripts, which initialize further processing steps. The first step is to scan the directory which contains the data partition files; for each new data partition, a document is created in the so-called ”`datadb`” database, and and the SAMBA header information of the file is written into that document in the form of key-value pairs. The document contains meta information about the file and keeps track of the file location and all processing steps. An example of such a database document is given in the appendix A.

The whole processing is data-base driven: new data partitions are found via their database document, by an automatic script listening to the so-called `_changes`-feed of the `datadb` database. If a new document is found, an SFTP (Secure File Transfer Protocol) copying job is launched to transfer the corresponding data partition to CC-IN2P3. This process is named ”`proc0`” and information about it, such as transfer method, file-name, file-size, etc., is written into the document. In case the copying fails, the error message is also written into the documented. The initial design of the KData framework involved multiple processing steps for data partitions (”`proc0`”, ”`proc1`, ”`proc2`”), which are all triggered consecutively by changes in the corresponding database documents. Processes, for example, create ROOT-based files on the monitoring Mac and transfers them to CC-IN2P3 (`proc1`)

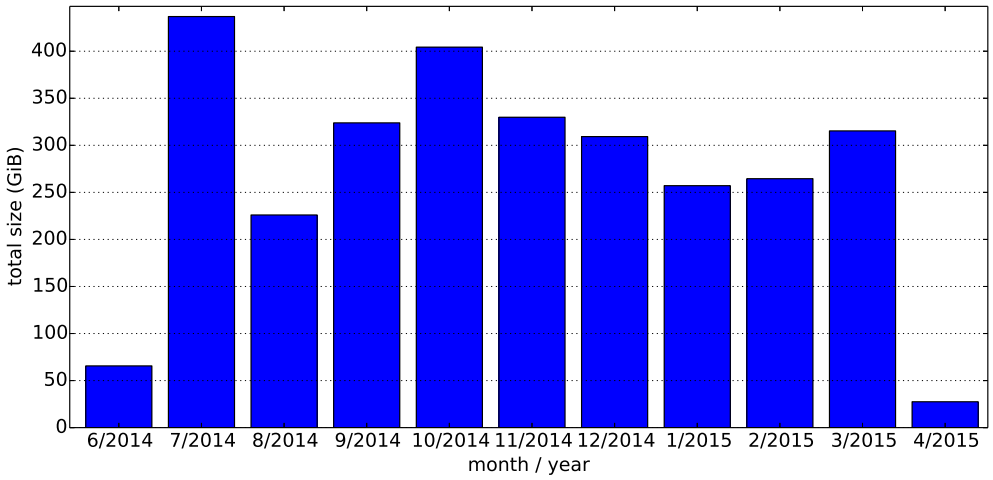

Figure 2.9.: Size of the total raw data recorded during the EDELWEISS-III Run308 which lasted from June 22nd, 2014 until April 3rd, 2015. Differences between months can be caused by the length of calibration measurements as well as duty-cycle. The plotted data volume has been archived on the long term type drive storage HPSS and includes a compression factor of ≈2.

or determine the amplitude of pulses (`proc2`).

Once copies of the data partition files are on CC-IN2P3, they have to be backed up, as they are located on a temporary storage with no automatic backup. For long term storage, all files are copied to the High Performance Storage System (HPSS) tape drive system [93]. While the actual backup is performed on CC-IN2P3, the script triggering the backup are launched from the monitoring Mac at LSM. All ≈1 h data partitions belonging to a SAMBA run (approximately one day of data recorded with the same acquisition Mac) are packed into a compressed archive and written to HPSS. This process is again initialized and documented in the `datadb` database. Each document receives a new key labelled "hpss", which contains information about the location of the file on HPSS, and for each compressed archive file of multiple data partitions, a separate document is created as well.

In the framework of this thesis, the data transfer from LSM to CC-IN2P3 (`proc0`) and the backup to HPSS was monitored and corrected. Several problems appeared during that time, which caused the system to halt and required manual intervention. These problems included corrupted or missing files, network connection problems, backup of incomplete SAMBA runs as well as frozen processing jobs. To better account for possible problems, some of the processing scripts were modified to perform checks before backing up files to HPSS. For easier monitoring of the status of the backup process, an additional CouchDB "view" was also created. An overview of the backup of the so-called Run308, the 1 year long WIMP search of EDELWEISS-III, is given in Fig. 2.9. In total, 27,549 data partitions (including SAMBA log-files) were backed up in 1431 archive-files with a combined size of 2960 GiB.

2.4. Residual backgrounds for dark matter search

As the shielding concept of the EDELWEISS experiment is very effective in attenuating the external radiation, most remaining backgrounds originate from inside the shielding. In the following, the backgrounds which might mimic a hypothetical WIMP signal in the analysis of EDELWEISS-III data in Ch. 4, are detailed along with their sources. One background of non-particle origin, most likely, is not discussed in this section. Features and properties of the so-caalled *heat-only* events are explained in detail in Sec. 4.3.2.

2.4.1. Cosmogenic and radiogenic neutrons

A priori, neutrons are the most relevant background for WIMP search as they induce the same type of nuclear recoil events in the detectors as the potential signal for WIMPs of mass $m_\chi = 10\,\mathrm{GeV}/c^2$. There are two different sources for neutrons in the experiment: cosmogenic and radiogenic neutrons.

Cosmogenic neutrons

Neutrons can be produced by cosmic ray induced muons. The production is either directly by the interaction of muons with matter via negative muon capture and muon nuclear interactions, or indirectly through the interaction of the muon-induced electromagnetic or hadronic showers. They are mostly produced in high-Z materials such as the lead shield surrounding the cryostat. Because of their production mechanism, the produced neutrons are on average more energetic than radiogenic neutrons. Therefore they are less attenuated by polyethylene shielding surrounding the experiment and the cryostat. Instead, the active muon-veto system is used to tag muons and therefore reject events recorded in the detectors which are in coincidence. As indicated in Sec. 2.1, the muon-veto efficiency is not 100% due to the reduced geometric coverage, and energy threshold effects. The residual background of unrejected muon-induced neutron events in EDELWEISS-III has been studied in [61]. Compared to radiogenic neutrons, the event topology of muon-induced neutrons is different, and shows a higher event-multiplicity, i.e. a scattering of the particle in more detectors. For a more dense detector array, the number of multiple scattering events increases, and these events can be rejected efficiently from a potential single detector WIMP signal. The estimation of this background for the EDELWEISS standard mass WIMP analysis is given in Sec. 3.2.2 and for the low mass WIMP search in Sec. 4.3.4.

Radiogenic neutrons

Another neutron source are radiogenic neutrons coming from the natural decay chains of ^{238}U and ^{232}Th as well as (α,n) reactions in light materials. The contamination of the rock and concrete of the underground laboratory with these isotopes has been measured in [94]. A more recent measurement of the neutron flux in LSM with a ^{3}He proportional counter has been performed in [95] and shows position and time dependent variations of a factor 2. The averaged 4π thermal neutron flux near the experimental setup was measured as $\Phi_\mathrm{n}^\mathrm{thermal} = (3.57 \pm 0.05\,(\mathrm{stat}) \pm 0.27\,(\mathrm{sys})) \times 10^{-6}\,\mathrm{neutrons/s/cm^2}$. Within the polyethylene shielding it is reduced by 5 to 6 orders of magnitude [64]. For fast neutrons with energies above 1 MeV, which have a chance to penetrate the shielding and produce nuclear recoils with energies similar to those of WIMP-interactions, the flux has been derived as $\Phi_\mathrm{n}^\mathrm{fast} = (1.1 \pm 0.1\,(\mathrm{stat})) \times 10^{-6}\,\mathrm{neutrons/s/cm^2}$ [96]. The dominating neutron background in the detectors comes from sources surrounding the detectors within the shielding. For this reason, all materials have been screened and selected by their extremely low contamination levels with radioactive ^{238}U and ^{232}Th isotopes and additional PE is installed within the cryostat to attenuate neutrons coming from the cold electronics. Simulations with upper limits or measured values for the contamination with U/Th-decay chains of different materials have been performed to derive the expected background. These simulations include rock and concrete from the laboratory walls, the lead and PE of the shielding, steel support structures, the electronics at various temperature levels as well as cables and connectors. The resulting energy spectra of neutrons produced in different materials around the detector are given in Fig. 4.19. About 50% of the radiogenic neutron background is expected to come from materials in close proximity of the detectors, such as Teflon holders and CuBe spring contacts of the Delrin connectors. For 24 detectors and $\approx$5000 kg·days of fiducial exposure, the total neutron background of single scatter events above $E_\mathrm{rec} = 20\,\mathrm{keV}$ has been estimated as 1.4 events. As it is shown in Sec. 3.2.2, this

value is an underestimation and an additional unknown source of neutrons is present in the experiment which has not been considered in the simulations.

2.4.2. Gamma radiation

The electron recoils which γ's produce in the bolometers which can, in principle, be separated from the nuclear recoils of WIMPs, as described in Sec. 2.2.2. However, it is still necessary to reduce this background as far as possible. Indeed, there is a small probability, that γ's can *"leak"* into the signal region. Leakage can happen when the ionization signal is misreconstructed, due to incomplete charge collection. In such cases the ionization yield is underestimated and of the order of nuclear recoil interactions. Also, the separation of the confidence bands describing ER and NR interactions deteriorates towards lower energies. This is particularly relevant when searching for low mass WIMPs, for which the expected signal is $\mathcal{O}(1\,\mathrm{keV})$ and near the trigger threshold of a detector.

Two γ-background sources can be distinguished for the EDELWEISS detectors: internal and external γ's. Internal γ's come from the electron capture of cosmogenically activated isotopes within the crystal, a process which is discussed in the following Sec. 2.4.3. A description of the external γ-background for EDELWEISS-III is given in the following and is based on the result that were published in [97]. This external γ-component is the result of natural radioactivity from the ^{238}U and ^{232}Th decay chains, as well as ^{40}K, ^{60}Co and ^{137}Cs in the rock of the laboratory or the materials surrounding the detectors. As the 20 cm thick lead shield attenuates external γ-radiation by several orders of magnitude [64], the remaining background is mostly from within the shielding. In the energy range of $E_{\mathrm{rec}} \in [100\,\mathrm{keV}, 4\,\mathrm{MeV}]$, which is above the region of interest for WIMP search, the overall rate Γ_γ of events measured in the experiment is dominated by γ events. From an EDELWEISS-III data sample with a fiducial exposure of 380 kg·days, which corresponds to the fiducial WIMP-search exposure of EDELWEISS-II, it was measured as $\Gamma_\gamma = 235 \pm 5$ counts/kg/day within the energy range. The energy spectrum for the selected data is given in Fig. 2.10a, and shows good agreement with Monte Carlo simulations. The measured spectrum features a clear Compton backscattering peak around 200 keV and several typical lines coming from the decay of ^{208}Ti (2614 keV), ^{40}K (1461 keV) and ^{60}Co (1173 keV and 1332 keV). All materials have been considered, which surround the detectors in the 10 mK and 1 K volumes of the cryostat, as well as the shielding, with contaminations of ^{238}U, ^{232}Th, ^{40}K, ^{60}Co and ^{137}Cs. The energy spectra for these individual contamination sources are shown in Fig. 2.10b. The different components have been scaled with individual fit factors to match the measured data, as only upper limits were available for some of them. The gamma background in the RoI for WIMP search of $E_{\mathrm{rec}} \in [20, 200]\,keV$ was estimated from these simulations, and compared with data. The rate of events per kilogram and day is given in Tab. 2.1 both for the fiducial and total volume as well as for different materials around the detectors.

2.4.3. Detector internal X-rays

During their production and temporary storage at the surface, at approximately sea level, the EDELWEISS-III detectors have been exposed to cosmic rays and their by-products. As a result, long-lived isotopes are produced within the Ge-crystals. The activation stopped once the detectors were brought to the LSM underground laboratory, where the rock overburden reduces the muon flux by several orders of magnitude. The activated isotopes then decay with typical half-lives $\mathcal{O}(100\,\mathrm{days})$. The most prominent decay channel is the process of electron capture (EC): an electron of mostly the K or L-shell gets captured by the nucleus, and via the weak interaction transfers a proton into a neutron (and an electron neutrino), thus tranforming the atom into a different chemical element. The new isotope is

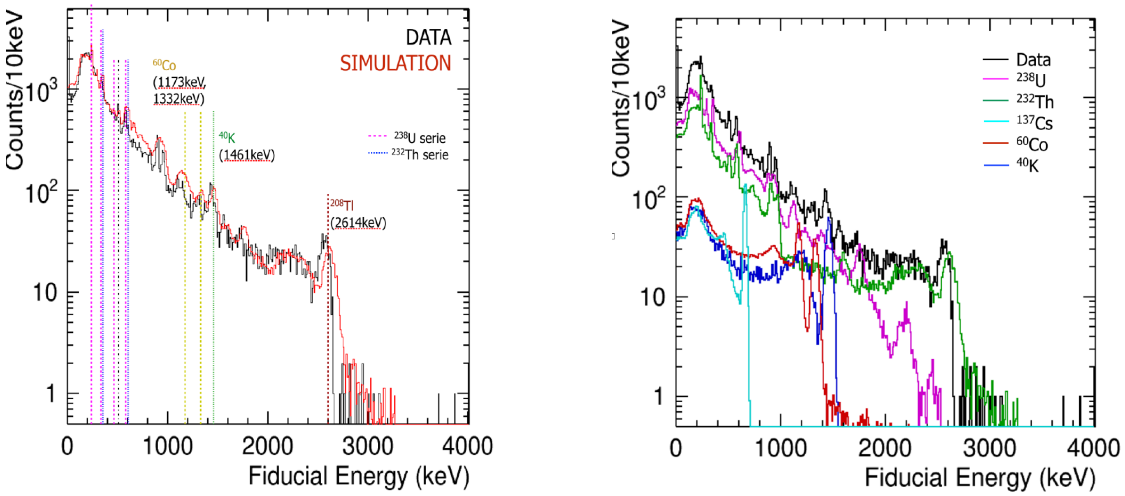

(a) (b)

Figure 2.10.: (a) Measured energy spectrum of the EDELWEISS-III γ-background (black) in the fiducial volume for an exposure of 380 kg·days in comparison with Monte Carlo simulation (red). (b) Simulated spectra from contamination of ^{238}U, ^{232}Th, ^{60}Co, ^{40}K and ^{137}Cs (see legend for colors). Extracted from [97].

Table 2.1.: Expected event rate Γ_γ of gamma events with $E_{\text{rec}} \in [20, 200]$ keV in the fiducial and total volume as derived from simulations andh data. Only materials with more than 3% contribution to the total simulated rate are listed. Values extracted from [97].

Material	$\Gamma_\gamma^{\text{fiducial}}$ evts/kg·days	$\Gamma_\gamma^{\text{total}}$ evts/kg·days
Copper	7.3 (10%)	12.8 (10%)
Brass	14.7 (20%)	22.9 (18%)
Brass in Cu	6.9 (9%)	10.3 (8%)
PE	2.6 (4%)	4.6 (4%)
Teflon	2.2 (3%)	4.0 (3%)
Connectors	39.7 (54%)	63.1 (50%)
Global simulation	78	128
Data Run308	70	125

Table 2.2.: Cosmogenic isotopes in the EDELWEISS-III detector with their respective half-lives $T_{1/2}$ and the energy of X-rays produced by K- or L-shell electron capture. Only L-shell peaks relevant for the low mass WIMP search in Ch. 4 are listed. Values from [99].

Element	$T_{1/2}$	$E_\gamma^{\mathrm{K-shell}}$ (keV)	$E_\gamma^{\mathrm{L-shell}}$ (keV)
^{71}Ge	11 d	10.37	1.30
^{68}Ge	271.0 d	10.37	1.30
^{68}Ga	67.7 min	9.66	1.20
^{65}Zn	243.9 d	8.98	1.10
^{56}Ni	6.0 d	7.71	
^{58}Co	70.9 d	7.11	
^{57}Co	271.7 d	7.11	
^{56}Co	77.2 d	7.11	
^{55}Fe	2.7 y	6.54	
^{54}Mn	312.1 d	5.99	
^{49}V	330.0 d	4.97	

in an excited state, as it is missing an inner K or L-shell electron. The hole is filled with an electron from an outer shell, and either an X-ray photon or Auger electron is produced which carries the energy difference of the electron shell configuration. X-ray photons produced by the electron capture of cosmogenically activated isotopes produce electron recoils in the detector, with energies $\mathcal{O}(10\,\mathrm{keV})$ which are a possible background for low mass WIMP search. An overview of relevant isotopes and the energy of their K- and L-shell X-rays is given in Tab. 2.2. The intensity relation between K and L-shell EC-reactions for different isotopes was studied in [98] and is approximately 11%. This ratio can be used to derive the expected rate of events of the L-shell peak from the measured population of K-shell electron recoils. As the activated isotopes are distributed homogeneously within the crystal, the electron recoils produced by the X-ray photons take place both in the bulk and surface volume. The most prominent peaks, which are measured in the data of the FID800 detectors, are the triplet of ^{65}Zn, ^{68}Ga and ^{68}Ge around 10 keV. Their intensity with and without fiducial cut can be used to determine the fraction of the fiducial volume, as will be shown in Sec. 4.1.4. Although ^{68}Ga only has a half-life of $T_{1/2} = 67.7\,\mathrm{min}$ it is constantly produced from EC of ^{68}Ge. It only decays via EC in 11% of the cases (otherwise via inverse β-decay). Consequently, the ratio between the peaks observed at 9.66 keV and 10.37 keV is given as 1:9.

2.4.4. Decay of internal tritium

With the reduction of the Compton background from external γ-radiation and the improved energy resolutions in EDELWEISS-III, another background component can be separated in the low energy electron recoil spectrum. These electron recoil events are produced by the beta decay of tritium within the detector. The endpoint energy of the produced electron is $Q_\beta = 18.6\,\mathrm{keV}$ and therefore in the low energy range relevant for WIMP search. Tritium is produced by nuclear reactions from cosmic rays with the material of the detector [101]. The intensity of the contamination depends on the exposure of the detector to cosmic rays at the surface. Only crude upper limits exist for the production rate of tritium [102], and there are large uncertainties in the model predictions due to the neutron flux model and the empirical nucleon cross sections. After installation underground at LSM, the activation is stopped, due to the reduced muon flux. Because of the half-life of tritium of $T_{1/2} = 12.3\,\mathrm{years}$, the activity of the subsequent decay can be regarded as approximately constant.

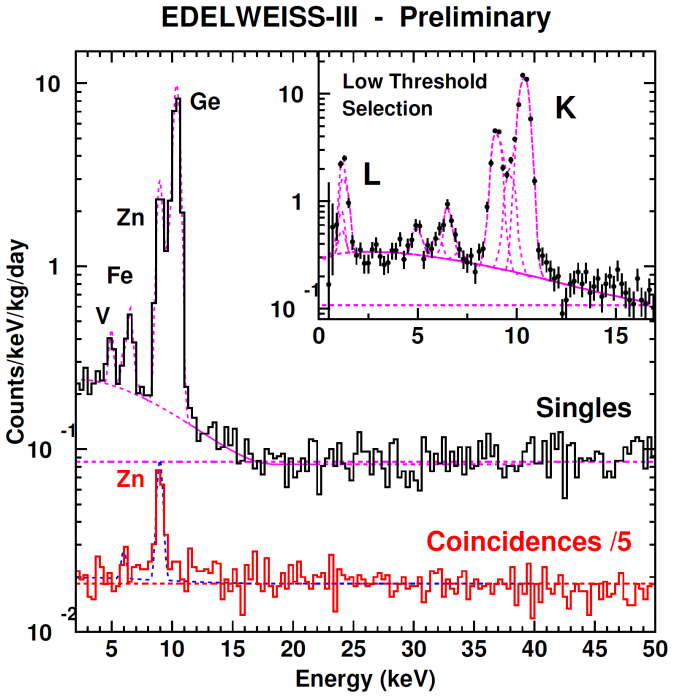

Figure 2.11.: Fit of the combined energy spectrum of fiducial events from 19 detectors and ≈1136 kg·days of exposure (magenta). A clear contamination compatible with tritium beta spectrum of $Q_\beta = 18.6\,\mathrm{keV}$ is seen only for single events (black) and not in the control sample of coincidences (red). *Inset*: Selection of events for a lower threshold energy than used in the tritium analysis to test for threshold and efficiency related effects. Extracted from [100]

The energy spectrum of betas from the decay of tritium as a function of the kinetic energy T is given as

$$\frac{dN}{dT} \propto \sqrt{T^2 + 2m_e c^2 T}\,(T + m_e c^2)\,(Q_\beta - T)^2\,F(T, Z{=}2) \tag{2.17}$$

where m_e is the mass of the electron and c the speed of light. The term $F(T, Z = 2)$ is the Fermi function for tritium. As the endpoint energy $Q_\beta << m_e c^2$, the betas are non-relativistic and $F(T, Z = 2)$ can be approximated as $x/(1 - e^{-x})$ with $x = 4\pi\alpha c/v$, where α is the fine-structure constant and v the beta velocity. Consequently, Eq. 2.17 can be written as

$$\frac{dN}{dT} \propto (T + m_e c^2)\,(Q_\beta - T)^2\,\left(1 - e^{\frac{-1.466172}{\sqrt{T}}}\right)^{-1} \tag{2.18}$$

The betas from tritium decay produce electron recoils in the detector, therefore the kinetic energy T is equal to the measured recoil energy E_{rec}. As the heat and ionization channels of the FID800 detectors are also calibrated with bulk electron recoils, the beta spectrum can be directly measured with the two observables E_{heat} and E_{ion}. Due to the low γ-background and the good energy resolution of the FID800 detectors on the ionization channels of ≈200 eV (RMS), EDELWEISS-III is the first Ge-based experiment to measure the intensity of internal tritium decay in Ge-detectors [100]. Figure 2.11 shows the combined low energy spectrum of 19 FID800 detectors and 1894 days of livetime with the fitted contribution from Compton γ's, cosmogenic peaks and a clear beta spectrum due to tritium decay. The

average rate of events from the decay of tritium over all detectors has been measured as

$$\Gamma_{\text{tritium}} = 1.60 \pm 0.10\,\text{events/kg/day} \tag{2.19}$$

Tritium decay betas are a background which is considered in the low mass WIMP search performed in the framework of this thesis. Although different cuts and a different fiducial volume was used compared to the analysis in [100], the rate found for individual detectors is in statistical agreement. A comparison of the rate for a selection of 8 FID800 detectors which were used in the EDELWEISS-III low mass WIMP search is given in Fig. 4.18.

2.4.5. Surface events

We identify *surface events* as events having a significant fraction of their charge collected by one of the two veto electrodes. These events are produced by charged particles, such as α's and β's from radioactive decay, which hit the detector surface. Depending on their energy, they can penetrate the crystal up to depths of ≈1 mm, as it is shown in Fig. 2.12. Considering that the fiducial volume for FID800 detectors was determined to make up ≈75% of the entire detector volume, the nominal thickness of the surface region corresponds to 3 mm on average. This means that any rejection of surface events via the fiducial cut, as described in Sec. 2.2.3, also excludes a significant fraction of events from cosmogenic isotopes, which have been described in Sec. 2.4.3. It also means that the fiducial cut effectively rejects a large fraction of the external γ-background described in Sec. 2.4.2, which for energies below 30 keV is attenuated by a factor ≈50 after 3 mm.

Thanks to the FID-design of the detectors ionization electrodes a rejection of surface events is possible with high efficiency (see Eq. 2.16). However, the rejection was measured for energies above $E_{\text{rec}} = 15\,\text{keV}$. Relevant for the search for low mass WIMP signals are events with significantly lower energies, close to the trigger threshold of the experiment. For these energies the rejection of surface events is significantly reduced, because the small ionization signals on the veto electrodes are of the order of baseline noise fluctuations. Therefore, unrejected surface events have to be considered as a residual background in the main analysis of this thesis, as is described in Sec. 4.3.5.

The origin of the surface events induced by charged particles is related to a radon contamination and then to the ^{210}Pb isotope and its daughters. ^{210}Pb has a half life of $T_{1/2} = 22.3$ years and is part of the natural decay chain of ^{222}Rn. Radon is a gas which adsorbs on surfaces can contaminate materials in the vicinity of the detectors. This contamination is local and varies between detectors depending on the environmental conditions (humidity, temperature, etc.). Particularly high contaminations of the long-lived radon decay product ^{210}Pb have been measured in copper, which is used as material for the casing around the detector. As it is shown in Fig. 2.13, ^{210}Pb can decay via two different decay channels into ^{210}Bi, producing low energy betas. In 20% of the cases, a β with an endpoint energy of $Q = 63.5\,\text{keV}$ is produced, while in the other 80% a β with $Q = 17.0\,\text{keV}$ is produced, followed by X-rays and conversion and auger electrons. After a beta decay of ^{210}Bi with a higher energy beta of $Q = 1161.5\,\text{keV}$, the resulting ^{210}Po further decays into a 5.3 MeV α and a stable ^{206}Pb nucleus, which has a recoil energy of 103 keV. The measured energy for both the α and the recoiling nucleus can be reduced, due to energy losses which depend on the implantation depth of the initial contamination.

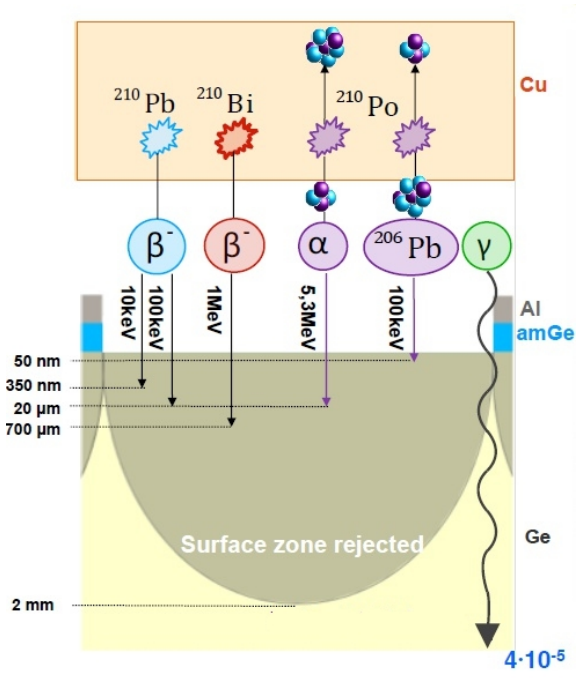

Figure 2.12.: Schematic of the decay of ^{210}Pb and its daughters implemented in the copper housing facing the detector. The penetration depth for α's, β's and ^{206}Pb-nuclei is much smaller than the surface zone due to the FID design (see Sec. 2.2.3). Only γ-radiation reaches the bulk or fiducial volume of a detector and has to be discriminated from a potential signal via its ionization yield (see Sec. 2.2.2).

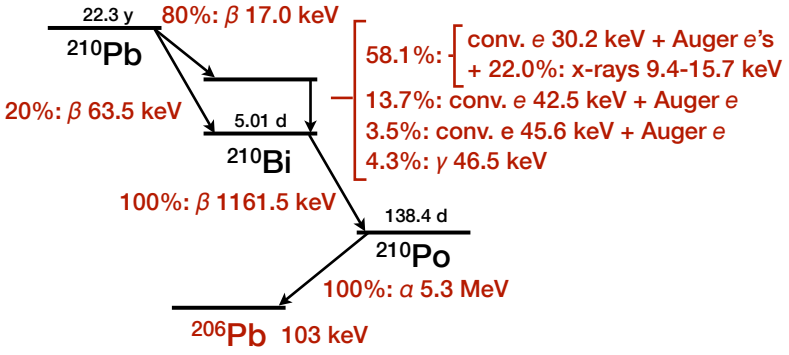

Figure 2.13.: Decay of the ^{210}Pb isotope from the ^{222}Rn decay chain into the stable ^{206}Pb. Only the most significant decays are shown. Extracted from [103].

3. Analysis methods for dark matter searches

The field of dark matter search via direct detection is not only experimentally demanding, but also challenging when it comes to the analysis and interpretation of the recorded data. The difficulties are manifold: for one, the expected signal from dark matter in current experiments would be only a few events per year, which is negligible compared to even the lowest achievable background intensities. And although most direct detection experiments use multiple channel readout to discriminate between a potential signal and different backgrounds (see Sec. 1.3.3), the discrimination power usually degrades towards lower energies. A reduced discrimination affects especially the search for low mass WIMPs with masses $\mathcal{O}(1)\,\mathrm{GeV}/c^2$, for which the recoil spectrum of WIMP-nucleon interactions extends up to energies of only a few keV. In many cases, the spectral shape and intensity of these low energy backgrounds are not known with great precision and need to be extrapolated from higher energy sidebands. Additional complications arise from reduced detection efficiencies at low energies as well as the systematic uncertainty on the detector response, which have to be estimated and taken into account. On top of all these uncertainties coming from the experimental side is the astrophysical model that enters into the expected WIMP interaction rate and signal shape. Many of the parameters that describe the galactic WIMP-halo, in particular the escape velocity v_{esc}, have a significant impact on the calculated recoil energy spectrum of a potential signal, especially for low mass WIMPs. All these conditions have to be considered in an analysis related to dark matter search.

Dark matter experiments can lead to two different types of results: when the rate and properties of measured events are compatible with background expectations, an exclusion limit is derived. This limit corresponds to the lowest value of the WIMP-nucleon scattering cross section σ_χ as a function of the WIMP mass m_χ which can be excluded at typically a confidence level of 90% (90% C.L.). While this is by far the most frequent outcome of all direct detection experiments, a small number of them have measured an excess of events in the region of interest for a potential signal. If the characteristics of the events causing this excess are compatible with a dark matter signal, one can estimate the properties of the dark matter particle. In the parameter space of WIMP-nucleon scattering cross section and WIMP mass, these signal claims are drawn as contours denoting the uncertainty on the estimated values. Experiments with an excess of events providing a signal contour are DAMA/LIBRA [104], CRESST-II [50], CoGeNT [105] and CDMS-Si [106] (see Fig. 1.8). Several of these experiments have since excluded the initial signal claim after performing new measurements with upgraded detectors and improved background rejection. In order

not to misinterpret upward fluctuations of backgrounds as a dark matter signal or derive an overly optimistic exclusion limit from downward fluctuations, a correct statistical treatment of the measured data is essential. In this chapter, several analysis methods will be presented, which are used in direct detection experiments.

In this chapter, various analysis methods used in the field of direct dark matter search will be introduced in Sec. 3.1. In Sec. 3.2, the analysis of EDELWEISS-III data for standard mass WIMPs based on the so-called *optimum interval method* as suggested by S. Yellin [107], will be summarized. This analysis is of relevance, as it was used to normalize the expected neutron background considered in this work. Section 3.3 then gives a detailed overview of the EDELWEISS-III low mass WIMP search with Boosted Decision Trees. While this BDT-analysis uses a similar selection of data than the likelihood analysis performed in this thesis, it is based on an entirely different approach and can therefore be used to validate the results obtained in the framework of this thesis. A comparison between the results of the two analyses follows in Ch. 4. Eventually, the maximum likelihood method is explained in Sec. 3.4: the theoretical foundation, from the likelihood function to the principle of so-called *hypothesis test*, is first introduced, followed by the analysis framework used in this thesis.

3.1. Strategies for rare event searches

3.1.1. Poisson statistics

A rather simple analysis method is shown in the left panel of Fig. 3.1. The Poisson counting method can be applied in experiments such as EDELWEISS, which can discriminate between backgrounds and a potential signal. The principle idea is to choose cuts which define a region with a high signal over background ratio. The number of observed events N_{obs} in this region is then used to derive a limit with Poisson statistics. This method is conservative as it does not subtract the expected background and each event is considered as a potential signal. The disadvantages are that the available knowledge about the distributions of signal and background are not taken into account, and any uncertainty on the background is neglected.
For an average signal rate of μ, the probability p to measure N events in the signal region is expected to follow the Poisson law:

$$p(N,\mu) = e^{-\mu}\frac{\mu^N}{N!} \tag{3.1}$$

The rate of events μ_{lim}, which can be excluded with a confidence level α, is the one for which the probability $p_{N\leq N_{\mathrm{obs}}}$ of a random experiment to result in more events than N_{obs} is given by $p \leq 1-\alpha$. From Eq. 3.1, this probability can be calculated as the sum of probabilities for all discrete values of N up to N_{obs}:

$$p_{N\leq N_{\mathrm{obs}}} = p(0,\mu) + p(1,\mu) + ... + p(N_{\mathrm{obs}},\mu) \tag{3.2}$$

To find the average signal rate μ of events which can be excluded with a confidence level α, one has to calculate

$$1-\alpha = e^{-\mu_{\mathrm{lim}}}\sum_{n=0}^{N_{\mathrm{obs}}}\frac{\mu_{\mathrm{lim}}^n}{n!} \tag{3.3}$$

The typical confidence level used to set exclusion limits in direct dark matter detection is $\alpha = 90\%$. For experiments which observe no events in the signal region or for the

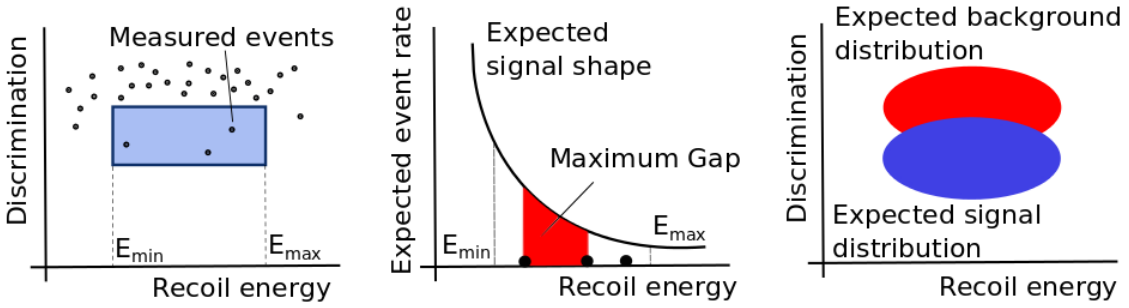

Figure 3.1.: Illustration of different analysis methods applied in dark matter search. *Left*: Simple Poisson counting of events in a possible signal region. *Middle*: Yellin's method, which uses event counting but also considered the shape of a potential signal. *Right*: Maximum likelihood fit of data with expected distibutions for background and signal. Figure from [31].

estimation of the background free limit, the expected rate corresponding to $N_{\mathrm{obs}} = 0$ is $\mu_{\mathrm{lim}} = 2.35$ events. The limit on the event rate extracted with this method is clearly independent of the WIMP mass m_χ, as no information about the shape of the signal is taken into account. To translate this limit on the event rate into a limit on the WIMP-nucleon scattering cross section σ_χ, one has to consider the potential signal in the selected region. For each WIMP mass, the expected rate of events μ in the signal region for a WIMP-nucleon cross section σ_χ can be calculated. To find the exclusion limit on the cross section of $\sigma_\chi^{\mathrm{lim}}$, σ_χ is increased until μ corresponds to the expected limit μ_{lim}.

In case a background prediction for the signal region is available one can also use a method developed by Feldman and Cousins [108] to derived either one sided (exclusion limits) or two sided (parameter uncertainties) confidence limits. The method is based on the likelihood ratio of Poisson distributions.

3.1.2. The "Yellin" method

S. Yellin proposed a more effective method for finding upper limits in the presence of unknown backgrounds [107] compared to simple Poisson counting. By design, this method cannot be used to make a discovery claim. In dark matter experiments in particular, the region of interest for a potential signal can be contaminated by one or even several types of background. If these backgrounds are understood and can be modelled, it is possible to use that knowledge in e.g. a likelihood based analysis and subtract them. However, if the background is unknown or not fully understood this is not possible anymore and one can resort to the Yellin method. It provides a conservative approach to extract upper limits on the signal if a background prediction is unavailable or the uncertainty on the background is too large. As background is not subtracted, the method is very robust against changes in the background model. Two techniques of the Yellin method exist: the *maximum gap* method and the *optimum interval* method. The first uses the absence of a signal between two consecutive events in the parameter space, while the latter uses the region with the lowest density of events to set a limit on the signal strength.

Maximum gap method

The illustration in Fig. 3.1 (middle) shows a possible outcome of a dark matter experiment. The dots represent the recoil energy E_{rec} of events which are passing a set of cuts in the region of interest for WIMP search. These events can either be a potential WIMP signal or the result of an unknown background process. The curve which is shown in the same

figure represents the typical nuclear recoil energy spectrum from WIMP-nucleon scattering. For a given WIMP-mass m_χ and a proposed cross section σ, one can calculate the event rate dN/dE_{rec} as a function of recoil energy E_{rec}. Between any two events i and $i+1$ in recoil energy, there is always a gap which, for a given cross section σ, should contain the expected number of signal events x:

$$x_{\mathrm{i}} = \int_{E_{\mathrm{i}}}^{E_{\mathrm{i+1}}} \frac{dN}{dE_{\mathrm{rec}}} dE_{\mathrm{rec}}. \tag{3.4}$$

The *maximum gap* is then defined as the gap between two events for which the expected number of signal events x for a given cross section σ is the largest. The principle of the maximum gap method is to vary the strength of the signal, i.e. the cross section σ, until one can reject the value of x because it would suggest too many events within a gap that evidently contains zero measured events. In this context, *"too many"* events means that σ can be rejected with a confidence level C_0 if the maximum gap "size" x for a random experiment is lower than the maximum gap size observed in the measured data with a probability C_0. It is possible to make a transformation of the event variable, e.g. from recoil energy E_{rec} to the expected number of events in a given interval. As is shown in [107], the confidence level C_0 to exclude a signal can be expressed as a function of maximum gap size x and the total number of expected events μ in the entire energy range:

$$C_0(x,\mu) = \sum_{k=0}^{m} \frac{(kx-\mu)^k e^{-kx}}{k!} \left(1 + \frac{k}{\mu - kx}\right) \tag{3.5}$$

with m being the defined as the greatest integer smaller or equal to μ/x. For the computation of a 90% C.L. upper limit on the cross section, σ is increased until μ and x lead to a value C_0 of 0.90. The maximum gap method does not require any binning of the data which can introduce a bias, nor does it need any Monte Carlo simulations to construct the confidence interval. A big advantage of the method compared to Poisson counting is that it automatically uses a region with low background because there the maximum gap is found. It therefore does not bias the selection of a region of interest, as could happen by choosing a lower limit which excludes as many events as possible.

Optimum interval method

The maximum gap method is most efficient in terms of limit setting when there are only few remaining events after all cuts, and therefore large gaps between them. For a higher background contamination leading to smaller gaps, it can be replaced by the optimum interval method, which is a generalization using intervals that contain $1, ..., n$ measured events. Similar to C_0 in Eq. 3.5, $C_n(x,\mu)$ can be defined. It is the probability that all intervals with containint $\leq n$ events have a smaller or equal number of expected signal events compared to the maximum gap, i.e. $\mu \leq x$. In order to not bias the limit, the value of n is chosen automatically by the method. The optimum interval is the one in which the event number most clearly conflicts with the proposed cross section σ. The values for $C_n(x,\mu)$ are usually tabulated with a Monte Carlo program. A detailed description of the method can be found in [107].

For the case of a higher number of measured events, the optimum interval method has been extended to the "high statistics" case making use of a Gaussian approximation. The extension, as well as a discussion on how the method could be extended to multiple dimensions are detailed in [109]. In [110], Yellin also proposed several methods to combine the data of different experiments which would individually be analysed with the optimum

interval method. Such a combination of results was performed in [111] for the CDMS and EDELWEISS-II experiment, resulting in an improvement of the limit for WIMPs with $m_\chi > 50\,\mathrm{GeV}/c^2$ by a factor of up to ≈1.6. Other current dark matter search experiments which have employed the Yellin method are SuperCDMS [48], CRESST-II [112] and PICO [113]. The optimum interval method was also applied in the standard mass WIMP search of EDELWEISS-III. A comparison of the results with the Poisson method for this data is given in Sec. 3.2.3.

3.1.3. Maximum likelihood

The maximum likelihood method, indicated on the right panel of Fig. 3.1, is a more optimistic approach compared to the methods described above: it exploits the full knowledge of the spectral distributions of signal and various backgrounds. By fitting them to the data it effectively subtracts the background in a region of mixed signal and background. Unlike other analysis strategies described above, the full signal expected in the RoI is used to derive a limit on the WIMP-nucleon cross section. No additional cuts, which reduce the signal efficiency, are needed as it is the case for other methods such as Yellin or Poisson. Consequently, a maximum likelihood analysis usually results in a stronger exclusion limit or a higher signal significance in case of discovery. To take into account known uncertainties on the background prediction or on other model parameters, a *profile likelihood* can be used to profile out the uncertainties on so-called *nuisance* parameters. Unlike the parameter of interest (usually the signal cross section σ_χ in the case of direct detection dark matter experiments), nuisance parameters describe backgrounds or detector parameters which are not of direct interest for the analysis.

Maximum likelihood based analyses have been performed in a variety of dark matter experiments. The method can be used both to set exclusion limits (one sided confidence intervals) as in XENON100 [114], LUX [115, 116], and CDMS II (Ge) [117], as well as to define a signal region (two sided confidence interval) as in CDMS II (Si) [106]. As the analysis performed in the framework of this thesis is based on a maximum likelihood method, a more extensive description of the principle and its application for setting limits is given in Sec. 3.4.

3.1.4. Boosted Decision Trees

Decision trees are a classification method which is used to classify events of a data sample into different categories. The most simple case scenario is the classification into a signal or a background. The working principle of a decision tree is illustrated in Fig. 3.2: the decision tree applies successive rectangular cuts on the parameters describing each measured event to separate signal and background. A decision tree consists of several nodes. At each node, the data is split into two samples by applying a cut c_i on one of the variables x_i. Which variable and which cut are used is determined by an algorithm and depends on the discrimination power of the variable. Depending on the size of the tree (the number of nodes), the phase space of data parameters is split into different regions that are either classified as signal- or background-like. At the end, each event is attributed with a discrimination value that classifies how signal- or background-like the event is.

To determine how signal and background events can be distinguished, a decision tree first has to be trained. During this training phase, it is fed with classified signal and background events and learns their characteristics. After the training, the application phase follows, where the new and unclassified data is given to the tree for evaluation. If the size of the tree is chosen too large the tree makes too many successive cuts which lead to a very specific choice of parameter space, so-called *overfitting*: the tree cannot generalize from the training data to arbitrary data. The boosting of a decision tree is a technique to improve its results:

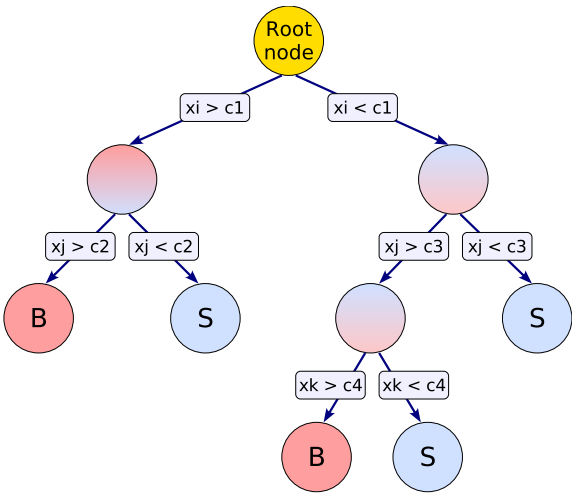

Figure 3.2.: Sketch of the working principle of a decision tree. At each node, the data is split to give the best separataion between signal (S) and background (B), by using one of the discriminating variables x. Extracted from [118].

after the decision tree is trained, all misclassified events are re-weighted according to their classification score. The tree is trained again with re-weighted events and this procedure is iterated several times. Finally, the classification is averaged over all decision trees.

The output of a boosted decision tree is a BDT-score for each event, which quantifies how signal- or background-like the event is. The distribution of BDT-scores for the actual data can be compared with the distribution for one or several simulated backgrounds which were used to train the tree (see following Fig.3.7 for an example). Different methods exist on how to derive a limit from the resulting distribution. In the application of a BDT to data from the SuperCDMS experiment [48], the output was combined with the optimum interval method described in Sec. 3.1.2 to derive a limit on the WIMP-nucleon scattering cross section σ_χ. A BDT has also been used to analyse low energy data from the EDELWEISS-III experiment. This analysis and the achieved results are described in detail in Sec. 3.3. Here, a cut was applied on the BDT output distribution and the limit on σ_χ was derived with a Poisson method. In principle, it is also possible to use a maximum likelihood analysis for all events, based on the 1-dimensional distribution of BDT scores.

Another type of supervised learning method which is gaining more momentum in data analysis, both in physics and in other fields, are Artificial Neutral Networks (ANN). These are machine learning algorithms which are inspired by nervous systems such as the brain. As no example was found for their application in direct detection experiments, they are not described in this chapter.

3.2. Application of the Yellin method in a search for standard mass WIMPs with EDELWEISS-III

From July 22$^{\text{nd}}$, 2014, until April 3$^{\text{rd}}$, 2015, EDELWEISS-III performed a long WIMP search run labelled Run308, which will be described in more detail in 4.1.1. All data taken after January 5$^{\text{th}}$, 2015, was blinded for a potential WIMP signal, i.e. single scattering events in the energy range $E_{\text{rec}} \in [0, 200]\,\text{keV}$ with an ionization yield $0 < Q < 0.5$ were withheld from the available dataset. The data until January 5$^{\text{th}}$ was analysed in terms of standard mass WIMPs with $m_\chi = \mathcal{O}(100)\,\text{GeV}/c^2$. This unblinded analysis was performed in the context of [119] and is summarised in the following. The analysis is cut-based and limits were derived from remaining events in the signal region with both the Poisson (see

Sec. 3.1.1) and Yellin's optimum interval method (see Sec. 3.1.2). A comparison of the difference in sensitivity achieved with these two methods is given at the end of the section. An analysis of the full Run308, with an additional 4 months of data and an improved data processing, is currently still in progress.

3.2.1. Data selection

Out of 24 detectors which were read out during Run308, 17 were included in the analysis [119]. The 7 excluded detectors were rejected due to either unstable heat channels, missing ionization channels, leakage currents or increased charge trapping. For each of the 17 analysed detectors, ≈1 h time periods for which the baseline resolution of all readout channels was considered to be good, were selected. However, instead of using fixed cuts on baseline noise of individual readout channels, a cut was applied on the so-called *magic point* E_{MP}. This magic point is a variable which combines information of the heat and ionization channels into a single recoil energy value, describing the separation of signal and background. It was constructed to select data for the representation in ionization yield plots, which are used to quantify the event discrimination of the FID800 detectors (see Sec. 2.2.2). The magic point was defined as the highest recoil energy E_{rec} for which the 90% C.L. nuclear recoil band (the signal region) intersects with either the 99.98% electron recoil band, or the 99.87% trigger efficiency curve, or the curve describing the cut on the so-called *heat-only* events (described in Sec. 4.3.2). Only periods with a magic point $E_{\mathrm{MP}} < 20\,\mathrm{keV}$ were selected for the analysis, which removed 4.7% of the data. This cut ensures strong signal discrimination as well as a high detection efficiency down to low energy: the remaining data showed non-zero efficiency down to 6.6 keV and an average trigger threshold (50% efficiency) of 9 keV. In addition to this cut on 1 h-periods, event based cuts were applied to the data. A standard cut is the fiducial cut, used to reject surface events as described in Sec. 2.2.3. It was designed for a large acceptance (99%) of fiducial events. The resulting fiducial volume was measured to be ≈75%. The only other event cut is the rejection of pile-up events, with a cut on the χ^2-value of the template fit to the recorded pulse of each channel.

The total livetime for the 17 detectors after all cuts was calculated by summing up all 1 h periods, with at least one event fulfilling requirements on the fiducial ionization E_{fid} and heat energy E_{heat} with respect to the FWHM baseline noise: $E_{\mathrm{fid}} > 2\,\mathrm{FWHM}_{\mathrm{fid}}$ and $E_{\mathrm{heat}} > 1.5\,\mathrm{FWHM}_{\mathrm{heat}}$. From this total livetime, 11% were removed to correct for dead-time induced by maintenance procedures. To derive the exposure, the remaining livetime was multiplied with a conservative value for the fiducial mass of 600 g per detector, giving a total exposure of 690 kg·days. Last, the acceptance of the signal region in the nuclear recoil band was determined as a function of energy from neutron calibration data and taken into account. Using a conservative lower value of 86%, the final exposure of the analysis after all cuts was derived to be 600 kg·days.

The combined data after all period and quality cuts is shown in the parameter plane of ionization yield Q vs. recoil energy E_{rec} in Fig. 3.3. Plotted for reference are the different confidence bands for nuclear and electron recoils, averaged over all detectors and time periods. In the signal region, which is the 90% C.L. NR-band for $E_{\mathrm{rec}} \in [6.6, 200]\,\mathrm{keV}$, a total of 17 detector hits[1] were found and have been studied in detail. Of these 17 hits, 5 were found to be in coincidence with the muon-veto system and other detectors and therefore likely to be muon-induced neutrons. Another 7 hits were found to be in coincidence with other detectors and therefore multiple scattering events which are caused by neutrons. Considering the exposure and energy threshold of this analysis together with exclusion limits from other experiments, a WIMP signal as origin of the remaining 5 single scatter

[1] Different hits in multiple bolometers can belong to the same particle and thus be summarized as an event.

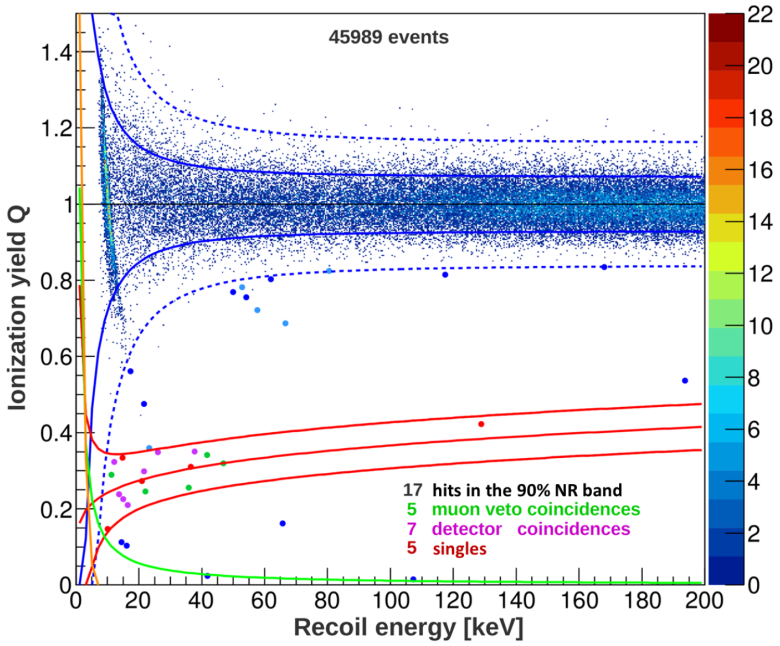

Figure 3.3.: Ionization yield Q vs. recoil energy E_{rec}, for data from 17 detectors which were used in the EDELWEISS-III standard mass WIMP analysis of Run308. Events below the detector averaged 99.98% C.L. band for electron recoils (dashed blue lines) are marked as blue points. A total of 17 detector hits were found within the 90% C.L. nuclear recoil band of their respective detectors (solid red line). Of these hits, 5 are potential WIMP candidates, while the remaining 7 and 5 bolometer hits are in coincidence with other bolometers and also additionally the muon-veto (see legend in the figure for colors). Extracted from [119].

events can be excluded with high probability. It will be shown in the discussion of the results derived from this data that the achievable sensitivity for standard mass WIMPs is at least one order of magnitude worse than the current exclusion limit from liquid noble gas experiments such as LUX [115]. The more likely explanation is therefore that the 5 single nuclear recoil events are an unconsidered background. Given the excellent performance of the EDELWEISS detectors in terms of event discrimination and surface event rejection (see Sec. 2.2.2 and Sec. 2.2.3), the most likely explanation is that these events are single scatter neutron events.

3.2.2. Excess of neutron background

Assuming that the 5 single scatter events remaining in the signal region are neutron events, they could potentially be induced by muons but not rejected by the muon-veto system due to an inefficiency. To investigate this possibility, a dedicated study on the muon-induced neutron background has been performed in [61]. This study involved Geant4 simulations of muons in the experimental setup for the detector configuration of Run308, considering the average response of each individual detector and the data selection cuts described in the previous section. The expected muon-induced neutron background in the 90% C.L. NR-band, before rejecting coincidences with the muon-veto, was determined as

$$N_{\mathrm{simu}}^{\mathrm{WIMP-like}} = 0.36 \pm 0.02\,(\mathrm{stat})\,^{+0.12}_{-0.08}\,(\mathrm{sys})\ \mathrm{events} \tag{3.6}$$

Taking into account the deadtime of the muon-veto and the lower limit on its efficiency of 93%, an upper limit on the expected irreducible background of muon-induced WIMP like

events after vetoing was derived:

$$N_{\text{simu}}^{\text{WIMP-like; after } \mu\text{-veto}} < 0.06 \text{ events at } 90\% \text{ C.L.} \tag{3.7}$$

These results demonstrate that the 5 observed events cannot be explained in terms of muon-induced neutron background. In addition, the observed event topology is in strong disagreement with muon-induced neutrons.
The more probable explanation for the observed events are radiogenic neutrons. However, simulations of all known sources of radiogenic neutrons cannot reproduce such a high number of events. These simulations were performed for one year of data taking with 24 detectors. A total of 4.8 nuclear recoil events are expected in the RoI, of which 1.4 would be single scattering events. Neglecting the acceptance of the nuclear recoil band, this corresponds to 0.6 expected events from neutrons (single or multiple) for the accumulated exposure of 690 kg·days considered in this analysis and therefore much below the observed 5 events. However, the so-called *single-over-multiple* ratio, which is the ratio between single over multiple scatter nuclear recoils, can be calculated as $5/7 \simeq 0.71$ and is in statistical agreement with the average value of $0.45 \pm 20\%$ extracted from simulations. Due to the large statistical uncertainty on the ratio for both simulation and measurement, the determination of a specific material as neutron source is not possible. Further simulations are ongoing to find the responsible source which produces such a rate and multiplicity of events.

3.2.3. Results

Without clear knowledge on the exact origin of the 5 events observed in the signal region, no background subtraction could be performed. Therefore, all 5 events were considered as signal candidates. A 90% C.L. upper limit on the spin-independent WIMP-nucleon scattering cross section was derived with two different methods which were introduced above: with the Poisson method (Sec. 3.1.1) and the optimum interval method as described by Yellin (Sec. 3.1.2). These exclusion limits are both shown in Fig. 3.4, in comparison with results from EDELWEISS-II. The more sensitive limit was derived with the optimum interval method, with an upper 90% C.L. value for the cross section of $\sigma = 5.15 \cdot 10^{-6}$ pb for a WIMP mass of $m_\chi = 60\,\text{GeV}/c^2$. For a large range of WIMP masses, this limit is a factor of $\approx$4 worse than the limit expected from a background free experiment. This can be easily understood when looking at the Poisson-limit: for 5 events, the 90% C.L. upper limit as calculated with Eq. 3.3 is 9.27 events, which is a factor of 4.03 higher than the background free limit of 2.35 events. The benefit of the more complex optimum interval method with respect to the simple Poisson method is not very significant. Responsible for this is the energy distribution of the 5 candidate events at $E_{\text{rec}} = 10.03, 14.90, 20.97, 36.68, 128.80\,\text{keV}$. For WIMPs with $m_\chi = 60\,\text{GeV}/c^2$, it leads to a choice of the optimum interval from 14.90 keV to 128.80 keV, which is not very different from the energy interval used with the Poisson method. It must be noted that for higher WIMP masses the limit is actually worse than the one derived with EDELWEISS-II, although both experiments measured 5 events in the signal region and the exposure of 600 kg·days analysed here is larger than the 384 kg·days accumulated with EDELWEISS-II. Again, the reason is in the energy distribution of the observed events. For EDELWEISS-II, this distribution was more beneficial for the optimum interval method, as 4 events were below 23.2 keV with a large gap to the fifth event at $E_{\text{rec}} = 172\,\text{keV}$.
It can be stated that the sensitivity of the Run308 EDELWEISS-III data to standard mass WIMPs is clearly limited by the appearance of an unknown background, which is most likely caused by radiogenic neutrons. However, due to the spectral shape of this neutron background, it mainly affects higher WIMP masses. For lower WIMP masses, the

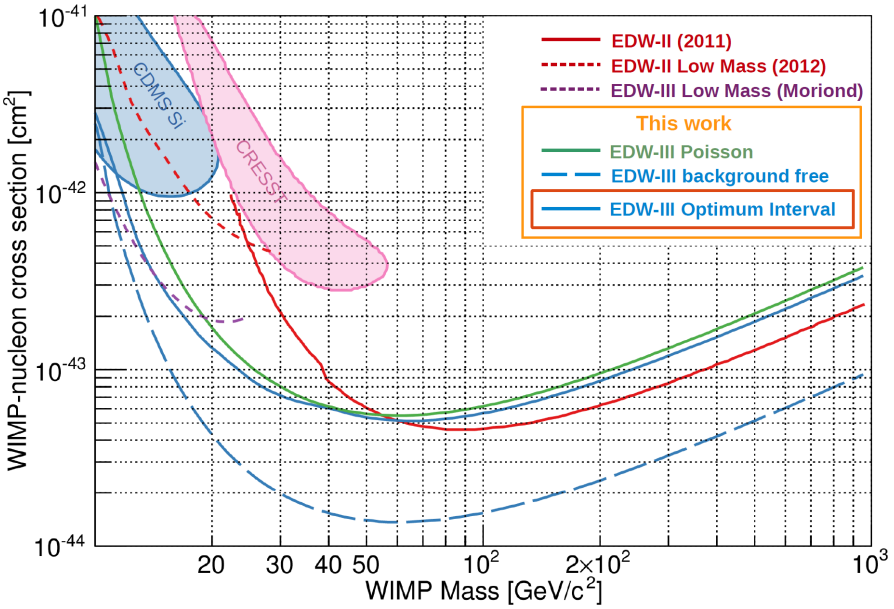

Figure 3.4.: Exclusion limit at 90% C.L. of the WIMP-nucleon scattering cross section as a function of WIMP mass m_χ. Three different exclusion curves are shown for the Run308 EDELWEISS-III data from 17 detectors. The limits derived with the optimum interval and a simple Poisson method are plotted as solid blue and green lines, respectively. Due to the observation of 5 single nuclear recoil events, both derived limits are significantly worse than the expected limit for a background free experiment (dashed blue line). Extracted from [119].

resulting exclusion limit from the optimum interval method is more promising and for very low masses even approaches the background free limit. For masses $m_\chi < 40\,\mathrm{GeV}/c^2$, the sensitivity achieved with EDELWEISS-III shows a significant improvement compared to EDELWEISS-II. This improvement is related to better resolutions and energy thresholds, as well as the selection of lower energy data with the cut on the magic point. A factor of $\approx$3 is gained for $m_\chi = 10\,\mathrm{GeV}/c^2$, which is twice more than expected from the difference in exposure. The availability of low energy data as well as the observation of a limiting neutron background for standard mass WIMPs favoured the analysis for low mass WIMPs, which will be discussed in the following section. Additional motivation to search for low mass WIMPs with EDELWEISS-III, comes from an excess of events, which different direct detection experiments [106, 50, 105] have observed in the recent past and possible signals of WIMP annihilation in the galactic center [28]. Both types of possible signals are incompatible with standard mass WIMPs in the GeV/c^2 to TeV/c^2 range, but could be an indication for asymmetric dark matter (see Sec. 1.2.3).

3.3. Application of a BDT in a search for low mass WIMPs with EDELWEISS-III

A first WIMP search with EDELWEISS-III data, based on the principle of Boosted Decision Trees, was performed in the framework of [120]. The analysed data was recorded from July 2014 until January 2015 during the first half of the Run308 WIMP search campaign. Only one detector labelled FID837 was used, which had an average performance in terms of baseline noise and trigger threshold. The applied cuts were designed to be conservative, e.g. with an analysis threshold in heat energy corresponding to a trigger efficiency of $\simeq$100%, which resulted in a total exposure of 35 kg·days[2]. Although the analysis was only performed

[2]For comparison: the low mass WIMP search with EDELWEISS-II data [58] was based on an accumulated exposure of 113 kg·days

on a small subset of the available EDELWEISS-III data, the exclusion limit which was extracted was already competitive with other direct detection experiments [86] (see purple dashed line in Fig. 3.4) and showed the potential of EDELWEISS-III in the low mass WIMP sector.

Based on the same BDT approach, a more extensive analysis of Run308 data was developed within the EDELWEISS collaboration [1]. This improved analysis used data from the full Run308 for 8 FID800 detectors with a total exposure of 582 kg·days. Various improvements were made compared to the initial analysis of FID837, such as more optimized cuts and a more adequate background description, which relies on sideband data to model some of the background components. The selection of detectors and cuts was optimized to search for low mass WIMPs with $m_\chi \in [4, 30]\,\mathrm{GeV}/c^2$. Both this BDT analysis and the likelihood analysis performed in this thesis were developed in parallel during the ongoing Run308, while the data was still blinded with respect to potential WIMP signals. With the exception of several (important) quality cuts, the data used by both analyses is the same. For this reason, all period and quality cuts will be explained in detail in Sec. 4.1 whereas only a short overview is given here. In the following, only the analysis using a BDT [1] will be summarized in detail.
A comparison between the results of the likelihood analysis of Ch. 4 and the BDT-based analysis described here follows in Sec. 4.4.5. To compare the subtleties between the maximum likelihood and BDT analysis, we describe here in detail the BDT results.

3.3.1. Data selection

The analysed data was recorded during the so-called Run308 of the EDELWEISS-III experiment. This 10 month long cool-down between July 2014 and April 2015 was dedicated to WIMP search, with regular γ-calibration measurements using a ^{133}Ba source and one neutron calibration with a ^{241}AmBe source. Out of the 24 detectors which were read-out by the DAQ-system, several had non-functioning channels which disqualified them for WIMP search. For the remaining detectors, the main selection criterion is the sensitivity to low mass WIMPs which requires a very low threshold energy. A total of 8 detectors were selected due to their low baseline noise on the heat channels and resulting low trigger threshold. For sufficient sensitivity to low mass WIMPs, only time periods with an average online threshold of less than $1.5\,\mathrm{keV_{ee}}$ were selected. Additional period cuts were applied for each detector individually: the FWHM of the combined heat and fiducial ionization baselines was required to be smaller than $1.0\,\mathrm{keV_{ee}}$ and $0.7\,\mathrm{keV_{ee}}$, respectively. A loose cut was also applied to each of the two veto electrodes, excluding periods with a baseline noise of more than $1.5\,\mathrm{keV_{ee}}$. A total of 927 live-days remained after these cuts, including all DAQ related dead-time. The resulting exposure of 582 kg·days was calculated considering an average fiducial volume of 630 g per detector. The fiducial volume of each detector was derived from a set of cosmogenic activation lines induced by decays which are homogeneously distributed within the detector and have been describe in Sec. 2.4.3. To reject pile-up events and only use well reconstructed energy signals, cuts were applied on the χ^2-value of the template fit for all readout channels of a detector. This cut also efficiently removes events from radioactive decays within one of the NTD heat sensors only. Remaining events were rejected by an additional cut applied on the difference of the two heat signals. The region of interest was defined with cuts on the energy of all readout channels. To exclude the triplet of cosmogenic activation lines around 10 keV as well as negative energy fluctuations, the total ionization energy was required to be in the range $E \in [0, 8]\,\mathrm{keV_{ee}}$. For the combined heat energy of events, a lower cut was applied depending on the trigger efficiency, measured to be at least 70% for all detectors. For the 4 detectors with lower baseline noise, a minimum heat energy of $1\,\mathrm{keV_{ee}}$ was required, such as for detector FID825 shown in Fig. 3.5. The other 4 detectors have a minimum heat energy of $1.5\,\mathrm{keV_{ee}}$. The upper bound on the heat

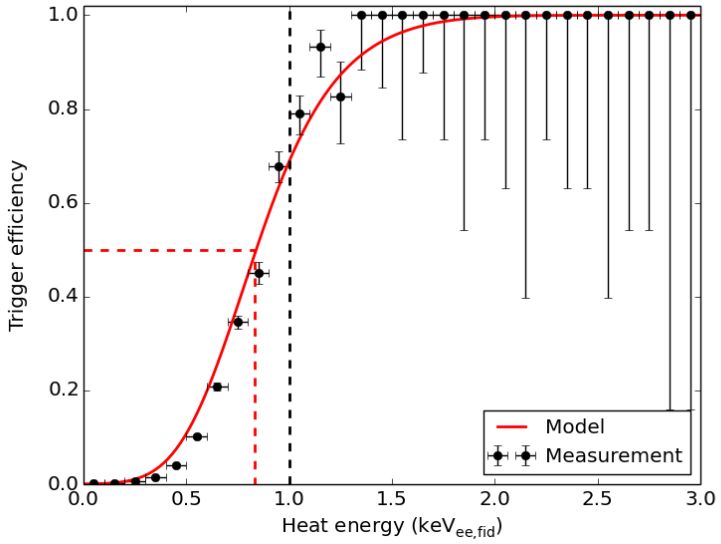

Figure 3.5.: Modelled trigger efficiency for detector FID825 (red curve) averaged over Run308. It shows a good agreement with the measured data (black points). The analysis threshold in heat energy of 1.0 keV$_{ee}$ (black dashed line) is shown together with the 50% trigger efficiency energy for reference (dashed red line). Figure from [1].

energy of the RoI is 12 keV$_{ee}$, which allows a sufficient efficiency for a $m_\chi = 30\,\mathrm{GeV}/c^2$ WIMP signal. To reduce the number of events to process, a lose pre-selection of fiducial events was performed: the signal on each of the veto electrodes was required to be smaller than $5\,\sigma$ of the baseline noise. The final discrimination between fiducial and surface events was performed event-by-event by the BDT, using the actual measured veto energy.

3.3.2. Modelled backgrounds

All background models used in the BDT analysis were derived from sidebands which do not overlap with a potential WIMP signal, before the unblinding of the data. In the low energy RoI for this analysis, several backgrounds were considered and are listed in the following. The dominant background consists of so-called heat-only events. These events are characterized by a significant heat signal but no measured ionisation signal apart from Gaussian noise on all ionisation channels. Their energy distribution can be approximated by a double exponential function, which overlaps with noise from baseline fluctuations for energies of 1−2 keV$_{ee}$ heat energy. The rate of these events above 3 keV$_{ee}$ varies between 1 and 100 events per day and detector. The origin of these events is still unknown but one possible source could be cracks at the level of the detector holders. A model for these events was derived from the large sideband of events with negative ionization energy. From this sideband, both energy and time distribution were extracted. A small cross-talk between the heat and fiducial ionization channels is taken into account as systematic error on the event rate as it leads to a possible bias of the Gaussian ionization distribution to higher energies. For a $m_\chi = 5\,\mathrm{GeV}/c^2$ WIMP signal, this bias could increase the estimated heat-only background after all cuts by up to 17%. More details on this background are given in Sec. 4.3.2.

The second largest background in the selected data in terms of event rate are electron recoils (ER) in the bulk of the detectors. The energy spectrum of these ER-events can be described by a continuous component from the Compton scattering of external γ's and of β's from the decay of internal tritium (see Sec. 2.4.4). On top of the continuous component is a set of cosmogenic activation lines: there are several K-shell EC lines between 5 and 7.7 keV, plus

a triplet of lines between 9 and 10.4 keV (see Sec. 2.4.3). This triplet has corresponding L-shell lines between 1.1 and 1.3 keV, which are particularly critical as they overlap with a potential signal for the lowest WIMP masses probed. Different ionization topologies exist for these events depending on the location of the decay: there can be a signal on both fiducial electrodes for clear bulk events, or a signal on fiducial and veto electrodes for clear surface events, as well as near surface events, which have a signal on both fiducial electrodes and one of the two veto electrodes (so-called *triple events*). An ER background model was derived from sideband data with $E_{\mathrm{ion}} \in [3, 12]\,\mathrm{keV_{ee}}$ and extrapolated to the whole energy range for each of these event categories. The underlying assumption is that the continuous component is approximately flat in the RoI and that the L/K ratio for the cosmogenic peaks is 0.11[98]. In the selected data, the average expected background from the continuous (flat) component in the fiducial volume is 0.18 events/kg/day/keV and 0.79 events/kg/day for the triplet of L-shell peaks. The combined systematic error on this background after all cuts for a $m_\chi = 5\,\mathrm{GeV}/c^2$ WIMP is $\pm 16\%$.

Due to the lose fiducial cut which was applied, the selected data contains a large number of unrejected low energy surface events. They are mostly due to β-radiation and lead-recoils which are produced during the radioactive decay chain of radon and its daughters (see Fig. 2.13) and are characterized by a small ionization yield of $Q \approx 0.4$ and $Q \approx 0.1$, respectively. Their energy spectra could not be predicted from simulations, due to large uncertainties, e.g. in the implantation depth of radioactive contamination on the detector surface or materials facing the detector. Instead, sideband data for each detector side (top or bottom) of a clear selection of surface events from betas and lead-recoils was fitted and extrapolated to zero energy. A description of this sideband and the resulting energy spectra is given in Sec. 4.3.5, as the same model is used for the likelihood analysis. For the 927 detector-days of exposure, the average rates of these two components was determined as 20.1 betas/kg/day and 4.5 lead−recoils/kg/day. The extrapolation of the energy spectrum for betas results in a large systematic uncertainty of $\pm 30\%$ in the predicted number of events after all cuts for a $m_\chi = 5\,\mathrm{GeV}/c^2$ WIMP search.

The last background which is the potentially most relevant one are neutrons. As indicated in Sec. 2.4.1, there are two different sources of neutrons in the experiment. For the data selection cuts applied for the low mass WIMP search, the background from muon-induced neutrons in the RoI was estimated from simulations to be less than 0.04 events at 90% C.L. [61] after rejection of coincidence events between muon-veto and Ge-detectors and was therefore neglected. For radiogenic neutrons, an empirical model based on simulations and sideband data was used. The average energy spectrum in energy range $E_{\mathrm{recoil}} \in [2, 20]\,\mathrm{keV_{nr}}$ was extracted from dedicated simulations of all known sources in the experimental setup(see Sec. 4.3.4 for more details) and can be parametrized by a double exponential function. A normalization of the spectrum was performed using multiple scatter events measured during Run308. As was shown in Fig. 3.3, the 17 detectors considered in the standard WIMP mass analysis, measured 9 multiple scatter events in the energy range $E_{\mathrm{recoil}} \in [10, 100]\,\mathrm{keV_{nr}}$ for an exposure of 1309 kg·days. The average single-to-multiple ratio in the same energy range was determined from simulations to be 0.45, with a large systematic uncertainty $\mathcal{O}(20\%)$. The total systematic error on this background due to the uncertainty on this ratio and the statistical error on the number of multiple scattering events was estimated to be 45%.

3.3.3. BDT classification

A BDT was trained to classify simulated background and signal events for each of the 8 detectors and for a selection[3] of WIMP masses covering the range $m_\chi \in [4, 30]\,\mathrm{GeV}/c^2$. All background components listed in the previous section were considered with their respective

[3]Only the following masses are considered: $m_\chi \in \{4, 5, 6, 7, 8, 10, 15, 20, 25, 30\}\,\mathrm{GeV}/c^2$

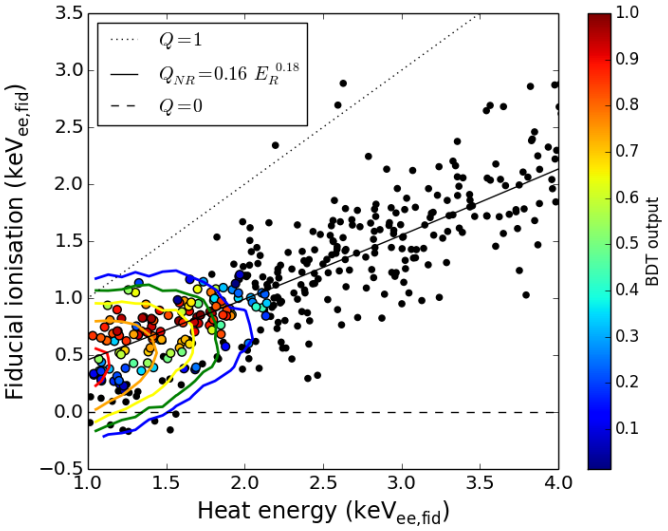

Figure 3.6.: Neutron calibration data for detector FID825 in fiducial ionization vs. heat energy, after the application of the same cuts as for WIMP data and processing with a BDT which was optimized for 5 GeV WIMPs. All events with a positive value of the BDT discrimination variable are colour coded. The distribution of these signal like events matches well with the expected contours of a WIMP signal of the same mass. Events slightly above the nuclear recoil ionization yield Q_{NR} are considered more signal like, as they are more easily discriminated from the low energy ER background (expected at $Q = 1$, dotted line) than from heat-only events (expected at $Q = 0$, dashed line). Figure from [1].

energy spectrum and ionization yield. The fiducial WIMP signal was constructed for each mass m_χ following Eq. 1.24 and assuming the empirical EDELWEISS parametrization for the ionization yield of nuclear recoils $Q_{\mathrm{NR}} = 0.16 \cdot E_{\mathrm{rec}}^{0.18}$. For each simulated toy event, which is used to train the BDT, a total of 6 observables were generated: the signals on the 4 ionization channels, a combined heat signal and a variable describing the rate of heat-only events during a given time period. Fluctuations of the baseline noise of all channels as well as the trigger efficiency of each detector were taken into account. The BDT reduces the information of each event into a single discriminating output variable normalized between -1 (background-like) and +1 (signal-like). An example of this is given in Fig. 3.6, where the discriminating BDT output variable is shown for neutron calibration data of detector FID825, together with a WIMP signal of $m_\chi = 5\,\mathrm{GeV}/c^2$ for which the BDT was trained for. The distributions of the normalized WIMP signal and the simulated backgrounds, scaled to the expected rate of events, are shown in Fig. 3.7. Based on the histogrammed distributions of simulated events, a cut on the BDT output variable was defined before the unblinding of the data in the RoI for WIMPs. It was chosen individually for each detector and WIMP mass to give the best signal over background ratio and maximize the sensitivity for the combination of the detectors. This BDT-cut induces a significant loss of signal for low WIMP-masses, as will be detailed in Sec. 4.4.5. Its effect on the efficiency of measuring a WIMP signal as a function of recoil energy is shown in Fig. 3.8 for two different masses and selection of detectors. For $m_\chi = 20\,\mathrm{GeV}/c^2$, the cut was optimized to exclude gamma and heat-only backgrounds at low energies as well as neutrons at higher energies, which have a harder recoil energy spectrum. Events kept as a potential signal are mostly in the energy range $E_{\mathrm{rec}} \in [6, 15]\,\mathrm{keV_{nr}}$ with a good efficiency of 87%. For a $m_\chi = 5\,\mathrm{GeV}/c^2$ WIMP, considering only detectors with a lower analysis threshold of $1\,\mathrm{keV_{ee}}$, the cut results in a severe loss of efficiency: in addition to the trigger efficiency and the analysis threshold in heat energy, only 20% of all recoils in the energy range $E_{\mathrm{rec}} \in [3, 4]\,\mathrm{keV_{nr}}$ are kept.

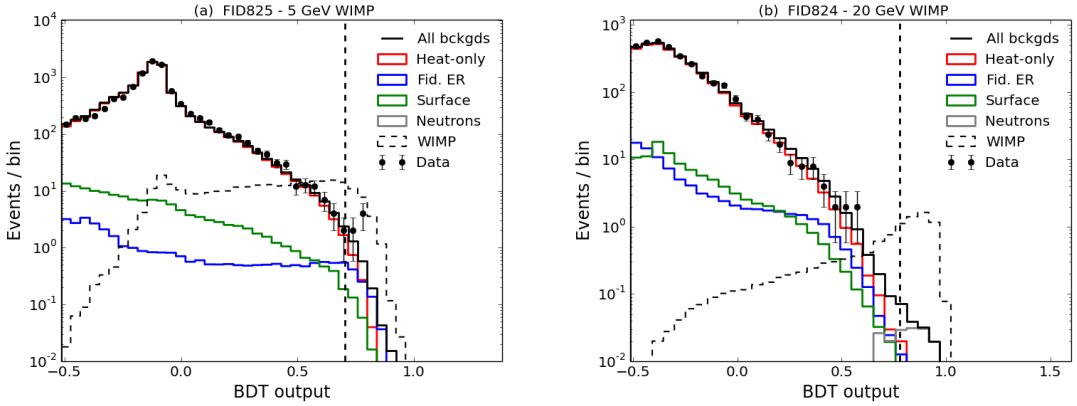

Figure 3.7.: Distribution of the discriminating BDT output variable for two detectors and different WIMP masses $m_\chi = 5\,\mathrm{GeV}/c^2$ (left) and $m_\chi = 20\,\mathrm{GeV}/c^2$ (right). The actual data (black dots with error bars) matches well the expected sum of all backgrounds (black histogram, individual components as colored histograms) calculated before unblinding. Events above the BDT cut (dashed vertical line) are used to derive the upper limit on the WIMP-nucleon scattering cross section for each WIMP mass m_χ. Figure from [1].

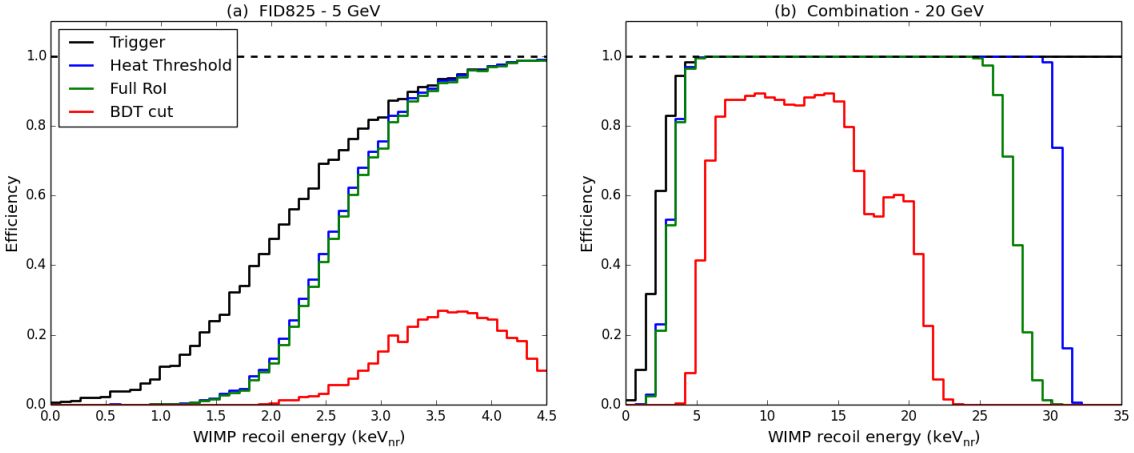

Figure 3.8.: Efficiency to measure a WIMP signal as function of nuclear recoil energy after different consecutive cuts applied on the data. (a) For the most sensitive detector FID825 and a BDT optimized for WIMPs with $m_\chi = 5\,\mathrm{GeV}/c^2$. (b) For the combination of all detectors and a WIMP mass of $m_\chi = 20\,\mathrm{GeV}/c^2$. The strong reduction of efficiency due to the BDT cut (red histogram) at low WIMP masses is evident. Figure from [1].

3.3.4. Results

As can be seen for the two different detectors and WIMP masses in Fig. 3.7, the distribution of the actual data after unblinding is in good overall agreement with the predicted overall rate summarizing all background components. The expected rate of events from different types of background after all cuts, including the BDT cut, is given in Tab. 3.1 for the combination of all considered detectors[4] and a representative selection of 4 different WIMP masses. For all masses, the number of 4 to 9 observed events is in slight excess of the expected total background of 1.07 to 6.14 events. The p-values, which describe the Poisson probability of measuring the observed number of events from the expected background-only hypothesis, range between 1.1% and 22%, with the highest excess of events for $m_\chi = 7\,\mathrm{GeV}/c^2$. The excess is caused by different events depending on the WIMP mass which is probed. The events causing the excess for the two WIMP masses $m_\chi = 5\,\mathrm{GeV}/c^2$ and $m_\chi = 20\,\mathrm{GeV}/c^2$ are shown in Fig. 3.9. The 9 excess events observed for a WIMP mass of $m_\chi = 5\,\mathrm{GeV}/c^2$ were measured in 3 different detectors and have a low heat energy between 1.0 and 1.7 $\mathrm{keV_{ee}}$. For $m_\chi = 20\,\mathrm{GeV}/c^2$ the 4 excess events were measured in 3 detectors and with ionization yields close to the expected value Q_{NR} for nuclear recoils. Using the Poisson method described in Sec. 3.1.1, a limit on the WIMP-nucleon scattering cross section was derived from the total number of observed number above the BDT cut, without the subtraction of the expected background. It is shown in Fig. 3.10 with the $1\,\sigma$ and $2\,\sigma$ uncertainty related to systematic uncertainties and statistical variations. The limit is worse than the expected sensitivity over the probed mass range due to the excess of different backgrounds. For $m_\chi > 10\,\mathrm{GeV}/c^2$, the excess is probably caused by radiogenic neutrons, which are the dominating background after BDT cut and a large systematic error associated to their expected rate. As for $m_\chi < 7\,\mathrm{GeV}/c^2$, the dominating backgrounds above the BDT-cut are heat-only events and low energy fiducial electron recoils. However, 3 of the observed events seem incompatible with the expected energy distribution of these background sources and are potentially related to a background which was not considered a priori. Calibration measurements showed that up to 5% of low energy betas could appear as triple-electrode events with measured energies hardly distinguishable from a fiducial low energy nuclear recoil. While considering this additional component would change the p-value for $m_\chi = 5\,\mathrm{GeV}/c^2$ to 43% the excess at $m_\chi = 7\,\mathrm{GeV}/c^2$ would still be described with a p-value of 2.3%.
Despite the observed excess in events, the conservative limit which was derived without any background subtraction represents a significant improvement with respect to the limit obtained with EDELWEISS-II [58]. A factor of 12 is observed for at $m_\chi = 10\,\mathrm{GeV}/c^2$ and at $m_\chi = 7\,\mathrm{GeV}/c^2$ the improvement is as high as a factor of 41, which is ≈10 times better than would be expected from the simple increase in exposure. Overall, the BDT based analysis presented here confirms the exclusion limits for low mass WIMPs set by LUX [115] and SuperCDMS [48] and disfavours all signal interpretations of event excess shown in Fig. 3.10. The good overall agreement between the observed data and the background model is an incentive to apply a more optimistic analysis method to the low energy data of Run308. Following this approach is the analysis based on the maximum likelihood principle, which is described in detail in Ch. 4 of this thesis. In the following section, the principle of maximum likelihood and the tools necessary to perform this analysis, are introduced.

[4] Depending on the WIMP mass, only detectors contributing to the sensitivity are considered, e.g. only the 4 detectors with an analysis threshold of 1 $\mathrm{keV_{ee}}$ for $m_\chi = 5\,\mathrm{GeV}/c^2$.

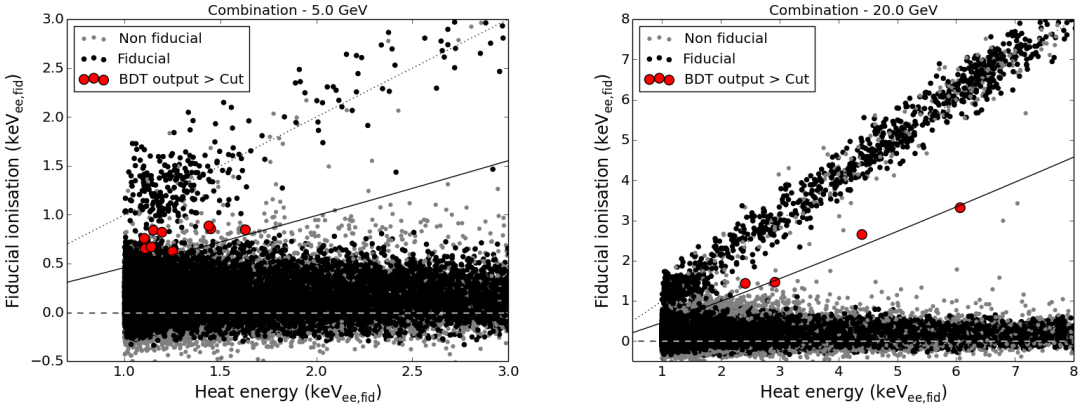

Figure 3.9.: Distribution of events from all detectors in the RoI in heat vs. fiducial ionization energy. Gray points are possible surface backgrounds with a signal $E > 0.4\,\mathrm{keV_{ee}}$ on one of the veto electrodes. Events of a detector passing the BDT cut for $m_\chi = 5\,\mathrm{GeV}/c^2$ (left) or $m_\chi = 20\,\mathrm{GeV}/c^2$ (right) are marked in red. The black lines (dotted, solid, dashed) indicate different ionization yields corresponding to those in Fig. 3.6. Figure from [1].

Table 3.1.: Number of expected and observed events after BDT cut for the combination of all detectors. *"Others"* summarized all non-fiducial events such as betas, lead-recoils and gammas with different electrode topologies. Table from [1].

WIMP mass	$5\,\mathrm{GeV}/c^2$	$7\,\mathrm{GeV}/c^2$	$10\,\mathrm{GeV}/c^2$	$20\,\mathrm{GeV}/c^2$
Fiducial neutrons	0.02 ± 0.01	0.15 ± 0.07	0.36 ± 0.16	1.05 ± 0.47
Fiducial ER	2.71 ± 0.43	1.02 ± 0.16	0.43 ± 0.07	0.12 ± 0.02
Heat-only events	$2.87^{+0.49}_{-0.03}$	$0.43^{+0.07}_{-0.00}$	$0.20^{+0.03}_{-0.00}$	$0.11^{+0.02}_{-0.00}$
Others	0.55 ± 0.16	0.12 ± 0.04	0.09 ± 0.03	0.07 ± 0.02
Total background	$6.14^{+0.67}_{-0.46}$	$1.71^{+0.19}_{-0.18}$	1.07 ± 0.18	1.35 ± 0.47
Events observed	9	6	4	4
p-value	22%	1.1%	2.8%	6.3%

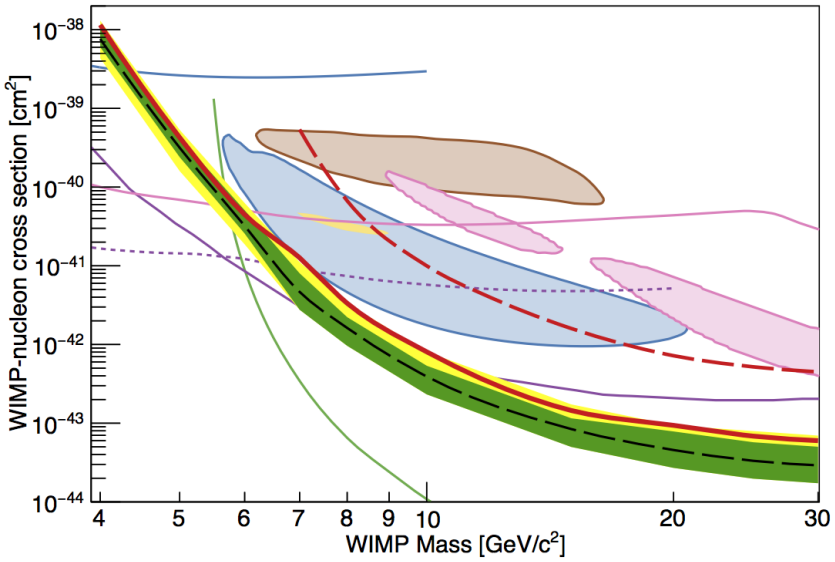

Figure 3.10.: 90% C.L. exclusion limit on the spin-independent WIMP-nucleon cross section as a function of WIMP mass, set with the BDT analysis of EDELWEISS-III data (red solid line). The green and yellow band represent the 1σ and 2σ confidence band of the expected median sensitivity (dashed black) and are derived from Poisson-statistics and systematic uncertainties of the background model. Contours show possible signals from CDMS-Si [106] (blue), DAMA [104] (brown), CRESST-II [50] (pink) and CoGeNT [105] (yellow). Other existing exclusion limits are from EDELWEISS-II [58] (dashed red), LUX [115] (green), DAMIC [121] (blue), CRESST [51] (pink), CDMSlite [49] (dashed violet) and SuperCDMS [48] (violet). Figure from [1].

3.4. Tools for a maximum likelihood analysis

The analysis of EDELWEISS-III data performed in the framework of this thesis is based on a maximum likelihood method. The selection of data and results will be explained in detail in Ch. 4. The following section introduces the maximum likelihood principle and its application to derive exclusion limits. Following [122], in Sec. 3.4.1 the description of data with an extended likelihood function and its minimization to estimate the best fit parameters. For a statistical evaluation of the resulting fit, a so-called hypothesis test can be performed. It allows to either calculate the significance of a discovered signal, or the setting of an exclusion limit with a required confidence level. The principle of such a hypothesis test, based on a well studied statistical approximation, is given in Sec. 3.4.2. Last, the software tools `RooFit` and `RooStats` which have been used for this thesis, are introduced in Sec. 3.4.3.

3.4.1. The likelihood function

In a typical direct detection dark matter experiment, several quantities are measured for each recorded event, which are called *observables* and denoted with $\vec{x}$ in the following. The most relevant observables for the events measured with EDELWEISS-III are the energies measured on the different readout channels of an FID800 detector. For a given class of events, for example a background process originating from γ-radiation, the expected distribution in these observables can be described with a *probability density function* (PDF) $f(\vec{x})$, which is positively defined and normalized to unity:

$$\int f(\vec{x})\mathrm{d}\vec{x} = 1 \tag{3.8}$$

Often, this PDF depends on a set of parameters $\vec{\theta} = \{\theta_1, ..., \theta_I\}$ and is then referred to as a *probability model* and denoted

$$f(\vec{x} \mid \vec{\theta}) \tag{3.9}$$

A simple case, which will be used in the analysis of this thesis, is that the probability model f consists of I different PDF components $f_\mathrm{i}(\vec{x})$, $i = 1, ..., I$ and the parameters θ_i describe the rate of events associated to each component

$$f(\vec{x} \mid \vec{\theta}) = \frac{1}{\nu}\sum_\mathrm{i} \theta_\mathrm{i} f_\mathrm{i}(\vec{x}) \tag{3.10}$$

where $\nu = \nu(\vec{\theta}) = \sum_{\mathrm{i}=1}^{\mathrm{I}} \theta_\mathrm{i}$ is the total rate of all components. For a given dataset $\mathcal{D} = \{\vec{x}_1, ..., \vec{x}_N\}$, one can define a likelihood function $\mathcal{L}$ which is the product of the individual probabilities for all N events:

$$\mathcal{L}(\vec{\theta}) = \prod_{\mathrm{n}=1}^{\mathrm{N}} f(\vec{x}_\mathrm{n} \mid \vec{\theta}) \tag{3.11}$$

In an experiment like EDELWEISS, the number of measured events N is related to the total rate μ for all background processes plus a potential signal. An additional Poisson term $\mathrm{Pois}(N \mid \nu) = \frac{\nu^N}{N!}e^{-\nu}$ can then be added to the likelihood function $\mathcal{L}$. It accounts for the fact that the number of measured events N is a statistical realization of the expected event

rate ν. A likelihood function including this additional Poisson term is a called *extended* likelihood [123]:

$$\mathcal{L}(\vec{\theta}) = \mathrm{Pois}(N \mid \nu) \times \prod_{\mathrm{n}=1}^{\mathrm{N}} f(\vec{x}_{\mathrm{n}} \mid \vec{\theta}) \tag{3.12}$$

Likelihood functions can incorporate the results of auxiliary measurements, which provide additional information on a parameter θ_{i}, in order to properly estimate or reduce its systematic uncertainty. If θ_{i} is not a parameter of interest, it is called a *nuisance* parameter. Nuisance parameters can often be determined from a sideband measurement to be of value θ'_{i} with a systematic uncertainty $\sigma_{\theta,\mathrm{i}}$. By multiplying Eq. 3.12 with a Gaussian PDF $\mathrm{Gaus}(\theta_{\mathrm{i}} \mid \theta'_{\mathrm{i}}, \sigma_{\theta_{\mathrm{i}}}) = \frac{1}{\sqrt{2\pi}} \exp{}^{(\theta_{\mathrm{i}}-\theta'_{\mathrm{i}})^2}/_{2\sigma^2_{\theta_{\mathrm{i}}}}$ for each available sideband measurement, a *constrained* likelihood function can be constructed:

$$\mathcal{L}(\vec{\theta}) = \mathrm{Pois}(N \mid \nu) \times \prod_{\mathrm{n}=1}^{\mathrm{N}} f(\vec{x}_{\mathrm{n}} \mid \vec{\theta}) \times \prod_{\mathrm{i}=1}^{\mathrm{I}} \mathrm{Gaus}(\theta_{\mathrm{i}} \mid \theta'_{\mathrm{i}}, \sigma_{\theta_{\mathrm{i}}}) \tag{3.13}$$

While the shape of the constraint terms depending on the type of auxiliary measurement, the application of Gaussian constraint terms for expected event rates (so-called *yield* parameters) is commonly used [124].
If the data of an experiment has been taken with different detectors $j = 1, ..., J$, one can combine the likelihoods of each data set:

$$\mathcal{L}(\vec{\theta}_1, ..., \vec{\theta}_J) = \prod_{\mathrm{j}=1}^{J} \mathrm{Pois}(N_{\mathrm{j}} \mid \nu_{\mathrm{j}}) \times \prod_{\mathrm{n}=1}^{\mathrm{N_j}} f(\vec{x}_{\mathrm{n,j}} \mid \vec{\theta}_{\mathrm{j}}) \times \prod_{\mathrm{i}=1}^{\mathrm{I_j}} \mathrm{Gaus}(\theta_{\mathrm{i,j}} \mid \theta'_{\mathrm{i,j}}, \sigma_{\theta_{\mathrm{i,j}}}) \tag{3.14}$$

For each likelihood, a separate Poisson term accounts for the number of measured events N_j in that detector. Nuisance parameters can be either individual for each detector, or shared, e.g. if they describe a common property of the signal (e.g. an astrophysical parameter such as the galactic escape velocity v_{esc} for WIMPs) or of the background. In this case, only one constraint term is added to the likelihood function.
A typical application for a likelihood function is parameter estimation, where the set of parameters $\vec{\theta}$ that describe the data are determined. One of the most widely used estimators for that is the *maximum likelihood estimator* (MLE). The MLE for a single parameter θ_{i} is defined as the value $\hat{\theta}_{\mathrm{i}}$ which maximizes the likelihood $\mathcal{L}(\theta_{\mathrm{i}})$. In practice, it is more convenient to minimize the negative logarithm $-\ln \mathcal{L}(\theta_{\mathrm{i}})$ with a tool such as MINUIT [125], a process that is often referred to as *"fitting"* (which makes $\hat{\theta}_{\mathrm{i}}$ the *"best fit value"*):

$$-\frac{\partial \ln \mathcal{L}(\theta_{\mathrm{i}})}{\partial \theta_{\mathrm{i}}} \stackrel{!}{=} 0 \tag{3.15}$$

Minimizing $-\ln \mathcal{L}(\theta_{\mathrm{i}})$ can be simplified by neglecting constant terms in θ_{i}, in particular if $\mathcal{L}$ is an extended likelihood function. In the simple case of an extended likelihood function $\mathcal{L}(\theta)$ with only one parameter θ, a single detector and no constraint terms, the function used for the minimization is given by:

$$-\ln \mathcal{L}(\theta) = \underbrace{\nu(\theta) - N \ln \nu(\theta)}_{\text{extended term}} - \sum_{\mathrm{n}=1}^{N} \ln f(x_n \mid \theta) + \underbrace{\ln N!}_{\text{constant}} \tag{3.16}$$

Likelihood functions are frequently used in parameter estimation, as the maximum likelihood estimator $\hat{\theta}$ performs well in several aspects: it is consistent (i.e. it converges to the true value θ_{true}) and, for a sufficiently large number of events N, it is unbiased and normally distributed.
For a model with more than one parameter, two different types of MLE exist: *unconditional* and *conditional*. The unconditional MLE $\bar{\theta}$ can be found by minimizing the likelihood $\mathcal{L}$ with respect to *all* parameters. If at least one parameter, for example θ_1, is fixed at a given value during the minimization of the likelihood, the conditional MLE $\hat{\hat{\theta}}(\theta_1)$ can be found. This conditional MLE will be used in the following to construct the so-called *profile likelihood ratio*.

3.4.2. Hypothesis tests for discovery or limit setting

The parameter estimation, i.e. finding the maximum likelihood estimator of a potential signal component with its associated uncertainty, is not sufficient to prove or disprove the existence of dark matter. For this, one needs to resort to more sophisticated statistical methods. Commonly used in high energy physics (HEP) are so-called *hypothesis tests*. They allow to make a statement about the statistical significance of a new discovery, or, in the absence of a signal, can be used to construct a one sided confidence interval on the signal strength. In this thesis, hypothesis tests are used to set an exclusion limit on the WIMP-nucleon scattering cross section. Described in this section is a hypothesis test based on the so-called *profile likelihood* test statistics. This hypothesis test can either be performed with Monte Carlo toy data, or with an asymptotic approximation which is described in [126]. In this section, a description of the principle of hypothesis tests and a summary of the results used within the approximation are given. For a detailed derivation of these results, the reader is referred to [126]

In a hypothesis test, one quantifies the agreement of a hypothesis H with the measured data. If the so-called *p-value*, i.e. the fraction of theoretical experiments which are less compatible with the hypothesis than the measured data, are below a given threshold, the hypothesis H can be excluded. For the discovery of a signal, one defines the null hypothesis H_0, which describes only known backgrounds and which needs to be rejected. It can be compared with the alternative hypothesis H_1, which, on top of the known backgrounds, includes an additional signal, e.g. originating from a WIMP-nucleon scattering cross section σ_χ. When setting exclusion limits, the two hypotheses are exchanged: the null hypothesis to be rejected is H_1 and compared with the alternative hypothesis H_0. To calculate the p-value, one defines a test statistics and compares the value of the test-statistics for the measured data with its distribution under a given hypothesis. The test statistics which are defined in this section, are all based on the so-called *profile likelihood ratio*:

$$\lambda(\mu) = \frac{\mathcal{L}(\mu, \hat{\hat{\vec{\theta}}})}{\mathcal{L}(\hat{\mu}, \hat{\vec{\theta}})} \tag{3.17}$$

where the single-hat parameters $\hat{\mu}$ and $\hat{\theta}$ are the respective *maximum likelihood estimators* (MLE) of the signal and the nuisance parameters. The *conditional MLE* $\hat{\hat{\theta}}$ is a function of μ and denotes the value of θ which maximized the likelihood $\mathcal{L}$ for a given μ. Compared to the likelihood function $\mathcal{L}(\mu, \theta)$, the shape of the profile likelihood ratio $\lambda(\mu)$ is wider. This is due to the presence of the nuisance parameters $\vec{\theta}$ and related to their systematic uncertainties, which reduce the information on σ. By definition, $0 \leq \lambda(\mu) \leq 1$, where a good agreement between data and the hypothesized signal of strength μ is given for $\lambda \approx 1$.

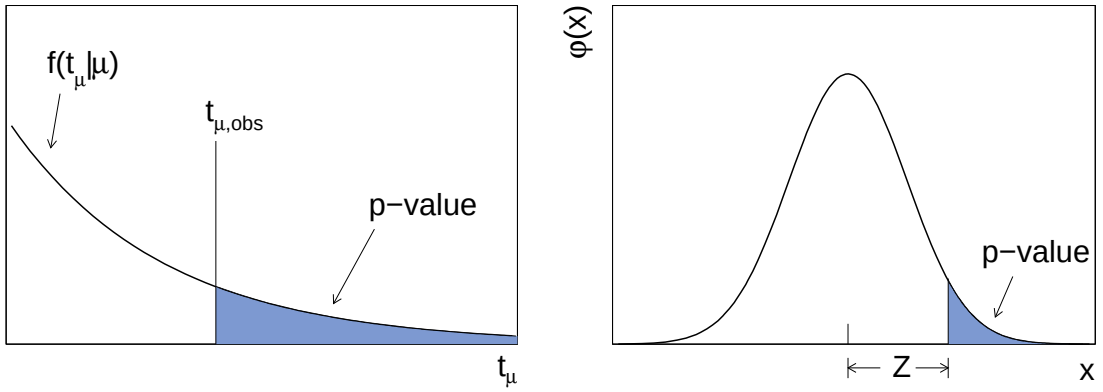

(a) (b)

Figure 3.11.: *Left*: Graphical depiction of how the p-value is defined via the area above the value t_μ^{obs} of the test statistics observed from data in comparison to its pdf $f(t_\mu \mid \mu)$. *Right*: Relation between p-value and significance Z of a standard normal distribution. Figures from [126].

For convenience, the test statistics based on the profile likelihood $\lambda(\mu)$ is defined as:

$$t_\mu = -\ln \lambda(\mu) \tag{3.18}$$

The test statistics can be used to quantify the disagreement between a hypothesized value of μ and the data. This disagreement can be quantified by computing the p-value:

$$p = \int_{t_\mu^{\text{obs}}}^{+\infty} f(t_\mu \mid \mu) \mathrm{d}t_\mu \tag{3.19}$$

where t_μ^{obs} is the value of the test statistics observed from data and $f(t_\mu \mid \mu)$ is the probability density function, which describes how t_μ is distributed for a given signal strength μ. A graphical depiction of Eq. 3.19 is given in Fig. 3.11a. The p-value can be converted into a corresponding significance Z with:

$$Z = \Theta^{-1}(1-p) \tag{3.20}$$

where Θ^{-1} is the inverse cumulative distribution of the standard Gaussian. The relationship between the significance Z and the p-value is depicted in Fig. 3.11b.
The test statistics t_μ given in Eq. 3.18 was defined in a general manner. In the following, two modified test statistics are introduced. The first is q_0, which is used for signal discovery. The second is q_μ, which is used when setting exclusion limits in scenarios where the parameter of interest μ can only take positive values, as is the case for the WIMP-nucleon scattering cross section.

Discovery of a positive signal

The test statistics q_0 is used to reject the background-only hypothesis H_0 ($\mu = 0$) and can therefore lead to the discovery of a new signal. It is defined as:

$$q_0 = \begin{cases} -2\ln\lambda(0) & \hat{\mu} \geq 0, \\ 0 & \hat{\mu} < 0, \end{cases} \tag{3.21}$$

where $\lambda(0)$ denotes the profile likelihood ratio for zero signal as defined in Eq. 3.17. Only cases in which the MLE of the parameter of interest $\hat{\mu}$ is larger than zero are considered as evidence against the background-only model. The other case, corresponding to an underfluctuation of the background, does not suggest an additional signal component but rather an underestimation of the background, which is expected to be dealt with by the systematic uncertainties of the nuisance parameters. Similarly to Eq. 3.19, one can quantify the disagreement of the data with the null hypothesis with a p-value:

$$p_0 = \int_{q_0^{\text{obs}}}^{+\infty} f(q_0 \mid H_0) \mathrm{d}q_0 \tag{3.22}$$

To calculate the p-value for the data, one needs the distribution $f(q_0 \mid H_0)$ of the test statistics q_0. This distribution can always be determined with computing extensive Monte Carlo trials, as was performed in the analysis of this thesis (see Sec. 4.4.3). As an alternative, the general distribution $f(q_\mu \mid \mu')$ can be parametrized, with μ' being a strength paramter. The parametrization is based on the following result found by [127]:

$$-2 \ln \lambda(\mu) = \frac{(\mu - \hat{\mu})^2}{\sigma^2} + \mathcal{O}(1/\sqrt{N}) \tag{3.23}$$

where $\hat{\mu}$ follows a Gaussian distribution with mean μ' and standard deviation σ and N denotes the number of events in the data sample.
In the case of large sample size N, the term $\mathcal{O}(1/\sqrt{N})$ can be neglected, and Eq. 3.21 simplifies to:

$$q_0 = \begin{cases} \hat{\mu}^2/\sigma^2 & \hat{\mu} \geq 0, \\ 0 & \hat{\mu} < 0, \end{cases} \tag{3.24}$$

The standard deviation σ can be estimated with the so-called *Asimov* dataset. This special, artificial data set is defined such that when using it to evaluate the estimators for all parameters, one obtains the true parameter values. For the case of the discovery hypothesis, the standard deviation σ can be calculated with this Asimov data set as

$$\sigma_{\text{A}} = \frac{\mu'^2}{q_{0,\text{A}}} \tag{3.25}$$

where $q_{0,\text{A}} = -2 \ln \lambda_{\text{A}}(\mu)$. The profile likelihood ratio $\lambda_{\text{A}}(\mu)$ for the Asimov data set is calculated from the "Asimov likelihood" $\mathcal{L}_{\text{A}}$, i.e. the likelihood function that is obtained with the generated Asimov data set:

$$-2 \ln \lambda_{\text{A}}(\mu) = \frac{\mathcal{L}_{\text{A}}(\mu, \hat{\vec{\theta}})}{\mathcal{L}_{\text{A}}(\hat{\mu}, \hat{\vec{\theta}})} = \frac{\mathcal{L}_{\text{A}}(\mu, \hat{\vec{\theta}})}{\mathcal{L}_{\text{A}}(\mu', \vec{\theta})} \tag{3.26}$$

From Eq. 3.23, the PDF $f(q_0 \mid H_0)$ for the discovery test statistics q_0 can be approximated following Wilks theorem [128] as a so-called *half chi-square* distribution:

$$f(q_0 \mid 0) = \frac{1}{2}\delta(q_0) + \frac{1}{2}\frac{1}{\sqrt{2\pi}}\frac{1}{\sqrt{q_0}} e^{-\frac{q_0}{2}} \tag{3.27}$$

It can be shown that the significance of the data is simply expressed by:

$$Z_0 = \Theta^{-1}(1 - p_0) = \sqrt{q_0} \tag{3.28}$$

where q_0 was given in Eq. 3.24.

Setting of an exclusion limit

Of particular relevance for the analysis presented in this thesis is the setting of exclusion limits on the parameter of interest μ. Again, one can define a test statistics q_μ[5] which can be used to reject the signal hypothesis H_μ:

$$q_\mu = \begin{cases} -2\ln\lambda(\mu) & \hat{\mu} < \mu \\ 0 & \hat{\mu} > \mu. \end{cases} \tag{3.29}$$

The p-value used to reject the signal hypothesis H_μ can then be calculated with

$$p_\mu = \int_{q_\mu^{\mathrm{obs}}}^{+\infty} f(q_\mu \mid H_\mu)\mathrm{d}q_\mu \tag{3.30}$$

where q_μ^{obs} is the value of the test statistics observed from data and the distribution $f(q_\mu \mid H_\mu)$ can be either derived with Monte Carlo toy data or parametrized using the asymptotic approximation.
Similarly to the discovery case described above, and assuming the approximation given in Eq. 3.23, the test statistics for setting upper limits can be simplified to:

$$q_\mu = \begin{cases} (\mu - \hat{\mu})^2/\sigma^2 & \hat{\mu} < \mu \\ 0, & \hat{\mu} > \mu. \end{cases} \tag{3.31}$$

From the same artificial Asimov data set, the standard deviation σ can be approximated as

$$\sigma_{\mathrm{A}}^2 = \frac{(\mu - \mu')^2}{q_{\mu,A}} \tag{3.32}$$

In the case of a large data sample N, the PDF $f(q_\mu \mid H_\mu)$, describing the distribution of the test statistic q_μ, also follows a half chi-square distribution, which simplifies the calculation of the p-value:

$$f(q_\mu \mid \mu) = \frac{1}{2}\delta(q_\mu) + \frac{1}{2}\frac{1}{\sqrt{2\pi}}\frac{1}{\sqrt{q_\mu}}e^{-\frac{q_\mu}{2}} \tag{3.33}$$

For a hypothesized μ the corresponding significance of the p-value is given by

$$Z_\mu = \Theta^{-1}(1 - p_\mu) = \sqrt{q_\mu} \tag{3.34}$$

To calculate an upper limit on μ, one has to find the value for which the p-value is below a given threshold α. It that case, μ can be excluded with a confidence level $1 - \alpha$. The

[5] In principle, this test statistics is based on the case that $\mu < 0$ is allowed, however, the approximation given in the following is valid also for cases where $\mu \geq 0$.

upper limit μ_{up} is the largest value of μ for which $p = \alpha$. It can be shown, that with the asymptotic approximation, the upper limit can be calculated as

$$\mu_{\text{up}} = \hat{\mu} + \sigma \cdot \Theta^{-1}(1 - \alpha) \tag{3.35}$$

For the typical case of 90% C.L. as it is used in direct detection dark matter experiments, $\alpha = 0.1$ and therefore $\Theta^{-1}(1 - \alpha) = 1.28$. As σ is a function of μ (see Eq. 3.32), in practice the limit is found with numerical methods.

To protect against underfluctuations of the background, which could lead to the exclusion of very small values for the parameter of interest μ, the p-value for the exclusion case can be modified according to a method described in [129, 130]:

$$p'_\mu = \frac{p_\mu}{1 - p_0} \tag{3.36}$$

where

$$p_0 = 1 - \int_{q_\mu^{\text{obs}}}^{\infty} f(q_\mu \mid H_0) \mathrm{d}q_\mu \tag{3.37}$$

gives the probability for the test statistics q_μ to be larger than the value q_μ^{obs} observed from data, under the background-only hypothesis H_0. With this method, the 90% C.L. limit μ_{up} is found by increasing μ until

$$p'_\mu(\mu{=}\mu_{\text{up}}) = 0.10 \tag{3.38}$$

In the analysis performed in this thesis, all upper limits are derived with this method, independent of the use of the approximation for the distribution of the test statistic.

Experimental sensitivity

The exclusion limit calculated with the approximation described above can be compared to the theoretical sensitivity of the experiment. This sensitivity is defined by the median significance, assuming that the data follows the background-only hypothesis H_0, with which one can reject a nonzero value for μ. An example of this is given in Fig. 3.12, which shows the distributions $f(q_\mu \mid \mu)$ and $f(q_\mu \mid 0)$ for Monte Carlo generated data. Both distributions are well approximated with the respective asymptotic formulae given in Eq. 3.27 and Eq. 3.33. As the p-value shown in Fig. 3.12 is $p = 0.05$, the value of μ for which this test statistics was evaluated corresponds to the median upper limit with 95% C.L.

With the use of the Asimov data set which was described above, it can be shown that the median exclusion significance is:

$$\text{med}[Z_\mu \mid 0] = \sqrt{q_{\mu,\text{A}}} \tag{3.39}$$

with $q_{\mu,\text{A}}$ calculated with Eq. 3.29 and Eq. 3.26. In an experiment, statistical fluctuations of the background can lead to a weaker or stronger observed limit compared to the expected median sensitivity med$[Z_\mu \mid 0]$ from the background only hypothesis H_0. The median upper limit for a strength parameter μ' is given by

$$\text{med}[\mu_{\text{up}} \mid \mu'] = \mu' + \mu \cdot \Theta^{-1}(1 - \alpha) \tag{3.40}$$

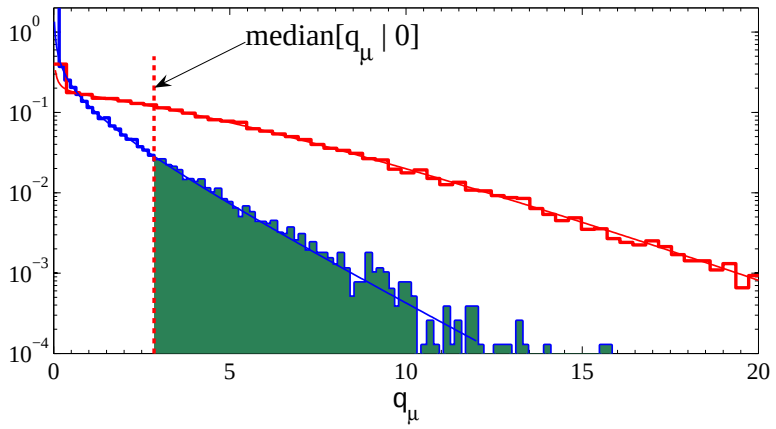

Figure 3.12.: Distibutions for $f(q_\mu \mid 0)$ (red) and $f(q_\mu \mid \mu)$ (blue) from Monte Carlo generated data and the asymptotic approximations (lines). The median signficance of the distribution $f(q_\mu \mid 0)$ leads to a p-value of 0.05. Therefore, the value of μ corresponds to the 95% C.L. upper limit. Figure from [126].

and the corresponding error band with $\pm n\sigma$ is given by

$$\text{band}_{n\sigma} = \mu' + \mu \cdot (\Theta^{-1}(1-\alpha) \pm n) \tag{3.41}$$

where σ can be obtained from the Asimov value of σ_μ.

3.4.3. The tools RooFit and RooStats for statistical analyses

For the likelihood analysis performed in this thesis and discussed in detail in chapter 4, several available analysis tools were used. The modelling of PDFs, the construction of different likelihood functions and their fitting to data were performed with `RooFit` [131]. `RooFit` is a tool for data modelling which was initially developed within the BaBar collaboration to facilitate different analyses related to the search for rare B-decays. It was later on made available to the entire HEP community and is now integrated and maintained within the `ROOT` framework [132]. `RooFit` is designed in an object-oriented way and consists of a library of C++ classes. Each mathematical object is represented by a C++ software object in `RooFit`. An overview of fundamental objects which are used in this maximum likelihood analysis and their corresponding `RooFit` classes are given in Tab. 3.2.

Table 3.2.: Correspondence between mathematical concepts and `RooFit` classes. Table from [131].

Concept	Math Symbol	`RooFit` class name
Variable	x, p	`RooRealVar`
Function	$f(\vec{x})$	`RooAbsReal`
PDF	$F(\vec{x}; \vec{p}, \vec{q})$	`RooAbsPdf`
Space point	$\vec{x}$	`RooArgSet`
Integral	$\int_{\vec{x}_{\min}}^{\vec{x}_{\max}} f(\vec{x}) d\vec{x}$	`RooRealIntegal`
List of space points	$\vec{x}_k$	`RooAbsData`

A variety of predefined classes exist for standard PDFs such as Gaussian (`RooGaussian`) or polynomial shaped (`RooPolynomial`) distributions. More complex PDFs can be built out of individual components via addition (`RooAddPdf`) or multiplication (`RooProdPdf`).

All operations, such as fitting and toy data generation for example, can be used on this more complex PDF and `RooFit` handles the necessary bookkeeping tasks, such as PDF-normalization. To perform an extended likelihood fit as in Eq. 3.12, PDFs can be marked as `extended`, in which case the number of expected events is calculated automatically. With the PDF class `RooSimultaneous`, it is also possible to create a combined PDF-model and therefore a likelihood function over multiple data sets as described in Eq. 3.14. PDFs can be constructed individually with multiple observables and an arbitrary number of parameters as precompiled C++ classes. This method was used in the framework of this thesis, as it offers the highest flexibility to implement the different detector backgrounds as needed. The determination of best fit parameters through the minimization of the (log-)likelihood function is implemented via the `RooMinuit` class interface to `MINUIT` [125]. `RooFit` provides many more features which have also been used in this thesis, such as the plotting of data and PDFs or the possibility to create toy data sets with Monte Carlo techniques to study possible model bias.

`RooFit` is mostly limited to parameter estimation, i.e. the determination of best fit parameters for a given model and data set. To conduct a statistical analysis and determine for example an exclusion limit as described in Eq. 3.35, a different analysis tool called `RooStats` [133] is used. The `RooStats` framework is built on top of the `RooFit`-classes and consolidates different statistical tools which are of use in HEP. The project is based on previously existing code which was used in ATLAS and CMS and is now distributed with `ROOT`. `RooStats` was used for example in the Higgs-search at LHC with complex models combining different search channels. `RooStats` is not limited to frequentist analysis methods but provides an open interface and classes to perform also Bayesian analyses. In the framework of this thesis, several classes have been used, which are related to hypothesis tests. The profile likelihood $\lambda(\mu)$, for example, is implemented via the class `ProfileLikelihoodCalculator`. To perform a single hypothesis test at a given value of μ, one needs to choose between the class `FrequentistCalculator`, which uses Monte Carlo generated toy events, or the class `AsymptoticCalculator`, which employs the asymptotic approximation introduced in the previous section. The calculation of exclusion limits is performed by scanning over a range of values for μ. This is implemented in the class `HypoTestInverter`. At each point for μ, a hypothesis test is performed and the corresponding p-values for the H_μ and H_0 distribution are calculated. `RooStats` automatically interpolates between scan points to derive the approximate upper limit. Results of a hypothesis test are stored in objects of the class `HypoTestResult` and `HypoTestInverterResult`. They can be plotted with the corresponding classes `HypoTestPlot` and `HypoTestInverterPlot`. Examples of for the implementation of a hypothesis test based on `RooStats` are given in the following Sec. 4.4.3.

After the description of the maximum likelihood function to model data, the hypothesis test method to derive upper limits and a short introduction to the software tools used to implement both, we now turn to the analysis of EDELWEISS-III data with a multidimensional maximum likelihood method.

4. Search for low mass WIMPs with a multidimensional maximum likelihood

After reviewing the different statistical methods to analyse data of direct detection experiments, this chapter now describes the analysis of EDELWEISS-III data using a maximum likelihood method. This data was recorded by the same detectors during the same WIMP search run as the data used in the BDT analysis which was presented in Sec. 3.3. Some differences exist however in the choice of observables for the events, the exact definition of a cut to reject surface events and the choice of the region of interest for individual detectors. While the BDT analysis derived limits on the WIMP-nucleon scattering cross section without the subtraction of backgrounds, the analysis presented in this chapter follows a more aggressive approach. All known backgrounds which are relevant for the selected data are modelled for each detector individually. In a likelihood fit of the data with the known backgrounds and an additional potential signal they are thus effectively subtracted. Additional constraint terms for each background are used to restrict this subtraction to values which are in agreement with the expected rate of events for each background. Compared to the BDT analysis, the initial cuts applied on the data are somewhat stricter and, due to the lower acceptance, lead to a reduced exposure. However, this is more than compensated by the background subtraction and the increased signal efficiency. In the BDT analysis, the cut on the BDT output drastically reduces the signal efficiency for low WIMP masses, for which the discrimination of signal and background is difficult. The results achieved with the likelihood method for the same WIMP search data therefore lead to an improved sensitivity for low WIMP masses compared to the BDT analysis.

The chapter starts in Sec. 4.1 with a description of Run308 and the format of the data that is used in this analysis. A comprehensive description of the basic quality and period cuts is of interest for both BDT and likelihood analysis, as they share the same underlying selection of data. Emphasis is put on the definition of the fiducial cut which was independently developed for this analysis and is of crucial importance, as it efficiently rejects surface events down to low energies. The corresponding fiducial volume is determined for each detector and the resulting exposure compared with the one for the BDT analysis. Last, the definition of the region of interest which is based on the individual trigger efficiency of each detector is explained.

Sec. 4.2 shows how probability density functions are constructed from energy spectra of different background and signal components in the parameter space used in this analysis.

The response of the EDELWEISS FID800 detectors to a particle recoil is taken into account to describe the (energy-)variables of the selected data. Efficiencies related to the fiducial cut and the trigger condition of the detector are also taken into account. For each detector a likelihood function is introduced which includes additional constraint terms for the background components. To fit the data of all detectors simultaneously with a common WIMP signal, a combined likelihood function can be constructed as the product of these individual likelihoods.

The backgrounds which are considered in the analysis are listed in Sec. 4.3. In a data-driven approach, the energy spectra for different backgrounds are extracted from sideband data of each detector. Again, several common properties of these backgrounds exist between BDT and likelihood analysis as they are based on the same data. Except for the energy spectra for surface events from β's and ^{206}Pb-recoils, however, all background models were derived independently and partly under different assumptions, for example the composition of the electron recoil background from Compton γ's and tritium β's. Particular importance is paid to the dominating background from so-called heat-only events and its systematic uncertainty due to a possible bias towards higher ionization energies.

Everything comes together in Sec. 4.4 with the discussion of the actual fit results. Both the fit of data from individual detectors as well as the combined fit over the data from all detectors with a common signal are presented. These fit results are analysed for correlations between the event rates of different components, and possible degeneracies between individual backgrounds and the signal are highlighted. Motivated by the absence of a statistically significant excess of signal events for any of the performed fits, exclusion limits on the WIMP-nucleon cross section are then calculated with the hypothesis test based on the profile likelihood. These limits are further put into the context of current direct detection experiments and in particular compared to the results obtained by the BDT analysis to understand the achieved improvements. Finally, an outlook of the EDELWEISS-III search for low mass WIMPs is given. Projections for future stages of the experiment were performed within the collaboration and are discussed here to once more make the case for a detailed likelihood analysis to achieve the highest sensitivity to WIMPs with EDELWEISS detectors.

4.1. Selection of low energy data

4.1.1. WIMP search during Run308

Run308 marks the 8$^{\text{th}}$ cool-down of the EDELWEISS-III experiment. It started on July 22$^{\text{nd}}$, 2014 and ended on April 3$^{\text{rd}}$, 2015 after a cryogenic incident caused a warm-up of the system. The measurement times of the experiment during the run before any dead-time correction is shown in Fig. 4.1. Out of the 204.2 days of data taking, 160.7 were dedicated to the primary objective of WIMP search. In between, regular calibration measurements with ^{133}Ba γ-sources were performed which were used for energy calibration and the monitoring of the γ-rejection performance. To test the empirical parametrization of nuclear recoil quenching in the detectors, a measurement with an ^{241}AmBe neutron source lasting 3.2 days was carried out in October 2014. The remaining 17.9 days were used to perform tests to improve the detector performance by applying different voltage settings as well as for different other R&D purposes.

During the run, 36 FID800 detectors were installed in the cryostat. They were organised in 9 towers of 4 detectors each. 24 of these detectors were fully connected to the read-out and are shown in Fig. 4.2. The reason for the reduced effective detector number is that part of the cabling at the 10 mK stage suffered from a manufacturing problem (delamination of some layers) in the previous run and was not replaced in time. Readout of these detectors

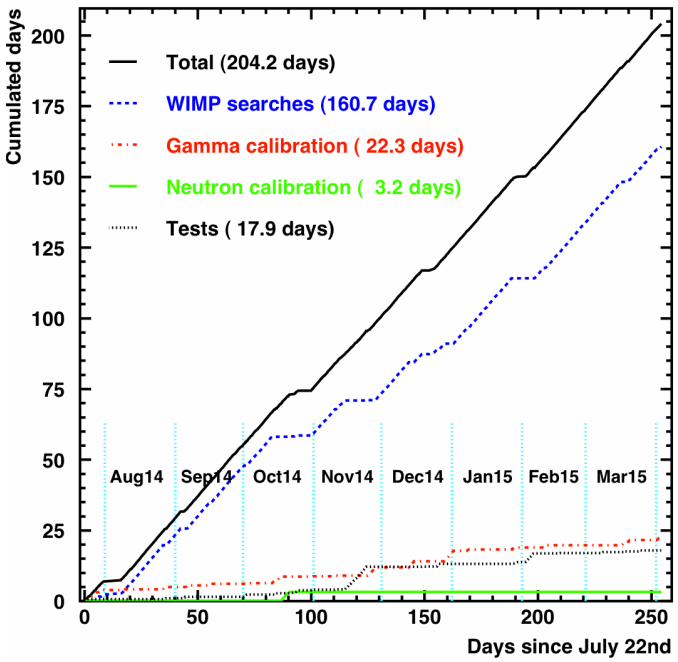

Figure 4.1.: Cumulated measurement time of Run308 since its start on June 22$^{\text{nd}}$, 2014, divided into different categories of data taking. The run was primarily dedicated to WIMP search. Measurements with a ^{133}Ba γ-source were performed regularly to calibrate the energy scale of the detector readout. A calibration with a ^{241}AmBe neutron-source was performed to test the nuclear recoil response of the detectors. Test measurements involved different voltage settings to study the Luke-Neganov amplification of signals.

was by three different Mac computers of the DAQ system labelled s1, s2 and s3 as indicated in the figure by different colours. Additionally, 3 detectors made from $ZnMoO_4$ were installed in towers T10-T12. These scintillating bolometers are under development by the LUMINEU collaboration to search for $0\nu2\beta$-decay of ^{100}Mo [135]. While installed in the same cryostat, their readout was carried out with an independent DAQ system and had no effect on the EDELWEISS data taking.

4.1.2. Data format and availability

All data of Run308 was processed with the *ANA* software developed at IPNL, Lyon [136]. This processing involves all necessary steps, from the fitting of raw pulse traces, via the definition of an energy scale using the ^{133}Ba γ-calibration data to the a posteriori calculation of average baseline noise levels in units of keV$_{\text{ee}}$ *Full Width Half Maximum* (FWHM). Several improvements of this data processing were done over the course of Run308. The final data used in this analysis has been processed with the j-version of ANA and the data processing was fixed on July 28$^{\text{th}}$, 2015. However for detector FID824 and FID826 a later update was necessary to improve the time domain fit of the heat signal and take into account specific noise. Additionally, several heat gains were recalibrated. Previous versions of the ANA-processing starting in January 2015 had all data in the WIMP RoI excluded from the data set ("blinded data"), by removing events fulfilling the following requirements:

- only one detector triggered the acquisition
- recoil energy is between 0 and 200 keV
- ionization yield is between 0 and 0.55

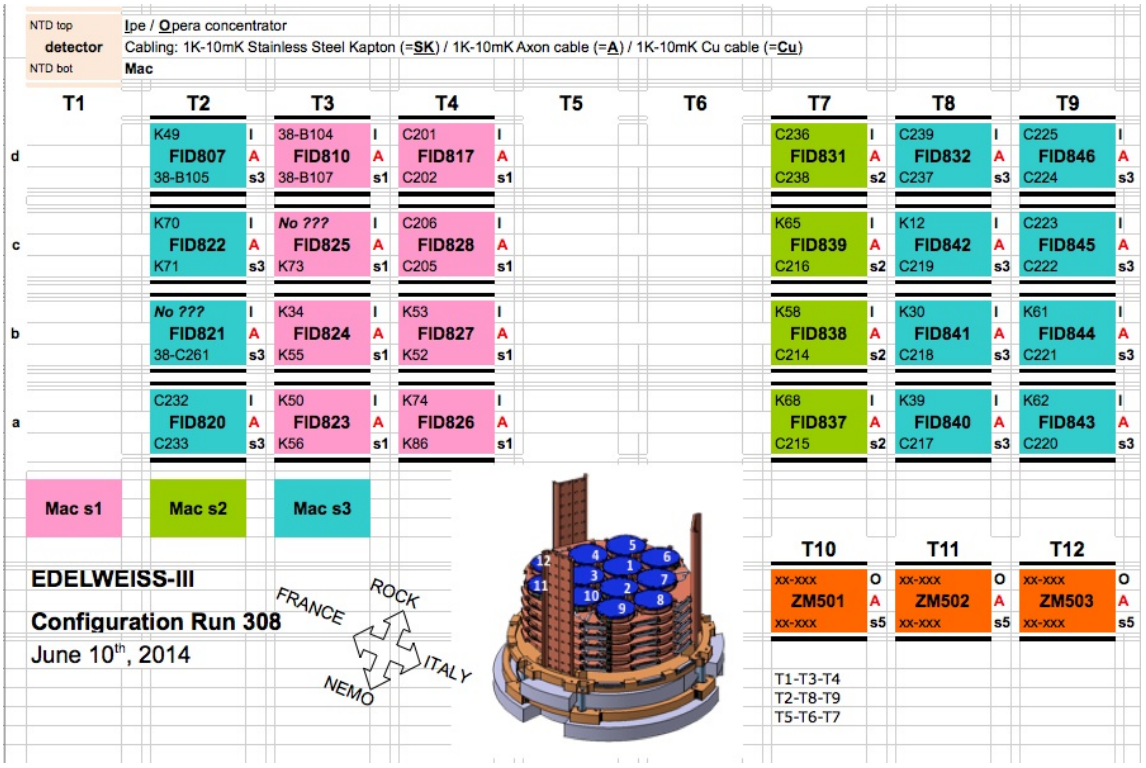

Figure 4.2.: Configuration of the detectors in EDELWEISS-III Run308, taken from [134]. Of the 36 FID800 detectors installed within the cryostat in towers T1 to T9, 24 were fully connected to the DAQ system and read out by 3 different acquisition computers (Mac s1, s2 and s3) as indicated by colours. Three additional $ZnMoO_4$-detectors of the LUMINEU experiment were installed for testing.

- no clear surface event, i.e. the signal on each of the two veto electrodes is smaller than $5\,\sigma$ of the baseline noise

In the finally used j-version of the ANA processing the blinding was applied to the whole data and allowed to develop all cuts and background models without bias. For the BDT analysis presented in Sec. 3.3 all background models and cut definitions were completed before the full unblinding of the data on August 31st, 2015, and only checks and re-evaluations of systematic errors were performed after this date. The likelihood analysis presented in this chapter can not be considered fully blind. Although it uses almost the same cuts and many of the background models of the BDT analysis, some parts of the likelihood analysis were developed and optimized on unblinded data. Nevertheless, attention was paid not to use the signal region to develop any of the background models which could have biased the analysis.

The data is stored on the IN2P3 Tier1 Computing Center Lyon in the form of multiple TTree ROOT-files per detector and run-type (WIMP search, γ-calibration, neutron-calibration and test run). These are so-called n-tuples: for each event more than 100 high level analysis variables are stored in these files, such as the event time, different calibrated energies or calculated values like the ionization yield. Only a small subset of these variables was actually used in this analysis. Those which are needed to perform all selection cuts on the data are listed and explained in Tab. 4.1. In the definition of these variables, the 4 ionization channels for each detector are labelled as A, B, C and D. By definition, channels A and C refer to the top and bottom veto electrodes, while channels B and D are used for the fiducial electrodes of the corresponding side. For the two heat channels, the abbreviations C1 and C2 are used. Several of the variables used in the analysis are combinations of

Table 4.1.: Subset of the variables for each event which are used to select the data from the high level analysis n-tuples. All energies listed here have been calibrated with a ^{133}Ba γ-source and are therefore given in units of keV$_{ee}$.

ANA-variable	description
$EIA/B/C/D$	Ionization energy on electrode A/B/C/D
$FWIA/B/C/D$	Baseline noise FWHM in this hour for electrode A/B/C/D
$CHIA/B/C/D$	$Log_{10}(\chi^2)$-value of signal fit on electrode A/B/C/D
$RCIA/B/C/D$	Average $Log_{10}(\chi^2)$-value of signals on A/B/C/D in this hour
EI	Total ionization energy: $EI = (EIA + EIC + EIC + EID)/2$
$EFID$	Fiducial ionization energy: $EFID = (EIB + EID)/2$
FWF	Baseline noise FWHM for $EFID$ in this hour
$EV1/2$	Energy of top/bottom veto electrode
$EDIF$	Difference of fiducial electrodes: $EDIF = (EIB - EID)/2$
$FWDI$	Baseline noise FWHM for $EDIF$ in this hour
$EC1/2$	Heat energy for top/bottom NTD
$CHIC1/2$	$Log_{10}(\chi^2)$-value of signal fit on NTD1/2 (time domain)
$RCIA/B/C/D$	Average $Log_{10}(\chi^2)$-value of signals on NTD1/2 in this hour
$XOC1/2$	$Log_{10}(\chi^2)$-value of signal fit on NTD1/2 (frequency domain)
EC	Averaged energy of the heat signal: $EC = (EC1 + EC2)/2$
FWC	Baseline noise FWHM for EC in this hour
TWC	Baseline noise FWHM for EC (time domain fit)
KTH	Online trigger level
$VOLT$	Voltage between the two fiducial electrodes
$MULT$	Multiplicity of the event
$JOUR$	Days since July 22nd, 2014

physical readout channels, such as the combined heat energy EC and the combined fiducial ionization energy $EFID$.

4.1.3. Basic quality and period cuts

The selection of bolometers as well as the definition of the basic quality and period cuts was performed within the EDELWEISS collaboration, in particular within the context of [1]. For the likelihood based analysis presented in this chapter, almost all of these cuts have been applied as well. The main differences with respect to the BDT analysis presented in Sec. 3.3 are the exact definition of the region of interest, in particular the minimum required heat energy for events, as well as the fiducial cut. Both will be discussed in more detail in the following sections. The main goal of the cuts was to achieve a high sensitivity for low mass WIMPs down to $m_\chi \approx 5\,\mathrm{GeV}/c^2$ without losing sensitivity for higher WIMP masses around $20 - 30\,\mathrm{GeV}/c^2$ by a restriction of the energy range or a significant loss of exposure. Another principle of the data selection was to get a homogeneous data set with comparable performance for all detectors in order to combine their results in a meaningful way.

Bolometer selection

From the initial 24 detectors with readout in Run308, two (FID822 and FID840) were not considered in the selection process but discarded due to their missing ionization channels. For the remaining detectors, the dominating selection parameter is the adaptive online threshold for triggering events on the heat channel, which is correlated to the baseline noise of the heat channels and denoted by the ANA-variable KTH. Due to the fact that low

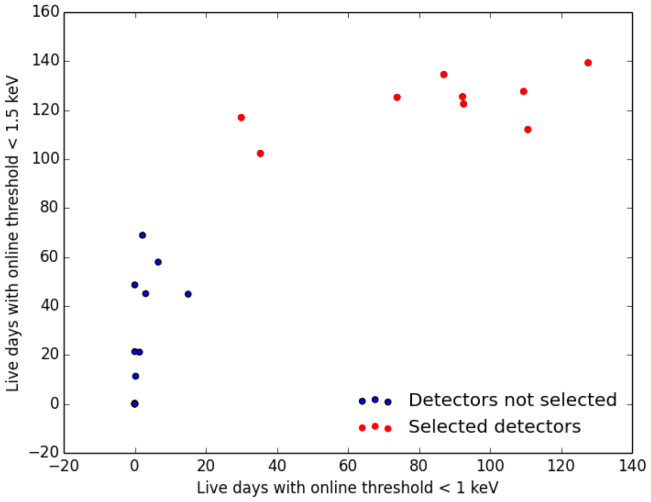

Figure 4.3.: Number of live days from periods with an online threshold $KTH < 1.5\,\mathrm{keV_{ee}}$ vs livedays from periods with $KTH < 1\,\mathrm{keV_{ee}}$ for all detectors in Run308 except 2 with a missing ionization channel. A group of 7 detectors (red markers, top right corner) shows a good performance with a large number of low online threshold periods. One of them, FID826, is later on excluded from the analysis due to other reasons. Two intermediate detectors, FID839 and FID842 (red markers, middle), bring less exposure with low online threshold but are still considered. Figure from [137].

mass WIMP signals are at very low energies of $\mathcal{O}(1\,\mathrm{keV})$, decreasing the threshold yields a huge gain in signal sensitivity. To search for low mass WIMPs it is therefore reasonable to only select data for which the average online threshold during an hour is $< 1.5\,\mathrm{keV_{ee}}$. As the available detectors in Run308 have different performance in terms of baseline noise on the heat channel and therefore trigger threshold, this effectively removes more than half of the 24 detectors. Figure 4.3 shows the selection of detectors by comparing the total number of live days with an online threshold $KTH < 1\,\mathrm{keV_{ee}}$ with live days for which $KTH < 1.5\,\mathrm{keV_{ee}}$. From this visualization of the detector performance, the group of 7 good detectors plus the 2 intermediate ones were selected. Of these 9 detectors, FID826 was later rejected due to an extraordinary low fiducial mass measurement which hinted at a possible anomaly in the electric field configuration. All rejected detectors would not have contributed much to the low mass analysis, as their performance would not allow to add much exposure or sensitivity for low mass WIMPs. Eventually, the following 8 detectors were selected for the analysis: FID824, FID825, FID827, FID837, FID838, FID839, FID841 and FID842.

Period cuts and resulting livetime

The 8 detectors were selected based on the accumulated live days of periods with online threshold below $1.5\,\mathrm{keV_{ee}}$. The first cut is therefore to remove all periods with higher threshold energies, by requiring:

$$KTH \overset{!}{<} 1.5\,\mathrm{keV_{ee}} \tag{4.1}$$

Figure 4.4 shows the distribution of livetime after this important cut. At the same time it was also necessary to remove periods with too low thresholds. As shown in Fig. 4.5 there is a clear correlation between the adaptive online threshold KTH of the DAQ system and the heat baseline resolution TWC which was calculated offline from the time-domain fit. Data periods for the selected detectors follow $KTH = 1.7 \times TWC$ on average, except for a

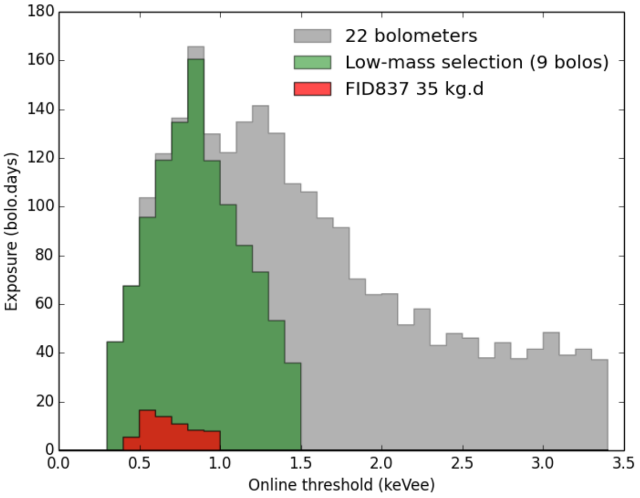

Figure 4.4.: Exposure for periods with different online thresholds KTH summed up over all 22 detectors with full readout on all channels. After application of a cut $KTH < 1.5\,\mathrm{keV_{ee}}$ the distribution for the selection of 9 detectors (including the later rejected FID826) is quite homogeneous (green). For comparison, the subset of data of a single detector from the first half of Run308 which was used in an initial BDT analysis [120] is shown as well (red). Figure from [137].

tail of periods with very low online thresholds down to $0.2\,\mathrm{keV_{ee}}$. While these periods are valid and the online threshold was actually set to such small values, it was still decided to remove them by requiring

$$KTH \overset{!}{>} 0.1 + 0.6 \times TWC \tag{4.2}$$

This prevents the analysis from dealing with partly uncontrolled, trigger-induced dead time due to the high rate of events, as well as from problems in modelling the trigger efficiency function which would be positive at zero energy. As both BDT and likelihood analysis use time averaged values for the baseline resolutions over the whole Run308, it was attempted to create a homogeneous data set in terms of these resolutions. Additionally to the cut in Eq. 4.1, periods with high FWHM baseline noise on the combined heat channel EC are removed from the data:

$$FWC \overset{!}{<} 1\,\mathrm{keV_{ee}} \tag{4.3}$$

For an effective discrimination of so-called heat-only events with homogeneous rejection performance over the whole data set, a cut is applied also on the FWHM baseline noise of the combined fiducial ionization channel $EFID$:

$$FWF \overset{!}{<} 0.7\,\mathrm{keV_{ee}} \tag{4.4}$$

To allow the rejection of surface events with high efficiency, only a loose cut is applied on the FWHM baseline noise of the two veto electrodes A and C:

$$\begin{aligned} FWIA &\overset{!}{<} 1.5\,\mathrm{keV_{ee}} \\ FWIC &\overset{!}{<} 1.5\,\mathrm{keV_{ee}} \end{aligned} \tag{4.5}$$

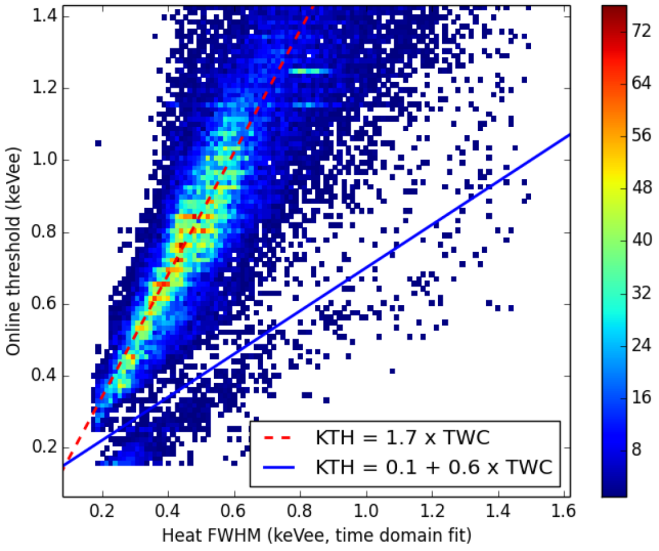

Figure 4.5.: Dependence of the adaptive online trigger threshold KTH to the baseline resolution TWC of the heat channel for the 8 selected detectors plus FID826 which is not included in the analysis. A clear correlation between the two can be seen and approximated by a simple factor (red dashed line). Periods with particularly low online threshold and an associated large deadtime due to a high trigger rate are rejected (blue curve). Figure from [137].

However, most veto electrodes show much smaller noise levels, and this cut mostly affects data for detector FID837. To protect from including periods with an incorrect reconstruction of noise conditions an additional cut is applied to remove all periods with anomalous baseline resolutions or online threshold values, by requiring

$$\begin{gathered} 0.1 \overset{!}{<} VAR \overset{!}{<} 9.9\,\mathrm{keV_{ee}} \\ \text{with } VAR = FWIA, FWIB, FWIC, FWID, FWID, FWF, FWC, KTH \end{gathered} \tag{4.6}$$

Additionally, periods with saturated ionization are removed. The different period cuts listed here reduce the livetime per detector as follows: from initial values which were homogeneously distributed between 155 to 161 days, the livetime decreases to between 95 to 21 days. The largest loss of livetime can be observed for the two detectors with highest average online threshold, FID839 and FID842 due to the cut on the online threshold KTH. Considered in the calculation of the final livetime is deadtime with different origin: a deadtime of 0.6 sec for each triggered event is induced by the online trigger and an additional 1.4 sec for physical pulses due to the offline reconstruction. Deadtime induced by reset pulses and maintenance procedures is considered by a reduction of the livetime of 9.7% for all periods with $JOUR < 93.5$ and of 4.3% after that day (change of reset and maintenance frequency).

Event based cuts

To select only events for which the energy has been determined correctly, cuts are applied on the quality of the pulse reconstruction. Within the EDELWEISS collaboration a study was performed [138] using the same WIMP search data to determine these cuts for each of the 6 readout channels of each of the detectors installed in Run308 including the 8 detectors of this analysis. The distribution of $CHIx - RCIx$ (where x stands for any of the 4 electrodes A, B, C and D), i.e. the fitted χ^2-value of the pulse template to recorded

pulse traces with respect to the mean value over 1 hour can be well fitted with a Gaussian function. The cut value is chosen such, that all events with $> 5\,\sigma$ of this distribution are rejected:

$$\begin{aligned} CHIx - RCIx &\overset{!}{<} 5\,\sigma_x \\ \text{with } x &= A, B, C, D \end{aligned} \tag{4.7}$$

For the two heat channels, similar χ^2-cuts were constructed for both the pulse fit in the time- and in the frequency-domain. To also reject pulses within anomalous noise conditions both upper and lower χ^2-cuts were applied for these channels:

$$\begin{aligned} |CHICi - RCCi| &\overset{!}{<} 5\,\sigma_{CHCi} \\ |XOCi| &\overset{!}{<} 5\,\sigma_{XOCi} \\ \text{with } i &= 1, 2 \end{aligned} \tag{4.8}$$

The efficiency loss induced by these cuts has been measured in [137] by comparing the triplet of cosmogenic events around 10 keV with and without cut. A typical efficiency loss of ≈10% was observed for all detectors, mainly coming from the χ^2-cut on the heat channel. It was shown that in the low energy region considered in this analysis, any energy dependence of these cut values can be regarded as negligible.
Another event-based cut that is applied concerns the reconstruction of the heat energy on the two different NTD sensors by limiting the difference of the two measured heat energies $|EC2 - EC1|$. This cut serves two purposes: first it removes noise events at low energies which are not already rejected by the χ^2-cut and therefore reduces the number of so-called heat-only events. At the same time it guarantees that the remaining events have similar energies on the two heat channels which makes it possible to combine the two heat signals into the averaged heat signal EC which is used in the following. However, the cut is applied under certain conditions only: it was observed that the signal coming from NTD2 (on the detector bottom) is generally more noisy for most detectors than the one from NTD1 (top), depending on both bolometer and time period. To only apply the cut on time periods where the noise on the two NTD signals is comparable it is connected with a requirement on the heat baseline noise $OWC1/2$ which is reconstructed from the time domain fit. If the condition:

$$OWC2 > 0.5 + 2 \cdot OWC1 \tag{4.9}$$

is fulfilled, the asymmetric cut on the difference of the heat signal is applied:

$$\text{cut}_{\text{EC,low}} \overset{!}{<} EC2 - EC1 \overset{!}{<} \text{cut}_{\text{EC,high}} \tag{4.10}$$

where $\text{cut}_{\text{EC,low}}$ and $\text{cut}_{\text{EC,high}}$ are detector dependent parameters which were constructed with a graphical cut on the plotted distribution. The initial requirement for this cut mostly affects detector FID841 as well as FID837 and FID839, for which long periods would be rejected otherwise. The cut was designed such, that the overall efficiency loss, which was again tested with a sample of cosmogenic events around 10 keV, is about 1%.

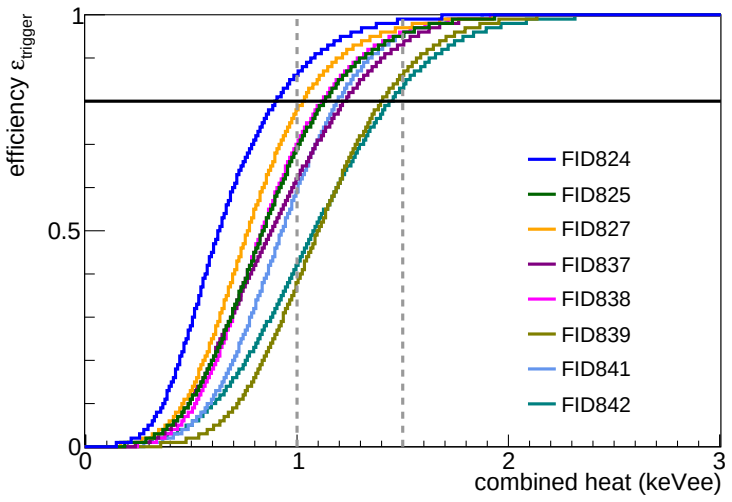

Figure 4.6.: Trigger efficiency $\epsilon_{\text{trigger}}$ on the combined heat channels averaged over the selected periods of this analysis. The horizontal black line corresponds to an efficiency of 80% and is used to find the analysis threshold $E_{\text{c}}^{\text{min}}$ for each detector. Values vary from $E_{\text{c}}^{\text{min}} = 0.9\,\text{keV}_{\text{ee}}$ for the best detector FID824 up to $E_{\text{c}}^{\text{min}} = 1.46\,\text{keV}_{\text{ee}}$ for FID842. Dashed gray lines represent the two $E_{\text{c}}^{\text{min}}$-values used in the BDT analysis.

Trigger efficiency

As described in Sec. 2.3.1, the EDELWEISS DAQ system records events after triggering on a signal of one of the two heat channels of a detector. The adaptive trigger threshold energy is adjusted on the order of minutes to the current baseline noise on the two heat channels, as can be observed in Fig. 4.5. The efficiency of this trigger is given by the convolution of a step-function with a Gaussian smearing due to the noise. It can be expressed analytically as a function of the heat energy EC for each of the subperiods for which the online threshold KTH and the heat baseline noise TWC have been determined, as

$$\epsilon_{\text{trigger}}(EC) = \frac{1}{2}\left[\text{erf}\left(\frac{EC - KTH}{\sqrt{2}\cdot TWC/2.35}\right) + 1\right] \tag{4.11}$$

where erf is the standard error function. To get the average trigger efficiency for a detector for the whole selected periods of Run308, the livetime weighted sum of trigger efficiencies from all subperiods is calculated. The average trigger efficiency for detector FID825 is shown in Fig. 3.5 together with data selected in the context of [137] showing the validity of this model. The plotted data is a histogram of events that were triggered by another bolometer readout with the same Mac computer and divided by those events which did not trigger FID825. Several other methods of modelling the trigger efficiency from data show reasonable to excellent agreement with the model given in Eq. 4.11. For some of these methods however, an offset can be seen between data and model of the order of $0.1\,\text{keV}_{\text{ee}}$. Although this might well be related to the selection of data for validation of the model, a systematic bias in the model cannot be entirely excluded.

The livetime averaged trigger efficiency for the selected periods of Run308 after all cuts is shown in Fig. 4.6 for all 8 selected detectors. A clear variation of this efficiency can be seen between individual detectors. For those detectors with worse heat channel resolution such as FID839 and FID842, the efficiency function is not only shifted proportionally to higher energies but also much wider. The detector with highest trigger efficiency at low energies is FID824, with a steep efficiency function. To assure a high efficiency in the RoI

for the following analysis, the average trigger efficiency is used to define the lower heat energy of the analysis for each detector. The offline threshold energy $E_c^{\min}$ of the combined heat energy EC is chosen such that the average trigger efficiency is at least 80%:

$$\epsilon_{\text{trigger}}\left(E_c^{\min}\right) = 80\% \tag{4.12}$$

For the 8 detectors this criterion leads to values ranging from $E_c^{\min} = 0.9\,\text{keV}_{\text{ee}}$ for detector FID824 up to $E_c^{\min} = 1.46\,\text{keV}_{\text{ee}}$ for detector FID842. The analysis threshold $E_c^{\min}$ in heat energy allows to reduce the rate of noise events due to false triggers and guarantees a comparable performance for all detectors. It also ensures that the calculated potential WIMP signal used in this analysis is not significantly affected by the precision of the trigger efficiency model and thus biased.

4.1.4. Fiducial cut to reject surface events

As described in Sec. 2.2.3, the FID800 detectors employed in the EDELWEISS experiment have a powerful rejection of surface events. Surface events can have insufficient charge collection and thus their ionization energy is not fully reconstructed. The ionization yield Q, which is used for the discrimination of electronic and nuclear recoils, is therefore reduced and the events can overlap with the signal region for WIMP interactions. To reject surface events, a so-called *fiducial cut* is used. It is designed to only keep events from the inner *bulk* volume of the Ge-crystal.

In the BDT analysis detailed in Sec. 3.3, only a rough fiducial cut is used to reject clear surface events with signals of more than $5\,\sigma_{\text{veto}}$ of the baseline noise of the corresponding veto electrode. As the BDT uses the information of all physical readout channels of a detector, including the two veto electrode signals, it can be trained to discriminate between surface and bulk events on an event by event basis and apply this to real data. The benefit of this rough $5\,\sigma$ fiducial cut is that it has a high acceptance of ≈100% and thus induces a negligible loss of exposure.

For the likelihood analysis this strategy cannot be applied without complications. It would in principle be possible to use a multidimensional parameter space which considers all energy observables, including the ionization signals on the two veto channels. However, this approach would significantly complicate the analysis, especially the normalization of the probability density functions used to describe the data. For this reason, the excellent surface rejection performance of the detectors is applied beforehand to select a clean sample of fiducial events down to very low energies[1]. In the framework of this thesis, a completely independent fiducial cut was developed and applied to select events in the WIMP search data. This cut is particularly suited for the low energy range that is used in the analysis. The general definition of the cut is given as:

$$|EIx - r_x \cdot EFID| \overset{!}{<} a_f \cdot \sigma_x(EFID) \tag{4.13}$$

It requires the energy of an event on channel x, for example the veto electrode A, to be within a certain acceptance fraction a_f of the distribution of bulk events. Bulk events are expected to have no reconstructed energy on the veto electrodes, except for Gaussian noise described with a width σ_x. The parameter r allows for the correction of a possible cross-talk between channel x and the fiducial electrodes. In that case, the energy EIx increases (or decreases) as a function of fiducial ionization energy $EFID$ and the Gaussian distribution

[1] At low energies the rejection capabilities decrease because ionization energies are of the same order as baseline fluctuations.

of EIx for bulk events has a mean value of $EIx \neq 0$ at a given value of $EFID$. The energy dependent width $\sigma_x(EFID)$ is calculated from the average FWHM baseline noise of the variable EIx and a slope-parameter s which is determined from a fit at $EFID = 10\,\mathrm{keV_{ee}}$:

$$\begin{aligned} \sigma_x(EFID) &= \sqrt{(\sigma_x^0)^2 + (s_x \cdot EFID)^2} \\ \text{with } \sigma_x^0 &= \frac{FWHM_x}{2.35} \end{aligned} \tag{4.14}$$

This cut is implemented for 3 different components: two of them control how large energy fluctuations on each of the two veto electrodes EIA and EIC can be to consider an event as fiducial and another component controls how large the difference $EDIF$ between the signals on the two fiducial electrodes can be. In principle, more criteria for such a cut could be considered, for example the difference of the timing between the signals on the two fiducial electrodes. For simplicity reasons, only the three aforementioned components are considered. Written out in full, the cut is given by the three following terms:

$$\begin{aligned} |EIA - r_{\mathrm{EIA}} \cdot EFID| &< 1.645 \times \sqrt{(FWIA/2.35)^2 + (s_{\mathrm{EIA}} \cdot EFID)^2} \\ |EIC - r_{\mathrm{EIC}} \cdot EFID| &< 1.645 \times \sqrt{(FWIC/2.35)^2 + (s_{\mathrm{EIC}} \cdot EFID)^2} \\ |EDIF - r_{\mathrm{EDIF}} \cdot EFID| &< 1.645 \times \sqrt{(FWDI/2.35)^2 + (s_{\mathrm{EDIF}} \cdot EFID)^2} \end{aligned} \tag{4.15}$$

The value $a_f = 1.645$ corresponds to $f = 90\%$ acceptance of a Gaussian distribution. It was chosen after initial tests with an unblinded subset of Run308 WIMP search data because it proved strong discrimination of surface events with an acceptable loss of efficiency due to the reduced acceptance. The two remaining cut parameters for each channel, r and s were extracted using WIMP search data from the same selected periods as described in the previous section and after removing of pile-up events through the application of the χ^2-cuts on all ionization and heat channels. The procedure to extract these parameters is shown in Fig. 4.7 for detector FID827 and channel EIA. After plotting EIA versus the fiducial energy $EFID$, the events in the 2 boxes around $EFID = 0$ and $EFID = 10\,\mathrm{keV_{ee}}$ are selected (left figure). The histogrammed distributions of these events in the variable EIA are then fitted with a Gaussian functions (middle figures). From the fitted mean μ^{10} at $EFID = 10\,\mathrm{keV_{ee}}$ and the widths σ^0 and σ^{10} of the two Gaussian functions, the parameters r and s describing the rotation and the slope can be calculated as follows:

$$\begin{aligned} r &= \frac{\mu^{10}}{10\,\mathrm{keV_{ee}}} \\ s &= \frac{\sqrt{(\sigma^{10})^2 - (\sigma^0)^2}}{10\,\mathrm{keV_{ee}}} \end{aligned} \tag{4.16}$$

Values for r and s for all detectors and each of the channels EIA, EIC and $EDIF$ are given in the Tab. C.1. The right plot in Fig. 4.7 shows which events have been selected after application of the corresponding fiducial cut component from Eq. 4.15. It is apparent that the cut is quite strict, i.e. has a reduced acceptance as a trade-off for a clean selection down to very low energies.

The effect of applying the complete fiducial cut on WIMP search data is shown in Fig. 4.8 for detector FID827. The cut effectively rejects all high energy surface events coming from β's, ^{206}Pb-recoils and surface γ's (blue markers). After applying the cut apparently events

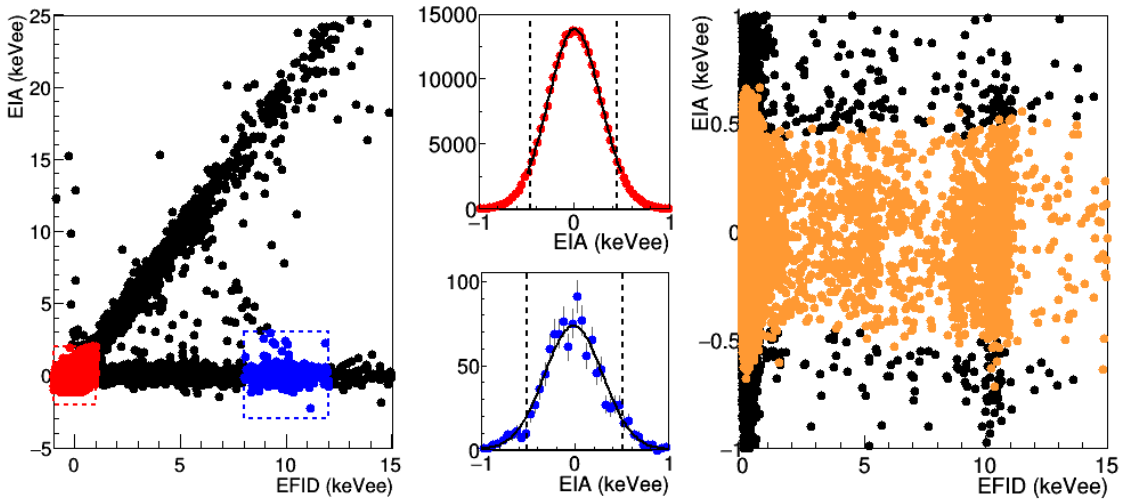

Figure 4.7.: Example plot for detector FID827 showing the construction of the EIA-component (veto electrode A) in the definition of the fiducial cut in Eq. 4.15. *Left*: Distribution of WIMP search data after χ^2-cuts in veto ionization energy EIA vs. fiduzial ionization energy $EFID$. Events with $EFID = 0 \pm 1\,\mathrm{keV_{ee}}$ (red) and $EFID = 10 \pm 2\,\mathrm{keV_{ee}}$ (blue) are selected to determine the width of the band for bulk events. *Middle*: Fit of the distribution in EIA of these selected events with a Gaussian to determine the mean μ and width σ. The distribution for $EFID = 10\,\mathrm{keV_{ee}}$ is slightly wider. *Right*: Effect of applying the relevant term of the fiducial cut for this electrode on the same data. The width of the distribution of accepted events (orange) increases slightly as a function of $EFID$. The widening of the distribution around $EFID = 0$ is caused by the high rate of (heat-only) events.

in the electron recoil band (for which $EFID = EC$) as well as heat-only events ($EFID \approx 0$) are kept (orange markers). However, at very low energies $\mathcal{O}(1\,\mathrm{keV_{ee}})$ the discrimination is not fully efficient, due to resolution effects. Therefore unrejected surface events are one of the components that are still to be considered in this analysis (see the following Sec. 4.3.5). Another aspect of this fiducial cut is also shown in the plot: several events in the electron recoil band are rejected although they are at energies expected by bulk electron recoil interactions. This is due to the 90% acceptance of each of the individual components of the cut.

An important parameter in WIMP search is the exposure for which the data was taken. While the livetime which is connected to the period and quality cuts introduced in the previous section has already been calculated, the mass of the detectors is another input when deriving the effective exposure. By applying a fiducial cut, only events from the bulk of the crystal are accepted. The effective mass (and therefore the exposure) are consequently reduced. Studies of the electrical field configuration of FID800 detectors with the applied voltage configuration give a typical fiducial volume of 75%. Due to its reduced acceptance, the stricter fiducial cut introduced for this analysis results in a smaller effective fraction of the detector mass which can be used. This fraction is calculated from the same WIMP search data: the cosmogenically activated isotopes from ^{65}Zn, ^{68}Ga and ^{68}Ge are distributed homogeneously throughout the detector. Via K-shell electron capture they produce X-rays with energies of 9.0 keV, 9.6 keV and 10.4 keV. Due to resolution effects these decays produce a peak-triplet around 10 keV. To calculate the effective fiducial fraction, clear electron recoil events with an ionization yield $0.5 < Q < 2.5$ are selected in a range of total ionization energy $6 < EI < 20$ around the peak triplet. This selection is performed once with the fiducial cut and once by requiring its opposite, i.e. specifically

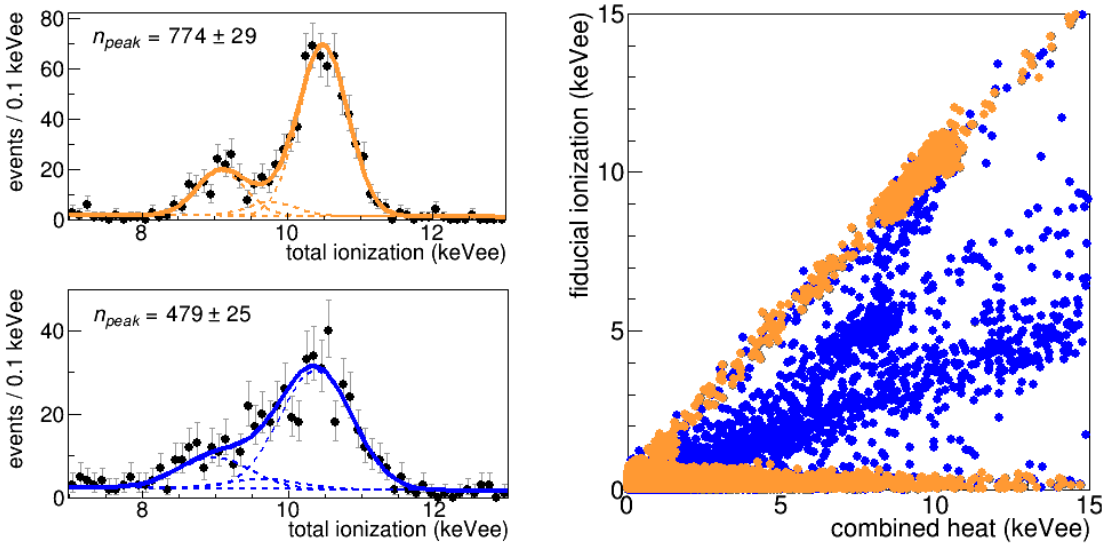

Figure 4.8.: Effect of the fiducial cut for data from detector FID827. *Left*: Spectrum of clear electron recoil events ($0.55 < Q < 2.5$) around $10\,\mathrm{keV_{ee}}$ where a triplet of cosmogenic K-shell EC peaks is located. The upper panel shows a selection of events after the fiducial cut where the peak triplet has been fitted (orange curve) to calculate the total number of cosmogenic events $n_{\mathrm{peak;fiducial}}$. The lower left panel shows events which do not pass the fiducial cut, i.e. surface events. The peak triplet was also fitted but with fixed peak ratios (blue curve) to determine the number of non-fiducial cosmogenic events. *Right*: WIMP search data after all cuts for detector FID827 in fiducial ionization vs. heat energy before (blue) and after (orange) application of the full fiducial cut. The cut very effectively rejects surface events from γ- and β-radiation at higher energies.

selecting non-fiducial events. The peak triplet around $EI = 10\,\mathrm{keV_{ee}}$ is fitted, as is shown in Fig. 4.8 (left), to determine the number of peak-events $n_{\mathrm{peak;fiducial}}$ ($n_{\mathrm{peak;non-fid}}$). The relative ratios between cosmogenic events from the different isotopes ^{65}Zn, ^{68}Ga and ^{68}Ge which are fitted to the fiducial selection are fixed for the fit to non-fiducial events. An underlying linear function, variable peak widths and small energy correction factors are independent for both fits. From the total number of peak-events for both selections the fraction of the effective fiducial volume can be calculated as

$$f_{\mathrm{fiducial}} = \frac{n_{\mathrm{peak,fiducial}}}{n_{\mathrm{peak,fid}} + n_{\mathrm{peak,non-fid}}} \tag{4.17}$$

The fiducial fractions for each detector with propagated fit errors are summarized in Tab. 4.2, together with the corresponding effective fiducial masses calculated from the total detector masses. Compared with the fiducial masses used in the BDT analysis, which were found with a different fiducial cut, a reduction of on average 15% is observed, as expected from the lower acceptance. As a cross check the acceptance of the fiducial cut has been increased to $f = 99\%$ by setting the value $a_f = 2.567$ in Eq. 4.13 and repeating all fits. The results extracted with this enhanced acceptance are in good agreement with the BDT fiducial mass values, proving the validity of the method applied here.

Table 4.2.: Calculated fiducial fraction and mass for all selected detectors after application of the fiducial cut from Eq. 4.15. Due to the reduced acceptance, the effective fiducial mass for each detector is, as expected, significantly lower than the fiducial mass used in the BDT analysis.

Detector	m_{total} (g)	f_{fiducial} (%)	$m_{\text{fid,LHD}}$ (g)	$m_{\text{fid,BDT}}$ (g)
FID824	877	57.9 ± 3.7	507.8 ± 32.5	543
FID825	878	64.0 ± 2.9	561.5 ± 25.2	649
FID827	874	61.8 ± 1.5	539.1 ± 13.3	647
FID837	873	61.4 ± 1.8	537.4 ± 15.5	620
FID838	875	61.1 ± 1.4	531.4 ± 11.9	637
FID839	869	63.1 ± 1.9	548.1 ± 16.7	650
FID841	878	60.0 ± 2.0	526.7 ± 17.8	645
FID842	878	59.6 ± 2.7	523.0 ± 23.8	619
Average	875	61.1 ± 0.8	534.4 ± 7.3	626
Sum	7002		4275.0 ± 53.3	5010

4.1.5. Region of interest and final dataset

For each of the events that pass all cuts described above, a multitude of information is available and stored in the variables of the data n-tuples. Most relevant for the classification of events is the calibrated energy on each of the six readout channels of a detector (four ionization and two heat). Obviously there is some redundancy within the information of these readout channels. By applying the cut on the symmetry of the heat signal (Eq. 4.10) the remaining events have similar signals on the two heat channels and their energy can thus be averaged to the combined heat energy given by the variable EC. Similarly, the application of the fiducial cut guarantees that the difference between the signals on the two fiducial ionization electrodes is small. These two energies can thus also be combined into the fiducial ionization energy, which is given by the ANA-variable $EFID$. To select the final dataset for this analysis, the last cut is applied on these two combined variables to define a region of interest:

$$\begin{aligned} E_{\text{c}}^{\text{min}} &< EC &&< 15\,\text{keV}_{\text{ee}} \\ 0. &< EFID &&< 15\,\text{keV}_{\text{ee}} \end{aligned} \tag{4.18}$$

As introduced with Eq. 4.12, the lower analysis threshold in heat energy of the RoI is chosen such that the trigger efficiency for each detector is at least 80%. This choice of lower analysis threshold in heat energy marks a first major difference to the BDT analysis, where the 4 better detectors have $E_{\text{c}}^{\text{min}} = 1.0\,\text{keV}_{\text{ee}}$ and the remaining 4 detectors $E_{\text{c}}^{\text{min}} = 1.5\,\text{keV}_{\text{ee}}$. Seven of the detectors thus have an analysis threshold in between these two values (some higher than the same detector in the BDT analysis, some lower), only detector FID824 has a threshold $E_{\text{c}}^{\text{min}} < 1\,\text{keV}_{\text{ee}}$ which increases its sensitivity with respect to the BDT analysis. For the fiducial ionization energy, a lower bound of $EFID = 0\,\text{keV}_{\text{ee}}$ was chosen so that half of the population of so-called heat-only events, which has no ionization energy except for Gaussian noise, is included. The upper boundaries of the RoI are set as to fully include the peak triplet of cosmogenic events at $10\,\text{keV}_{\text{ee}}$ and some margin above to fit the onset of the flat ER spectrum. This choice of cuts which define the RoI allows to study potential signals for both very low mass WIMPs of $m_\chi = 4\,\text{GeV}/c^2$ up to higher masses of $m_\chi = 30\,\text{GeV}/c^2$. For the lowest WIMP masses the analysis threshold $E_{\text{c}}^{\text{min}}$ defines how much of the steep exponentially falling spectrum is still in the RoI. For higher masses the spectrum flattens and $E_{\text{c}}^{\text{min}}$ becomes negligible while the upper energy boundary becomes

Table 4.3.: Overview of the selected data for all 8 detectors. The analysis threshold E_c^{min} defines the lower boundary of the RoI in heat energy. The number of events N after all cuts depends on the size of the RoI, the exposure M and the rate of dominant background components (mostly heat-only and electron recoils).

Detector	E_c^{min} (keV$_{ee}$)	N	M (kg·days)
FID824	0.91	5685	55.3
FID825	1.14	5896	66.1
FID827	1.04	10476	65.2
FID837	1.24	5268	63.5
FID838	1.13	8486	62.9
FID839	1.41	7270	62.8
FID841	1.20	4440	70.3
FID842	1.46	3194	49.7
sum		50,715	495.8

significant. A small efficiency gain is expected for high mass WIMPs in comparison with the BDT analysis for which the upper energy cut in (total) ionization energy is set to $EI < 8\,\mathrm{keV_{ee}}$.

The number of events in the RoI for each detector after applying all quality-, time-period and event-based cuts is given in Tab. 4.3, together with the analysis threshold E_c^{min} and the final exposure. Between the different detectors, the number of events varies from slightly more than 3000 for FID842 up to more than 10<,000 for detector FID827. Differences in the rate of events after cuts are mainly due to the different intensities of the dominating backgrounds as well as the size of the RoI due to the choice of E_c^{min}. The data for each of the 8 individual detectors is given in Fig. B.1. These are the data fitted in this analysis. Only to demonstrate the general principles, Fig. 4.9 shows the combined data for all detectors in the parameter space of fiducial ionization energy $EFID$ versus combined heat energy EC. The data is dominated by two event components: So-called heat-only events around $EFID = 0\,\mathrm{keV_{ee}}$ and the electron recoil component of events in the bulk of the detector. These ER events have an ionization yield of $Q = 1$ and consist of γ's from Compton scattering and the EC-decay of isotopes which were activated by cosmogenic radiation as well as β's from the decay of internal tritium (see Sec. 2.4.4). With these two main components, most of the data can already be described. In between the two event bands in Fig. 4.9 a few outlying events can be identified which were recorded in different detectors (see individual detector plots in the appendix). Several of them are close to the ionization yield for nuclear recoils and are therefore likely to be neutrons. Another possible source is unrejected surface background, as is indicated in the plot with data points before application of the fiducial cut with ionization yields for surface events. With the maximum likelihood method it is possible to describe each of the known background components and fit the data of each detector with a known model of all backgrounds and an additional signal. The description of the exact likelihood model and the construction of the probability functions which are used to model these backgrounds are given in the following section. For their construction in the two observables, combined heat energy and fiducial ionization energy, the individual detector resolutions on these two channels are of great importance, as they define the width of bands describing the events of each population. Figure 4.10 gives the FWHM baseline noise in EC and $EFID$ as an average over all events after cuts for each detector. Due to the period cuts described in this section, the average performance of the detectors is rather homogeneous, especially in terms of baseline noise of the fiducial ionization channel.

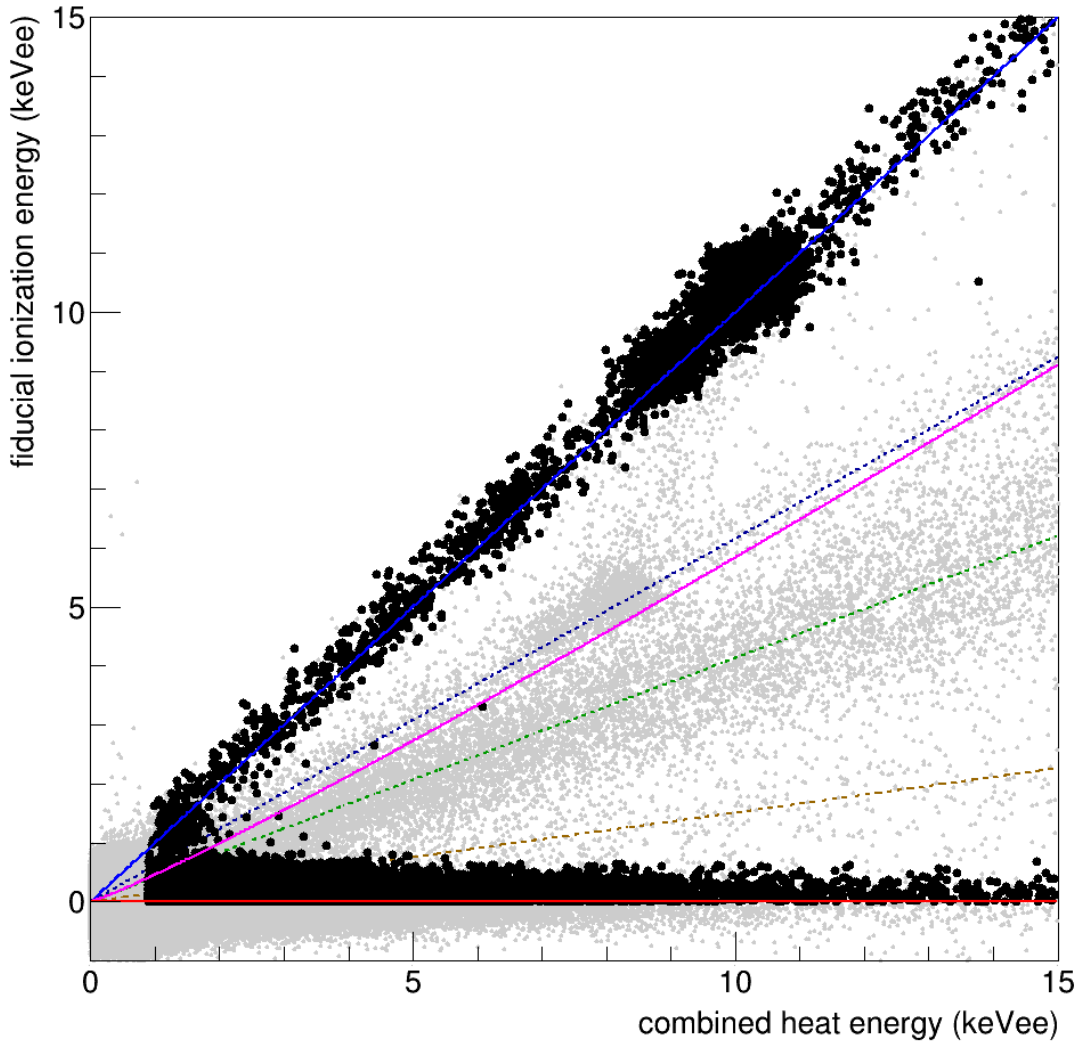

Figure 4.9.: WIMP search data combined for all 8 detectors after cuts in the RoI of the respective detector in the two observables fiducial ionization vs. combined heat energy (black markers). Events before the fiducial cut and in the full energy range are shown as gray points. Coloured lines indicate the detector-averaged ionization yield that is expected for different background components which are considered in the analysis. From top to bottom: $Q = 1$ for Compton and cosmogenic gammas in the fiducial volume (blue), $Q = 0.9$ for surface gammas (dark blue), $Q_{\mathrm{n}} = 0.16 \cdot E_{\mathrm{rec}}^{0.18}$ for WIMPs and neutrons (magenta), $Q = 0.4$ for surface betas (green) and $Q = 0.1$ for ^{206}Pb-recoils (brown). The dominant heat-only events have only noise on the ionization channels and thus $Q = 0$ (red). The combination of all datasets in this plot is only for demonstrative purposes. Note that the overall likelihood fit is performed for data from each detector (see Fig. B.1) with a separate background model.

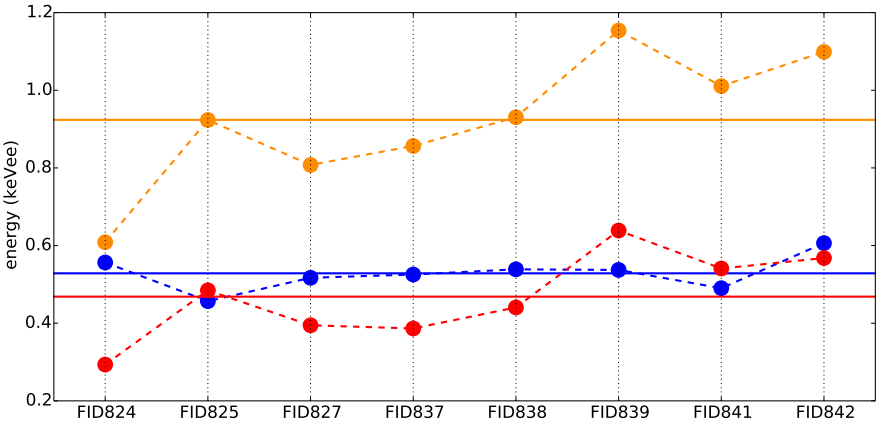

Figure 4.10.: Average values of the FWHM baseline for the combined heat FWC (red) and fiducial ionization FWF (blue) of events after all cuts. The trigger threshold KTH (orange) on the heat channel is adaptive and therefore proportional to the baseline noise. Median values for each variable over all detectors are indicated with horizontal lines. While all detectors have comparable noise on the ionization channels, the heat baseline varies more strongly. Detector FID824 has the smallest baseline noise and therefore the lowest trigger threshold.

4.2. Construction of a maximum likelihood model

To analyse the data that was defined in the previous section a likelihood model is constructed for each of the eight detectors used in this analysis. Each model is based on a set of probability density functions (PDFs) that describe all relevant backgrounds as well as a potential signal from WIMP-nucleon scattering. In this section the construction of these PDFs is described, starting from the basic principles of the detector response. It is followed by the definition of the likelihood function from these PDFs for each detector with additional constraint terms for each of the backgrounds. Finally, the individual likelihood functions for all 8 detectors are combined and used to fit all selected data simultaneously with a common signal cross section.

4.2.1. Probability density functions

In this analysis, different event populations are described with probability density functions in two observables, i.e. the combined heat energy EC and the fiducial ionization energy $EFID$. While it would be in principle possible to consider all of the 6 readout channels of a detector in a likelihood analysis, this approach is not followed here. The reason for this is that high dimensionality results in complications in the numeric integration which is necessary to normalize the PDFs. Also, the two observables considered here are already a combination of two channels each and therefore include the information of 4 out of the 6 readout channels of a detector. The remaining two channels, the two veto ionization energies $EV1$ and $EV2$, are indirectly also included in the form of the strict fiducial cut (see Eq. 4.15). For very low energy events near the analysis threshold $E_c^{\min}$, this fiducial cut has a reduced efficiency, which will be considered in the construction of the corresponding PDFs. The symbols and structure used in the following to describe the construction of PDFs from the detector response are directly based on [119]. However, for the more realistic modelling of backgrounds from actual data, several modifications were necessary. Examples are the description of energy dependent detector resolutions or the construction of PDFs from heat energy spectra which were extracted from sideband data directly. To improve the readability of the equations which are used in the following, the variable names that have been used so far are replaced by similar symbols. The combined heat energy EC, which is

the average sum of the signals on the two NTD sensors will be denoted as E_{c}. Similarly, the fiducial ionization energy $EFID$ which is given by the mean of the two fiducial electrode signals, will be denoted as E_{fid}. And last, the energy on any of the two veto electrodes will be labelled E_{veto} and complemented with an index if necessary:

$$\begin{aligned} E_{\mathrm{c}} &= EC \quad = 0.5 \times (EC1 + EC2) \\ E_{\mathrm{fid}} &= EFID = 0.5 \times (EIB + EID) \\ E_{\mathrm{veto}} &= EV1/2 = EIA/C \end{aligned} \tag{4.19}$$

All three energy variables are measured observables and the result of a physical process including the detector response to it. The following equations describe how these observables are calculated for the physical recoil energy E_{r} of a particle interaction in the detector:

$$\begin{aligned} E_{\mathrm{c}} &= f(E_{\mathrm{r}}) = \frac{1 + Q(E_{\mathrm{r}})^{V/3}}{1 + {}^{V_{\mathrm{ref}}}/_{3}} \times E_{\mathrm{r}} \\ E_{\mathrm{fid}} &= g(E_{\mathrm{r}}) = \alpha \times Q(E_{\mathrm{r}}) \times E_{\mathrm{r}} \\ E_{\mathrm{veto}} &= k(E_{\mathrm{r}}) = \beta \times Q(E_{\mathrm{r}}) \times E_{\mathrm{r}} \end{aligned} \tag{4.20}$$

The first term described how the heat energy E_{c} is affected by the Neganov-Luke effect as described in Sec. 2.2.1. Depending on the ionization yield Q of the event, the number of charges drifting in the electric potential V between the two (sets of) electrodes creates additional heat energy. For bulk events the applied potential between the fiducial electrodes was $V = 8\,\mathrm{V}$ for all eight detectors. For surface events this voltage was $V = 5.5\,\mathrm{V}$ for each detector side. The reference potential in the denominator is $V_{\mathrm{ref}} = 8\,\mathrm{V}$ for all detectors, as bulk events from a ^{133}Ba γ-source were used for the calibration of the heat channels. The term $f\,(E_{\mathrm{r}})$ describes how the heat energy of events with lower quenching than $Q = 1$ or of surface events is shifted to lower values. For surface gammas, this effect can be seen in Fig. 4.9 which also shows events before the fiducial cut. In perfect agreement with the term $f\,(E_{\mathrm{r}})$, the peak triplet of cosmogenic surface γ's is found at an energy of $E_{\mathrm{c}} \approx 7.7\,\mathrm{keV_{ee}}$ for an expected recoil energy of $E_{\mathrm{r}} \approx 10\,\mathrm{keV}$.

The other two terms of Eq. 4.20 describe how charges are collected on the different electrodes and what the effect of their different calibration is. The function $g\,(E_{\mathrm{r}})$ is used to calculate the fiducial ionization energy of events. For events in the bulk of the crystal, the electron-hole pairs produced in a recoil drift to the electrodes with the highest potential. These are by design the two fiducial electrodes, which for the detectors used in this analysis had an applied voltage of $\pm 4\,\mathrm{V}$. No charges are collected on the veto electrodes which have a smaller voltage of $\mp 1.5\,\mathrm{V}$. As the fiducial electrodes are calibrated with bulk γ's from the ^{133}Ba-source, $\alpha(\mathrm{bulk}) = 1$ for bulk events. For surface events however, the created charges are drifted perpendicular to the detector surface and are shared by the set of fiducial and veto electrodes on the side of the interaction. Therefore only half the energy is measured on the fiducial electrode and thus $\alpha(\mathrm{surf}) = 0.5$. For this reason, the aforementioned peak triplet of cosmogenic surface γ's in Fig. 4.9 is also shifted to lower fiducial ionization energies and located at $E_{\mathrm{fid}} \approx 5\,\mathrm{keV_{ee}}$. Finally, the function $k\,(E_{\mathrm{r}})$ describes the measured energy on one of the two veto electrodes. For surface interactions, the factor used here is $\beta(\mathrm{surf}) = 1$ as these electrodes are calibrated with surface events as well. For bulk events, no energy should be measured on a veto electrode, except for electronic noise. By definition, $\beta(\mathrm{bulk}) = 0$ therefore.

Constructing a probability density function in the two observables E_c and E_fid starts with an input recoil spectrum of the signal or background component:

$$\rho\left(E_\mathrm{r}\right) = \frac{\mathrm{d}N\left(E_\mathrm{r}\right)}{\mathrm{d}E_\mathrm{r}} \tag{4.21}$$

An event density in E_r and the two observables of this analysis can be defined as

$$\rho\left(E_\mathrm{r}, E_\mathrm{c}, E_\mathrm{fid}\right) = \frac{\mathrm{d}^3N\left(E_\mathrm{r}, E_\mathrm{c}, E_\mathrm{fid}\right)}{\mathrm{d}E_\mathrm{r}\,\mathrm{d}E_\mathrm{c}\,\mathrm{d}E_\mathrm{fid}} \tag{4.22}$$

With the detector response as described in Eq. 4.20, but neglecting any resolution effects for the moment, the event density from an input spectrum $\rho\left(E_\mathrm{r}\right)$ becomes:

$$\rho\left(E_\mathrm{r}, E_\mathrm{c}, E_\mathrm{fid}\right) = \rho\left(E_\mathrm{r}\right) \times \delta\left(E_\mathrm{r} - f^{-1}(E_\mathrm{c})\right) \times \delta\left(E_\mathrm{r} - g^{-1}(E_\mathrm{fid})\right) \tag{4.23}$$

where δ is the delta-function and the inverse of the functions f and g is used to calculate the recoil energy corresponding to a given energy E_c and E_fid. To take into account the detector resolution in the two observables, Eq. 4.23 has to be convoluted with two Gaussian terms:

$$\rho\left(E_\mathrm{r}, E_\mathrm{c}, E_\mathrm{fid}\right) = \frac{1}{2\pi\sigma_\mathrm{c}\sigma_\mathrm{fid}}\rho\left(E_\mathrm{r}\right) e^{-\left(\frac{E_\mathrm{c}-f(E_\mathrm{r})}{\sqrt{2}\sigma_\mathrm{c}}\right)^2} e^{-\left(\frac{E_\mathrm{fid}-g(E_\mathrm{r})}{\sqrt{2}\sigma_\mathrm{fid}}\right)^2} \tag{4.24}$$

Here, σ_c and σ_fid describe the detector resolutions in the two observables E_c and E_fid which increase with energy, due to physical effects such as charge trapping [139]. They can be calculated by error propagation from the baseline resolutions $\sigma_\mathrm{c}^0 = {}^{FWC}/_{2.35}$ and $\sigma_\mathrm{fid}^0 = {}^{FWF}/_{2.35}$ and a measurement of the width of the 10.37 keV peak from cosmogenic activation of ^{68}Ge:

$$\begin{aligned}
\sigma_\mathrm{c}(E_\mathrm{c}) &= \sqrt{\left(\sigma_\mathrm{c}^0\right)^2 + \left(\left(\sigma_\mathrm{c}^0\right)^2 - \left(\sigma_\mathrm{c}^{10.37}\right)^2\right) \times \left(E_\mathrm{c}/10.37\,\mathrm{keV_{ee}}\right)^2} \\
\sigma_\mathrm{fid}(E_\mathrm{fid}) &= \sqrt{\left(\sigma_\mathrm{fid}^0\right)^2 + \left(\left(\sigma_\mathrm{fid}^0\right)^2 - \left(\sigma_\mathrm{fid}^{10.37}\right)^2\right) \times \left(E_\mathrm{fid}/10.37\,\mathrm{keV_{ee}}\right)^2}
\end{aligned} \tag{4.25}$$

While the average values for the FWHM baseline noise FWC and FWF have been shown in Fig. 4.10 for all detectors, the resolutions at 10.37 keV, $\sigma_\mathrm{c}^{10.37}$ and $\sigma_\mathrm{fid}^{10.37}$, are determined in the following Sec. 4.3.3 as a by-product of the sideband fit of the electron recoil background. Integration over the input recoil energy spectrum finally yields the event density in the two analysis observables:

$$\rho\left(E_\mathrm{c}, E_\mathrm{fid}\right) = \frac{1}{2\pi\sigma_\mathrm{c}\sigma_\mathrm{fid}} \int_0^\infty \rho\left(E_\mathrm{r}\right) e^{-\left(\frac{E_\mathrm{c}-f(E_\mathrm{r})}{\sqrt{2}\sigma_\mathrm{c}}\right)^2} e^{-\left(\frac{E_\mathrm{fid}-g(E_\mathrm{r})}{\sqrt{2}\sigma_\mathrm{fid}}\right)^2} \mathrm{d}E_\mathrm{r} \tag{4.26}$$

This density has to be corrected for two efficiencies: $\epsilon_\mathrm{trigger}(E_\mathrm{c})$ describing the online trigger efficiency on the heat channel of a detector as given in Eq. 4.11. And most importantly an efficiency $\epsilon_\mathrm{fid}(E_\mathrm{r})$ related to the fiducial cut on the data. For densities describing events in

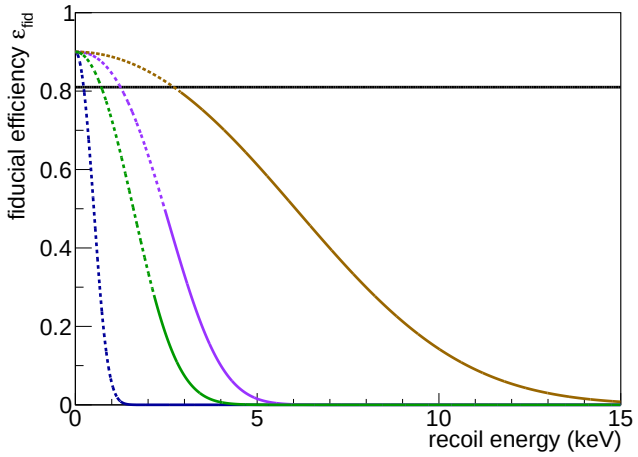

Figure 4.11.: Efficiency ϵ_{fid} of surviving the fiducial cut as a function of recoil energy, for different types of surface event backgrounds: Compton and cosmogenic γ's (dark blue), β's (green), nuclear recoils from WIMPs and neutrons (magenta) and ^{206}Pb-recoils (brown). All efficiencies have been calculated for side 1 of detector FID824, for an average veto electrode baseline noise of $\sigma_{\text{veto}} = 0.28\,\text{keV}_{\text{ee}}$ and the measured ionization yield values Q for this side. The dashed part of each efficiency curve marks energies below the analysis threshold $E_{\text{c}}^{\text{min}} = 0.91\,\text{keV}_{\text{ee}}$ in heat energy for this detector and depends on the ionization yield Q following Eq. 4.20. Only surface β's and ^{206}Pb-recoils have a sufficient survival probability and significant event rates to be considered as background in the analysis. For bulk events, the energy independent efficiency $\epsilon_{\text{fid}}^{\text{bulk}}(E_{\text{r}}) = 81\%$ of the fiducial cut is indicated as solid horizontal line

the bulk of the crystal, this efficiency can be calculated from the total acceptance of the cut for each of the two veto electrodes:

$$\epsilon_{\text{fid}}^{\text{bulk}}(E_{\text{r}}) = \prod_{i=1,2} \frac{1}{\sqrt{2\pi}\sigma_{\text{veto;i}}} \int_{-1.64\,\sigma_{\text{veto;i}}}^{+1.64\,\sigma_{\text{veto;i}}} e^{-\left(\frac{E_{\text{veto;i}} - k(E_{\text{r}})}{2\,\sigma_{\text{veto;i}}}\right)^2} \mathrm{d}E_{\text{veto;i}} \tag{4.27}$$

where $k(E_{\text{r}}) = 0$ for bulk events. By definition of the fiducial cut with a lower and upper cut value of $1.645\,\sigma_{\text{veto}}$, the efficiency for bulk events is energy independent and has a value of $\epsilon_{\text{fid}}^{\text{bulk}}(E_{\text{r}}) = 81\%$. For unrejected surface events, the efficiency is of course much smaller and energy dependent:

$$\epsilon_{\text{fid}}^{\text{surf}}(E_{\text{r}}) = \frac{1}{\sqrt{2\pi}\sigma_{\text{veto;i}}} \int_{-1.64\,\sigma_{\text{veto;i}}}^{+1.64\,\sigma_{\text{veto;i}}} e^{-\left(\frac{E_{\text{veto;i}} - k(E_{\text{r}})}{2\,\sigma_{\text{veto;i}}}\right)^2} \mathrm{d}E_{\text{veto;i}} \tag{4.28}$$
$$\text{with } k(E_{\text{r}}) = Q \cdot E_{\text{r}}$$

For surface events and the efficiency therefore strongly depends on the ionization yield Q of the events. For unrejected surface events from ^{206}Pb-recoils with a very small ionization yield of $Q_{\text{lead}} \approx 0.1$, only a small fraction of the recoil energy produces an ionization signal which can be vetoed. Consequently, the insufficient rejection extends up to much higher energies than for other background components such as β's, as is shown in Fig. 4.11.

Taking into account both efficiencies $\epsilon_{\text{trigger}}(E_{\text{c}})$ and $\epsilon_{\text{fid}}(E_{\text{r}})$, the event density as in Eq. 4.26

becomes:

$$\rho\left(E_{\mathrm{c}}, E_{\mathrm{fid}}\right) = \frac{\epsilon_{\mathrm{trigger}}(E_{\mathrm{c}})}{2\pi\sigma_{\mathrm{c}}\sigma_{\mathrm{fid}}} \int_0^{\infty} \epsilon_{\mathrm{fid}}(E_{\mathrm{r}})\rho\left(E_{\mathrm{r}}\right) e^{-\left(\frac{E_{\mathrm{c}}-f(E_{\mathrm{r}})}{\sqrt{2}\sigma_{\mathrm{c}}}\right)^2} e^{-\left(\frac{E_{\mathrm{fid}}-g(E_{\mathrm{r}})}{\sqrt{2}\sigma_{\mathrm{fid}}}\right)^2} \mathrm{d}E_{\mathrm{r}} \tag{4.29}$$

In case the event density describes cosmogenic events with discrete energies, the input spectrum is a δ-function. The integral is then only evaluated at the nominal peak energy $E_{\mathrm{r}}^{\mathrm{peak}}$:

$$\rho\left(E_{\mathrm{c}}, E_{\mathrm{fid}}\right) = \frac{\epsilon_{\mathrm{trigger}}(E_{\mathrm{c}})}{2\pi\sigma_{\mathrm{c}}\sigma_{\mathrm{fid}}} \epsilon_{\mathrm{fid}}(E_{\mathrm{r}}^{\mathrm{peak}})\rho\left(E_{\mathrm{r}}^{\mathrm{peak}}\right) e^{-\left(\frac{E_{\mathrm{c}}-f\left(E_{\mathrm{r}}^{\mathrm{peak}}\right)}{\sqrt{2}\sigma_{\mathrm{c}}}\right)^2} e^{-\left(\frac{E_{\mathrm{fid}}-g\left(E_{\mathrm{r}}^{\mathrm{peak}}\right)}{\sqrt{2}\sigma_{\mathrm{fid}}}\right)^2} \tag{4.30}$$

For some of the backgrounds described in the following section, the input spectrum is not given in recoil energy, but rather extracted as $\rho\left(E_{\mathrm{c}}\right)$ from sideband data directly as a function of heat energy. In that case, the smearing of the event density with the detector resolution in heat energy is already included. The event density can thus be described more simply by:

$$\rho\left(E_{\mathrm{c}}, E_{\mathrm{fid}}\right) = \frac{\epsilon_{\mathrm{trigger}}(E_{\mathrm{c}})}{\sqrt{2\pi}\sigma_{\mathrm{fid}}} \rho(E_{\mathrm{c}})\epsilon_{\mathrm{fid}}(E_{\mathrm{r}}) e^{-\frac{\left(E_{\mathrm{fid}}-g(E_{\mathrm{r}})\right)^2}{2\sigma_{\mathrm{fid}}^2}} \tag{4.31}$$

where the recoil energy E_{r}, which is needed to calculate the fiducial cut efficiency $\epsilon_{\mathrm{fid}}(E_{\mathrm{r}})$ and the fiducial ionization energy $g(E_{\mathrm{r}})$ is determined from the heat energy via $E_{\mathrm{r}} = f^{-1}(E_{\mathrm{c}})$. To calculate the expected number of background events n_{exp} for a given input spectrum, the event density is integrated over the two observables within the range of the RoI for the detector:

$$n_{\mathrm{exp}} = \int_{0\,\mathrm{keV_{ee}}}^{15\,\mathrm{keV_{ee}}} \int_{E_{\mathrm{c}}^{\mathrm{min}}}^{15\,\mathrm{keV_{ee}}} \rho\left(E_{\mathrm{c}}, E_{\mathrm{fid}}\right) \mathrm{d}E_{\mathrm{c}}\mathrm{d}E_{\mathrm{fid}} \tag{4.32}$$

The PDF $\mathcal{P}$ that will be used in the following likelihood model can be constructed by simply normalizing the event density to the number of expected events:

$$\mathcal{P}\left(E_{\mathrm{c}}, E_{\mathrm{fid}}\right) = \frac{\rho\left(E_{\mathrm{c}}, E_{\mathrm{fid}}\right)}{n_{\mathrm{exp}}} \tag{4.33}$$

Integration of PDFs for normalization and for the calculation of the expected event rates of backgrounds are performed numerically. The relevant procedures are already implemented in the code of the `RooFit` package which is used for all PDF constructions and likelihood fits.

4.2.2. Likelihood function for individual detectors

With the different definitions of PDFs for individual components, a total PDF $\mathcal{P}_{\mathrm{j}}$ can be constructed which describes the selected data for each detector j. This total PDF is the sum of all modelled detector backgrounds plus a WIMP signal, each weighted by the rate of events of the corresponding component. While the backgrounds are defined once for each detector, the signal PDF $\mathcal{P}_{\chi}$ depends on the nuclear recoil spectrum of WIMPs in

germanium and is therefore a function of the WIMP mass m_χ. Consequently, the total PDF has to be constructed separately for each WIMP mass that is probed in the analysis:

$$\mathcal{P}_\mathrm{j}\left(E_\mathrm{c}, E_\mathrm{fid} \mid m_\chi\right) = \frac{\mu_\chi}{\mu_\mathrm{fit}} \mathcal{P}_\chi\left(E_\mathrm{c}, E_\mathrm{fid} \mid m_\chi\right) + \sum_\mathrm{i} \frac{\mu_\mathrm{i}}{\mu_\mathrm{fit}} \mathcal{P}_\mathrm{i}\left(E_\mathrm{c}, E_\mathrm{fid}\right) \tag{4.34}$$

The nuisance parameters μ_i describe the rate of events for each background i given the exposure of the selected data set of a detector. The sum of all rates μ_fit includes the rate of signal events μ_χ and is needed needed to normalize the total PDF $\mathcal{P}_\mathrm{j}$:

$$\mu_\mathrm{fit} = \mu_\chi + \sum_i \mu_\mathrm{i} \tag{4.35}$$

The fitted rate of signal events μ_χ is defined for each WIMP mass m_χ as a function of the actual parameter of interest, the WIMP-nucleon scattering cross section σ_χ. It can be calculated by integration of the WIMP signal density $\mathcal{P}_\chi$ in the RoI for a given normalization cross section of the input spectrum, which was set to $\sigma_\chi^0 = 10^{-6}\,\mathrm{pb}$:

$$\mu_\chi(m_\chi) = \frac{\sigma_\chi}{\sigma_\chi^0} \times \int_\mathrm{RoI} \rho_\chi\left(E_\mathrm{c}, E_\mathrm{fid} \mid m_\chi\right) \tag{4.36}$$

With these definitions the unbinned, extended likelihood function for fitting data of individual detectors can be constructed. It is the product of the individual probabilities for all N events of a detector, multiplied with a Poisson-term constraining the fitted total rate of events μ_fit. For each background i, an additional Gaussian PDF constrains the fitted rate of this component. The mean of the Gaussian is the expected value $n_\mathrm{i}^\mathrm{exp}$, as calculated from the integrated event density for the RoI given the input spectrum (see Eq. 4.32) and the Gaussian width is the systematic error σ_i on this value. Following Eq. 3.13, the likelihood function for a given WIMP mass m_χ is therefore given by

$$\mathcal{L}_\mathrm{j}\left(\sigma_\chi, \vec{\mu}_\mathrm{j} \mid m_\chi\right) = \mathrm{Pois}(N \mid \mu_\mathrm{fit}) \times \prod_{\mathrm{n}=1}^{N} \mathcal{P}_\mathrm{j}(E_\mathrm{c}^\mathrm{n}, E_\mathrm{fid}^\mathrm{n}) \times \prod_i \mathrm{Gauss}(\mu_\mathrm{i} \mid n_\mathrm{i}^\mathrm{exp}, \sigma_i) \tag{4.37}$$

To find the set of fit parameters for the different event rates μ_i and the signal cross section σ_χ that describing the data best, the likelihood function $\mathcal{L}_\mathrm{j}$ is maximized as described in Sec. 3.4.1.

4.2.3. Combination of detectors

The combination of detectors is a powerful tool that can be applied in many likelihood analyses. It is often used in particle physics experiment to combine the results of different signal channels, e.g. in Higgs-search. Different likelihood functions with the same parameter of interest can be multiplied to one combined likelihood function. Instead of performing individual fits and combining the results, one single fit is performed on a combined model. One benefit of this method is, that model uncertainties in the description of one of the individual likelihood functions are outweighted and do not impact the fit significantly. The analysis presented in this thesis is a natural candidate for the combination of likelihood functions. The data of the eight detectors which has been described with likelihood functions was taken during the same measuring phase and the performance of all detectors in terms of baseline resolutions is very similar. Due to the expected weak interaction, a

significant signal from WIMP-nucleon scattering is expected to appear homogeneously in all detectors, independent of their position in the cryostat. For each of the probed WIMP masses m_χ, the eight individual likelihood functions $\mathcal{L}_\mathrm{j}$ described in Eq. 4.37 are therefore multiplied to one combined likelihood function $\mathcal{L}_\mathrm{comb}$:

$$\mathcal{L}_\mathrm{comb}\left(\sigma_\chi, \vec{\mu}_1, ..., \vec{\mu}_8 \mid m_\chi\right) = \prod_{\mathrm{j}=1}^{8} \mathcal{L}_\mathrm{j}\left(\sigma_\chi, \vec{\mu}_\mathrm{j} \mid m_\chi\right) \tag{4.38}$$

The fit to the data is still performed on the level of individual detectors, i.e. each individual dataset is fitted with the correct model for this detector, including all background component PDFs, event rates μ_i and constraint terms. The only connection between the different likelihood functions which have been combined is the common parameter of interest, the WIMP-nucleon scattering cross section σ_χ. For a better understanding of this signal, a total rate of WIMP events in all eight detectors can be calculated in analogy to Eq. 4.36. For each WIMP mass m_χ and cross section σ_χ, the total rate $\mu_{\chi;\mathrm{comb}}$ is calculated by summing up the different integrated signals of each detector j:

$$\mu_\chi^\mathrm{comb}(m_\chi) = \frac{\sigma_\chi}{\sigma_\chi^0} \times \sum_{\mathrm{j}=1}^{8} \int_\mathrm{RoI} \rho_{\chi;\mathrm{j}}\left(E_\mathrm{c}, E_\mathrm{fid} \mid m_\chi\right) \tag{4.39}$$

where σ_χ^0 is the normalization cross section used to construct each of the signal densities $\rho_{\chi;\mathrm{j}}$.

4.3. Modelling of signal and background components

To construct a likelihood function $\mathcal{L}_\mathrm{j}$ for each detector, the different backgrounds which are relevant for this analysis have to be determined and modelled. For each background i, the corresponding event density function $\rho_\mathrm{i}\left(E_\mathrm{c}, E_\mathrm{fid}\right)$ is constructed, with either Eq. 4.29 or Eq. 4.31 or Eq. 4.30, depending on the available input spectrum. These event density functions are then used to calculate the number of expected events n_exp in the RoI, which defines the mean of the Gaussian constraint term in the likelihood function. Systematic errors in the determination of n_exp define the width σ_i of this constraint. By normalization, the event densities are transformed into PDFs which are used in the likelihood function.

4.3.1. WIMP signal

A different signal PDF for each WIMP mass m_χ has to be constructed from the signal density given in Eq. 4.29 based on the nuclear recoil energy spectrum $\rho\left(E_\mathrm{r}\right)$. This spectrum of WIMP-nucleon interactions is calculated for a normalization cross section of $\sigma_\chi^0 = 10^{-6}\,\mathrm{pb}$ using Eq. 1.24 and the exposure after all cuts as tabulated in Tab. 4.3. To allow for a comparison of the results with the BDT analysis as well as all other direct detection experiments, all astrophysical parameters are in agreement with the *Standard Halo Model*:

$$\begin{aligned} \rho_\mathrm{DM}^\mathrm{local} &= 0.3\,\mathrm{GeV/c^2/cm^3} \\ v_\mathrm{esc} &= 544\,\mathrm{km/s} \\ v_0 &= 220\,\mathrm{km/s} \\ v_\mathrm{earth} &= 230\,\mathrm{km/s} \end{aligned}$$

Despite their significant uncertainties, these values are taken as fixed in this analysis. It would be possible to implement them as additional nuisance parameters, as has been

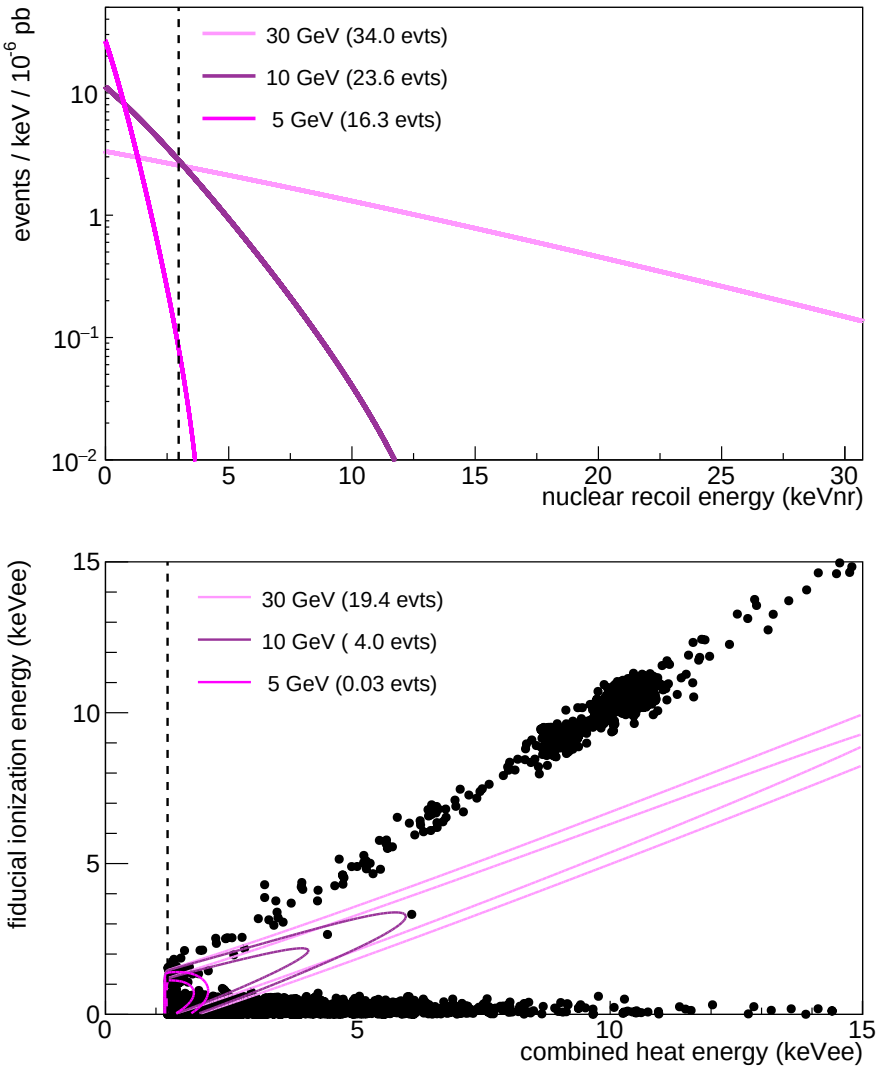

Figure 4.12.: *Top*: Nuclear recoil energy spectrum $\rho_\chi(E_\mathrm{r})$ for WIMP-nucleon interactions in detector FID837 for three different WIMP masses m_χ and a cross section of $\sigma_\chi^0 = 10^{-6}\,\mathrm{pb}$. The analysis threshold in heat $E_\mathrm{c}^\mathrm{min} = 1.24\,\mathrm{keV_{ee}}$ for this detector corresponds to a lower cutoff at $2.97\,\mathrm{keV_{nr}}$ (dashed black line). The spectra for higher mass WIMPs are also cut off due to the upper boundary of the RoI, corresponding to $30.7\,\mathrm{keV_{nr}}$. The numbers in brackets give the integrated number of events for the total spectrum (not limited to the RoI). *Bottom*: Signal density $\rho_\chi(E_\mathrm{c}, E_\mathrm{fid} \mid m_\chi)$ in the RoI for these energy spectra (coloured contours). Black markers show the WIMP search data for this detector after all cuts. Only for higher masses does the signal PDF extend to the two outlier events at $E_\mathrm{c} \approx 4.5\,\mathrm{keV_{ee}}$ and $E_\mathrm{c} \approx 6\,\mathrm{keV_{ee}}$. Numbers in brackets give the integrated signal in the RoI.

done in [114] for the escape velocity v_{esc}. However, the focus of this analysis is not on astrophysical models, therefore all astrophysical parameters are taken at face value. For the calculation of the nuclear recoil energy spectrum $\rho(E_{\mathrm{r}})$ in the EDELWEISS crystals, an atomic mass number for germanium of $A = 72.63$ was used. This value is averaged over the different fractions of isotopes present in natural germanium: ^{70}Ge: 20.57%, ^{72}Ge: 27.45%, ^{73}Ge: 7.75%, ^{74}Ge: 36.50% and ^{76}Ge: 7.73% as tabulated in [140]. An alternative implementation would be to add up individual recoil spectra calculated for the mass fraction of each isotope. Tests performed in the context of [137] show a negligible difference of $< 1\%$ in the calculated rate for low WIMP masses for this approach, thus it is not applied here. For EDELWEISS detectors, the ionization yield Q_{NR} observed for nuclear recoils as a function of recoil energy E_{r} has been parametrized as:

$$Q_{\mathrm{NR}} = a \cdot E_{\mathrm{r}}^{b} \tag{4.40}$$

The determined parameters $a = 0.16$ and $b = 0.18$ are consistent with the Lindhard theory for germanium ([73]). The correct parametrization of this ionization yield affects the WIMP density in the RoI and therefore the shape of the PDF used for fitting a potential WIMP signal. A study of the neutron calibration data which was taken during Run308 was performed within the EDELWEISS collaboration to validate the parametrization of Q_{NR} and derive its uncertainty. It was found that the Q_{NR} for actual data is in agreement with the parametrization within an uncertainty of $\Delta Q_{\mathrm{NR}} = \pm 5\%$. To account for this uncertainty in the fit, the likelihood function $\mathcal{L}_{\mathrm{j}}$ for each detector is modified by multiplying an additional constraint term:

$$\mathcal{L}_{\mathrm{j}}^{\star}\left(\sigma_{\chi}, \vec{\mu}_{\mathrm{j}}, a_{\mathrm{j}} \mid m_{\chi}\right) = \mathcal{L}_{\mathrm{j}}\left(\sigma_{\chi}, \vec{\mu}_{\mathrm{j}} \mid m_{\chi}\right) \times \mathrm{Gauss}\left(a_{\mathrm{j}} \mid a^{\mathrm{exp}}{=}0.16, \sigma_{a}{=}0.008\right) \tag{4.41}$$

The uncertainty on the nuclear recoil ionization yield Q_{NR} is now described by a new nuisance parameter a_{j}, which is different for each detector and constrained in the fit to within $\pm 5\%$. For detector FID837, Fig. 4.12 shows the nuclear recoil energy spectrum $\rho(E_{\mathrm{r}})$ and the resulting signal density $\rho(E_{\mathrm{c}}, E_{\mathrm{fid}})$ for three different WIMP masses m_{χ} and the standard ionization yield Q_{NR}. With increasing mass, the nuclear recoil spectrum becomes flatter and extends to higher energies. Consequently, the signal density extends to higher energies in the parameter space of the two observables $(E_{\mathrm{c}}, E_{\mathrm{fid}})$. Detector FID837 has two clear events near the ionization yield for nuclear recoils, and the signal probability for these two events is clearly dependent on the WIMP mass m_{χ}.
The application of all efficiencies and cuts, in particular the analysis threshold $E_{\mathrm{c}}^{\mathrm{min}}$ of the RoI, significantly reduces the signal density. For the lowest WIMP mass $m_{\chi} = 4\,\mathrm{GeV}/c^2$ considered in this analysis, only a very small tail of the approximately exponential nuclear recoil spectrum is above $E_{\mathrm{c}}^{\mathrm{min}}$. A further reduction comes from the trigger efficiency $\epsilon_{\mathrm{trigger}}$, which by definition of the RoI is between 80% and 100%. Eventually, the remaining signal is further reduced by the acceptance of the fiducial cut of $\epsilon_{\mathrm{fid}}^{\mathrm{bulk}} = 81\%$. For higher WIMP masses such as $m_{\chi} = 30\,\mathrm{GeV}/c^2$ the upper part of the spectrum is cut as well, inducing an additional loss of efficiency. The integrated signal density in the RoI and its efficiency due to the applied cuts as a function of m_{χ} is shown in Fig. 4.13 for all detectors. For the smallest WIMP mass the signal efficiency after cuts is only between $10^{-3}\%$ and 0.1%, but increases to more than 1% for most detectors at $m_{\chi} = 6\,\mathrm{GeV}/c^2$. The maximum efficiency is $\approx$60% for all detectors at $m_{\chi} = 30\,\mathrm{GeV}/c^2$. Detector FID824 clearly has the highest efficiency for low mass WIMPs, due to the lowest analysis threshold among the 8 detectors of only $E_{\mathrm{c}}^{\mathrm{min}} = 0.9\,\mathrm{keV_{ee}}$, corresponding to $2.2\,\mathrm{keV_{nr}}$.

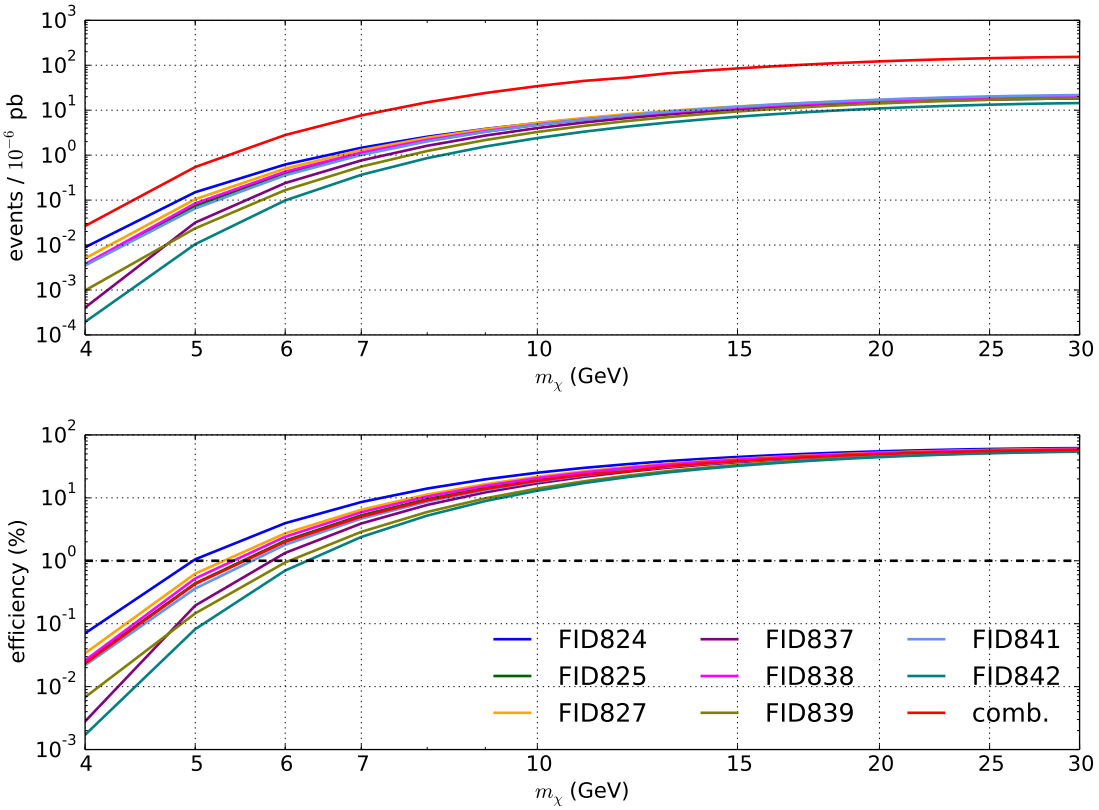

Figure 4.13.: *Top*: Integrated signal density $\int_{\mathrm{RoI}} \rho\,(E_\mathrm{c}, E_\mathrm{fid})$ after all cuts and efficiency corrections for a WIMP-nucleon scattering cross section of $\sigma_\chi^0 = 10^{-6}$ pb as a function of WIMP mass m_χ. *Bottom*: Signal efficiency, i.e. fraction of the input spectrum $\rho\,(E_\mathrm{r})$ for a given exposure. Detector FID824 has both the largest signal and the highest signal efficiency. The so-called *WIMP safe-mass*, for which at least 1% of the signal is kept (dashed black line) is $m_\chi = 5\,\mathrm{GeV}/c^2$ for detector FID824 and $m_\chi \approx 6\,\mathrm{GeV}/c^2$ for all other detectors.

4.3.2. Heat-only events

In terms of event rate, so-called *heat-only* events are by far the dominating background in the EDELWEISS data taking. They are present in all detectors with different intensity. In this analysis, between 85% and 95% of the events in the RoI are expected to be part of the heat-only background. For such events the DAQ system triggered on a clear signal on one of the two heat channels but only noise can be reconstructed on all of the 4 ionization channels. During individual time periods, the energy spectrum of heat-only events has an approximately exponential shape. At very low energies near the detector threshold, it cannot be separated from the baseline noise. Some fraction of heat-only events in EDELWEISS come from internal radioactivity of the two NTD sensors of a detector. However, such events have a bad χ^2-value when fitted with the usual heat pulse template and have thus been efficiently rejected from the analysed data with the heat χ^2-cut described in Eq. 4.8. Additionally, the measured heat energy is much larger on one of the NTDs and these events are therefore rejected as well by the cut on the heat symmetry (Eq. 4.10). While their exact origin is yet unknown, the extremely high rate and their properties exclude that these events come from physical particles, for example from lead-recoils on the electrodes[2]. Studies performed in the context of [137] showed that the distribution of the time difference

[2]No ionization signal can be measured for events directly hitting one of the electrodes, which cover ≈10% of the detector surface.

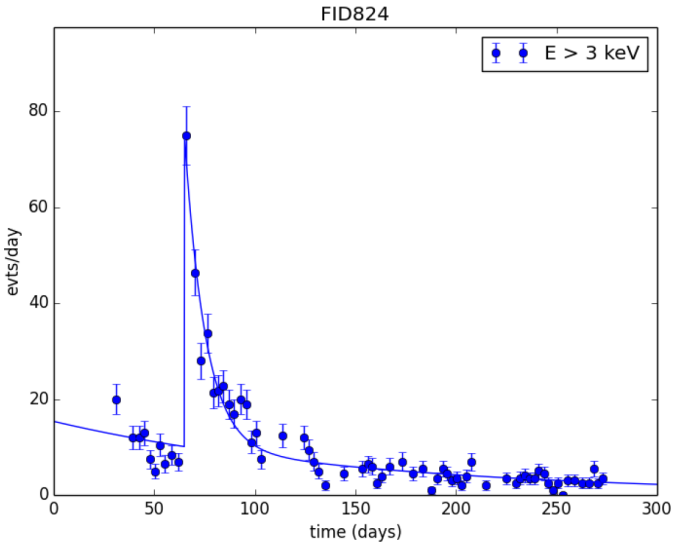

Figure 4.14.: Rate of events with $E_c > 3\,\mathrm{keV_{ee}}$ as a function of days since the start of Run308 on July 22$^{\mathrm{nd}}$ 2014 in the heat-only sideband $E_{\mathrm{fid}} < 0\,\mathrm{keV_{ee}}$ of detector FID824. The observed rate can be well approximated with 2 exponential functions of different decay constant. The significant rise around day 65 can also be observed in the heat-only rate of other detectors. Figure from [137].

between events for the second half of Run308 is exponential and therefore compatible with a constant rate. No hints were found that heat-only events appear in bursts and the average rate of events in coincidence with at least one other detector (multiplicity) of 2% was found to be in good agreement with that of noise events, not showing any indication for a correlation between detectors. Several theories as to where this background is coming from have been put forward. Some of them, such as a desorption of ^{4}He on the surface have already been rejected after tests performed in a later run. Other possible sources, such as friction of the detectors with the Teflon holders are under investigation. A further possible explanation are cracks at the level of the holders, similar to [141]. As heat-only events are a limiting factor in the search for low mass WIMPs, several R&D efforts are ongoing to find the origin of this background and to reduce it in future runs of the EDELWEISS experiment.

The time variation of the heat-only rate shows a universal behaviour for all 8 detectors: Above an energy of $E_c = 3\,\mathrm{keV_{ee}}$, where the baseline noise can be neglected, the heat-only rate as a function of time can be modelled with 2 different exponential functions, as is shown in Fig. 4.14. Over the whole of Run308 it shows a general decrease. On day 65, corresponding to Sep. 25$^{\mathrm{th}}$ 2014, there is a strong increase in rate of heat-only events for all detectors, which is followed by a fast decay. The decay time of ≈20 days is incompatible with any known radioactive sources in the vicinity of the experiment. The exact origin of this increase is not known but it followed a cryogenic and hardware intervention on the experiment. While information on the time dependence of the rate of heat-only events is used as an additional discriminating observable in the BDT analysis, the analysis presented here only includes information on the combined heat and fiducial ionization energy of these events.

To model heat-only events, we use the fact that they are expected to follow a Gaussian distributed around $E_{\mathrm{fid}} = 0\,\mathrm{keV_{ee}}$. The sideband $E_{\mathrm{fid}} < 0\,\mathrm{keV_{ee}}$ and $E_c^{\mathrm{min}} < E_c < 15\,\mathrm{keV_{ee}}$ is therefore used to construct a model with which the events in the RoI can be described. It has been checked that any contamination of this sideband due to underfluctuations in E_{fid} by other background components is $\mathcal{O}(10)$ events and therefore negligible. For the cross

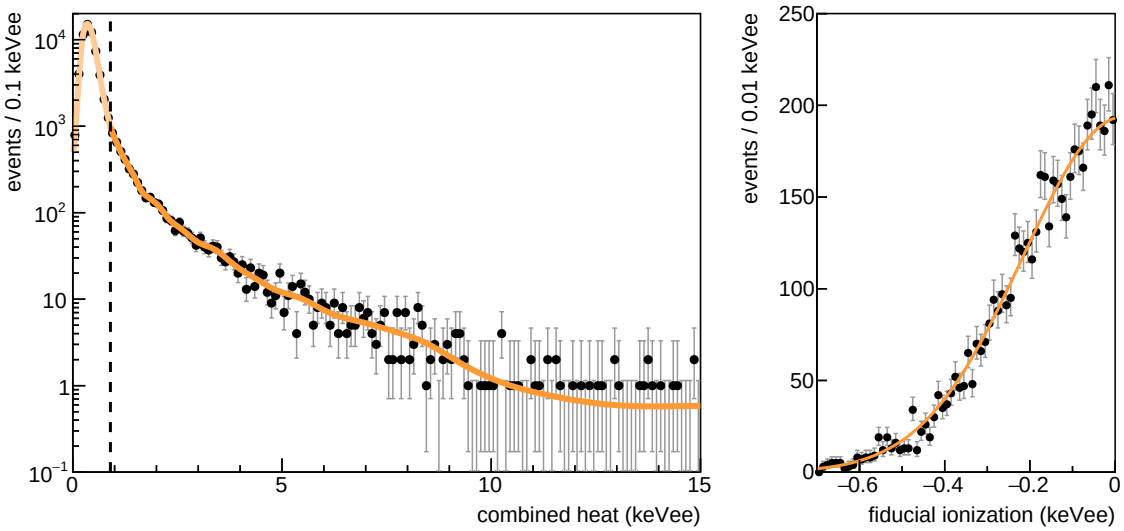

Figure 4.15.: *Left*: Energy spectrum of events in the *"heat-only"* sideband with ionization energy $E_{\mathrm{fid}} < 0\,\mathrm{keV_{ee}}$ for detector FID824 after application of the same quality and period cuts as for the analysed data. The spectrum can be modelled with a *Kernel Density Estimation* function (orange). Out of a total of 63,400 events, 5386 are above the analysis threshold of $E_{\mathrm{c}}^{\mathrm{min}} = 0.9\,\mathrm{keV_{ee}}$ for this detector (dashed line). *Right*: spectrum in fiducial ionization E_{fid} for those events above the analysis threshold. An unbinend likelihood fit with a (half-)Gaussian of fixed width $\sigma_{\mathrm{fid}} = 0.237\,\mathrm{keV_{ee}}$ gives a fitted mean of $\mu = 0.021 \pm 0.005\,\mathrm{keV_{ee}}$ hinting at a possible asymmetry of the heat-only events in E_{fid}.

Table 4.4.: Results of an unbinned likelihood fit of the fiducial ionization energy for N_{sb} events in the heat-only sideband with $E_{\mathrm{fid}} < 0\,\mathrm{keV_{ee}}$. Fitted is a Gaussian function with a free mean and a fixed width $\sigma_{\mathrm{fid}}^{0} = FWF/2.35$ corresponding to the average baseline noise. For some detectors a possible offset of the mean with respect to $E_{\mathrm{fid}} = 0\,\mathrm{keV_{ee}}$ is observed and leads to an additional systematic error σ_{sys} on the number of events expected in the RoI. This uncertainty can be much larger than the statistical error $\sigma_{\mathrm{stat}} = \sqrt{N_{\mathrm{sb}}}$.

Detector	width ($\mathrm{keV_{ee}}$)	mean ($\mathrm{keV_{ee}}$)	N_{sb}	σ_{stat} (%)	σ_{sys} (%)
FID824	0.24	0.021 ± 0.005	5386	1.4	14.9
FID825	0.19	0.012 ± 0.005	5159	1.4	9.9
FID827	0.22	0.011 ± 0.004	9155	1.0	8.2
FID837	0.22	0.009 ± 0.006	4399	1.5	6.9
FID838	0.23	0.001 ± 0.004	7285	1.2	0.6
FID839	0.23	0.010 ± 0.005	6416	1.2	6.9
FID841	0.21	0.007 ± 0.006	3578	1.7	5.5
FID842	0.26	-0.001 ± 0.008	2744	1.9	0.4

sections considered in this analysis, a contamination with a possible WIMP signal can also be neglected. As the energy spectrum of heat-only events is the superposition of all different time periods during Run308 with vastly different average rates (see Fig. 4.14) it cannot be well approximated with simple analytical functions. For this reason an adaptive *Kernel Densitiy Estimator* (KDE) [142], which is implemented in the `RooFit` package, is used to describe the energy spectrum $\rho(E_c)$. The bandwidth parameter of the KDE is chosen such that it can reproduce the overall shape of the spectrum without over-fitting small statistical fluctuations at the tail. An example of such a KDE describing the heat energy spectrum of sideband data from detector FID824 is given in Fig. 4.15 (left). The distribution of the sideband data in E_{fid} should ideally be described with a Gaussian centered at $E_{fid} = 0\,\mathrm{keV_{ee}}$ and a width determined by the average baseline noise FWF for all events. However, in the framework of this thesis it was discovered that for some detectors there is a slight asymmetry in the fitted fiducial ionization energy spectrum. This asymmetry is energy dependent and most likely related to uncorrected cross-talk affecting some of the ionization channels. For this analysis, any energy dependence of this cross-talk is neglected, as the exact heat-only density is only relevant at energies near the analysis threshold E_c^{min} where an overlap with a possible WIMP signal exists. The possible shift is therefore determined from the projection of the heat-only sideband data in E_{fid} over the whole energy range E_c. To avoid any bias due to the choice of binning, an unbinned likelihood fit was performed with a Gaussian distribution of fixed width $\sigma_{fid}^0 = {}^{FWF}/_{2.35}$ and free mean. The results of this fit for the different detectors are given in Tab. 4.4. For some detectors a small offset of $\mathcal{O}(0.01)\,\mathrm{keV_{ee}}$ is observed. In the case of FID824 the fitted mean of $0.021 \pm 0.005\,\mathrm{keV_{ee}}$ is a statistically significant deviation from 0, for other detectors, this value is much smaller and statistically negligible. As the fit of half a Gaussian is not deemed reliable enough, the value of this shifted mean is not used to construct the heat-only PDF in the RoI. Instead, to account for a possible asymmetry of the heat-only PDF, the systematic error of the expected number of events is calculated. For this, the number of sideband events N_{sb} is multiplied with the fraction of a Gaussian with shifted mean in the RoI, and the relative error compared to N_{sb} is calculated. This systematic error σ_{sys} is between 0.4% (FID842) and 14.9% (FID824) and therefore much larger than the statistical error $\sigma_{stat} = \sqrt{N_{sb}}$ originating from Poisson statistics. Both errors are combined to give the width of the constraint PDF for each detector, which can be as large as ±800 events for FID824. The number of expected events defining the mean of the constraining PDF is given directly by the number of events in the sideband.

With the extraction of the heat energy spectrum $\rho(E_c)$ the modelled heat-only event density for each detector can now be constructed using Eq. 4.31: an ionization yield of $Q = 0$ is used as well as a constant, energy independent width of σ_{fid}^0 as given in Tab. 4.4. Both trigger efficiency $\epsilon_{trigger}$ and fiducial cut efficiency ϵ_{fid} are set to 100% as they are already included in the extracted energy spectrum $\rho(E_c)$. The binned heat-only sideband data and the resulting PDF for detector FID824 are shown in Fig. 4.16, for illustrative purposes also below the analysis threshold E_c^{min}. Shown for comparison are the contours for two different WIMP signals at 10% and 90% integrated probability. For $m_\chi = 10\,\mathrm{GeV}/c^2$ the two PDFs seem to be well separated although there is some overlap near the analysis threshold E_c^{min}. In case of $m_\chi = 4\,\mathrm{GeV}/c^2$ the signal density does not extend beyond the heat-only PDF. Considering the high rate of the heat-only background compared to a search for small signals, some degeneracy between the two PDFs is expected and actually observed for several detectors, as will be shown in Sec. 4.4.

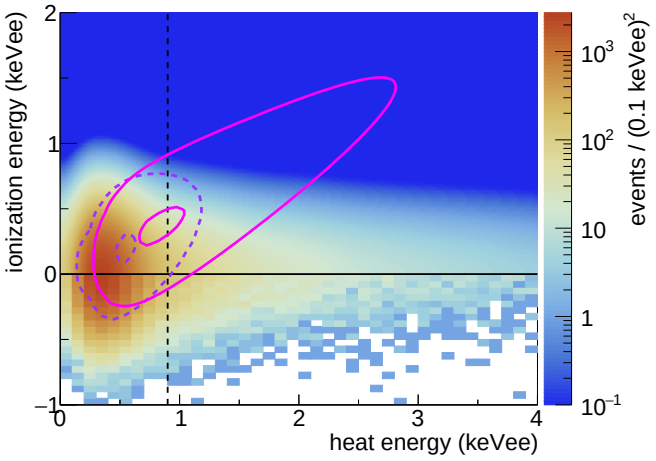

Figure 4.16.: Binned sideband data ($E_{\mathrm{fid}} < 0\,\mathrm{keV_{ee}}$) and modelled heat-only PDF ($E_{\mathrm{fid}} > 0\,\mathrm{keV_{ee}}$) for detector FID824. Coloured contours indicate the 10% and 90% signal density for a WIMP with $m_\chi = 4\,\mathrm{GeV}/c^2$ (dashed violet) and $m_\chi = 10\,\mathrm{GeV}/c^2$ (solid magenta). A black dashed line indicates the analysis threshold $E_{\mathrm{c}}^{\mathrm{min}} = 0.9\,\mathrm{keV_{ee}}$, above which a possible signal contribution to the sideband can be considered negligible.

4.3.3. Electron recoil events

The second largest background in the data of this analysis are electron recoils in the bulk of the crystal, coming from three different sources: γ-radiation from outside the detector as well as X-rays and β's from inside the detector. In the energy range of the RoI, γ-radiation from external sources, as introduced in Sec. 2.4.2, has an approximately flat energy spectrum. Mono-energetic X-rays emerge from EC-capture reactions of mainly cosmogenically activated isotopes in the crystal and produce a set of peaks widened by the energy resolution of the readout channels. These isotopes have been activated by cosmic radiation during production of the detector on the surface, or during neutron calibration underground. There are several isotopes with peak energies in the RoI: between 5 and 7.7 keV there are peaks from the K-shell EC of ^{49}V ($E = 4.97\,\mathrm{keV}$), ^{51}Cr (5.46 keV), ^{54}Mn (5.99 keV), ^{55}Fe (6.54 keV), ^{56,57,58}Co (7.11 keV) and ^{56}Ni (7.71 keV). Around 10 keV a peak triplet can be observed which has a much higher intensity and is the result of K-shell EC reactions of ^{65}Zn (8.98 keV), ^{68}Ga (9.66 keV) and ^{68}Ge (10.37 keV). This triplet also has corresponding L-shell peaks at 1.10 keV, 1.19 keV and 1.30 keV which are still in the RoI for some detectors. The intensity of these peaks is proportional to the K-shell peaks, with an L/K-ratio of ≈11% [98]. As their energy is close to the trigger threshold for some detectors, the rate of measured events for a detector depends on its trigger efficiency. For detectors with higher analysis threshold such as FID842 ($E_{\mathrm{c}}^{\mathrm{min}} = 1.46\,\mathrm{keV_{ee}}$) only the tail of the Gaussian peaks above $E_{\mathrm{c}}^{\mathrm{min}}$ is within the RoI. Of all ER background components it is mostly the L-shell peaks which are relevant for WIMP search, as they can have significant overlap with a signal for low WIMP masses.
Another background source which produces ER in the bulk of the crystal is the decay of tritium (see Sec. 2.4.4). The produced β's have a typical decay spectrum with an endpoint energy of 18.6 keV and scatter off the electron shells, producing electron recoils. A recent analysis within the EDELWEISS collaboration has for the first time found significant evidence for this interaction in the FID detectors [100].

To model the total electron recoil background coming from these different sources, another sideband of the analysed data is used, in an energy range from 3 to 30 $\mathrm{keV_{ee}}$ for both combined heat energy E_{c} and fiducial ionization energy E_{fid}. The energy scale in the

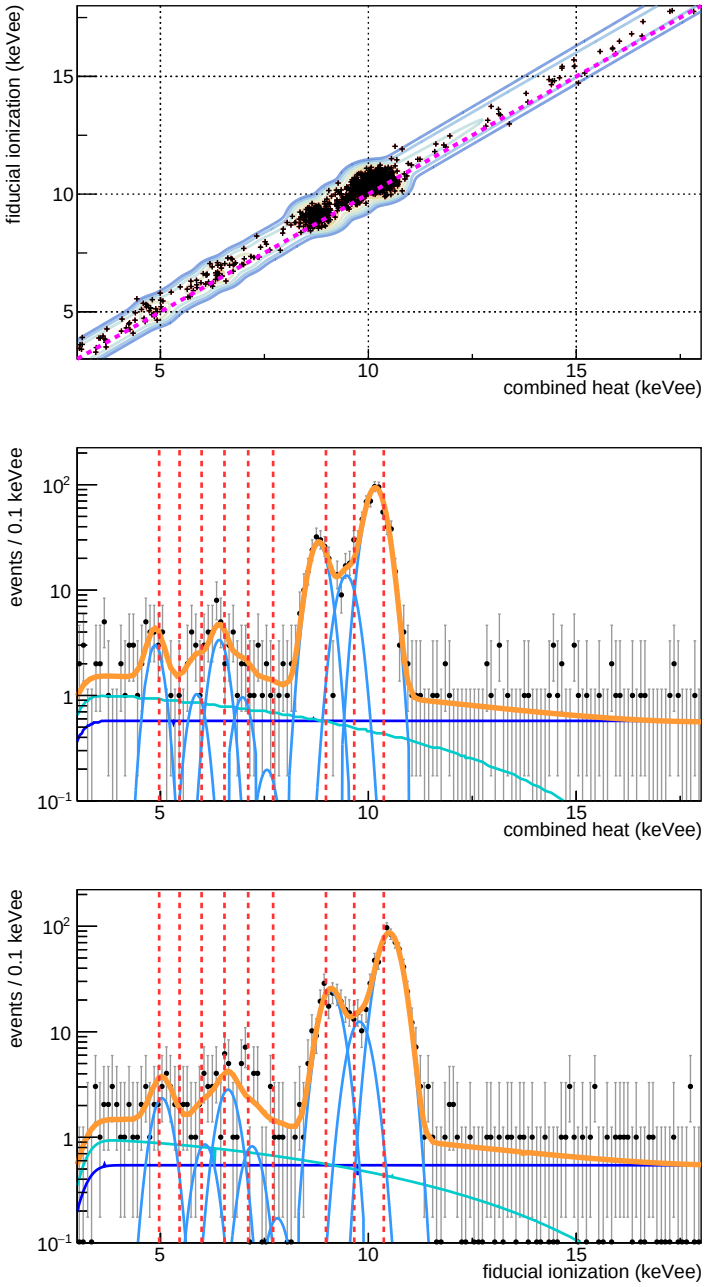

Figure 4.17.: Result of an unbinned likelihood fit to the bulk electron recoil sideband of detector FID827 in the energy range $3 < E_c, E_{fid} < 30\,\mathrm{keV_{ee}}$. *Top*: sideband events and 2d best fit with event density as coloured contours. The centroid of the events shows a visible offset to the expected quenching of $Q = 1$ (magenta dashed line), related to an imprecision in the energy calibration. This is considered in the fit. *Bottom*: Projection of data and best fit PDF (orange) in the two observables E_c and E_{fid}. Plotted are the fitted PDFs for the two continuous components from Compton γ's (dark blue) and tritium β's (turquoise) as well as eight different K-shell peaks (light blue). Vertical dashed red lines indicate the nominal peak positions of these peaks.

experiment is calibrated such, that bulk electron recoils have an ionization yield of $Q_{\mathrm{ER}} = 1$ by definition. Due to resolution effects, the electron recoil component can be described by a band, centred around $E_{\mathrm{fid}} = E_{\mathrm{c}}$ in the 2-dimensional parameter space of this analysis. To achieve a pure selection of electron recoils, only events within $E_{\mathrm{fid}} = E_{\mathrm{c}} \pm 1\,\mathrm{keV_{ee}}$ are used as sideband data. This corresponds to $\approx 5{-}6\,\sigma$ variations around the expected ionization yield $Q_{\mathrm{ER}} = 1$, which occur due to energy uncertainties. With the choice of the lower energy boundary $E_{\mathrm{c}}, E_{\mathrm{fid}} > 3\,\mathrm{keV_{ee}}$, any overlap of the ER-sideband with a WIMP signal of arbitrary mass m_χ can be considered negligible. The motivation for the upper boundary of the sideband is to include the transition of the continuous component from the β-spectrum of tritium decay to the approximately flat spectrum from Compton γ's. For each detector, the electron recoil events in the ER-sideband are fitted with an unbinned maximum likelihood model in the two observables E_{c} and E_{fid}. The PDF used in the likelihood function has a total of 10 components: β's from the decay of tritium, Compton γ's and 8 different K-shell peaks. For the construction of the peak PDFs, the event density described in Eq. 4.30 is used. The energy dependent width of each peak in E_{c} (E_{fid}) is calculated with Eq. 4.25 from the average baseline resolution σ_{c}^{0} ($\sigma_{\mathrm{fid}}^{0}$) and the resolution $\sigma_{\mathrm{c}}^{10.37}$ ($\sigma_{\mathrm{fid}}^{10.37}$) of the most prominent K-shell peak from the decay of ^{68}Ge. As this peak has the highest intensity, its widths in E_{c} and E_{fid} are used as free fit parameters for calibrating the energy dependence of the resolutions. The PDFs for tritium β's and Compton γ's are constructed from the event densities described in Eq. 4.29, using the β-spectrum introduced in Sec. 2.4.4 and a flat recoil energy spectrum, respectively. As the energy scale for all detector channels is calibrated with bulk electron recoils, the calculation of E_{c} and E_{fid} from the recoil energy E_{r} as described in Eq. 4.20 simplifies to $E_{\mathrm{c}} = E_{\mathrm{fid}} = E_{\mathrm{r}}$ for these events. However, it is necessary to multiply both observables with an additional factor each, to correct for small uncertainties in the calibration of this energy scale. As described in Sec. 2.3.1, the energy calibration is performed using the 356 keV peak from a ^{133}Ba γ-source. Uncertainties in the calibration lead to a shift for both cosmogenic peaks and continuous components by approximately 1%−3%. In the construction of all PDFs belonging to the bulk ER-background, including the L-shell peaks which are not part of the ER-sideband fit, the nominal energy is therefore corrected to adjust to the data:

$$\begin{aligned} E_{\mathrm{c}} &= f^{\star}\left(E_{\mathrm{r}}\right) = c_{\mathrm{heat}} \cdot E_{\mathrm{r}} \\ E_{\mathrm{fid}} &= g^{\star}\left(E_{\mathrm{r}}\right) = c_{\mathrm{ion}} \cdot E_{\mathrm{r}} \end{aligned} \tag{4.42}$$

With the 10 PDF components and the 4 additional calibration parameters, the likelihood function used for the fit of the ER-sideband has a total of 14 fit parameters and is defined as follows:

$$\mathcal{L}^{\mathrm{ER}}\left(\vec{\mu}, c_{\mathrm{heat}}, c_{\mathrm{ion}}, \sigma_{\mathrm{c}}^{10.37}, \sigma_{\mathrm{fid}}^{10.37}\right) = \mathrm{Pois}(N_{\mathrm{ER}} \mid \mu_{\mathrm{fit}}) \prod_{\mathrm{n}=0}^{N_{\mathrm{ER}}} \sum_{\mathrm{i}=1}^{10} \frac{\mu_{\mathrm{i}}}{\mu_{\mathrm{fit}}} \mathcal{P}_{\mathrm{i}}(E_{\mathrm{c}}^{\mathrm{n}}, E_{\mathrm{fid}}^{\mathrm{n}}) \tag{4.43}$$

where i stands for each PDF components and N_{ER} is the total number of events in the sideband. The fit for detector FID827, which has a considerable ER-background, is shown in Fig. 4.17. For this detector, the fitted energy correction factors are $c_{\mathrm{heat}} = 0.981 \pm 0.001$ and $c_{\mathrm{ion}} = 1.013 \pm 0.001$. All fit values of the sideband fit are given in the appendix in the form of three tables: the fitted energy correction factors in E_{c} and E_{fid} of all detectors can be found in Tab. C.3. The baseline noise resolutions and the fitted width of the ^{68}Ge K-shell peak in the two observables together with the increase (in percent) are given in Tab. C.4. Last, the fitted rates $\vec{\mu}$ of the different components can be found in Tab. C.5. All fitted rates of the K-shell peaks are directly used as constraints for the fit to WIMP

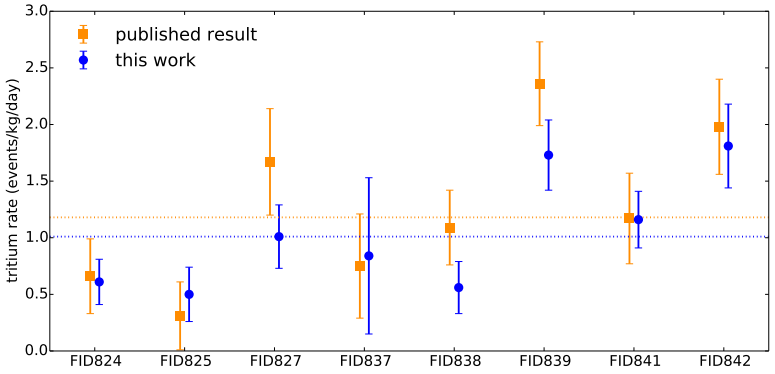

Figure 4.18.: Extrapolated rate of fitted tritium decay β's in the bulk volume of the detectors, normalized to the fiducial exposure. For three of the detectors some deviation between the normalized rate in [100] and the extrapolated rate from the sideband fit of this analysis exists. The average rates are indicated with horizontal dashed lines. See text for details.

search data, while the expected rate of Compton γ's and tritium β's in the RoI has to be calculated from the fitted rate in the sideband.

Of particular interest for the EDELWEISS experiment is the rate of β's from tritium decay, as the fit performed in the framework of this thesis confirms the findings on this background [100] introduced in Sec. 2.4.4. With its application of an unbinned maximum likelihood method in the two energy observables E_c and E_{fid} on a selection of data with different quality cuts, it can be regarded as a completely independent approach compared to the analysis presented there. For cross-checks of the intensity of this background with those found in [100], the rate of tritium β-events fitted in this analysis was extrapolated to the whole energy range of the decay spectrum and normalized to the effective fiducial mass m_{fid} given in Tab. 4.2. A comparison of the resulting rates is shown in Fig. 4.18. Except for three detectors, the extrapolated rates after normalization to the respective fiducial volumes are in very good agreement within errors. For detectors FID827, FID838 and FID839, a discrepancy of $\approx 2\,\sigma$ is observed between the two analyses. However, a third independent analysis performed within the EDELWEISS collaboration gives tritium rates for these 3 detectors which are exactly in between the two presented values. Predominantly for this reason, no further investigation on this matter was conducted. The average, extrapolated rate of β-events from the decay of tritium over the 8 fitted detectors is

$$\langle \Gamma_{\text{tritium}} \rangle = 1.01 \pm 0.13\,\text{events/kg/day} \tag{4.44}$$

Within statistical and systematic uncertainties, e.g. in the implementation of the χ^2-cut efficiency of $\mathcal{O}(10)\%$, this value is in agreement with the average, extrapolated rate of $\langle \Gamma_{\text{tritium}} \rangle = 1.18 \pm 0.13\,\text{events/kg/day}$ found for the 8 detectors in [100] with a fit in a slightly different energy range. Both values are however below the average rate which is given in Eq. 2.19 but was derived with a different selection of detectors.
Relevant in terms of fitting the selected WIMP search data is the sum of both continuous components from Compton γ's and tritium decay β's. The BDT analysis presented in Sec. 3.3 therefore employs only a single flat ER-background which (below $E_{fid} < 8\,\text{keV}_{ee}$) includes both components together.

The ER background in the RoI of this analysis is directly based on the previously described sideband fit. All PDFs used in the sideband fit are also part of the background model used for the WIMP search. Additional PDFs are constructed for the 3 L-shell peaks in the RoI,

with expected event rates calculated from the rates of the fitted K-shell partners. Taken into account is the L/K-shell ratio of 11%, the trigger efficiency $\epsilon_{\text{trigger}}$ and the analysis threshold $E_{\text{c}}^{\text{min}}$. The expected rates of the 8 K-shell peaks in the RoI are equal to the fitted rates in the ER-sideband fit. For the two continuous components from tritium β's and Compton γ's, the expected rates in the RoI are extrapolated from the sideband fit. The errors of all fitted rates are propagated to the RoI and used as systematic errors for the Gaussian constraint terms. Overall, the bulk electron recoil background in the RoI consists of 13 components, of which 11 are the different cosmogenic K- and L-shell peaks and 2 are continuous components.

4.3.4. Neutrons

Nuclear recoils from neutrons are a background which is most similar to a WIMP signal. Their interaction in the crystal produces the same ionization yield Q_{NR} which is expected from WIMP-nucleon scattering and an exponentially falling recoil energy spectrum similar to that calculated for higher WIMP masses m_χ. As introduced in Sec. 2.4.1, there are two different sources for neutrons in the experiment: muon-induced and radiogenic. Neutrons induced by cosmogenic muons have been studied in [61] and dedicated simulations have been performed before the unblinding of Run308 data, to determine their expected impact on the low mass WIMP search. These simulations used a detailed model of the EDELWEISS-III setup and the installed detectors, including the average response function in terms of baseline noise and trigger efficiency for the eight detectors of this analysis. The goal of the study was to determine whether the vetoing of muon-induced neutrons, which would reduce the effective livetime of the data taking[3], was necessary. The resulting rate of WIMP-like events was calculated for the detector dependent analysis thresholds of $E_{\text{c}}^{\text{min}} = 1\,\text{keV}_{\text{ee}}$ and $E_{\text{c}}^{\text{min}} = 1.5\,\text{keV}_{\text{ee}}$ and the RoI used in the BDT analysis. The rate of WIMP-like events before vetoing which is expected for an exposure based on the fiducial volumes which were used in the BDT analysis, was determined as

$$N_{\text{simu}}^{\text{WIMP-like}} = 0.45 \pm 0.03\,(\text{stat})\,^{+0.14}_{-0.09}\,(\text{sys})\ \text{events} \tag{4.45}$$

As this measurement was determined for a 99% C.L. nuclear recoil band it is an upper limit. With a conservative lower limit of the muon-veto efficiency of 93%, the remaining background of muon-induced neutrons in the RoI was calculated to be

$$N_{\text{simu}}^{\text{WIMP-like;after } \mu\text{-veto}} < 0.04 \text{ events at } 90\% \text{ C.L.} \tag{4.46}$$

A subsequent analysis after the unblinding showed that none of the events in the RoI of the BDT was in coincidence with the EDELWEISS muon-veto. The relevant differences between likelihood analysis and BDT analysis in terms of muon-induced neutrons are the choice of the RoI and the fiducial cut. Considering that the latter has an even higher rejection and the differences in terms of RoI are only small, muon-induced neutrons are not considered a relevant background for this analysis.

A background that cannot be neglected are radiogenic neutrons. As was shown in Sec. 3.2.2, EDELWEISS has a clear excess of radiogenic neutrons which is a limiting factor in the search for standard mass WIMPs. The exact origin of this excess is unknown. Simulations performed within the EDELWEISS collaboration indicated that it could originate from the Cu-Be sockets at the 10 mK stage of the cryostat. The recoil energy spectra of all known contributions in the experiment, as derived from GEANT4 Monte Carlo simulations, are shown in Fig. 4.19. For this simulation, no resolution effects or fiducial cuts were considered.

[3] due to additional dead-time related to the muon-veto system

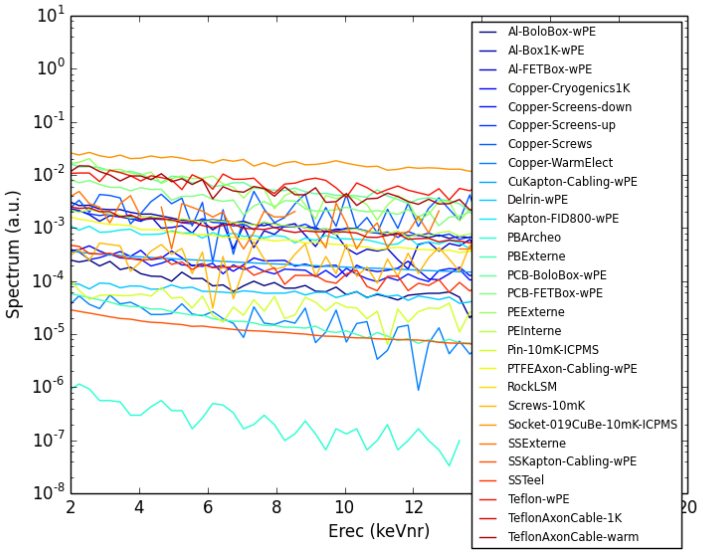

Figure 4.19.: Recoil energy spectra of neutrons from different sources as simulated with GEANT4 for the EDELWEISS-III detectors. The dominant contribution results from CuBe sockets at the 10 mK stage of the cryostat. Figure from [137].

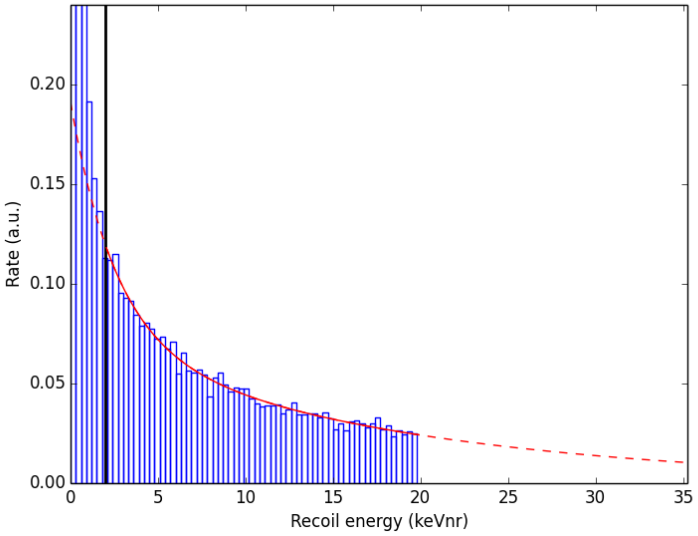

Figure 4.20.: Summed recoil energy spectrum of all simulated neutron sources in the experiment. A double exponential function (see Eq. 4.47) is fitted in the energy range $E_\mathrm{r} \in [2, 20]\,\mathrm{keV_{nr}}$ and extrapolated to both higher and lower energies. Below $E_\mathrm{r} = 2\,\mathrm{keV_{nr}}$ (solid black line) threshold effects render the simulated spectrum unreliable. Figure from [137].

The shape of the stacked spectrum combining all sources proved to be stable with respect to variations of the contributions from individual sources and is shown in Fig. 4.20. In the context of [1] it was fitted in the energy range $2 < E_\mathrm{r} < 20\,\mathrm{keV_{nr}}$ with a double exponential function:

$$\rho_\mathrm{neutron}^\mathrm{unnormalized}\left(E_\mathrm{r}\right) = 0.118 \cdot e^{-E_\mathrm{r}/2.56} + 0.073 \cdot e^{-E_\mathrm{r}/18.02} \tag{4.47}$$

Below $2\,\mathrm{keV_{nr}}$ the simulation is not reliable due to threshold effects and the spectrum was therefore extrapolated according to Eq. 4.47. This analytic parametrization was used to model the neutron background for all detectors of this analysis. The overall normalization of the spectrum was derived from Run308 WIMP search data data, with a different data selection described in Sec. 3.2 and taken with 17 detectors for a total exposure of $1309\,\mathrm{kg{\cdot}days}$. Of the nuclear recoil events observed in the energy range $E_\mathrm{r} \in [10, 100]\,\mathrm{keV_{nr}}$, 9 events were classified as multiple scattering events in different detectors, without coincident signal in the muon veto system. From the simulations described initially, the single-over-multiple-ratio is known to 0.45 ± 0.15. With these values, the energy spectrum $\rho\left(E_\mathrm{r}\right)$ for each detector j can be calculated, considering the exposure M_j given in Tab. 4.3:

$$\rho_\mathrm{neutron;j}\left(E_\mathrm{r}\right) = 0.45 \times 9 \times \frac{M_\mathrm{j}}{1309\,\mathrm{kg{\cdot}days}} \times \rho_\mathrm{neutron}^\mathrm{unnormalized}\left(E_\mathrm{r}\right) \tag{4.48}$$

Each spectrum is then used to construct the event-density (and PDF) for neutrons following Eq. 4.29. The large systematic error $\sigma_\mathrm{sys} = 30\%$ of the single over multiple ratio and the statistical error on the measured multiple events of $\sigma_\mathrm{stat} = \sqrt{9}$ are combined to a total error of 45% on the rate of neutrons. The number of expected neutrons in the RoI is calculated from the integrated event density for each detector and used in the constraint term. Due to the similar exposure, the differences in expected rate are only small, and on average $\langle n_\mathrm{neutron} \rangle = 0.20 \pm 0.07$ radiogenic neutrons are expected for each detector in the selected data.

4.3.5. Unrejected surface events

The background of events which deposit energy on the detector surface via scattering mainly arises from particles with low penetration depth, such as ^{206}Pb-recoils and β's. They are part of the radioactive decay chain of ^{238}U and its ^{222}Rn daughter isotopes which are implanted in the materials surrounding the detectors (see Sec. 2.4.5). The application of the strict fiducial cut introduced in Sec. 4.1.4 allows to efficiently reject all surface events with high energies, as they induce a clear signal E_veto on one of the two veto electrodes. This rejection however can fail for low energy events: if the ionization energy deposited by a particle on one of the detector sides is low enough so that $E_\mathrm{veto} < 1.645\,\sigma_\mathrm{veto}$, the event passes the fiducial cut and is not rejected. Since the fraction of ionization energy depends on the ionization yield Q, event types with a small Q-value remain unrejected up to higher energies than events with a higher ionization yield. As was shown in Fig. 4.11, the efficiency ϵ_fid as a function of initial recoil energy E_r for surface events to pass the fiducial cut is highest for ^{206}Pb-recoils and much smaller for β's and γ's. In principle, all particles can interact within the surface volume of the detector. However, for both neutrons and a possible WIMP signal, the expected rates in the surface volume of a detector after the application of the fiducial cut have been calculated and can be considered negligible. For the continuous electron recoil component in the surface volume from Compton γ's and tritium decay β's, a similar argument is valid: the combination of a small survival probability of the fiducial cut due to their high ionization yield Q_ER and the analysis threshold $E_\mathrm{c}^\mathrm{min}$ above which events are considered effectively removes this background from the analysis.

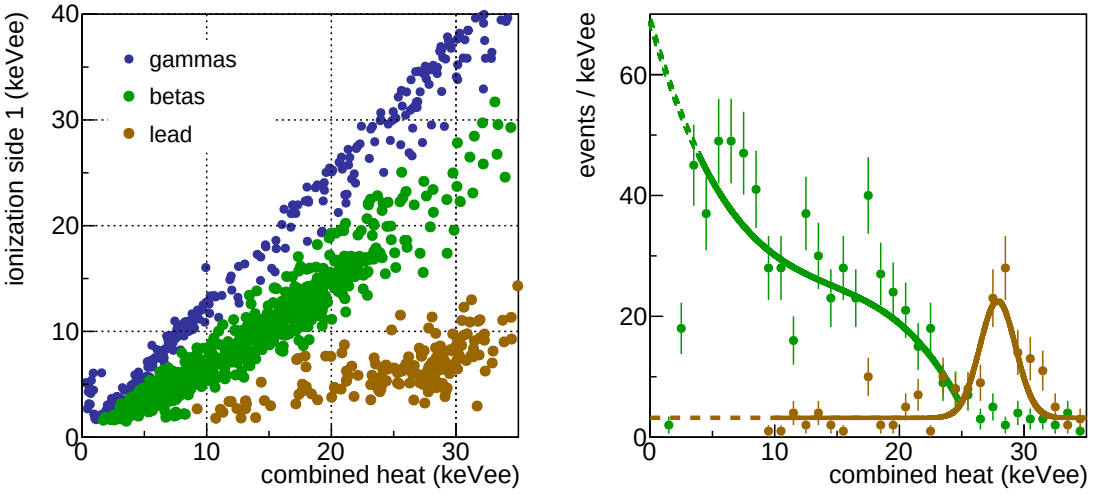

Figure 4.21.: *Left*: Selection of surface events with $E_{\mathrm{veto}} > 5\,\sigma_{\mathrm{veto}}$ for side 1 of detector FID824. Different event types have been separated based on their ionization yield Q: γ's (dark blue), β's (green) and ^{206}Pb-recoils (brown). *Right*: Heat energy spectra for β (^{206}Pb-recoil) events with fitted spectrum down to $4\,\mathrm{keV_{ee}}$ ($10\,\mathrm{keV_{ee}}$). Below this energy the spectrum is extrapolated because the efficiency of the selection criterion reduces significantly the measured rate.

Calculations of the expected number of events in the RoI for a rate determined from a fit to sideband data gave values below 10^{-2} events for all detectors. X-rays from cosmogenic events in the surface volume also have a negligible rate: all K-shell peaks have energies $E_{\mathrm{r}} > 5\,\mathrm{keV_{ee}}$ and therefore large signals E_{veto} which can be fully rejected. For L-shell X-rays originating in the surface volume, the measured heat energy for a $E_{\mathrm{r}} = 1.3\,\mathrm{keV}$ recoil from ^{68}Ge is shifted down to

$$E_{\mathrm{c}} = 1.3 \cdot \frac{1 + 1.0 \cdot {}^{5.5}/_{3}}{1 + {}^{8}/_{3}} = 1.0\,\mathrm{keV_{ee}} \tag{4.49}$$

according to Eq. 4.20. This is below the analysis threshold $E_{\mathrm{c}}^{\mathrm{min}}$ for all detectors except FID824. Considering the small fraction of surface X-ray events with respect to the bulk X-rays from L-shell EC reactions, this background can be neglected as well. Tests of a fit of the WIMP search data with the negligible additional surface background showed no difference in terms of fitted rates for all other components. For this reason, the only background components arising from unrejected surface events considered in this analysis are ^{206}Pb-recoils and β-particles.

For both these particle types, sideband data is used to determine the ionization yield Q and extract the heat energy spectrum $\rho\,(E_{\mathrm{c}})$, for every detector and each surface (top and bottom), which are needed to construct the corresponding PDF. This sideband data consists of events with a clear signal of $E > 5\sigma$ of the baseline noise on both veto and fiducial electrode of a detector side and the absence of such a signal on the two electrodes of the opposite side. An example of the data selected with this cut for the top side of detector FID824 is shown in Fig. 4.21. With a cut on the ionization yield Q, the three distinct event categories of surface β's, ^{206}Pb-recoils and γ's can be separated. The latter ones, although labelled *"gammas"* in the plot, not only include γ's from Compton scattering and cosmogenic decays but also the β's from the decay of tritium near the surface. As was described in Sec. 2.4.5, the (standard) fiducial cut selects events in an inner volume of ≈75%. Applying the opposite cut consequently includes events in the remaining 25% volume below the surface layer.

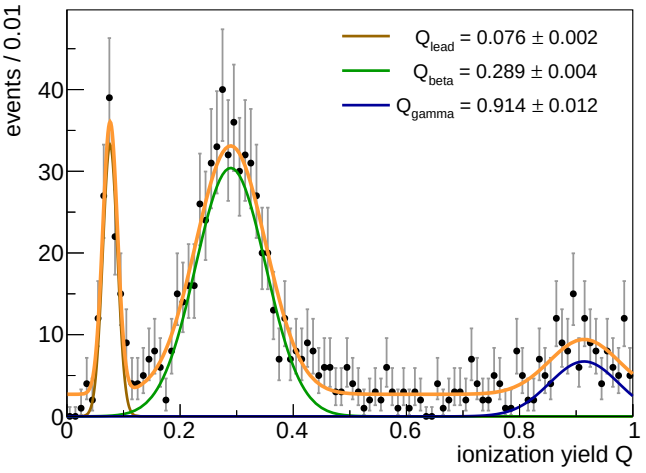

Figure 4.22.: Distribution of the calculated ionization yield value for a selection of clear surface events with $0 < E_c < 40\,\mathrm{keV_{ee}}$ from side 1 of detector FID824. An unbinned likelihood fit of the data gives the average ionization yield Q_i for three different event populations from ^{206}Pb-recoils, β's and γ's which is used to model the PDF for these backgrounds.

In the context of [1], the heat energy spectra $\rho(E_c)$ for ^{206}Pb-recoils and β's were described with different parametrizations: for β's, a spline function was used to model the events in the energy range $4 < E_c < 24\,\mathrm{keV_{ee}}$ (Fig. 4.21 right). Below $4\,\mathrm{keV_{ee}}$ the spectrum is linearly extrapolated down to $0\,\mathrm{keV_{ee}}$ not to include the selection criterion of the sideband which leads to a reduced efficiency and a resulting decrease of the rate. The motivation for this ad-hoc modelling comes from simulations, which show that the β-spectrum rises down to low energies. As the exact location and density of the contamination with the radioactive sources of these β's is not known, it is not possible to simulate the implantation depth and therefore the exact shape of the β-spectra in the detectors reliably. Detailed tests performed in the framework of this thesis to fit a combination of the two β-spectra of known endpoint energies which are expected from the decay chain given in Sec. 2.4.5 have shown no conclusive results and could thus not be used. However, due to the fiducial cut efficiency ϵ_{fid} imposed on this spectrum, the exact shape is expected to play a minor role compared to the expected rate of events which is used in the likelihood constraint. To account for a possible inaccuracy in the spectral shape, a large systematic error is assumed for this background component. This systematic error is $\mathcal{O}(40\%)$ for most detectors and is calculated from the difference of the integrated event density of the nominal spectrum compared to one with a flat extrapolation below $E_c = 4\,\mathrm{keV_{ee}}$.
For ^{206}Pb-recoils the extraction of the spectrum $\rho(E_c)$ is considerably simpler. In the energy range $10 < E_c < 35\,\mathrm{keV_{ee}}$ a constant component plus a Gaussian peak were fitted to the heat energy spectrum of sideband data (Fig. 4.21 right). The initial recoil energy of the ^{206}Pb-nucleus is $E_r = 103\,\mathrm{keV}$, but the observed heat energy depends on the exact ionization yield and therefore varies between different detectors surfaces. For an average ionization yield of $\langle Q_{\mathrm{lead}} \rangle = 0.1$, the observed heat energy calculated with Eq. 4.20 is

$$E_c = 103 \cdot \frac{1 + 0.1 \cdot {}^{5.5}/_{3}}{1 + {}^{8}/_{3}} = 33.2\,\mathrm{keV_{ee}} \tag{4.50}$$

This value is above the fitted energy of the ^{206}Pb-peak found for detector FID824 in Fig. 4.21, indicating a smaller measured ionization yield $\langle Q_{\mathrm{lead}} \rangle(\mathrm{FID824}) < 0.1$. A fit with a free linear

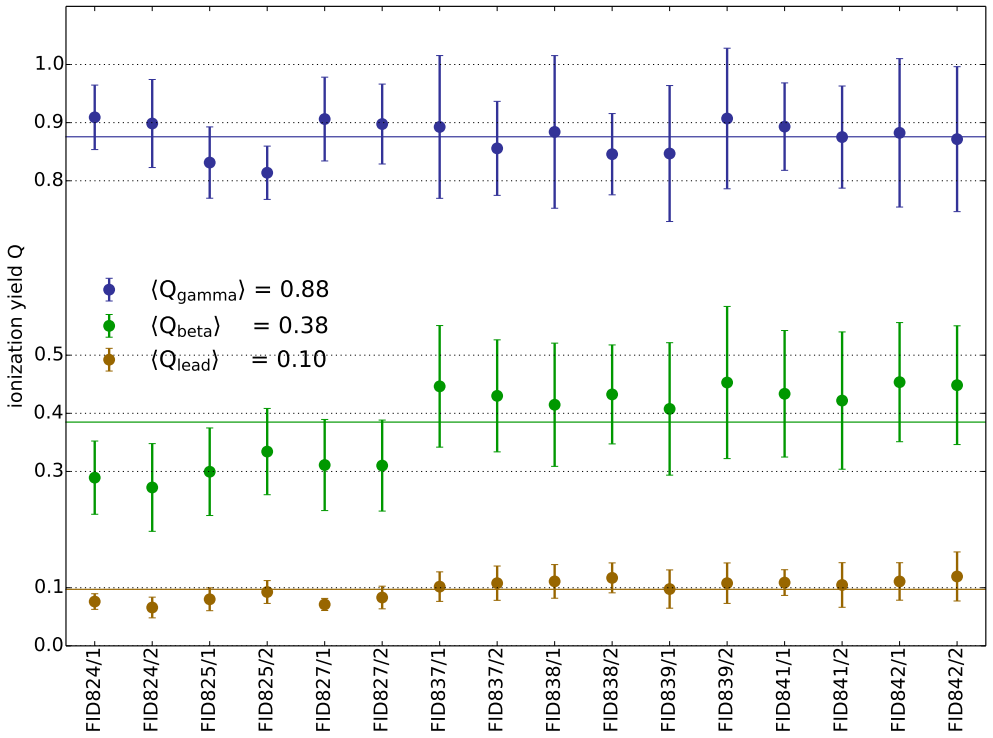

Figure 4.23.: Overview of the fitted ionization yield for the three surface event populations of ^{206}Pb-recoils (red), β (green) and γ events (blue), for both sides of each detector. Vertical error bars indicate the $\pm 1\,\sigma$ width of the fitted Gaussian, which is a sum of both resolution effects and an intrinsic uncertainty of the ionization yield. Detectors FID82x show a significantly smaller ionization yield for ^{206}Pb-recoils and β-events which is possibly related to a different surface treatment of this detector group.

instead of a constant component gave no indication of a rise of the energy spectrum towards low energies. For this reason the constant component is extrapolated down to $0\,\mathrm{keV_{ee}}$ with a considered systematic uncertainty of the fit of 10%. Integrating the extrapolated spectra of both lead- and beta-backgrounds in the energy range $0 < E_c < 40\,\mathrm{keV_{ee}}$ shows that the ratio N_β/N_{Pb} is not 1 as expected from the decay chain but rather 2−3. This deviation is not explicable with systematic uncertainties and is considered a property of the radioactive contamination, e.g. due to the implantation depth.

The ionization yield Q of beta and lead components is determined for each detector surface from the corresponding sideband data. For this, the distribution in Q of all sideband events is fitted with a maximum likelihood function as is shown in Fig. 4.22 for the top side of detector FID824. Fit components are three Gaussian PDFs, one for each of the components lead, betas and gammas, as well as an underlying constant to account for outliers between them. The position and width of each peak as well as the rate of events were free fit parameters within reasonable ranges. An overview of the fitted ionization yield values and the $1\,\sigma$ width of the fitted peak is shown for all detector sides in Fig. 4.23. Ionization yield values for surface gammas are included in the overview for comparison, although this background component is not considered in the WIMP search. Several observations can be made:

- The average fitted ionization yield for gammas is $\langle Q_{\mathrm{gammas}} \rangle = 0.88$ and therefore much smaller than the expected value of $Q = 1.0$. This is a consequence of charge trapping for bulk events as described in [119], which changes the effective fiducial

voltage used for calibration and therefore reduces the calculated Q-values for surface events.

- A clear systematic difference in the fitted ionization yield Q for betas is seen between different detectors. For detectors from the FID82x-series, the average ionization yield for either side is $\langle Q_{\text{betas}} \rangle = 0.30$, while for all other detectors, from the series FID83x and FID84x, this value is $\langle Q_{\text{gammas}} \rangle = 0.43$. This effect is most likely related to a different surface treatment which was applied for different batches of detectors.
- The width of the fitted peak in Q is different for all three components. In fact, this width is a superposition of an intrinsic uncertainty of the ionization yield and the uncertainty on the measured energies E_{c} and E_{fid} which are used to calculate Q. As the latter are the dominating factor and included in the modelling of the PDFs, the fitted ionization yield values are considered as energy independent in this analysis.

With the extracted heat energy spectra $\rho\,(E_{\text{c}})$ and fitted ionization yields Q for each side, the PDFs for lead and beta backgrounds can be calculated for each detector following Eq. 4.31.

4.3.6. Overview of component PDFs and expected rates

For each of the signal and background components described in this section, the energy spectrum in either recoil or heat energy was used to construct the corresponding signal density and consequently the normalized PDF (Eq. 4.33). Not all of these PDFs are directly relevant for fitting a WIMP signal. The PDFs for the 8 K-shell peaks for example are quite distinct from a possible signal of any WIMP mass m_χ. However, they are still needed to describe properly the ER-band of the data with its fit of the Compton γ and tritium decay β component, both of which also extend down to low energies near the threshold $E_{\text{c}}^{\text{min}}$ where they have some overlap with a WIMP signal. To visualize, which part of the data is described best by which background component, a selection of the most relevant PDFs for detector FID824 is shown in Fig. 4.24. Several observations can be made with regard to the expected fit results:

- For unrejected surface events such as β's and ^{206}Pb-recoils the PDFs describing the different detector sides show only few differences although they are constructed individually with three independent parameters each: the (extrapolated) energy spectrum from sideband data $\rho\,(E_{\text{c}})$, the fitted ionization yield Q and the average baseline resolution of the corresponding veto electrode σ_{veto}.
- The two PDFs for the (flat) Compton γ's and the β-spectrum from tritium decay show very little difference near the analysis threshold $E_{\text{c}}^{\text{min}}$. Consequently a degeneracy between the two rates can be observed during fitting.
- The three L-shell peaks from cosmogenic γ's are separated by only $\approx 0.1\,\text{keV}$, which is smaller than the resolution in each of the two energy observables. A separation is only possible due to the constrained expected rates.

By normalizing over the event density, the expected number of events $n_{\text{i}}^{\text{exp}}$ in the RoI can be calculated for each background component. It is used to constrain the fitted rate μ_{i} of the component. The uncertainty $\sigma_{\text{i}}^{\text{exp}}$ of this constraint is propagated from the uncertainty of the input spectrum and combines both statistical and systematic uncertainties. For the cosmogenic K-shell peaks the expected number of events and the uncertainty is taken directly from the sideband fit without any modifications (see Tab. C.5). An overview over the expected rates in the RoI for all other components, and therefore the input values for the constraint terms of the likelihood function in Eq. 4.37 for all backgrounds is also given

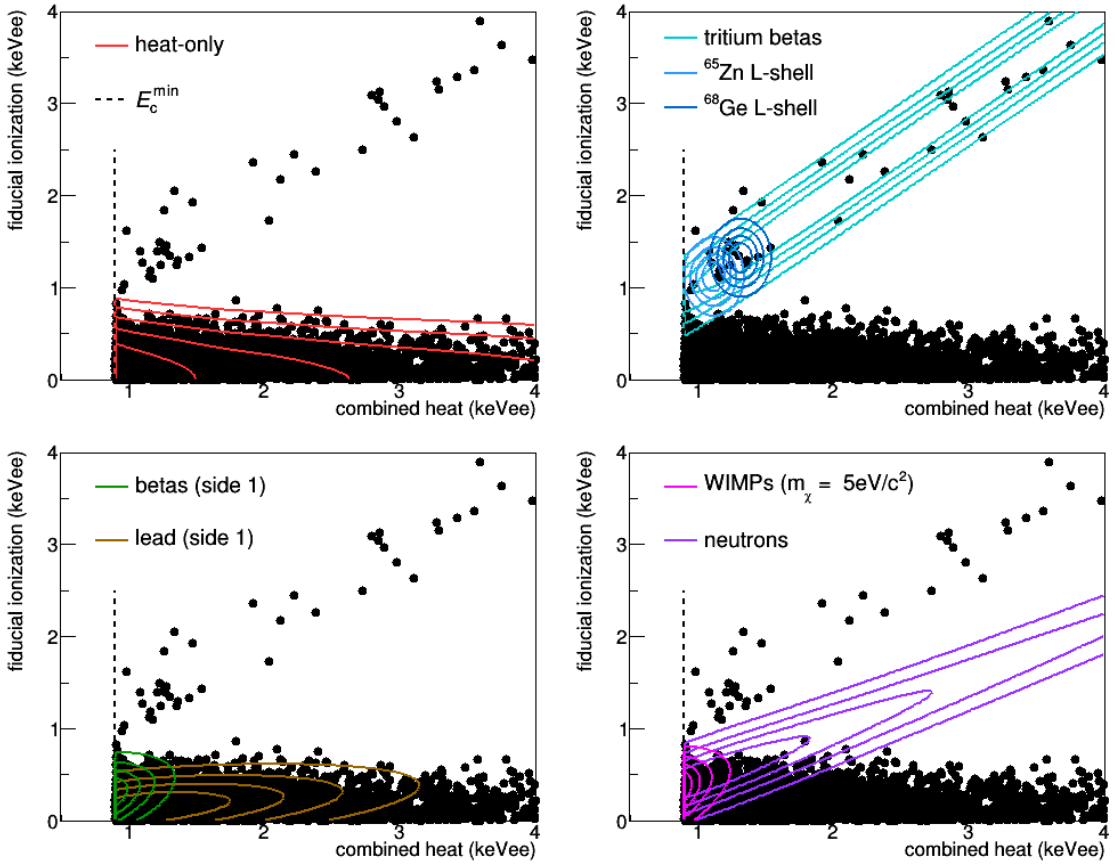

Figure 4.24.: Zoom at the low energy region of the RoI ($0 < E_c, E_{fid} < 4\,\mathrm{keV_{ee}}$) for WIMP search data from detector FID824 after all cuts (same data shown in all subplots). Coloured contour lines indicate the PDFs for different background components which are relevant for WIMP search. *Top Left*: PDF for heat-only events, plotted as equidistant contours on a log-scale to account for the steep spectrum. *Top Right*: PDFs for bulk electron recoil components. Not shown is the PDF for Compton gammas which is superimposable with the tritium beta PDF, as well as the PDF for ^{68}Ga in between the two plotted L-shell peaks. *Bottom Left*: PDFs for unrejected surface events are only shown for side 1 here. *Bottom Right*: PDFs for nuclear recoils from neutrons and from a $m_\chi = 5\,\mathrm{GeV}/c^2$ WIMP signal.

Table 4.5.: Condensed overview of different categories of background components. All three L-shell peaks, the continuous ER components and unrejected surface events of both sides are summarized with a propagated error. The full overview of all individual background components is given in the appendix in Tab. C.6 and Tab. C.5 (for the K-shell peaks).

Detector	$n_{\mathrm{heat-only}}$	n_{neutron}	$n_{\mathrm{contin.}}$	$n_{\mathrm{L-shell}}$	n_{beta}	n_{lead}
FID824	5386 ± 804	0.19 ± 0.09	84 ± 15	13.1 ± 1.5	8.5 ± 2.4	6.2 ± 0.8
FID825	5159 ± 518	0.22 ± 0.10	111 ± 21	15.0 ± 1.6	2.4 ± 0.9	4.3 ± 0.5
FID827	9155 ± 757	0.22 ± 0.10	160 ± 24	54.4 ± 4.7	7.3 ± 2.5	5.4 ± 0.7
FID837	4399 ± 311	0.20 ± 0.09	150 ± 57	26.4 ± 2.5	1.7 ± 0.2	4.2 ± 0.6
FID838	7285 ± 94	0.21 ± 0.09	103 ± 20	56.0 ± 5.2	0.4 ± 0.2	3.6 ± 0.4
FID839	6416 ± 448	0.19 ± 0.09	185 ± 25	12.7 ± 1.2	0.15 ± 0.02	4.8 ± 0.5
FID841	3578 ± 204	0.23 ± 0.10	166 ± 23	22.4 ± 2.2	0.5 ± 0.2	4.9 ± 0.5
FID842	2744 ± 53	0.15 ± 0.07	158 ± 23	4.4 ± 0.5	0.06 ± 0.01	2.1 ± 0.3

in Tab. C.6). For the most relevant PDF components at low energies a more condensed overview is given in Tab. 4.5. Here, backgrounds of similar origin, such as unrejected β's for both detector sides, have been added up.

4.4. Extraction of exclusion limits

4.4.1. Fit to individual detectors

After the description of the signal and all different background PDFs in the previous section, the likelihood model for each detector can be constructed following Eq. 4.41. The Poisson-term in this model, which renders it an extended likelihood, limits the total fitted rate for all component to the observed number of events N in the RoI. This number N ranges from ≈3000 for detector FID842 to ≈10,000 events for detector FID827. The Gaussian constraint terms of the model are defined for every background component of each detector, with a mean corresponding to the number of expected events and a width given by the systematic uncertainty on that value. In total, the constructed likelihood function $\mathcal{L}_{\mathrm{j}}^{\star}$ for each detector has one parameter of interest and 21 constrained nuisance parameters:

- the parameter of interest is the WIMP-nucleon scattering cross section σ_χ which according to Eq. 4.36 is proportional to the fitted rate of signal events μ_χ for a given WIMP mass m_χ
- the parameter a of the ionization yield Q_{NR} for nuclear recoils from WIMPs and neutrons (see Eq. 4.40)
- the event rates μ_{i} for all background components: heat-only events, neutrons, Compton γ's, β's from tritium decay, the 3 cosmogenic L-shell peaks, 9 cosmogenic K-shell peaks and 2 types of unrejected surface events from betas and lead-recoils on each of the two detector sides

Thanks to the `RooFit` package which was used for the construction of all models and the fitting of the likelihood function, the high number of 22 fit parameters does not pose a problem. For each WIMP mass $m_\chi \in [4, 30]\,\mathrm{GeV}/c^2$ and steps of $1\,\mathrm{GeV}/c^2$ the corresponding signal PDF $\rho_\chi\left(m_\chi\right)$ was constructed and the likelihood function $\mathcal{L}_{\mathrm{j}}^{\star}\left(\sigma_\chi, \vec{\mu}_{\mathrm{j}}, a_{\mathrm{j}} \mid m_\chi\right)$ was calculated. The resulting 27 likelihood functions for each of the 8 detectors were then fitted to the corresponding data. These fits could be highly parallelized and were running on the local computer cluster[4]. The time for fitting was of the order of hours and was significantly slowed down by the implementation of the nuisance parameter a for the ionization yield Q_{NR}. A simple explanation is that for each variation of a, the event density for both WIMP signal and neutrons changes and the PDFs thus had to be renormalized. All other PDFs describing background components have a fixed shape and therefore are only normalized once in the beginning. With a few exceptions the minimization of $-\ln\left(\mathcal{L}_{\mathrm{j}}^{\star}\right)$ succeeded without any problems. An example of the best fit for detector FID824 and a potential WIMP signal with $m_\chi = 4\,\mathrm{GeV}/c^2$ is shown in Fig. 4.25. Plotted is the data and the best fit PDF in the parameter space of the two observables as well as the projection of data and the different PDF components in E_{c} and E_{fid} individually. Now signal distribution from WIMPs are shown since the best fit result is $\mu_\chi \approx 0$. It is apparent from these plots that heat-only events are by far the dominating background in terms of magnitude. In the following, the results for the individual detector fits will be discussed in more detail and some observations will be highlighted.

[4]The Kalinka computing cluster at the institute for nuclear physics IKP at KIT.

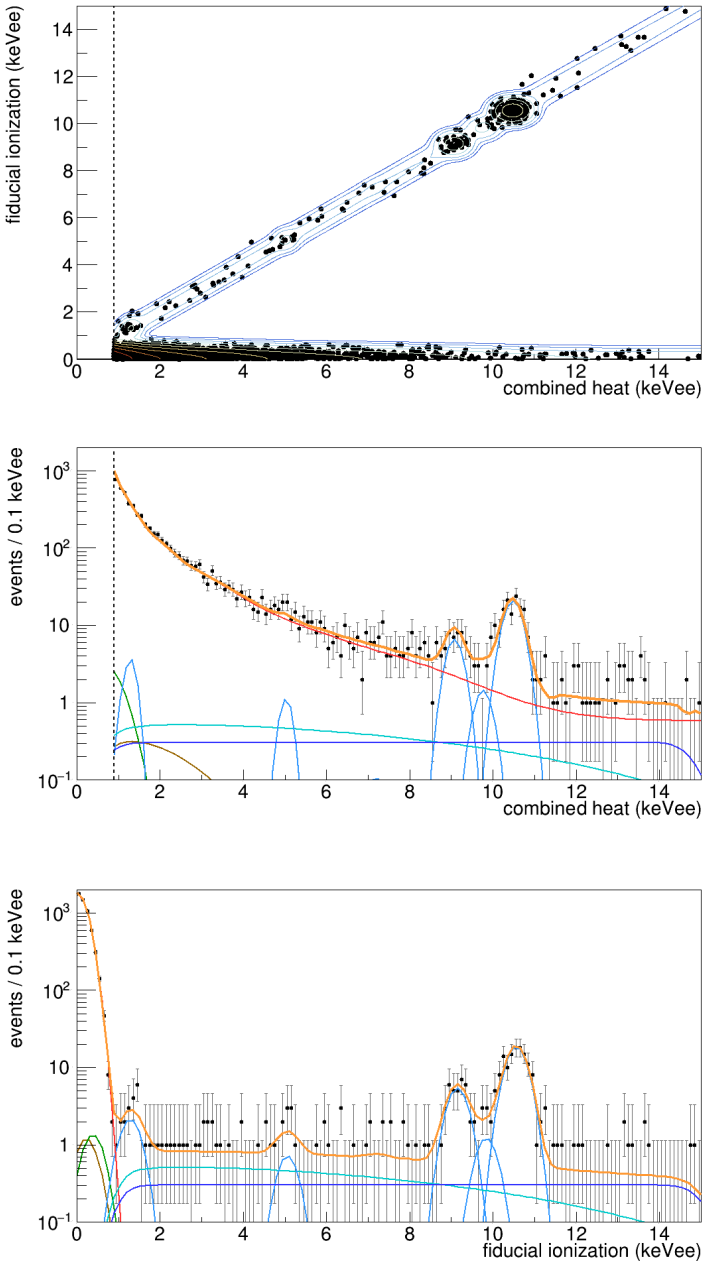

Figure 4.25.: Result for the individual fit of data from detector FID824 with a model including a $m_\chi = 4\,\mathrm{GeV/c^2}$ WIMP signal. *Top*: Data for this detector in the plane of the two energy observables, combined heat E_c and fiducial ionization E_fid. The best fit (extended) PDF is overlayed as coloured contours indicating the event-density. *Middle*: Energy spectrum in combined heat energy for the data with best fit PDF in orange. Individual components of this fit are scaled according to their fitted event rate μ_i: heat-only (red), compton gammas (dark blue), tritium betas (turquoise), cosmogenic K-shell and combined L-shell peaks (light blue), neutrons (violet), unrejected surface betas (green) and lead-recoils (brown) combined for both detector sides. The spectrum is clearly dominated by heat-only events. *Bottom*: Best fit projection in fiducial ionization energy showing a clear separation between heat-only events and ER backgrounds. Note that no WIMP component is visible since the best fit result is achieved for $\mu_\chi \approx 0$.

Significance of the fitted signal component

For all detectors the fitted signal is compatible with zero within $< 2\sigma$ and no statistically significant excess of signal events can be observed for any of the probed WIMP masses m_χ. For a selection of representative WIMP masses, the fitted rate of signal events μ_χ which can be calculated from the best fit cross section σ_χ is given in Tab. 4.6. With a minor exception, the three detectors FID824, FID827, FID839 have no events in the selected data which are compatible with a nuclear recoil component and therefore the fitted signal corresponds to a rate $\mu_\chi \approx 0$ events for all m_χ. It is worth noting again that, a priori, detector FID824 has the highest sensitivity to WIMPs due to its low analysis threshold $E_\mathrm{c}^\mathrm{min}$ and therefore high signal efficiency. Two other detectors, FID841 and FID842, show a strong dependence of the fitted signal with the WIMP mass: for the lowest m_χ the rate of fitted signal events starts with high values $\mathcal{O}(10)$ and continuously decreases when fitting signals for higher masses. Just as the previously listed detectors, these two detectors have no clear outlier events near the expected ionization yield Q_NR for nuclear recoils which could be fitted with a WIMP signal (see also individual dataset plots in Fig. B.1). A potential non-zero signal is thus only possible for small m_χ, for which there is enough overlap between the signal PDF and the high statistics population of heat-only events. For the remaining three detectors the situation is somewhat reversed: FID825, FID837 and FID838 clearly show outlier events with $E_\mathrm{c} > 2\,\mathrm{keV_{ee}}$ which are compatible with nuclear recoils. For these detectors, a zero signal is fitted for the lowest WIMP masses[5] until, with increasing m_χ, the PDF of the signal extends to the candidate events, as was shown in Fig. 4.12. From then on, signal rates of $\hat{\mu}_\chi \approx 2{-}4$ events are fitted for these detectors. A noticeable deviation of the nuisance parameter describing the relevant ionization yield Q_NR from $a = 0.16$ can be observed only for detectors FID837 and FID838. In the case of FID837 it is only a minor increase to $a \approx 0.162$ with minor variations depending on the WIMP mass. For detector FID838 however, the Q_NR is increased more drastically by fitting $a \approx 0.18$. This is caused by a single outlier event at $(E_\mathrm{c}, E_\mathrm{fid}) \approx (14\,\mathrm{keV_{ee}}, 10.5\,\mathrm{keV_{ee}})$ (see Fig. B.1) which is significantly above the expected standard EDELWEISS parametrization for nuclear recoils. It has been found, that the fitted parameter a is limited by the corresponding constraint term and becomes even higher when the constraint is loosened.

Effect of constraints on fitted background rates

Due to the additional constraint terms in the likelihood function $\mathcal{L}_\mathrm{j}^\star$, the different rates μ_i for all background components are fitted within the $\pm 1\,\sigma$ error range of the respective Gaussian constraint PDF. In many cases the fitted rate and its uncertainty correspond directly to the mean and width of the constraint term. In particular, for all detectors the rates for the two backgrounds describing unrejected surface events from β's and ^{206}Pb-recoils are fitted with the expected rate and uncertainty, with only a minor deviation. A possible explanation of this good agreement is, that the PDFs for all unrejected surface events show a large overlap with the heat-only PDF. Due to the much larger number of these heat-only events, it is easily possible to fit a small surface event component of arbitrary amplitude which is only controlled by the constraint term. For all other components, this is not possible, as their overlap with the heat-only event population is much smaller. This means on the other hand, that there is no significant disagreement between the background model and the data, which would require a larger contribution from these backgrounds. The good agreement between fitted and expected (constrained) rate is shown in Fig. 4.26: for detector FID824 and a selection of backgrounds which are most relevant for a fitted WIMP signal of $m_\chi = 4\,\mathrm{GeV}/c^2$, the constraint PDFs are plotted with the best fit rate and its uncertainty superimposed.
As indicated in the description of heat-only events, a small but measurable asymmetry of

[5] except FID838 which has a non-zero signal at $m_\chi = 4\,\mathrm{GeV}/c^2$ only

Table 4.6.: Rate of signal events μ_χ calculated with Eq. 4.36 from the best fit cross section value $\hat{\sigma}_\chi$ for different WIMP masses m_χ.

Detector	$4\,\mathrm{GeV}/c^2$	$5\,\mathrm{GeV}/c^2$	$6\,\mathrm{GeV}/c^2$	$8\,\mathrm{GeV}/c^2$	$10\,\mathrm{GeV}/c^2$	$30\,\mathrm{GeV}/c^2$
FID824	$0.0^{+\ 4.7}_{-\ 0.0}$	$0.0^{+\ 3.5}_{-\ 0.0}$	$0.0^{+2.9}_{-0.0}$	$0.0^{+1.9}_{-0.0}$	$0.0^{+1.4}_{-0.0}$	$0.0^{+0.6}_{-0.0}$
FID825	$0.0^{+\ 3.6}_{-\ 0.0}$	$0.0^{+\ 4.7}_{-\ 0.0}$	$1.9^{+4.9}_{-1.9}$	$4.1^{+4.0}_{-2.7}$	$3.1^{+3.3}_{-2.1}$	$1.2^{+1.8}_{-1.0}$
FID827	$3.9^{+22.6}_{-\ 3.9}$	$0.4^{+16.6}_{-\ 0.4}$	$0.0^{+5.4}_{-0.0}$	$0.0^{+1.7}_{-0.0}$	$0.0^{+1.1}_{-0.0}$	$0.0^{+0.6}_{-0.0}$
FID837	$0.0^{+12.3}_{-\ 0.0}$	$0.0^{+\ 8.2}_{-\ 0.0}$	$0.0^{+5.6}_{-0.0}$	$0.0^{+3.5}_{-0.0}$	$2.9^{+4.3}_{-2.8}$	$2.4^{+2.3}_{-1.4}$
FID838	$26.3^{+26.4}_{-22.9}$	$0.0^{+\ 6.2}_{-\ 0.0}$	$0.5^{+6.0}_{-0.5}$	$2.2^{+3.5}_{-1.8}$	$1.9^{+2.8}_{-1.5}$	$2.2^{+2.2}_{-1.4}$
FID839	$0.0^{+16.7}_{-\ 0.0}$	$0.0^{+\ 5.6}_{-\ 0.0}$	$0.0^{+3.2}_{-0.0}$	$0.0^{+3.5}_{-0.0}$	$0.1^{+3.0}_{-0.1}$	$0.0^{+0.9}_{-0.0}$
FID841	$39.7^{+23.0}_{-19.1}$	$19.2^{+14.7}_{-11.8}$	$10.0^{+9.7}_{-7.2}$	$2.8^{+4.8}_{-2.8}$	$1.2^{+3.2}_{-1.2}$	$0.0^{+0.9}_{-0.0}$
FID842	$6.7^{+17.3}_{-\ 6.7}$	$3.6^{+11.6}_{-\ 3.6}$	$4.8^{+7.1}_{-4.4}$	$2.0^{+3.6}_{-1.9}$	$1.2^{+2.6}_{-1.2}$	$0.0^{+1.1}_{-0.0}$

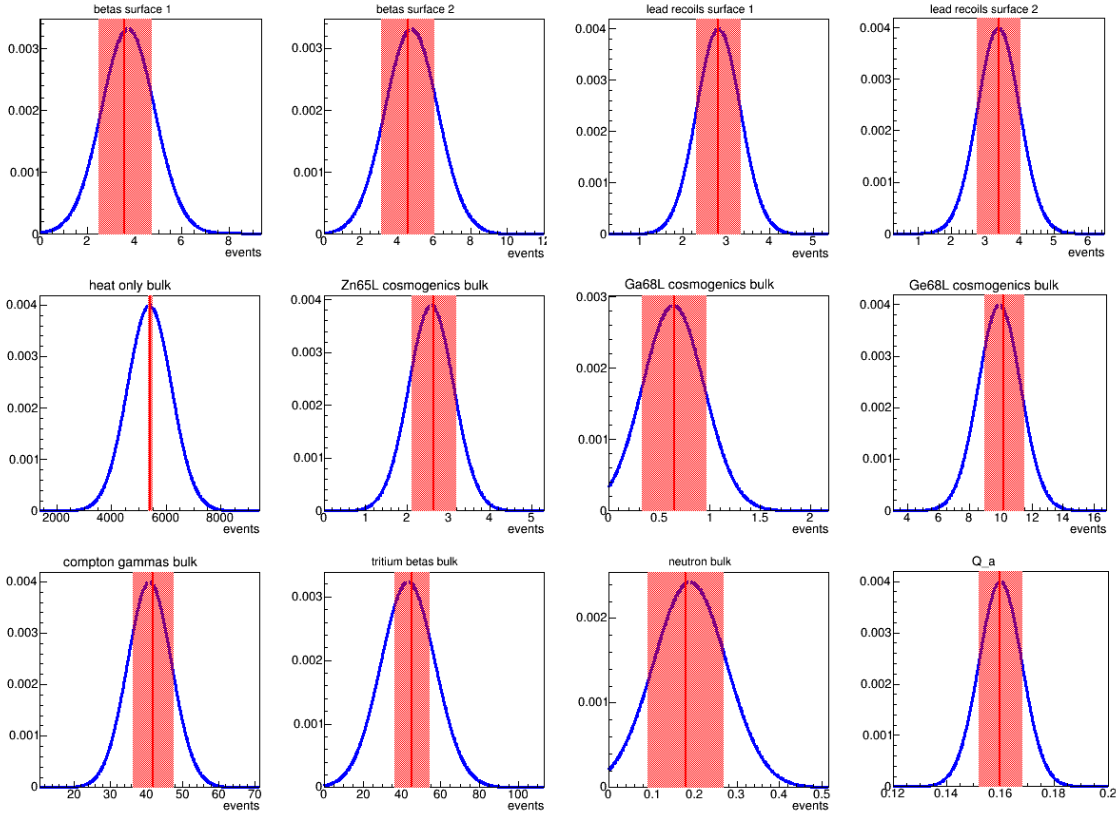

Figure 4.26.: Fit result for a selection of nuisance parameters for detector FID824. Blue curves are the Gaussian shaped PDFs used to constrain the most critical, low energy background components for this detectors. Mean expected values (center of the gaussian PDF) are indicated with black lines. The best fit values for a likelihood fit with a signal component with $m_\chi = 4\,\mathrm{GeV}$ are shown as red lines together with their $\pm 1\sigma$ uncertainty. All fit values are well within the uncertainty of the constraint term, and the best fit errors are mostly dominated by the width of the gaussian PDF, i.e. the uncertainty on the constraint value. An exception is the best fit for $n_{\mathrm{heat-only}}$ which is constrained only loosely due to the large uncertainty on the symmetry of heat only events (see Sec. 4.3.2). The 1σ-error is only 73.3 events and corresponds to the Poisson error of the best fit value.

their sideband distribution with respect to $E_{\mathrm{fid}} = 0$ was fitted for some detectors. Indeed, for 7 out of 8 detectors, the fitted rate $\mu_{\mathrm{heat-only}}$ is larger than the expected value from the number of heat-only sideband events N_{sb}. Only for detector FID842 it is found that $\mu_{\mathrm{heat-only}} < N_{\mathrm{sb}}$, in perfect agreement with the fitted asymmetry listed in Tab. 4.4. While the asymmetry has been considered in all cases as a systematic uncertainty of up to $\approx 15\%$ in the width of the corresponding constraint terms, the error on the fitted rate of heat-only events is only of the order of the Poisson error $\sqrt{\mu_{\mathrm{heat-only}}}$ and thus much smaller for most detectors. The most significant deviation is observed for detector FID825, for which a rate of $\hat{\mu}_{\mathrm{heat-only}} \approx 5495$ events[6] is fitted compared to an expected number of events of only $n^{\mathrm{exp}}_{\mathrm{heat-only}} = 5159 \pm 518$.

Correlations between components

For each fit result, a matrix giving the correlation between all components is provided by `RooFit`. For most detectors and WIMP masses, almost all correlation factors are zero, with the general exception of a strong correlation between the flat Compton γ component and the rate of β's from tritium decay. This is expected, as both components have a similar spectral shape in the RoI and therefore also similar PDFs. Connected to these components is a correlation of the K-shell peaks between 5 and 7.7 $\mathrm{keV_{ee}}$ which strongly depend on the fitted tritium rate. Further, small correlations isolated to a few individual fits can be observed between the L-shell peak events from ^{65}Zn and ^{68}Ge and the signal cross section σ_χ. As indicated in the discussion of the fitted signal rate, there is a strong correlation between the PDF for low WIMP masses of $m_\chi \approx 4{-}10\,\mathrm{GeV}/c^2$ and the heat-only PDF for the detectors FID841 and FID842. Figure 4.27 shows the fitted rate for these two components for detector FID841 together with the correlation factor between their best fit values indicating a degeneracy: as the number of fitted signal events decreases the fitted rate of heat-only events goes up by a similar amount.
A more significant and expected correlation is the one between the signal and neutron events. For detector FID824, FID827, FID839, FID841 and FID842 the fitted rate of neutrons is in good agreement with the expected values although slightly lower. These five detectors have no clear nuclear recoil candidate events at higher energies, and therefore the fitted rate is increased by the additional constraint term for each detector. The other three detectors show a small excess of fitted neutrons, still within the $1\,\sigma$ uncertainty of the constraint term. This excess can be understood when looking at the selected data for these detectors (see Fig. B.1): FID825 has at least one event at $(E_{\mathrm{c}}, E_{\mathrm{fid}}) = (3\,\mathrm{keV_{ee}}, 1.5\,\mathrm{keV_{ee}})$ with an ionization yield compatible to nuclear recoils. The energy of this event is already too high to be fitted with the steep recoil spectrum for a low mass WIMP signal and is thus assigned to the neutron component. For higher WIMP masses hower the event is best fitted to the signal component. FID837 has two events at $(E_{\mathrm{c}}, E_{\mathrm{fid}}) = (4.5\,\mathrm{keV_{ee}}, 2.5\,\mathrm{keV_{ee}})$ and $(E_{\mathrm{c}}, E_{\mathrm{fid}}) = (6\,\mathrm{keV_{ee}}, 3.2\,\mathrm{keV_{ee}})$ which are attributed to a WIMP signal above $m_\chi = 9\,\mathrm{GeV}/c^2$, as can be seen in Fig. 4.28. Again, a strong correlation is observed for these WIMP masses between the signal and the fitted rate of neutrons. However, as the constraint for neutrons is rather strict, the degeneracy is not 1:1. For FID838, which has one outlier event with a fiducial ionization energy significantly above what is expected for nuclear recoils, the correlation is not only between signal and neutron rate but also includes the nuisance parameter a for the nuclear recoil ionization yield Q_{NR}.

[6] as the fitted rate varies within a few events for different m_χ, this value is an average over the range $m_\chi \in [4, 30]\,\mathrm{GeV}/c^2$

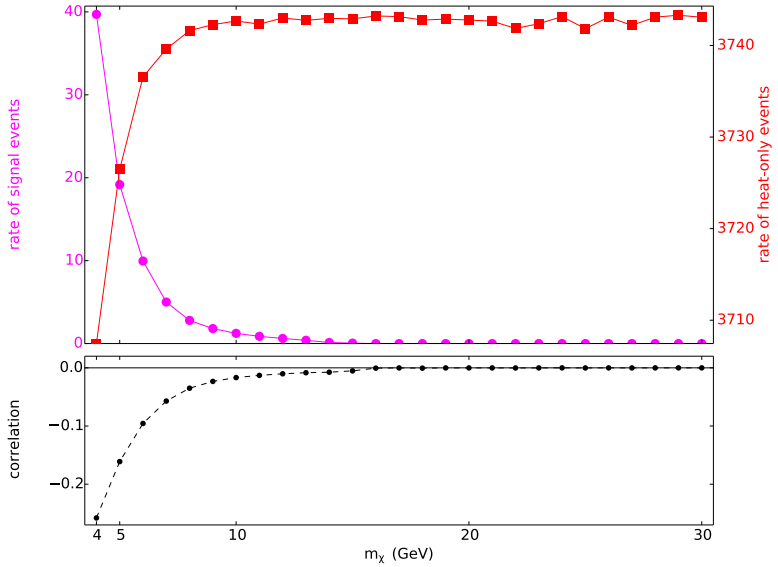

Figure 4.27.: Best fit rate for heat-only events (red) and the WIMP signal (magenta) for detector FID841 as a function of fitted WIMP mass m_χ. Due to the overlap of the signal PDF with the heat-only population for small m_χ, a large signal is fitted for these masses. The constraint for heat-only events for this detector is $n^{\text{exp}}_{\text{heat-only}} = 3578 \pm 204$ events. The correlation between the two best fit rates indicates in which mass range the degeneracy exists (bottom plot).

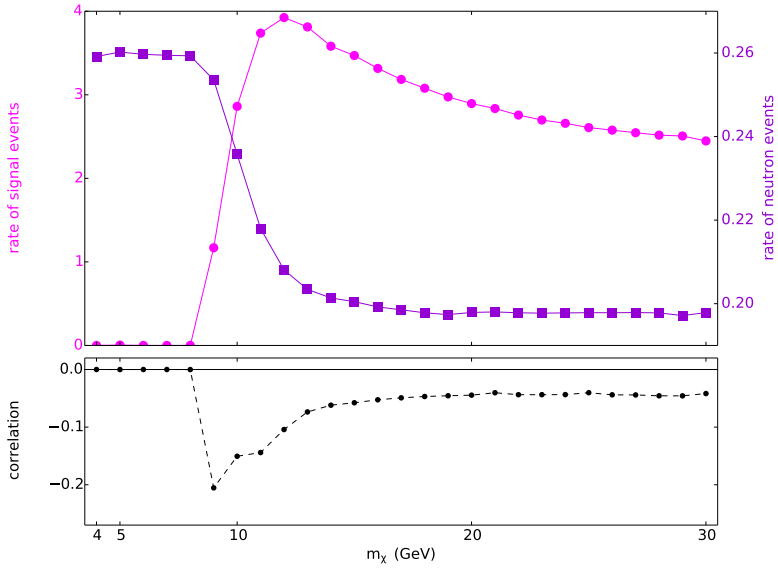

Figure 4.28.: Best fit rate for neutron events (violet) and the WIMP signal (magenta) for detector FID837. Starting at $m_\chi = 9\,\text{GeV}/c^2$, a signal component is fitted to the two nuclear recoil candidate events seen in Fig. 4.12. Due to the constraint of $n^{\text{exp}}_{\text{neutron}} = 0.20 \pm 0.09$ events, the best fit rate shows only a small variation for different WIMP masses. The correlation factor between the two rates indicates the beginning of the degeneracy between the two components.

4.4.2. Fit results for the combination of all 8 detectors

The degeneracy between different background components and the signal, which is observed for some of the detectors depending on the signal WIMP mass m_χ, can be effectively suppressed by performing a simultaneous fit of all data. Following Eq. 4.38, the individual likelihood functions the 8 detectors can be combined to construct a likelihood model $\mathcal{L}_{\text{comb}}\left(\sigma_\chi, \vec{\mu}_1, \vec{\mu}_2, ... \mid m_\chi\right)$ for each probed WIMP mass m_χ. In this model all detectors have their separate PDFs and nuisance parameters, including the ionization yield Q_{NR} for nuclear recoils. Each detector also has its own PDF describing the signal component, but the cross section σ_χ used to calculate the weight of this component via the signal rate μ_χ is the common parameter of interest for all. The reason for such a construction is the occurrence of a WIMP signal being seen in all detectors with similar signal strength. Possible differences could only come from the detector specific signal sensitivity, due to detector parameters such as the analysis threshold $E_{\text{c}}^{\text{min}}$ or the exposure M and small statistical fluctuations.

The combined fit implemented this way is much more computing intensive than the individual detector fits and takes several days per WIMP mass m_χ. One reason for that is that the total number of events which are fitted is now $\approx$50,000. And although the fitting of data from different detectors could in principle be performed in parallel, this is not expected to speed up the fit. Responsible for that is the necessary normalization of the signal and neutron PDFs which is calculated after any changes to the nuisance parameter a for the nuclear recoil ionization yield Q_{NR}. This numerical integration slows down the fit significantly and requires a much larger number of minimization steps to achieve convergence. In total, the full combined model for each WIMP mass has 168 component PDFs, 168 nuisance parameters, which are each constrained by an additional Gaussian PDF and one parameter of interest σ_χ. Although the number of fit parameters seems high and the fit thus somewhat arbitrary, it should be reminded that the fit is performed on a detector level, i.e. only 21 component PDFs are actually fitted to each data set, and, for example, all K-shell peak PDFs have no overlap with the signal PDF.

The best fit values for the fitted cross section σ_χ and the combined rate of signal events μ_χ^{comb} calculated following Eq. 4.39 are given in Tab. 4.7 for a representative selection of WIMP masses. The combined signal rate for all WIMP masses is also plotted in Fig. 4.29. Just as for the individual detector fits, the signal rate for all WIMP masses is compatible with zero within $2\,\sigma$ errors. In particular, the best fit cross section for the two lowest WIMP masses corresponds to a signal of $\approx$0 events. Starting at $m_\chi = 6\,\text{GeV}/c^2$, the nuclear recoil candidate events of detectors FID825, FID837 and FID838 enter the signal PDF regions for these detectors and are best fitted with the signal component. As a result, the combined best fit rate increases up to a maximum of $\mu_\chi^{\text{comb}} = 12.0$ events at $m_\chi = 7\,\text{GeV}/c^2$ before decreasing again to a level of $\approx$5 events for the highest masses probed. Although the fitted cross section σ_χ is the same for all detectors, the rate of fitted signal events for each detector can in principle vary. Such variations depend on the integrated signal for each detector, which depends on the analysis threshold $E_{\text{c}}^{\text{min}}$ and the exposure M. For higher

Table 4.7.: Best fit cross section $\hat{\sigma}_\chi$ (in picobarn) and calculated rate of signal events μ_χ^{comb} for the combined fit over all detectors and a selection of WIMP masses m_χ.

m_χ	$4\,\text{GeV}/c^2$	$7\,\text{GeV}/c^2$	$10\,\text{GeV}/c^2$	$30\,\text{GeV}/c^2$
$\hat{\sigma}_\chi$ (pb)	$(1.2^{+6579}_{-1.2}) \cdot 10^{-7}$	$(1.6^{+1.5}_{-1.6}) \cdot 10^{-6}$	$(2.7^{+2.0}_{-1.5}) \cdot 10^{-7}$	$(3.3^{+2.4}_{-1.8}) \cdot 10^{-8}$
μ_χ^{comb} (events)	$0.003^{+17.5}_{-0.003}$	$12.0^{+11.7}_{-8.5}$	$9.1^{+6.7}_{-5.1}$	$5.1^{+3.6}_{-2.7}$

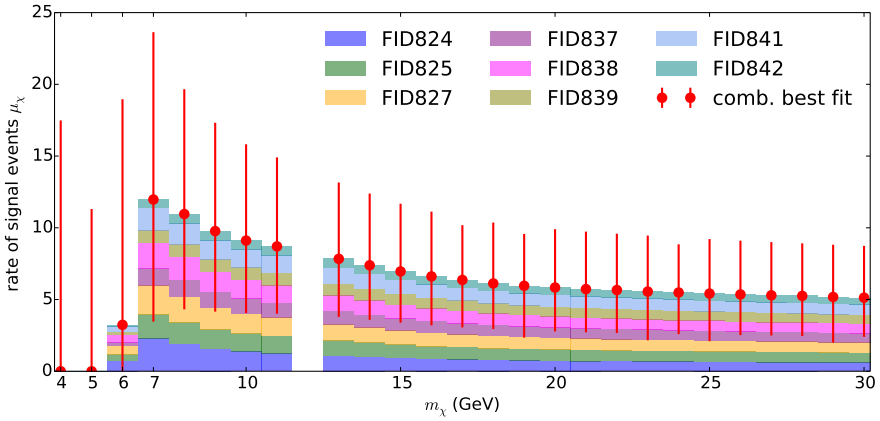

Figure 4.29.: Combined rate of fitted signal events μ_χ^{comb} with $1\,\sigma$ uncertainties as a function of the WIMP mass m_χ for the combined fit over all detectors (red error bars). The values at $m_\chi = 12\,\text{GeV}/c^2$ is missing due to a convergence problem of the combined fit. For masses $m_\chi \geq 5\,\text{GeV}/c^2$ the nuclear recoil candidate events present in the datasets of different detectors enter the respective signal regions are best fitted with the signal PDF. However, all fitted signals are compatible with zero within $2\,\sigma$ errors. Stacked coloured bars indicate how the combined signal rate is distributed among the 8 fitted detectors.

WIMP masses, however, the differences in $E_{\text{c}}^{\text{min}}$ have a minor effect on the integrated signal, and the exposure is very similar for the different detectors. The combined signal rate is therefore distributed rather homogeneously among the 8 detectors, as can also be seen in Fig. 4.29. Only for the lowest WIMP masses, the signal fraction for FID824 is marginally higher due to its low analysis threshold $E_{\text{c}}^{\text{min}}$. And for all masses, the signal fraction for FID842 is the lowest due to the small exposure for this detector.

The best fit values of the different background rates μ_{i} are almost equal to the ones fitted for single detectors for most of the components. The only exception are heat-only and neutron events. For FID837 and FID838 the rate of fitted neutrons for larger WIMP masses above $m_\chi = 10(20)\,\text{GeV}/c^2$ is slightly higher to compensate for the change in WIMP signal in the combined fit. Another difference can be observed in the rate of fitted heat-only events: for those detectors with a strong degeneracy between heat-only PDF and signal PDF for low WIMP masses, the fitted heat-only rate is now stable over all WIMP masses. This is a good example for how a combined fit can alleviate detector specific correlations between components, which in the case of individual detector fits would decrease the achievable sensitivity.

4.4.3. Construction of the profile likelihood test statistics

The results discussed on the previous section show that no statistically significant signal is observed for any of the probed WIMP masses $m_\chi \in [4, 30]\,\text{GeV}/c^2$, both for individual detector fits and the combined fit of all data with a common signal. This observation motivates the setting of an upper limit on the signal cross section σ_χ. The extraction of this limit is performed with the principle of a hypothesis test, which was introduced in Sec. 3.4.2.

For a signal cross section value σ_χ which is tested, the value of the profile likelihood based test statistics q_μ^{obs} is calculated from the measured data following Eq. 3.29. Based on this value, the p-values for null hypothesis H_μ (signal plus background) to be rejected, and the alternative hypothesis H_0 (background-only), can be calculated. Smaller p-values correspond to a stronger disagreement of the hypothesis with the observed data. Following

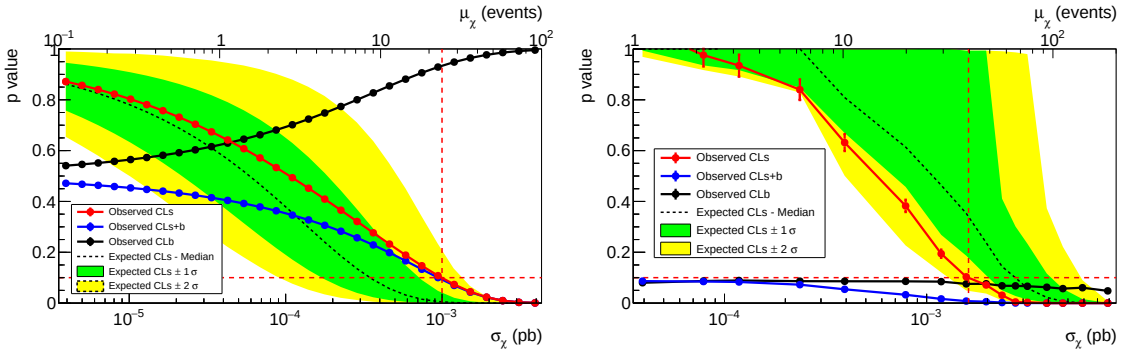

Figure 4.30.: Result of the hypothesis test scan for the combination of all detectors and a WIMP mass $m_\chi = 4\,\mathrm{GeV}/c^2$ performed with the `RooStats` framework. The scan over different hypothesis tests with the asymptotic approximation is shown in the left panel, while the Monte Carlo data is shown in the right panel. Plotted are the p-values for a hypothesis test performed at different WIMP-nucleon scattering cross sections σ_χ. The corresponding rate of signal events μ_χ is shown as second x-axis on top. The p-value for the signal plus background hypothesis (blue markers) are divided by the p-values for the background-only hypothesis (black markers) to account for underfluctuations of the background (red markes). The cross section limit $\sigma_\chi^{\mathrm{lim}}$ is found for the (interpolated) value of $CL_\mathrm{s} = 0.1$ (intersection of red dashed lines). The median expectation value is drawn as black dotted line, with 1σ and 2σ uncertainty band in green and yellow, respectively. See text for more details.

the notation used in the `RooStats` analysis tool, we denote with CL_sb and CL_b the probability to measure a larger test statistics value than observed from data for the H_μ and H_0 hypothesis, respectively. Eq. 3.36, which is used to correct for underfluctuations of the background can then be written as:

$$CL_\mathrm{s} = \frac{CL_\mathrm{sb}}{CL_\mathrm{b}} \tag{4.51}$$

The principle of the method to set limits is to scan over different signal cross sections σ_χ, and perform a hypothesis test for each value until

$$CL_\mathrm{s}(\sigma_\chi{=}\sigma_\chi^{\mathrm{lim}}) = 0.10 \tag{4.52}$$

is reached, which is the 90% confidence level limit $\sigma_\chi^{\mathrm{lim}}$. To calculate the p-values CL_sb, CL_b and the resulting value CL_s the distributions $f(q_\mu \mid H_\mu)$ and $f(q_\mu \mid H_0)$ are needed. It was shown in Sec. 3.4.2, that in the case of a large data sample, these distributions can be approximated with half-chi-square functions. This approximation avoids large Monte Carlo studies and is, for example, employed in the likelihood analyses performed by the experiments XENON100 [114] and LUX [116].

Under the assumption of this asymptotic approximation, a limit can be derived for each individual detector as well as the combination of all 8 detectors. For each WIMP mass m_χ for which a likelihood model has been constructed and fitted, a hypothesis scan is performed over different values of the cross section σ_χ, as described above. The result of such a test for the combination of all detectors and a WIMP mass $m_\chi = 4\,\mathrm{GeV}/c^2$ is shown in Fig. 4.30 (left). To interpret Fig. 4.30 (right) we first describe how the Monte Carlo p-values are constructed:
To test the validity of the applied approximation, a hypothesis test has been performed with

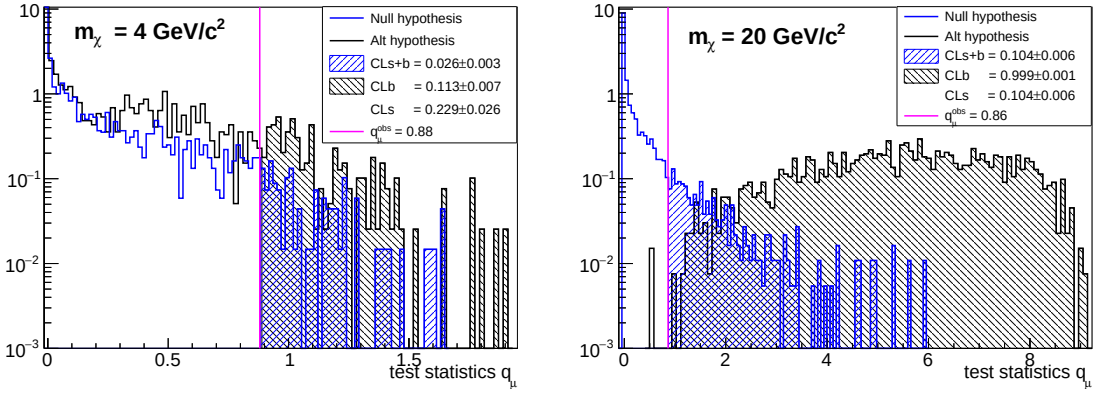

Figure 4.31.: Hypothesis tests performed with 4000 and 3000 Monte Carlo toy data sets for the combined likelihood model. The tested value is the cross section limit $\sigma_\chi^{\mathrm{lim}}$ (approx.) derived with the asymptotic approximation. For $m_\chi = 4\,\mathrm{GeV}/c^2$ (left panel) the observed distributions give a value $CL_\mathrm{s} > 0.1$ (see Eq. 4.51), which means that the frequentist coverage does not allow to set a 90% C.L. exclusion limit at this value. For $m_\chi = 20\,\mathrm{GeV}/c^2$ (right panel) the approximation holds and the coverage is correct.

Monte Carlo generated data at the value $\sigma_\chi^{\mathrm{lim}}$ found for the combination of all detectors and a selection of 10 WIMP masses $m_\chi \in [4, 30]\,\mathrm{GeV}/c^2$. To keep the necessary computing time within reasonable limits, this test was performed without the constrained nuisance parameter a for the nuclear recoil quenching, which was added to the detector likelihood function in Eq. 4.41. As was discussed in Sec. 4.4.1, fitting the nuclear recoil ionization yield Q_NR results in a significant increase of the time needed to fit data, as the WIMP signal PDF ρ_χ and the PDF describing neutrons, have to be renormalized for each variation of the parameter a. For studies with Monte Carlo toy data, which require $\mathcal{O}(10^3)$ generated event sets to be fitted, the required time frame would be exceedingly large. It was verified, that the difference in the resulting exclusion limit with and without floating nuclear recoil ionization yield Q_NR, is $< 10\%$. This difference is in most cases within the uncertainty due to the interpolation of the limit from a smaller number of tested cross section values σ_χ in the case of a variable ionization yield[7]. Figure 4.31 shows the result of such a hypothesis for the two masses $m_\chi = 4\,\mathrm{GeV}/c^2$ and $m_\chi = 20\,\mathrm{GeV}/c^2$, which were performed with 4000 and 3000 Monte Carlo toy data sets for the null hypothesis and half as many for the alternative hypothesis. For $m_\chi = 4\,\mathrm{GeV}/c^2$, the resulting value $CL_\mathrm{s} = 0.229 \pm 0.026$ is clearly incompatible with the value $CL_\mathrm{s} \stackrel{!}{=} 0.1$ required for a 90% C.L. For $m_\chi = 20\,\mathrm{GeV}/c^2$, however, the resulting value for CL_s is in good agreement with this requirement. A table giving an overview of the CL_s values from Monte Carlo toy data, which were derived for the approximated 90% C.L., can be found in the appendix C.7. For WIMP masses $4 \leq m_\chi \leq 7\,\mathrm{GeV}/c^2$, the so-called *coverage*, which is at the basis of frequentist statistics, is insufficient. Thus, the limit derived with the asymptotic approximation is to strict and cannot be used.

To account for this, we performed extensive Monte Carlo studies to derive the limit. For each detector as well as the combination of detectors, the scan over different cross section values σ_χ was performed with MC generated toy data for the hypothesis test. Due to limitations regarding the computation time, only $\approx$2000$-$10000 toy data sets for each value in σ_χ for a given m_χ could be generated and fitted in the case of the combination of detectors. For the derivation of limits for individual detectors, a larger number of

[7] Only for detector FID838, which has a large fitted value for the ionization yield parameter a, the limit becomes worse by 15% to 60% when a is fixed.

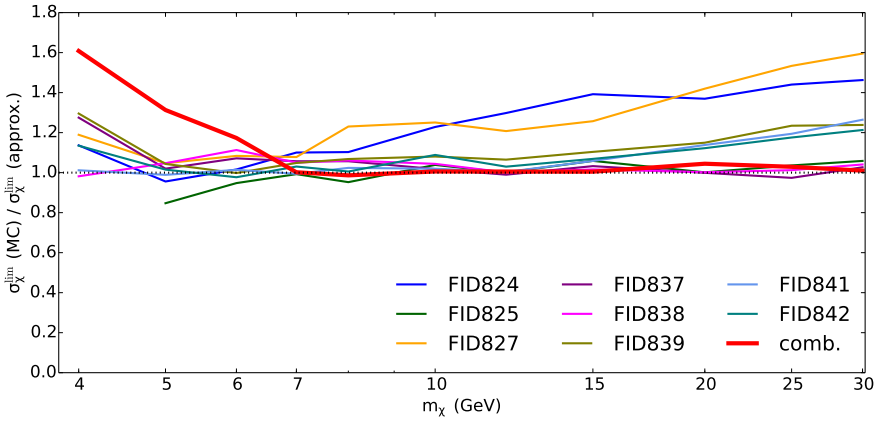

Figure 4.32.: Correction factor for the 90% C.L. exclusion limit derived from Monte Carlo based hypothesis test compared to the asymptotic approximation. Factors below 1 are related to statistical uncertainty due to the number of test toy data sets and the uncertainty due to the interpolation between test values of σ_χ (see also Fig. 4.30). The value at $m_\chi = 4\,\mathrm{GeV}/c^2$ for detector FID825 is missing due to lack of statistics. A degradation of the combined limit is found for WIMP masses $m_\chi < 10\,\mathrm{GeV}/c^2$.

≈4000−9000 toy event sets, again for each value of σ_χ and m_χ, were generated and fitted. The resulting hypothesis test scan for the combined data and $m_\chi = 4\,\mathrm{GeV}/c^2$ is shown in Fig. 4.30 (right). Large error bars especially for low values of σ_χ are a result of the relatively small statistics. While the limit for $m_\chi = 4\,\mathrm{GeV}/c^2$ is corrected upwards by 60% from $1.0 \cdot 10^{-3}\,\mathrm{pb}$ to $1.6 \cdot 10^{-3}\,\mathrm{pb}$ with the Monte Carlo method, the more significant change is related to the sensitivity band. Using the approximation, the median sensitivity is more stringent than the observed exclusion limit, while with MC toy data this is reversed. This can be understood by considering that the limit at $m_\chi = 4\,\mathrm{GeV}/c^2$ is driven by detectors FID824 and FID825, both of which have an underfluctuation of the data and of the derived exclusion limit for this mass. Figure 4.32 shows the correction factors of the MC limit for all probed masses with respect to the limit derived with the approximation. A degradation of the limit of at most 60% is observed, depending on the fitted detector and considered WIMP mass. For detectors FID824 and FID827, both of which have no possible nuclear recoil events at higher energies, the correction is most significant. Indeed, the derived limits for these masses under the asymptotic approximation correspond to less then $\mu_\chi^{\mathrm{lim}} = 2.35\,\mathrm{events}$, which is the 90% C.L. Poisson limit for a background free experiment (see Sec. 3.1.1). This somewhat unphysical result is overcome when using the more appropriate MC test statistics. Overall, the comparison of the two test statistics demonstrates the necessity to use specific, data-driven MC toy data sets to extract proper limits. Nevertheless, the difference of up to 60% vanishes for larger values of m_χ, also justifying the use of the asymptotic approximation for these cases.

4.4.4. Discussion of the resulting exclusion limits

The limits for each likelihood model, i.e. for different detectors and WIMP masses, were derived for the parameter of interest, the WIMP-nucleon scattering cross section σ_χ. For a more intuitive discussion of the limits, we remind that according to Eq. 4.36, the cross section σ_χ can be expressed with the signal rate μ_χ. We therefore can calculate the 90% C.L. exclusion limit on the signal rate as:

$$\mu_\chi^{\mathrm{lim}} = \frac{\sigma_\chi^{\mathrm{lim}}(m_\chi)}{\sigma_\chi^0} \cdot \int_{E_c^{\mathrm{min}}}^{15\,\mathrm{keV_{ee}}} \int_{0\,\mathrm{keV_{ee}}}^{15\,\mathrm{keV_{ee}}} \rho_\chi(E_c, E_{\mathrm{fid}} \mid m_\chi) \tag{4.53}$$

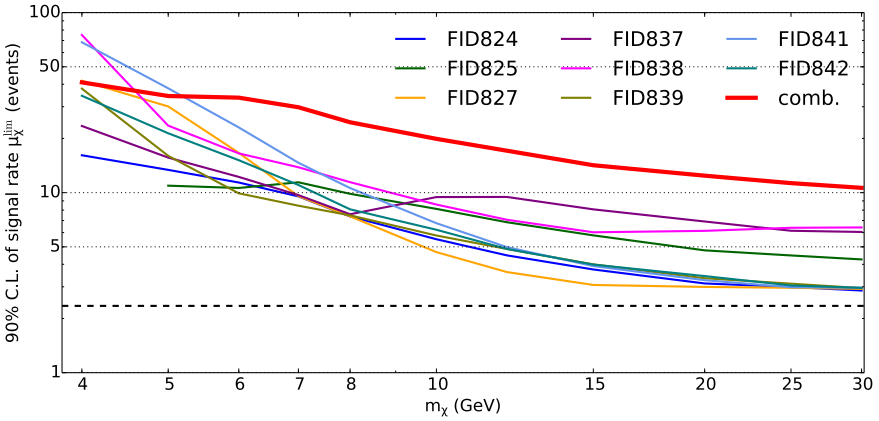

Figure 4.33.: 90% C.L. upper limit $\mu_\chi^{\lim}$ on the signal rate as a function of WIMP mass m_χ for the fit of data from individual detectors. In general, the highest limits are observed for the lowest WIMP masses, which is caused by an excess of the heat-only background and a degeneracy between the heat-only PDF and the signal for most detectors. For detectors FID825, FID837 and FID838 the limit increases at specific masses, in correspondence with a fitted signal due to nuclear recoil candidate events entering the signal region. The dotted line shows the achievable upper limit of 2.35 events in the background free case. The value at $m_\chi = 4\,\mathrm{GeV}/c^2$ for detector FID825 is missing due to lack of statistics.

A comparison of the upper 90% C.L. signal rate limits $\mu_\chi^{\lim}$ for all likelihood functions is shown in Fig. 4.33. As expected, the limits are approximately proportional to the upper error of the best fit rates $\hat{\mu}_\chi$ and therefore *"trace"* the best fit values given in Tab. 4.6. For all detectors, the limit is highest for a signal of WIMP mass $m_\chi = 4\,\mathrm{GeV}/c^2$. The degeneracy between signal and heat-only PDF is responsible for either a large fitted signal or a large uncertainty on the fitted signal. The highest upper limits for the overall signal rate are found for detectors FID838 and FID841. For the latter, the degeneracy between heat-only PDF and signal PDF shown in Fig. 4.27 leads to a high fitted signal rate $\hat{\mu}_\chi = 39.7^{+23.0}_{-19.1}$ events for $m_\chi = 4\,\mathrm{GeV}/c^2$. As a result, the fitted limit is as high as $\mu_\chi^{\lim} = 68.4$ events. For all detectors, the limit on the signal rate decreases for increasing WIMP masses up to $m_\chi = 30\,\mathrm{GeV}/c^2$, as the separation of the signal PDF with all other background components becomes clearer. An exception are the three detectors FID825, FID837 and FID838 which have a clear excess of nuclear recoil candidate events, causing the limit to converge at moderately high values of $\mu_\chi^{\lim} \approx 3$–$6$ events. Detector FID824 has one of the lowest limits in terms of signal rate at $m_\chi = 4\,\mathrm{GeV}/c^2$, which in combination with its low analysis threshold $E_\mathrm{c}^{\min}$ and the resulting large signal efficiency leads to the highest sensitivity of all detectors.

Figure 4.33 also highlights the benefit of the combined fit of all detectors with a common signal cross section. In a standard analysis, as has been performed with EDELWEISS in the past, a combination of the upper limits of individual detectors is typically applied. For $m_\chi = 4\,\mathrm{GeV}/c^2$ this would lead to a limit which is at least as high the highest individual limit. With the combined fit performed in this thesis, high individual limits due to background fluctuations and degeneracies of individual detectors have been suppressed. As a result, the combined limit is $\mu_\chi^{\lim} \approx 41$ events and therefore in between the limits of individual detectors for this mass. At higher masses, the presence of 5 observed possible nuclear recoil events above $E_\mathrm{c} = 2\,\mathrm{keV_{ee}}$ (see Fig. 4.9), most likely related to the presence of a radiogenic neutron background, leads to a flattening of the limit at $\mu_\chi^{\lim} \approx 10$ events, significantly higher than the background-free "best limit" of 2.35 events (dotted line in Fig. 4.33).

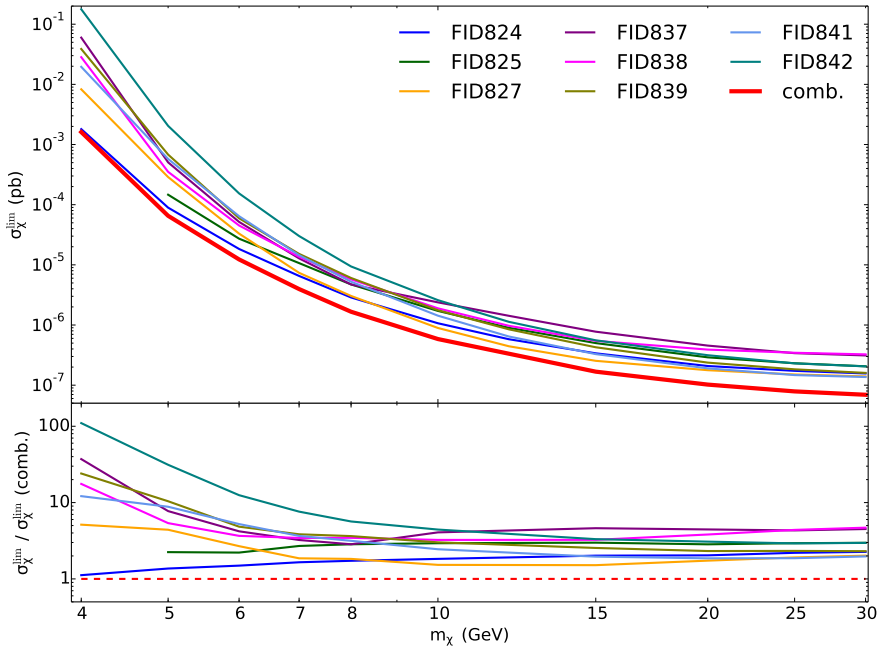

Figure 4.34.: *Top*: 90% C.L. upper limits for the fitted WIMP-nucleon scattering cross section $\sigma_\chi^{\rm lim}$ for individual detector fits as well as the combined fit over all detectors. *Bottom*: Ratio of upper limits for individual detectors compared to the combined fit. For the lowest WIMP masses probed, the sensitivity is defined by the remaining signal after cuts and the order of detectors is therefore in very good agreement with the different analysis thresholds $E_{\rm c}^{\rm min}$. For the highest WIMP masses probed, $E_{\rm c}^{\rm min}$ becomes negligible and detectors with a fitted signal due to an excess of high energy nuclear recoil candidate events (FID825, FID837 and FID838) have the highest upper limits. The value at $m_\chi = 4\,\mathrm{GeV}/c^2$ for detector FID825 is missing due to lack of statistics.

The relative improvement of the upper limit $\sigma_\chi^{\rm lim}$ of the combined fit with respect to the individual detector fits is shown in Fig. 4.34. An improvement in sensitivity of a factor of up to 2 is observed for the combined fit, when compared to the limit coming from the best detectors at each WIMP mass m_χ. At low WIMP masses $4 < m_\chi < 8\,\mathrm{GeV}/c^2$ the best individual detector limit is from FID824, because of its low analysis threshold $E_{\rm c}^{\rm min}$ and low background. Above $m_\chi = 8\,\mathrm{GeV}/c^2$, the best limit is set by FID827, the detector with the second lowest threshold $E_{\rm c}^{\rm min}$ and a 20% higher exposure compared to FID824. As this detector has no nuclear recoil candidate events which would be relevant for WIMPs with $m_\chi > 10\,\mathrm{GeV}/c^2$, this higher exposure brings a small improvement in terms of exclusion limit. Between individual detectors, the differences are much larger: at $m_\chi = 4\,\mathrm{GeV}/c^2$ the ratio between the best detector FID824 and the worst detector FID842 is $\mathcal{O}(100)$. For the lowest WIMP masses probed, the ranking of exclusion limits $\sigma_\chi^{\rm lim}$ for the eight detectors, when fitting their data individually, is in good agreement with the order of their respective analysis threshold $E_{\rm c}^{\rm min}$. The reason for that is that the sensitivity for low mass WIMPs is mainly driven by this parameter, as it has a crucial effect on the efficiency of the signal. For the highest WIMP masses probed, the order of detectors is indifferent to the threshold $E_{\rm c}^{\rm min}$. Here, a more relevant parameter is the exposure, which is fairly homogeneous for the different detectors. Therefore, the three detectors with visible nuclear recoil candidate events at higher energies, FID825, FID838 and FID837 also have the highest cross section limit.

The comparison of the combined exclusion limit on the WIMP-nucleon scattering cross section derived in this analysis with respect to other experiments is given in Fig. 4.35. The

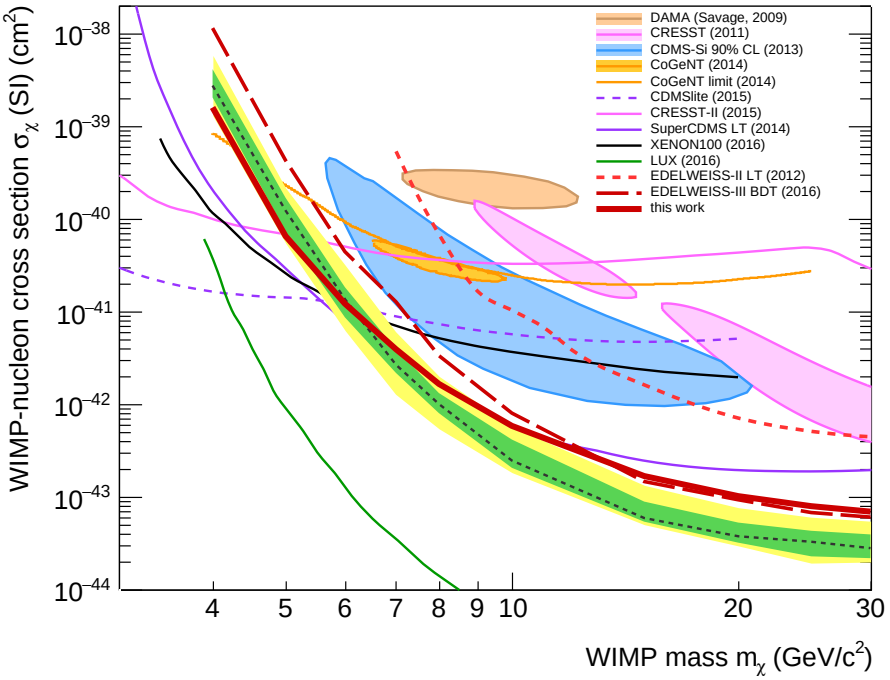

Figure 4.35.: Calculated 90% C.L. exclusion limit on the spin-independent WIMP-nucleon scattering cross section σ_χ as a function of WIMP mass m_χ for the combined fit of all detectors (solid red curve). Also plotted is the expected limit in case of the background only hypothesis (dashed black curve) with its $1\,\sigma$ and $2\,\sigma$ band accounting for statistical fluctuations (green and yellow, respectively).

figure shows an overview of the current status of direct dark matter detection in the low mass range for WIMPs with $m_\chi \in [3, 30]\,\mathrm{GeV}/c^2$. The limit at 90% C.L. obtained with this analysis clearly disfavours the different existing signal claims by DAMA/LIBRA [104], CoGeNT [105], CRESST-II [50] and CDMS-II(Si) [106]. For WIMP masses $m_\chi < 5\,\mathrm{GeV}/c^2$, for which the signal efficiency achieved in this analysis is the lowest, the limit is surpassed by multiple cryogenic solid state experiments, such as CRESST [51] and CDMSlite [49]. However, between $m_\chi = 7\,\mathrm{GeV}/c^2$ and $m_\chi = 10\,\mathrm{GeV}/c^2$, the exclusion limit is competitive with the findings of SuperCDMS [48], the most sensitive cryogenic experiment in this region of parameter space. Above $m_\chi \approx 10\,\mathrm{GeV}/c^2$, the limits of the BDT-based analysis [1] and of this work lead the sensitivity for solid state experiments. It must be noted, that the parameter space under consideration is excluded from $\approx 4\,\mathrm{GeV}/c^2$ by the liquid noble gas experiment LUX [116], which is also the current leading experiment in terms of sensitivity for higher WIMP masses. Not shown in the plot is the limit of XMASS-1 [143], which is at $4.3 \cdot 10^{-41}$ for $m_\chi = 8\,\mathrm{GeV}/c^2$. In the following section, a more detailed comparison between the results derived here and the BDT-based analysis of EDELWEISS-III data is presented.

4.4.5. Comparison with BDT analysis

The analysis presented here has numerous features in common with the BDT bases analysis, which was summarized in Sec. 3.3. For one, the two sets of data for are based on the same period and quality cuts and therefore have an identical livetime per detector. The main differences between likelihood and BDT analysis are the considered event observables, the fiducial cut applied to reject surface events and the exact definition of the region of interest. The difference in terms of event observables is less critical than one could think: while the BDT analysis uses 6 observables to describe each event, only 2 different observables are used in the likelihood analysis. However, these 2 observables already include information

on 4 out of the 6 different readout channels of a detector: the averaged fiducial ionization energy E_{fid} and the combined heat energy E_{c} of an event. Not considered in the likelihood analysis are the time dependent rate of heat-only events and the energy E_{veto} on each of the two veto electrodes on an event-by-event base. Clear surface events are already removed during data selection by the strict fiducial cut which is applied. For the remaining events, the information about the signal on the two veto channels has only negligible information content: by definition of the cut, the event is fully compatible with a fiducial event. Ultimately, both analyses have to deal with the same events as potential WIMP candidates: clear fiducial electrode signals with negligible veto energy and an ionization yield Q compatible with nuclear recoils. However, the likelihood analysis has to pay a price for this strict fiducial cut instead of additional observables describing the veto signal on an event-by-event-base: the cut comes with a reduced efficiency. The acceptance of the cut via the efficiency $\varepsilon_{\mathrm{fid}}^{\mathrm{bulk}} = 81\%$ as introduced in Eq. 4.27 is considered in the construction of the signal density and reduces the signal efficiency accordingly. Additionally, the fiducial cut leads to a reduced effective fiducial mass m_{fid} and therefore the total exposure M_{tot} is reduced by ≈15% compared to the BDT analysis. The difference between the two analyses in the definition of the RoI is more heterogeneous: the BDT analysis uses a common analysis threshold of $E_{\mathrm{c}}^{\mathrm{min}} = 1\,\mathrm{keV_{ee}}$ for the four detectors with better trigger efficiency (FID824, FID825, FID827 and FID838) and a higher value of $E_{\mathrm{c}}^{\mathrm{min}} = 1.5\,\mathrm{keV_{ee}}$ for the 4 other detectors (FID837, FID839, FID841 and FID842). Compared to that, the analysis threshold used in the likelihood analysis is chosen such that the trigger efficiency $\varepsilon_{\mathrm{trigger}}$ is at least 80%. The resulting values are distributed between $E_{\mathrm{c}}^{\mathrm{min}} = 0.9\,\mathrm{keV_{ee}}$ and $E_{\mathrm{c}}^{\mathrm{min}} = 1.46\,\mathrm{keV_{ee}}$, as was shown in Tab. 4.3. For some detectors the threshold is therefore at higher values compared to the BDT analysis, for some at lower values. FID824, the detector with the most stringent exclusion limit for low WIMP masses, profits from this choice of $E_{\mathrm{c}}^{\mathrm{min}}$. For $m_\chi = 4\,\mathrm{GeV}/c^2$, the signal efficiency between $E_{\mathrm{c}}^{\mathrm{min}} = 0.9\,\mathrm{keV_{ee}}$ and $E_{\mathrm{c}}^{\mathrm{min}} = 1\,\mathrm{keV_{ee}}$ more than triples from 0.7% to 2.2%.

Tab. 4.8 compares the results for the combination of all detectors between BDT and likelihood analysis. For different WIMP masses m_χ, the table lists the two relevant values to understand the calculation of the cross section limit $\sigma_\chi^{\mathrm{lim}}$ following Eq. 4.53: the upper limit on the signal rate μ_χ^{lim} (or events n^{lim} above the BDT cut) and the integrated signal in the RoI $\int_{\mathrm{RoI}} \rho_\chi$ (for the BDT analysis before and after the BDT cut). One has to keep in mind, that the two event(rate) limits are of entirely different nature: the value of μ_χ^{lim} from the likelihood analysis was extracted using a combined fit over all detectors and with known backgrounds fitted (subtracted). The value of n^{lim} is the 90% C.L. Poisson limit of the number of events above the BDT cut. Although the number of background events above this cut (see Tab. 3.1) has been estimated, backgrounds are not subtracted, which is a more conservative approach. The other main difference is, that in the BDT analysis detectors are fitted independently and the results are then combined. Which detectors are considered depends on the WIMP mass: for $m_\chi = 4\,\mathrm{GeV}/c^2$, only the 4 detectors with a threshold of $E_{\mathrm{c}}^{\mathrm{min}} = 1\,\mathrm{keV_{ee}}$ contribute to the limit. For $m_\chi = 7\,\mathrm{GeV}/c^2$ all detectors except FID842 are used and only for masses of $m_\chi = 10\,\mathrm{GeV}/c^2$ and above all detectors. While the signal rate limit found for the likelihood analysis for $m_\chi = 4\,\mathrm{GeV}/c^2$ is $\mu_\chi^{\mathrm{lim}} = 41.0$ and therefore higher than the event limit of the BDT analysis of $n^{\mathrm{lim}} = 17.8$, this is more than compensated by the more than 10 times higher integrated signal efficiency after all cuts. As Tab. 4.8 clearly shows, the signal efficiency of the BDT analysis *after* the BDT cut is drastically reduced and lower by a factor of 10 to 1.5 between $m_\chi = 4\,\mathrm{GeV}/c^2$ and $m_\chi = 30\,\mathrm{GeV}/c^2$ compared to the likelihood analysis. The combined signal in the RoI *before* the BDT cut is even larger than that of the likelihood analysis for all masses, even though not all detectors are used at the lowest m_χ. The reason for that is a combination of lower thresholds $E_{\mathrm{c}}^{\mathrm{min}}$ for 3 detectors (at low m_χ) and a higher exposure (at high m_χ). For

Table 4.8.: Calculation of the excluded cross section $\sigma_\chi^{\lim}$ at 90% C.L. for the BDT and the likelihood analysis, for different WIMP masses m_χ. The excluded signal rate $\mu_\chi^{\lim}$ is different than the limit on the observed number of events $n^{\lim}$ of the BDT analysis, which is extracted from a smaller signal region without background subtraction. The integrated signal $\int_{\mathrm{RoI}} \rho_\chi$ for a cross section of $\sigma_\chi^0 = 10^{-6}\,\mathrm{pb}$ is given after all cuts. The signal before BDT cut on the discriminating variable is given for comparison. Numbers in brackets give the efficiency compared to the full WIMP-nucleon recoil spectrum.

m_χ	$4\,\mathrm{GeV}/c^2$	$7\,\mathrm{GeV}/c^2$	$10\,\mathrm{GeV}/c^2$	$30\,\mathrm{GeV}/c^2$
$\mu_\chi^{\lim}$ (Likelihood)	41.0	29.8	19.9	10.6
$n^{\lim}$ (BDT)	17.8	10.5	8.0	8.0
$\int_{\mathrm{RoI}} \rho_\chi$ (Likelihood)	0.027 (0.023%)	7.7 (5.0%)	34 (18%)	154 (58%)
$\int_{\mathrm{RoI}} \rho_\chi$ (BDT before cut)	0.037 (0.056%)	7.4 (4.6%)	37 (17%)	188 (60%)
$\int_{\mathrm{RoI}} \rho_\chi$ (BDT)	0.002 (0.002%)	0.8 (0.5%)	10 (5%)	133 (43%)
$\sigma_\chi^{\lim}$ (Likelihood) [pb]	$1.6 \cdot 10^{-3}$	$4.0 \cdot 10^{-6}$	$5.8 \cdot 10^{-7}$	$6.9 \cdot 10^{-8}$
$\sigma_\chi^{\lim}$ (BDT) [pb]	$1.2 \cdot 10^{-2}$	$1.3 \cdot 10^{-5}$	$8.1 \cdot 10^{-7}$	$6.0 \cdot 10^{-8}$
$\sigma_\chi^{\lim}$ (BDT)/$\sigma_\chi^{\lim}$ (Likelihood)	7.2	3.2	1.4	0.9

$m_\chi = 4\,\mathrm{GeV}/c^2$ the necessary BDT cut on the distribution of the discriminating variable reduces the signal by 96%. For the likelihood analysis, no additional cut is necessary and the full signal in the RoI can be used to calculate the exclusion limit. For that reason the exclusion limit found with the likelihood analysis for a WIMP signal with $m_\chi = 4\,\mathrm{GeV}/c^2$ is a factor 8 more stringent than the one for the BDT analysis. This factor decreases with increasing WIMP mass and for $m_\chi = 30\,\mathrm{GeV}/c^2$ the BDT analysis even performs better by 20%.

A comparison between the 90% C.L. cross section limits for BDT and likelihood analysis is shown in Fig. 4.36 (top). For the lowest WIMP masses probed, a significantly stricter exclusion limit is observed for the likelihood analysis with respect to the BDT result. For higher masses the limit approaches the BDT limits and for $m_\chi \geq 15\,\mathrm{GeV}/c^2$ the limits of both analyses are in good agreement, with small benefits for the BDT analysis. Also shown in Fig. 4.36 (bottom) is a comparison of the ratios between observed and expected limits. These ratios show a similar trend, although with some differences. For both analyses the ratio is above one for masses above $m_\chi = 7\,\mathrm{GeV}/c^2$, due to the observed excess of a radiogenic neutron background in the data. The largest discrepancy between BDT and likelihood analysis is seen at $m_\chi = 4\,\mathrm{GeV}/c^2$, for which the observed limit of the likelihood analysis is ≈0.5 times better than expected, compared to a factor of ≈1.5 less strict for the BDT analysis. A likely explanation for this difference is, that the BDT result is dominated by detector FID825, which shows a clear excess of heat-only events. As discussed in Sec. 4.3.2, the heat-only background in both analyses is constructed with a Gaussian distribution around a fiducial ionization energy of $E_{\mathrm{fid}} = 0\,\mathrm{keV_{ee}}$ and the expected rate in the RoI is determined from the number of heat-only sideband events. A small, positive bias of the heat-only distribution in E_{fid} which several detectors show, leads to an excess of heat-only events in the RoI, which is not taken into account in the calculation of the expected limit and degrades the observed sensitivity. However, the impact of this excess is smaller for the BDT analysis: for small m_χ the signal region selected with the BDT cut

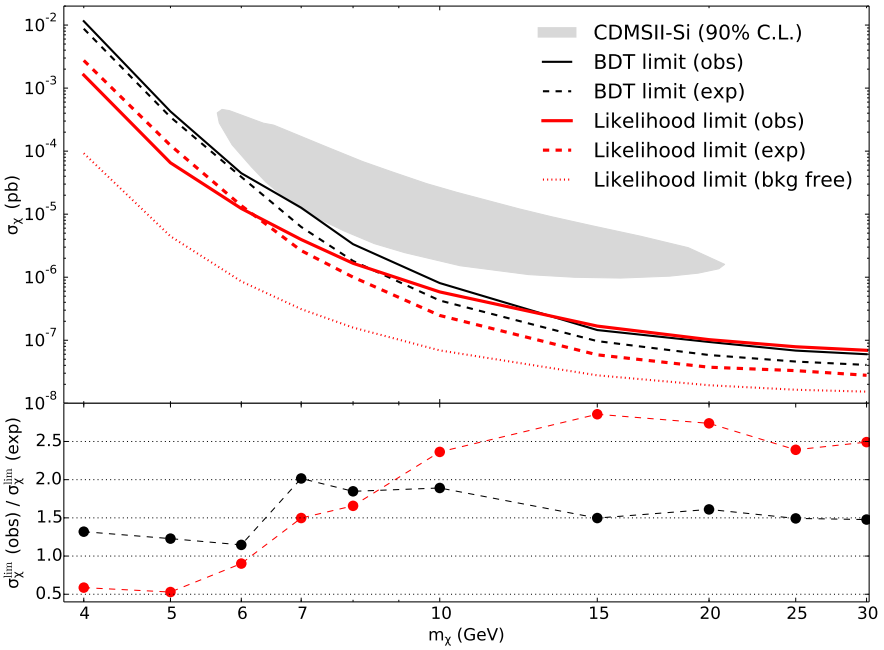

Figure 4.36.: *Top*: Observed and expected exclusion limits on the WIMP-nucleon scattering cross section as a function of WIMP mass m_χ. Compared are the exclusion limits between BDT and likelihood analysis for a combination of all 8 detectors. For the likelihood analysis the theoretical extreme case of $\mu_\chi^{\text{lim}} = 2.35$ events is also shown (90% Poisson-limit in case of 0 observed events). *Bottom*: Ratio between observed and expected exclusion limit as a function of WIMP mass m_χ. For masses $m_\chi \geq 7\,\text{GeV}/c^2$, both analyses have an excess of events (neutron candidates) and therefore the observed limit is clearly above the expected value.

specifically avoids the distribution of heat-only events and is therefore less affected by a possible excess. For the likelihood analysis, the most sensitive detector is FID824, which has no excess of heat only events but a general underfluctuation of the background. As a result, the combined limit is also better than the median sensitivity.
Both analyses also show an excess at higher masses which is related to the observed excess of the radiogenic neutron background compared to the expected rate of events. Again, the ratio between observed and expected limit is larger for the likelihood (≈2.5) than for the BDT analysis (≈1.5). One reasonable explanation for that is the difference in the definition of the RoI between the two analyses. The RoI of the BDT analysis only extends up to $8\,\text{keV}_{\text{ee}}$ in (total) ionization and $12\,\text{keV}_{\text{ee}}$ in combined heat energy (compared to $E_{\text{c}}, E_{\text{fid}} < 15\,\text{keV}_{\text{ee}}$ for the likelihood analysis). At least one nuclear recoil candidate event for detector FID838 at $(E_{\text{c}}, E_{\text{fid}}) \approx (10\,\text{keV}_{\text{ee}}, 14\,\text{keV}_{\text{ee}})$ (see data for this detector in Fig. B.1) is therefore only included in the likelihood analysis and increases the fitted WIMP signal rate. The similarities between the two analyses are even stronger when comparing the individual detector fits of the likelihood analysis with those of the BDT analysis. In particular, for the most sensitive detector FID824, the ratio between observed and expected limit shows a very good agreement, as can be seen in Fig. B.2.
Overall, the results of the two analyses are compatible for high masses $m_\chi > 15\,\text{GeV}/c^2$ and the improvement of the likelihood analysis for low WIMP masses with respect to the BDT results can be attributed to the significantly larger signal efficiency.

4.4.6. Outlook

The analysis presented in this work clearly demonstrates that for a given dataset the highest sensitivity to low mass WIMPs can be achieved with a maximum likelihood approach.

Compared to the analysis of data from the same Run308 with a BDT based approach, a significant improvement in sensitivity is observed for WIMP masses $m_\chi < 10\,\mathrm{GeV}/c^2$. Some aspects of the likelihood analysis can be considered conservative: the analysis threshold $E_\mathrm{c}^\mathrm{min}$ is chosen such that the trigger efficiency is at least 80%. As discussed in Sec. 4.3.1, the efficiency for measuring low mass WIMP signals in the RoI depends crucially on this threshold. Lowering $E_\mathrm{c}^\mathrm{min}$ to values which correspond to a trigger efficiency $\epsilon_\mathrm{trigger}$ of e.g. 50% would increase the sensitivity of the analysis further. Although tests with lower threshold $E_\mathrm{c}^\mathrm{min}$ were performed, this more aggressive choice of data selection was not followed here and would require an extension of the likelihood model to include the systematic error on the trigger efficiency. Another possible improvement of the analysis is related to the model for heat-only events. As shown in Sec. 4.3.2, the ionization energy E_fid for these events is biased with respect to $E_\mathrm{fid} = 0$ for several detectors, which is only taken into account with a large systematic uncertainty $\mathcal{O}(10\%)$ on the number of expected events in the RoI. An improved cross talk correction or more detailed modelling of these events would decrease the systematic uncertainty, which in return should improve the accuracy on the fitted signal.
Both BDT and likelihood analysis show that the backgrounds limiting the achieved sensitivity are different depending on the WIMP mass m_χ. For WIMPs with masses $m_\chi > 7\,\mathrm{GeV}/c^2$, the excess of radiogenic neutrons in the EDELWEISS dataset is a clear limiting factor. Investigations are ongoing and simulations and material screenings are performed to identify the source of these neutrons. A possible reduction of this background would significantly improve the sensitivity for standard mass WIMPs for the EDELWEISS experiment. For much lower WIMP masses down to $m_\chi = 4\,\mathrm{GeV}/c^2$ the overall sensitivity is limited by the dominant background of heat-only events, as both BDT and likelihood analysis showed. Several R&D efforts are ongoing within EDELWEISS to find the origin of this background and to reduce it in future WIMP search runs. Further efforts aim at the reduction of heat baseline noise: the goal is a reduction from the current values of $\mathrm{FWHM}_\mathrm{heat} \approx 500\,\mathrm{eV}_\mathrm{ee}$ down to values of $\mathrm{FWHM}_\mathrm{heat} = 100\,\mathrm{eV}_\mathrm{ee}$. Ongoing work on this topic involves both the theoretical modelling of the heat exchange system between detectors, thermal bath and heat sensors, as well as dedicated measurements with detectors on a test stand. Further research is dedicated to the improvement of the ionization baseline noise to achieve resolutions of $\mathrm{FWHM}_\mathrm{ion} = 100\,\mathrm{eV}_\mathrm{ee}$. Lower ionization noise would improve the discrimination between the ionization yield of electron recoils and nuclear recoils as well as the discrimination of surface from bulk events.

However, the most rewarding scenario for the future for low mass WIMP search with EDELWEISS lies in the Luke-Neganov enhancement of the heat signal, i.e. by applying larger fiducial voltages of up to 100 V to the detectors. As described in Sec. 2.2.1, a boosting of the measured heat energy allows achieve to much lower energy thresholds. This is necessary for a sensitivity to low mass WIMPs with masses down to $m_\chi \approx 1\,\mathrm{GeV}/c^2$. A thesis performed within the EDELWEISS collaboration [119] studied the projected sensitivity which can be achieved by this approach. To determine the sensitivity, the study used Monte Carlo generated toy data from background models, and a simplified though similar maximum likelihood approach including the setting of limits using a hypothesis test as was used in this thesis. Both analyses are also based on the same principles for the description of the response function which is inherent to the EDELWEISS detection scheme. The projected sensitivity of such an improved WIMP search with boosted heat signal is shown in Fig. 4.37, for an exposure of 350 kg·days and the different choices of applied fiducial voltage and heat and ionization baseline resolution. For practical reasons, the underlying assumptions about the background models which went into these projections are different compared to the actual data studied in the context of this thesis. For the lower energy range which was studied, new low energy backgrounds have to be considered such as M-shell peaks of cosmogenic isotopes. While all backgrounds which have been presented in Sec. 4.3

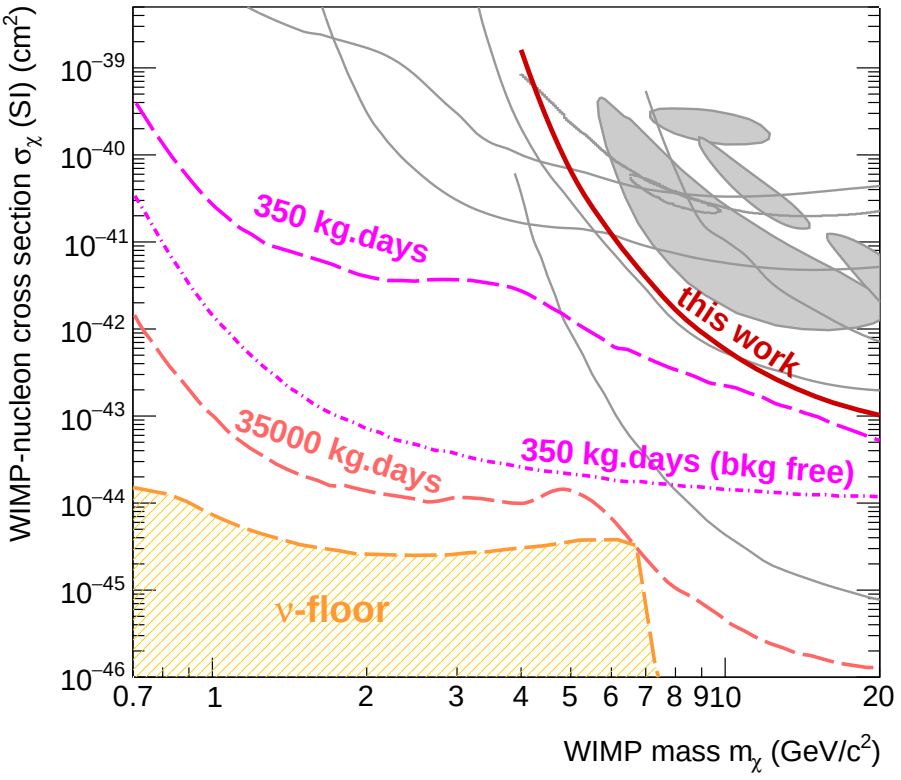

Figure 4.37.: Exclusion limit on the WIMP-nucleon scattering cross section found in this analysis presented in this in the context of future low mass WIMP searches with EDELWEISS (solid red line). The projected sensitivity for 350 kg·days of exposure with 100 V Neganov-Luke enhanced detectors and improved resolutions of 100 eV on heat and ionization channels is denoted with dashed magenta lines. The 35000 kg·days of exposure for a joint EDELWEISS and SuperCDMS experiment at SNOLAB could even be sensitive to solar neutrinos (orange shaded area).

were considered with intensities based on measured Run308 data, the background models which are used are somewhat simplified in terms of spectral shapes. One main difference to the analysis of real data presented in this thesis, is that a single dataset from a detector with averaged properties is modelled, compared to the more cumbersome combination of different detectors with individual peculiarities. The projected sensitivities are then given by the median of the expected limit from statistical fluctuations of the different Monte Carlo datasets. As has been shown in this thesis for Run308 data, any excess of a background component in the actual data leads to a degradation of the observed limit with respect to the projected sensitivity. These projections show, that with with a modest exposure and improvements in the achieved resolutions of heat and ionization channel in combination with a Neganov-Luke boosting of heat signals, EDELWEISS can significantly increase its sensitivity for low mass WIMPs of $m_\chi = 1 - 10\,\mathrm{GeV}/c^2$. A possible future beyond the measurements at the LSM underground laboratory is the installation of upgraded detectors in a cleaner environment in SNOLAB, in the framework of a collaboration between EURECA and SuperCDMS. The goal would be to push the sensitivity even further down to the neutrino floor, to explore low mass WIMP parameter space which is unknown and therefore shed more light on the nature of dark matter.

5. Conclusion

The nature of dark matter is one of the most fundamental open questions in modern physics. With the high precision measurement of the temperature fluctuations in the Cosmic Microwave Background, its fraction to the total energy density in the Universe has been measured as 27% [2] compared to only 5% from known baryonic matter. A favoured class of particle candidates to account for this dark matter are Weakly Interacting Massive Particles (WIMPs) with masses in the range of GeV/c^2 to TeV/c^2, which are found in extensions of the SM such as SuperSymmetry. Since the beginning of the 1980's, rare event search experiments have been established to directly measure WIMPs in an earth based detector via rare scattering processes of WIMPs off nuclei, but no convincing signal has been found so far.

Participating in this endeavour is the EDELWEISS experiment. In its 3rd phase, EDELWEISS-III employs up to 40 FID800 detectors. These are cylindrical germanium bolometers of ≈800 g mass each, which are cooled down to 18 mK. The experiment is installed in the LSM underground laboratory in the French-Italian Alps where 4800 m w.e. of overburden reduce the flux of cosmic-ray induced muons by a factor of more than 10^6. To reduce the background from natural radioactivity in the surrounding rock, the detector array is enclosed by several layers of passive and active shielding. The principle of the experiment is to measure the potential scattering of a dark matter halo WIMP on a Ge-nucleus, with an expected exponential recoil energy spectrum extending up to $\mathcal{O}(10)$ keV, depending on the WIMP mass m_χ and the atomic mass of Ge ($\langle A \rangle \approx 73$). Two Ge-NTD heat sensors on the detector's top and bottom surface measure the phonons related to the minuscule temperature increase of a particle recoiling in the detector, while 4 sets of ring electrodes on all surfaces collect the produced electric charges. The ratio of measured ionization to heat energy can then be used to discriminate on an event-by-event basis between a nuclear recoil from a WIMP or neutron, and the background of electron recoils produced by radiation from β's and γ's. The *Fully Inter Digitized* electrode design of the detectors with different sets of so-called *fiducial* and *veto* electrodes on all detector sides allows to define an inner fiducial volume and to efficiently reject particle interactions on the detector surface due to a signal on the veto electrodes. These surface interactions are of particular interest to suppress since, due to incomplete charge collection for these events, the background discrimination via the recoil type (electronic or nuclear) is diminished and they can mimic a signal.

The results of the EDELWEISS experiment have contributed significantly to the field of direct detection dark matter search and ruled out claims of potential signals in other

experiments. Previous analyses of EDELWEISS data [57, 58, 1] all used a cut-based principle to define a region of interest (RoI) with a high signal-to-background ratio and consider all events in it as WIMP candidates. Exclusion limits were then derived using either Yellin's optimum interval method [107] or simple Poisson statistics.
The multidimensional maximum likelihood analysis, which is performed in the framework of this thesis, is based on a more complex but rewarding strategy. It includes the full knowledge of different backgrounds and their uncertainty, and does not require a strict cut on the signal. As a result, the sensitivity for a potential signal increases significantly. For each detector, an unbinned maximum likelihood function $\mathcal{L}_\mathrm{j}(\sigma_\chi, \vec{\mu})$ is defined (Sec. 4.2.2). It describes different background components i, which are modelled as PDFs in the two considered observables for each event, the combined heat energy E_c and the fiducial ionization energy E_fid. The background PDFs ρ_i are each weighted with their respective event rates μ_i, while the weight of the signal PDF ρ_χ, constructed for each WIMP mass m_χ, is proportional to the WIMP-nucleon cross section σ_χ. The background rates μ_i are constrained with a Gaussian PDF each, as is the total event rate with respect to the observed number of events N.
An important feature of the analysis is the combination of multiple, individually described detectors via the combined likelihood function $\mathcal{L}_\mathrm{comb} = \prod_\mathrm{j} \mathcal{L}_\mathrm{j}$ (Sec. 4.2.3). This is a novel approach compared to what has been done previously in EDELWEISS analyses. Instead of combining the results of individual detector fits, a simultaneous fit of all data is performed, with a common parameter of interest, the WIMP-nucleon cross section σ_χ. Thanks to this method, anomalous event excess in single detectors can be distinguished from a signal.

A dataset optimized for low mass WIMP search was analysed with this maximum likelihood method. The data was recorded from 2014 to 2015, during the 10 months long WIMP search of EDELWEISS-III. Out of the 24 FID800 detectors taking data, 8 were selected due to their good performance at low energies. After rejection of low quality time intervals the dataset comprised a total livetime of 927 days. The RoI for WIMP search was defined in the two energy observables E_c and E_fid. The energy range was chosen as $E_\mathrm{c}^\mathrm{min} < E_\mathrm{c} < 15\,\mathrm{keV_{ee}}$ and $0 < E_\mathrm{fid} < 15\,\mathrm{keV_{ee}}$, where $E_\mathrm{c}^\mathrm{min}$ is the analysis threshold. As the EDELWEISS DAQ system triggers events on their heat signal, a conservative value for $E_\mathrm{c}^\mathrm{min}$ was chosen for each detector to ensure a high trigger efficiency $\epsilon_\mathrm{trigger} \geqslant 80\%$. The resulting threshold energies range from $0.91\,\mathrm{keV_{ee}}$ for the most sensitive detector FID824 up to $1.46\,\mathrm{keV_{ee}}$.
Thanks to these low analysis thresholds, even for a WIMP mass of $m_\chi = 5\,\mathrm{GeV}/c^2$ more than 1% of the signal is within the RoI of the analysis. This efficiency increases up to 60% for a mass of $m_\chi = 30\,\mathrm{GeV}/c^2$, while for WIMP masses smaller than $m_\chi \approx 4\,\mathrm{GeV}/c^2$, the hard energy spectrum of the interaction leads to heat energies below the analysis threshold.

The analysis of such low energy data requires a strategy to reject surface events, as the measured energy on the veto electrodes is of the order of the baseline noise. To be able to still select a clean sample of events from the bulk volume of the detector, we constructed a new, strict fiducial cut for each detector (Sec. 4.1.4). It is designed on purpose for the low energy region around 10 keV and rejects events with more than $E_\mathrm{veto} > 1.64\,\sigma_\mathrm{veto}$ on each of the veto electrodes. A rather high total acceptance of the cut of 81% was achieved as a trade-off between a high rejection efficiency and a reasonably large signal acceptance. The acceptance and effective fiducial mass for each detector after this cut was determined by fitting cosmogenic events, which are homogeneously distributed within the detector. A resulting effective fiducial fraction of on average $f_\mathrm{fid} = (61.1 \pm 0.8)\%$ was found. After this cut, the combined exposure of the analysis is 496 kg·days for the 8 selected detectors, and a total of $N = 50{,}062$ events are left after all cuts. While the exposure is reduced by ≈20% compared to the BDT analysis [1] of the same selected livetime periods, this fiducial cut is the only additional cut in this analysis and no further reduction of the signal efficiency is necessary, in contrast to the strict BDT-cuts in [1].

To perform a maximum likelihood analysis, a crucial requirement is the detailed modelling of the backgrounds. For each detector, a total of 20 components for backgrounds arising in different parts of a single detector were implemented as PDFs in the likelihood model. These PDFs were constructed in the two observables E_c and E_{fid} using a detector response model. It includes efficiencies related to the DAQ trigger and the fiducial cut, as well as energy dependent resolution effects related to charge trapping in the crystal. The primary input for these PDFs is the differential energy spectrum of a background in either recoil energy E_{rec} or heat energy E_c. An additional important parameter is the ionization yield Q of a particle, defined as the fraction of ionization over recoil energy. The following categories of background events were included in the likelihood model:

- electron recoils in the fiducial volume, either produced by Compton scattered γ's (from external radiation), by X-rays (from the decay of cosmogenic isotopes) or by β's (from the decay of cosmogenic tritium),
- nuclear recoils from radiogenic neutrons,
- so-called *heat-only* events with a clear heat signal but only noise on the ionization channels,
- low energy surface events from β's and ^{206}Pb-recoils which were not fully rejected by the fiducial cut.

For each of these backgrounds, the energy spectrum was extracted either from sideband data or, in the case of radiogenic neutrons and β's from tritium decay, via Monte Carlo simulations and theory, respectively. Consequently, the rate of expected events in the RoI could be calculated and constrained within systematic uncertainties.

Three important observations have been made during the phase of background modelling, leading to significant improvements in the general understanding of the EDELWEISS data analysis:

1. We found that the distribution of heat-only events, the dominant background in terms of intensity, is not centred at $E_{fid} = 0$, as expected from ionization-less events, but biased towards higher ionization energies E_{fid}. This effect, most likely related to uncorrected cross-talk of the ionization readout channels, induces a significant uncertainty on the prediction of this important background for low mass WIMP search. It was incorporated as a relative systematic uncertainty of up to 15% in the constraint for each detector.

2. Thanks to the low overall rate of the Compton γ-background and the excellent energy resolution of the FID800-detectors, EDELWEISS-III is the first experiment to perform a convincing measurement of the β-decay of cosmogenic tritium in germanium [100]. In the context of modelling the electron recoil background from sideband data, this tritium component has been determined independently in this analysis. The extrapolated total rate for the 496 kg·days of exposure was determined as

$$\Gamma_{\text{tritium}} = 1.01 \pm 0.13\,\text{events/kg/day} \tag{5.1}$$

   which is in agreement with the value of 1.18 ± 0.13 events/kg/day found in [100] for the same 8 detectors within statistical and systematic uncertainties[1].

[1] For a total of 17 detectors and 1894 live-days, the tritium rate measured in [100] is larger, with 1.60 ± 0.10 events/kg/day.

3. For background components from unrejected surface events, the detector dependent values of the ionization yield Q have been determined from sideband data. It was shown that the value of Q for surface β's from the ^{210}Pb decay chain varies between 0.29 and 0.45. This effect shows a clear correlation with the detector production number and is most likely related to different types of surface treatment.

After a detailed modelling of all considered background components as PDFs, the likelihood function $\mathcal{L}$ was constructed for each detector. Due to the dependence of the signal PDF $\rho_\chi(m_\chi)$ on the WIMP mass m_χ, this was calculated for a selection of WIMP masses $m_\chi \in [4, 30]\,\mathrm{GeV}/c^2$. All astrophysical parameters which enter the calculation of the nuclear recoil spectrum of WIMPs in the detector were set to their standard halo model values.

No statistically significant signal was found for any of the fitted likelihood functions $\mathcal{L}$. For 3 of the individually fitted detectors, in particular the most sensitive detector FID824, best fit values for σ_χ corresponding to $\mu = 0.0$ events were observed for all probed WIMP masses (see Tab. 4.6). The best fits for other detectors showed a degeneracy between the signal and the fitted event rate of different backgrounds, for example a clear correlation between heat-only events and a WIMP signal with $m_\chi < 10\,\mathrm{GeV}/c^2$. These degeneracies can be effectively suppressed by performing the simultaneous fit of all data with the combined likelihood function $\mathcal{L}_{\mathrm{comb}}$ and a common signal cross section σ_χ. The method thus effectively addresses the problem, that uncertainties in the background model of one detector can lead to a misinterpreted signal, whereas WIMPs are expected to interact homogeneously in the detector array.
Also, the combined fit is compatible with the background-only hypothesis within $< 2\sigma$ uncertainty for all m_χ. In particular, for the two lowest masses of $m_\chi = 4\,\mathrm{GeV}/c^2$ and $m_\chi = 5\,\mathrm{GeV}/c^2$ the fitted signal rate is compatible with zero within numerical precision. For larger masses m_χ, the presence of 5 events with $E_\mathrm{c} > 2\,\mathrm{keV_{ee}}$ in the region for nuclear recoils (see Fig. 4.9) leads to a fitted signal corresponding to a rate of at most $\mu_\chi^{\mathrm{comb}} = 12.0^{+11.7}_{-8.5}$ for $m_\chi = 7\,\mathrm{GeV}/c^2$. These events are also present in the BDT analysis [1] and are likely to be radiogenic neutrons. For this type of background, the expected rate of single scattering events in the RoI was derived from the EDELWEISS-III analysis for standard mass WIMPs (Sec. 3.2). In that analysis, 9 events with scattering in multiple detectors were measured for a total exposure of 1309 kg·days. With the expected single-over-multiple scattering ratio of $0.45 \pm 20\%$ and the energy spectrum from simulations, a total expected neutron background of 1.60 ± 0.72 was derived for this analysis and is statistically compatible with the observed events. Due to the implementation of the expected neutron rate as a constraint on the basis of individual detectors, this background is preferably fitted as a signal for WIMP masses $m_\chi \geq 7\,\mathrm{GeV}/c^2$, leading to a small excess in the signal rate.

In the absence of a statistically significant signal, an exclusion limit was set on the WIMP-nucleon scattering cross section σ_χ as a function of WIMP mass m_χ. The limit was derived with a so-called *hypothesis test* based on the profile likelihood ratio. Typically, a statistical approximation is used to calculate these exclusion limits, as e.g. in [114] and [116]. Computing-extensive studies with Monte Carlo toy data were performed to validate this approximation for the likelihood model applied in this analysis. It could be shown that, for the smallest m_χ, the approximation does not result in the correct frequentist coverage and the limit has a confidence level smaller than 90%. Consequently, the limit was derived using Monte Carlo data, leading to a correction compared to the statistical approximation of up to 60% for both individual detectors (at high masses m_χ) and the combined fit (at low masses m_χ, see Sec. 4.4.3). The resulting exclusion limit on the spin-independent WIMP-nucleon cross section σ_χ for the entire dataset is shown in Fig. 4.35. The two

extreme values are:

$$\begin{aligned}\sigma_\chi^{\mathrm{up}} &< 1.6 \times 10^{-39}\,\mathrm{cm}^2 \ (90\%\,\mathrm{C.L.}) \text{ for } m_\chi = 4\,\mathrm{GeV}/c^2 \text{ and} \\ \sigma_\chi^{\mathrm{up}} &< 6.9 \times 10^{-44}\,\mathrm{cm}^2 \ (90\%\,\mathrm{C.L.}) \text{ for } m_\chi = 30\,\mathrm{GeV}/c^2\end{aligned} \tag{5.2}$$

For the lowest WIMP masses $m_\chi \approx 4 - 6\,\mathrm{GeV}/c^2$ the limit is stricter than the expected sensitivity of the experiment, due to the low background observed in the most sensitive detector. At higher WIMP masses, $m_\chi > 7\,\mathrm{GeV}/c^2$, a $\approx 2\sigma$ excess is caused by the onset of the radiogenic neutron background in the experiment. Over the entire probed mass range, the limit allows to confidently exclude the existing claims of a potential signal from CDMS-Si [106], DAMA/LIBRA [104], CRESST-II [50] and CoGeNT [105].
Compared to the cut based analysis in [1], the limit derived at $m_\chi = 4\,\mathrm{GeV}/c^2$ represents an improvement by factor of ≈ 7. The improvement is based on the >10 times higher signal efficiency due to the absence of an additional signal cut, as well as the subtraction of background.

The analysis performed in the framework of this thesis is the first application of a multi-dimensional likelihood in EDELWEISS. It employs a consistent combination of detectors to reduce individual uncertainties in the background modelling. A clear improvement in sensitivity for low WIMP masses was achieved with the detailed modelling of all relevant backgrounds and their subtraction within constrained uncertainties. The exclusion limit which was derived is competitive with current results from SuperCMDS [48] above $m_\chi = 6\,\mathrm{GeV}/c^2$.
The principle of maximum likelihood which was applied in this thesis is a new analysis tool for the future low mass WIMP search in EDELWEISS. Sensitivity projections based on the maximum likelihood of a simplified detector model were performed in the context of [119] and are used to set the roadmap for the development of EDELWEISS. They showed (see Fig. 4.37) that, with the current detector technology in combination with improved resolutions, reduced low energy background and the boosting of signals via the Neganov-Luke effect, EDELWEISS can further increase significantly its sensitivity towards low mass WIMPs of $m_\chi = 1 - 10\,\mathrm{GeV}/c^2$ and test this yet unexplored parameter range for dark matter particles.

Bibliography

[1] Armengaud, E.; Arnaud, Q.; Augier, C.; et al. *Constraints on low-mass WIMPs from the EDELWEISS-III dark matter search.* J. Cosmol. Astropart. Phys., 2016(05):019–019, may 2016. doi:10.1088/1475-7516/2016/05/019.

[2] Planck Collaboration; Adam, R.; Ade, P.a.R.; et al. *Planck 2015 results. I. Overview of products and scientific results.* Astron. Astrophys., 571:A1, feb 2015.

[3] Jeans, J.H. *The Motions of Stars in a Kapteyn-Universe.* Mon. Not. R. Astron. Soc., 82(3):122–132, jan 1922. doi:10.1093/mnras/82.3.122.

[4] Zwicky, F. *Die rotverschiebung von extragalaktischen nebeln.* Helv. Phys. Acta, 1933.

[5] Alpher, R.; Bethe, H.; and Gamow, G. *The Origin of Chemical Elements.* Phys. Rev., 73(7):803–804, apr 1948. doi:10.1103/PhysRev.73.803.

[6] Penzias, A. and Wilson, R. *A Measurement of Excess Antenna Temperature at 4080 Mc/s.* Astrophys. J., 1965.

[7] Bennett, C.L.; Banday, A.; Gorski, K.M.; et al. *4-Year COBE DMR Cosmic Microwave Background Observations: Maps and Basic Results.* Astrophys. J., 464(1):L1–L4, jan 1996. doi:10.1086/310075.

[8] Jarosik, N.; Bennett, C.L.; Dunkley, J.; et al. *Seven-Year Wilkinson Microwave Anisotropy Probe (WMAP) Observations: Sky Maps, Systematic Errors, and Basic Results.* Astrophys. J. Suppl. Ser., 192(2):14, jan 2010. doi:10.1088/0067-0049/192/2/14.

[9] Clowe, D.; Bradač, M.; Gonzalez, A.H.; et al. *A Direct Empirical Proof of the Existence of Dark Matter.* Astrophys. J., 648(2):L109–L113, sep 2006.

[10] Rubin, V.C. and Ford, W. Kent, J. *Rotation of the Andromeda Nebula from a Spectroscopic Survey of Emission Regions.* Astrophys. J., 159:379, feb 1970. doi:10.1086/150317.

[11] Navarro, J.F.; Frenk, C.S.; and White, S.D.M. *A Universal Density Profile from Hierarchical Clustering.* Astrophys. J., 490(2):493–508, dec 1997. doi:10.1086/304888.

[12] Sofue, Y. *Grand Rotation Curve and Dark-Matter Halo in the Milky Way Galaxy.* Publ. Astron. Soc. Japan, 64(4):75, 2012. doi:10.1093/pasj/64.4.75.

[13] Corbelli, E. and Salucci, P. *The extended rotation curve and the dark matter halo of M33.* Mon. Not. R. Astron. Soc., 311(2):441–447, jan 2000. doi:10.1046/j.1365-8711.2000.03075.x.

[14] Milgrom, M. *A modification of the Newtonian dynamics as a possible alternative to the hidden mass hypothesis.* Astrophys. J., 1983.

[15] Milgrom, M. *MOND theory 1.* Can. J. Phys., 93(2):107–118, feb 2015. doi:10.1139/cjp-2014-0211.

[16] Monroy-Rodríguez, M.A. and Allen, C. *The end of the MACHO era- revisited: new limits on MACHO masses from halo wide binaries.* pages 1–25, 2014. doi: 10.1088/0004-637X/790/2/159.

[17] Peccei, R.D. and Quinn, H.R. *CP Conservation in the Presence of Pseudoparticles.* Phys. Rev. Lett., 38(25):1440–1443, jun 1977. doi:10.1103/PhysRevLett.38.1440.

[18] Peccei, R.D. and Quinn, H.R. *Constraints imposed by CP conservation in the presence of pseudoparticles.* Phys. Rev. D, 16(6):1791–1797, sep 1977. doi:10.1103/PhysRevD.16.1791.

[19] Weinberg, S. *A New Light Boson?* Phys. Rev. Lett., 40(4):223–226, jan 1978. doi:10.1103/PhysRevLett.40.223.

[20] Graham, P.W.; Irastorza, I.G.; Lamoreaux, S.K.; et al. *Experimental Searches for the Axion and Axion-Like Particles.* Annu. Rev. Nucl. Part. Sci., 65(1):485–514, oct 2015. doi:10.1146/annurev-nucl-102014-022120.

[21] Asztalos, S.J.; Carosi, G.; Hagmann, C.; et al. *SQUID-Based Microwave Cavity Search for Dark-Matter Axions.* Phys. Rev. Lett., 104(4):4, jan 2010. doi:10.1103/PhysRevLett.104.041301.

[22] Arik, M.; Aune, S.; Barth, K.; et al. *New solar axion search using the CERN Axion Solar Telescope with ^{4}He filling.* Phys. Rev. D - Part. Fields, Gravit. Cosmol., 92(2):1–6, 2015. doi:10.1103/PhysRevD.92.021101.

[23] Ehret, K.; Frede, M.; Ghazaryan, S.; et al. *Resonant laser power build-up in ALPS-A "light shining through a wall" experiment.* Nucl. Instruments Methods Phys. Res. Sect. A Accel. Spectrometers, Detect. Assoc. Equip., 612(1):83–96, 2009. doi:10.1016/j.nima.2009.10.102.

[24] Armengaud, E.; Arnaud, Q.; Augier, C.; et al. *Axion searches with the EDELWEISS-II experiment.* J. Cosmol. Astropart. Phys., 2013(11):067–067, nov 2013. doi:10.1088/1475-7516/2013/11/067.

[25] Jungman, G.; Kamionkowski, M.; and Griest, K. *Supersymmetric dark matter.* Phys. Rep., 267(5-6):195–373, 1996. doi:10.1016/0370-1573(95)00058-5.

[26] Wess, J. and Zumino, B. *Supergauge transformations in four dimensions.* Nucl. Physics, Sect. B, 70(1):39–50, 1974. doi:10.1016/0550-3213(74)90355-1.

[27] Feng, J.L. *Dark Matter Candidates from Particle Physics and Methods of Detection.* Annu. Rev. Astron. Astrophys., 48(1):495–545, 2010. doi:10.1146/annurev-astro-082708-101659.

[28] Hooper, D. and Linden, T. *Origin of the gamma rays from the Galactic Center.* Phys. Rev. D - Part. Fields, Gravit. Cosmol., 84(12):1–13, 2011. doi:10.1103/PhysRevD.84.123005.

[29] Lee, B.W. and Weinberg, S. *Cosmological Lower Bound on Heavy-Neutrino Masses.* Phys. Rev. Lett., 39(4):165–168, jul 1977. doi:10.1103/PhysRevLett.39.165.

[30] Petraki, K. and Volkas, R.R. *Review of asymmetric dark matter.* Int. J. Mod. Phys. A, 28(19):1330028, may 2013. doi:10.1142/S0217751X13300287.

[31] Undagoitia, T.M. and Rauch, L. *Dark matter direct-detection experiments.* J. Phys. G Nucl. Part. Phys., 43(1):013001, jan 2016. doi:10.1088/0954-3899/43/1/013001.

[32] Khachatryan, V.; Sirunyan, A.M.; Tumasyan, A.; et al. *Search for dark matter, extra dimensions, and unparticles in monojet events in proton–proton collisions at $\sqrt{s} = 8$ TeV.* Eur. Phys. J. C, 75(5), aug 2015. doi:10.1140/epjc/s10052-015-3451-4.

[33] Adriani, O. and Others. *Observation of an anomalous positron abundance in the cosmic radiation.* Nature, 458:607–609, 2009. doi:10.1038/nature07942.

[34] Ackermann, M.; Ajello, M.; Allafort, A.; et al. *Measurement of Separate Cosmic-Ray Electron and Positron Spectra with the Fermi Large Area Telescope.* Phys. Rev. Lett., 108(1):011103, jan 2012. doi:10.1103/PhysRevLett.108.011103.

[35] Accardo, L.; Aguilar, M.; Aisa, D.; et al. *High statistics measurement of the positron fraction in primary cosmic rays of 0.5-500 GeV with the alpha magnetic spectrometer on the international space station.* Phys. Rev. Lett., 113(12):1–10, 2014. doi:10.1103/PhysRevLett.113.121101.

[36] Gaskins, J.M. *A review of indirect searches for particle dark matter.* Contemp. Phys., 57(1):60–82, mar 2016. doi:10.1080/00107514.2015.1063233.

[37] Lewin, J. and Smith, P. *Review of mathematics, numerical factors, and corrections for dark matter experiments based on elastic nuclear recoil.* Astropart. Phys., 6(1):87–112, dec 1996. doi:10.1016/S0927-6505(96)00047-3.

[38] Savage, C.; Freese, K.; and Gondolo, P. *Annual Modulation of Dark Matter in the Presence of Streams.* Nucl. Phys. B - Proc. Suppl., 173(4):91–94, jul 2007. doi:10.1016/j.nuclphysbps.2007.08.032.

[39] Frandsen, M.T.; Kahlhoefer, F.; McCabe, C.; et al. *The unbearable lightness of being: CDMS versus XENON.* J. Cosmol. Astropart. Phys., 2013(07):023–023, jul 2013. doi:10.1088/1475-7516/2013/07/023.

[40] Amaré, J.; Cebrián, S.; Cuesta, C.; et al. *From ANAIS-25 towards ANAIS-250.* Phys. Procedia, 61:157–162, 2015. doi:10.1016/j.phpro.2014.12.026.

[41] Cherwinka, J.; Grant, D.; Halzen, F.; et al. *First data from DM-Ice17.* Phys. Rev. D - Part. Fields, Gravit. Cosmol., 90(9):1–14, 2014. doi:10.1103/PhysRevD.90.092005.

[42] Kim, S.C.; Bhang, H.; Choi, J.H.; et al. *New limits on interactions between weakly interacting massive particles and nucleons obtained with CsI(Tl) crystal detectors.* Phys. Rev. Lett., 108(18):2–6, 2012. doi:10.1103/PhysRevLett.108.181301.

[43] Aalseth, C.E.; Barbeau, P.S.; Colaresi, J.; et al. *Search for An Annual Modulation in Three Years of CoGeNT Dark Matter Detector Data.* 4:1–8, jan 2014.

[44] Giovanetti, G.K.; Abgrall, N.; Aguayo, E.; et al. *A Dark Matter Search with MALBEK.* 00:1–8, 2014.

[45] Liu, S.K.; Yue, Q.; Kang, K.J.; et al. *Limits on light WIMPs with a germanium detector at 177 eVee threshold at the China Jinping Underground Laboratory.* Phys. Rev. D - Part. Fields, Gravit. Cosmol., 90(3):1–5, 2014. doi:10.1103/PhysRevD.90.032003.

[46] Ahmed, Z.; Akerib, D.S.; Arrenberg, S.; et al. *Results from the Final Exposure of the CDMS II Experiment.* Search.

[47] Agnese, R.; Ahmed, Z.; Anderson, A.J.; et al. *Silicon detector results from the first five-tower run of CDMS II.* Phys. Rev. D, 88(3):031104, aug 2013. doi:10.1103/PhysRevD.88.031104.

[48] Agnese, R.; Anderson, A.J.; Asai, M.; et al. *Search for Low-Mass Weakly Interacting Massive Particles with SuperCDMS.* Phys. Rev. Lett., 112(24):241302, jun 2014. doi:10.1103/PhysRevLett.112.241302.

[49] Agnese, R.; Anderson, A.J.; Aramaki, T.; et al. *New Results from the Search for Low-Mass Weakly Interacting Massive Particles with the CDMS Low Ionization Threshold Experiment.* Phys. Rev. Lett., 116(7):071301, feb 2016. doi:10.1103/PhysRevLett.116.071301.

[50] Angloher, G.; Bauer, M.; Bavykina, I.; et al. *Results from 730 kg days of the CRESST-II Dark Matter search.* Eur. Phys. J. C, 72(4):1971, apr 2012. doi:10.1140/epjc/s10052-012-1971-8.

[51] Angloher, G.; Bento, A.; Bucci, C.; et al. *Results on light dark matter particles with a low-threshold CRESST-II detector.* Eur. Phys. J. C, 76(1):25, jan 2016. doi:10.1140/epjc/s10052-016-3877-3.

[52] XENON100 Collaboration; Aprile, E.; Alfonsi, M.; et al. *Dark Matter Results from 225 Live Days of XENON100 Data.* Phys. Rev. Lett., 109(18):6, jul 2012. doi:10.1103/PhysRevLett.109.181301.

[53] Akerib, D.; Bai, X.; Bedikian, S.; et al. *The Large Underground Xenon (LUX) experiment.* Nucl. Instruments Methods Phys. Res. Sect. A Accel. Spectrometers, Detect. Assoc. Equip., 704:111–126, mar 2013. doi:10.1016/j.nima.2012.11.135.

[54] Hiraide, K. *XMASS: Recent results and status for the XMASS Collaboration.* pages 11–15, 2015.

[55] O'Hare, C.A.J.; Green, A.M.; Billard, J.; et al. *Readout strategies for directional dark matter detection beyond the neutrino background.* Phys. Rev. D, 92(6):063518, sep 2015. doi:10.1103/PhysRevD.92.063518.

[56] Sanglard, V.; Benoit, A.; Bergé, L.; et al. *Final results of the EDELWEISS-I dark matter search with cryogenic heat-and-ionization Ge detectors.* Phys. Rev. D, 71(12):122002, jun 2005. doi:10.1103/PhysRevD.71.122002.

[57] Armengaud, E.; Augier, C.; Benoît, A.; et al. *Final results of the EDELWEISS-II WIMP search using a 4-kg array of cryogenic germanium detectors with interleaved electrodes.* Phys. Lett. B, 702(5):329–335, aug 2011. doi:10.1016/j.physletb.2011.07.034.

[58] Armengaud, E.; Augier, C.; Benoît, A.; et al. *Search for low-mass WIMPs with EDELWEISS-II heat-and-ionization detectors.* Phys. Rev. D, 86(5):051701, sep 2012. doi:10.1103/PhysRevD.86.051701.

[59] Simard, L. *The NEMO-3 experiment and the SuperNEMO project.* Prog. Part. Nucl. Phys., 64(2):270–272, apr 2010. doi:10.1016/j.ppnp.2009.12.026.

[60] Schmidt, B.; Armengaud, E.; Augier, C.; et al. *Muon-induced background in the EDELWEISS dark matter search.* Astropart. Phys., 44:28–39, apr 2013. doi:10.1016/j.astropartphys.2013.01.014.

[61] Kéfélian, C. *Search for dark matter with EDELWEISS-III excluding background from muon-induced neutrons.* Phd thesis, UCBL and KIT, 2016.

[62] L'Hour, M. *Un site sous-marin sur la côte de l'Armorique. L'épave antique de Ploumanac'h.* Rev. archéologique l'ouest, 4(1):113–131, 1987. doi:10.3406/rao.

[63] Schmidt, B. *Background discrimination of EDELWEISS-III cryogenic Ge-detectors for dark matter search.* Ph.D. thesis, 2015.

[64] Armengaud, E.; Augier, C.; Benoit, A.; et al. *Background studies for the EDELWEISS dark matter experiment.* Astropart. Phys., 47:1–9, jul 2013. doi:10.1016/j.astropartphys.2013.05.004.

[65] Hehn, L. *Suche nach einer jahreszeitlichen Modulation der EDELWEISS-2 Ereignisrate als Signal Dunkler Materie.* Diploma thesis, KIT, 2012.

[66] Zhang, X. *A Novel Phonon-Scintillation Cryogenic Detector and Cabling Solution for Dark Matter Direct Detection.* Ph.D. thesis, Oxford University, 2015.

[67] Censier, B.; Benoit, A.; Bres, G.; et al. *EDELWEISS read-out electronics and future prospects.* J. Low Temp. Phys., 167(5-6):645–651, 2012. doi:10.1007/s10909-012-0568-9.

[68] Klein, C.A. *Bandgap Dependence and Related Features of Radiation Ionization Energies in Semiconductors.* J. Appl. Phys., 39(4):2029, 1968. doi:10.1063/1.1656484.

[69] Billard, J.; De Jesus, M.; Juillard, A.; et al. *Characterization and Optimization of EDELWEISS-III FID800 Heat Signals.* J. Low Temp. Phys., feb 2016. doi:10.1007/s10909-016-1500-5.

[70] Chen, P. *Dark energy and the hierarchy problem.* Nucl. Phys. B - Proc. Suppl., 173:137–140, 2007. doi:10.1016/j.nuclphysbps.2007.08.038.

[71] Luke, P.N. *Voltage-assisted calorimetric ionization detector.* J. Appl. Phys., 64(12):6858, 1988. doi:10.1063/1.341976.

[72] Neganov, B. and Trofimov, V. *USSR Pat. No 1037771*, 1985.

[73] Lindhard, J.; Nielsen, V.; Scharff, M.; et al. *Integral equations governing radiation effects.* Mat. Fys. Medd. Dan. Vid. Selsk., 33(10), 1963.

[74] Di Stefano, P.; Bergé, L.; Chambon, B.; et al. *Background discrimination capabilities of a heat and ionization germanium cryogenic detector.* Astropart. Phys., 14(4):329–337, jan 2001. doi:10.1016/S0927-6505(00)00127-4.

[75] Lazanu, I. and Lazanu, S. *Contribution of the electron-phonon interaction to Lindhard energy partition at low energy in Ge and Si detectors for astroparticle physics applications.* Astropart. Phys., 75:44–54, 2016. doi:10.1016/j.astropartphys.2015.09.007.

[76] Gascon, J. and Bastidon, N. *The EDELWEISS-III project and the rejection performance of its cryogenic germanium detectors.* J. Low Temp. Phys., 176(5-6):870–875, 2014. doi:10.1007/s10909-014-1096-6.

[77] Censier, B.; Broniatowski, a.; Juillard, a.; et al. *Surface trapping and detector degradation in Ge bolometers for the EDELWEISS Dark Matter search: experiment and simulation.* Nucl. Instruments Methods Phys. Res. Sect. A Accel. Spectrometers, Detect. Assoc. Equip., 520(1-3):156–158, mar 2004.

[78] Broniatowski, A.; Defay, X.; Armengaud, E.; et al. *A new high-background-rejection dark matter Ge cryogenic detector.* Phys. Lett. B, 681(4):305–309, nov 2009. doi:10.1016/j.physletb.2009.10.036.

[79] Marnieros, S.; Bergé, L.; Broniatowski, A.; et al. *Controlling the Leakage-Current of Low Temperature Germanium Detectors Using XeF_2 Dry Etching.* J. Low Temp. Phys., 176(3-4):182–187, 2014. doi:10.1007/s10909-013-0997-0.

[80] Broniatowski, A. *Intervalley scattering of hot electrons in germanium at millikelvin temperatures.* J. Low Temp. Phys., 176(5-6):860–869, 2014. doi:10.1007/s10909-014-1091-y.

[81] Siebenborn, B. *Discrimination of surface events with time resolved ionization channels in the EDELWEISS dark matter search.* Ph.D. thesis, KIT, 2016.

[82] Kopmann, A.; Bergmann, T.; Gemmeke, H.; et al. *FPGA-based DAQ system for multi-channel detectors.* IEEE Nucl. Sci. Symp. Conf. Rec., pages 3186–3190, 2008. doi:10.1109/NSSMIC.2008.4775027.

[83] Gemmeke, H.; Kleifges, M.; Kopmann, A.; Kunka, N.; Menchikov, A.; Tcherniakhovski, D. *First Measurements with the AUGER Fluorescence Detector Data Acquisition System.* In *ICRC*, page 769. nov 2001.

[84] Steinbrink, N.; Hannen, V.; Martin, E.L.; et al. *Neutrino mass sensitivity by MAC-E-Filter based time-of-flight spectroscopy with the example of KATRIN.* New J. Phys., 15(11):113020, nov 2013. doi:10.1088/1367-2630/15/11/113020.

[85] Butterworth, S. *On the theory of filter amplifiers.* Exp. Wirel. Wirel. Eng., 7:536–541, 1930.

[86] Main de Boissière, T. *Low mass WIMP search with EDELWEISS-III: First Results.* arxiv:1504.00820, apr 2015.

[87] Bird, I.; Robertson, L.; and Shiers, J. *Deploying the LHC Computing Grid - The LCG Service Challenges.* In *2005 IEEE Int. Symp. Mass Storage Syst. Technol.*, pages 160–165. IEEE, 2005. doi:10.1109/LGDI.2005.1612486.

[88] Cox, G.; Armengaud, E.; Augier, C.; et al. *A multi-tiered data structure and process management system based on ROOT and CouchDB.* Nucl. Instruments Methods Phys. Res. Sect. A Accel. Spectrometers, Detect. Assoc. Equip., 684:63–72, aug 2012. doi:10.1016/j.nima.2012.04.049.

[89] Angloher, G.; Armengaud, E.; Augier, C.; et al. *EURECA Conceptual Design Report.* Phys. Dark Universe, 3:41–74, apr 2014. doi:10.1016/j.dark.2014.03.004.

[90] The Apache Software Foundation. *CouchDB.* `http://couchdb.apache.org/`, 2016.

[91] IBM Cloudant. *IBM Corporation.* `https://cloudant.com/`, 2016.

[92] Chesneau, B. *Couchdbkit.* `http://couchdbkit.org/`, 2016.

[93] Watson, R. and Coyne, R. *The parallel I/O architecture of the high-performance storage system (HPSS).* In *Proc. IEEE 14th Symp. Mass Storage Syst.*, pages 27–44. IEEE Comput. Soc. Press, 1995. doi:10.1109/MASS.1995.528214.

[94] Chazal, V.; Brissot, R.; Cavaignac, J.; et al. *Neutron background measurements in the Underground Laboratory of Modane.* Astropart. Phys., 9(2):163–172, 1998. doi:10.1016/S0927-6505(98)00012-7.

[95] Rozov, S.; Armengaud, E.; Augier, C.; et al. *Monitoring of the thermal neutron flux in the LSM underground laboratory.* Bull. Russ. Acad. Sci. Phys., 74(4):464–466, 2012.

[96] Lemrani, R.; Gerbier, G.; and EDELWEISS Collaboration. *Update of neutron studies in EDELWEISS.* J. Phys. Conf. Ser., 39:145–147, 2006. doi:10.1088/1742-6596/39/1/033.

[97] Scorza, S. *Background investigation in EDELWEISS-III.* In *AIP Conf. Proc.*, page 100002. 2015. doi:10.1063/1.4928002.

[98] Bahcall, J.N. *Exchange and overlap effects in electron capture and in related phenomena.* Phys. Rev., 132(1):362–367, 1963. doi:10.1103/PhysRev.132.362.

[99] International Atomic Energy Agency (IAEA). *NuDat 2.* `http://www.nndc.bnl.gov/nudat2/`, 2015.

[100] Armengaud, E.; Arnaud, Q.; Augier, C.; et al. *Observation of tritium β decay from cosmogenic activation in the volume of cryogenic germanium detectors, in preparation.*

[101] Miley, H.; Avignone, F.; Brodzinski, R.; et al. *New techniques and results in ^{76}Ge double-beta decay.* Nucl. Phys. B - Proc. Suppl., 28(1):212–215, jul 1992. doi: 10.1016/0920-5632(92)90172-O.

[102] Mei, D.M.; Yin, Z.B.; and Elliott, S. *Cosmogenic production as a background in searching for rare physics processes.* Astropart. Phys., 31(6):417–420, jul 2009.

[103] Agnese, R.; Anderson, A.J.; Balakishiyeva, D.; et al. *Demonstration of surface electron rejection with interleaved germanium detectors for dark matter searches.* Appl. Phys. Lett., 103(16):1–5, 2013. doi:10.1063/1.4826093.

[104] Bernabei, R.; Belli, P.; Cappella, F.; et al. *Final model independent result of DAMA/LIBRA-phase1.* Eur. Phys. J. C, 73(12):2648, dec 2013. doi:10.1140/epjc/s10052-013-2648-7.

[105] Aalseth, C.E.; Barbeau, P.S.; Bowden, N.S.; et al. *Results from a Search for Light-Mass Dark Matter with a P-type Point Contact Germanium Detector.* Phys. Rev. Lett., 106(13):4, feb 2010. doi:10.1103/PhysRevLett.106.131301.

[106] Agnese, R.; Ahmed, Z.; Anderson, A.J.; et al. *Silicon Detector Dark Matter Results from the Final Exposure of CDMS II.* Phys. Rev. Lett., 111(25):251301, dec 2013. doi:10.1103/PhysRevLett.111.251301.

[107] Yellin, S. *Finding an Upper Limit in the Presence of Unknown Background.* Phys. Rev. D, 66(3):8, mar 2002. doi:10.1103/PhysRevD.66.032005.

[108] Feldman, G.J. *Unified approach to the classical statistical analysis of small signals.* Phys. Rev. D, 57(7):3873–3889, apr 1998. doi:10.1103/PhysRevD.57.3873.

[109] Yellin, S. *Extending the optimum interval method.* arxiv:0709.2701, 2007.

[110] Yellin, S. *Some ways of combining optimum interval upper limits.* arxiv:1105.2928, 2011.

[111] Ahmed, Z.; Akerib, D.S.; Armengaud, E.; et al. *Combined limits on WIMPs from the CDMS and EDELWEISS experiments.* Phys. Rev. D, 84(1):011102, jul 2011. doi:10.1103/PhysRevD.84.011102.

[112] Angloher, G.; Bento, A.; Bucci, C.; et al. *Results on low mass WIMPs using an upgraded CRESST-II detector.* Eur. Phys. J. C, 74(12):3184, dec 2014. doi: 10.1140/epjc/s10052-014-3184-9.

[113] Amole, C.; Ardid, M.; Asner, D.M.; et al. *Dark Matter Search Results from the PICO-2L C_3F_8 Bubble Chamber.* Phys. Rev. Lett., 114(23):231302, feb 2015. doi: 10.1103/PhysRevLett.114.231302.

[114] Aprile, E.; Arisaka, K.; Arneodo, F.; et al. *Likelihood approach to the first dark matter results from XENON100.* Phys. Rev. D, 84(5):052003, sep 2011. doi:10.1103/PhysRevD.84.052003.

[115] Akerib, D.S.; Araújo, H.M.; Bai, X.; et al. *First Results from the LUX Dark Matter Experiment at the Sanford Underground Research Facility.* Phys. Rev. Lett., 112(9):091303, mar 2014. doi:10.1103/PhysRevLett.112.091303.

[116] Akerib, D.S.; Araújo, H.M.; Bai, X.; et al. *Improved Limits on Scattering of Weakly Interacting Massive Particles from Reanalysis of 2013 LUX Data.* Phys. Rev. Lett., 116(16):161301, apr 2016. doi:10.1103/PhysRevLett.116.161301.

[117] Agnese, R.; Anderson, A.J.; Balakishiyeva, D.; et al. *Maximum likelihood analysis of low energy CDMS II germanium data.* Phys. Rev. D, 91(5):052021, mar 2015. doi:10.1103/PhysRevD.91.052021.

[118] Therhaag, J. and TMVA Core Developer Team. *TMVA - Toolkit for multivariate data analysis.* In *AIP Conf. Proc.*, volume 1504, pages 1013–1016. 2012. doi:10.1063/1.4771869.

[119] Arnaud, Q. *Détection directe de matière noire avec l'expérience EDELWEISS-III : Etude des signaux induits par le piégeage de charges, analyse de données et caractérisation de la sensibilité des détecteurs cryogéniques aux WIMPs de basse masse.* Ph.D. thesis, Université Claude Bernard Lyon 1, 2015.

[120] Main de Boissière, T. *Recherches de WIMPs de basse masse et d'axions avec l'expérience EDELWEISS.* Phd thesis, Université Paris-Sud, 2015.

[121] Barreto, J.; Cease, H.; Diehl, H.; et al. *Direct search for low mass dark matter particles with CCDs.* Phys. Lett. B, 711(3-4):264–269, may 2012. doi:10.1016/j.physletb.2012.04.006.

[122] Cranmer, K. *Practical Statistics for the LHC.* pages 14–17, mar 2015. doi:10.5170/CERN-2014-003.267.

[123] Barlow, R. *Extended maximum likelihood.* Nucl. Instruments Methods Phys. Res. Sect. A Accel. Spectrometers, Detect. Assoc. Equip., 297(3):496–506, dec 1990. doi:10.1016/0168-9002(90)91334-8.

[124] Karbach, T.M. and Schlupp, M. *Constraints on Yield Parameters in Extended Maximum Likelihood Fits.* arxiv:1210.7141, oct 2012.

[125] James, F. and Roos, M. *Minuit - a system for function minimization and analysis of the parameter errors and correlations.* Comput. Phys. Commun., 10(6):343–367, dec 1975. doi:10.1016/0010-4655(75)90039-9.

[126] Cowan, G.; Cranmer, K.; Gross, E.; et al. *Asymptotic formulae for likelihood-based tests of new physics.* Eur. Phys. J. C, 71(2):1–19, feb 2011. doi:10.1140/epjc/s10052-011-1554-0.

[127] Wald, A. *Tests of statistical hypotheses concerning several parameters when the number of observations is large.* Trans. Am. Math. Soc., 54(3):426–426, mar 1943. doi:10.1090/S0002-9947-1943-0012401-3.

[128] Wilks, S.S. *The Large-Sample Distribution of the Likelihood Ratio for Testing Composite Hypotheses.* Ann. Math. Stat., 9(1):60–62, mar 1938. doi:10.1214/aoms/1177732360.

[129] Junk, T. *Confidence level computation for combining searches with small statistics.* Nucl. Instruments Methods Phys. Res. Sect. A Accel. Spectrometers, Detect. Assoc. Equip., 434(2):435–443, 1999. doi:10.1016/S0168-9002(99)00498-2.

[130] Read, A.L. *Presentation of search results: the CL s technique.* J. Phys. G Nucl. Part. Phys., 28(10):2693–2704, oct 2002. doi:10.1088/0954-3899/28/10/313.

[131] Verkerke, W. and Kirkby, D. *The RooFit toolkit for data modeling.* arxiv:0306116, jun 2003.

[132] Brun, R. and Rademakers, F. *ROOT - An object oriented data analysis framework.* Nucl. Instruments Methods Phys. Res. Sect. A Accel. Spectrometers, Detect. Assoc. Equip., 389(1-2):81–86, apr 1997. doi:10.1016/S0168-9002(97)00048-X.

[133] Schott, G. and Team, f.t.R. *RooStats for Searches.* In *ACAD 2010 Conf. Proc.* mar 2012.

[134] Paul, B. *Configuration of bolometer detectors for Run308.* Internal note, 2014.

[135] Poda, D.V.; Armengaud, E.; Arnaud, Q.; et al. *Scintillating bolometers based on $ZnMoO_4$ and $Zn^{100}MoO_4$ crystals to search for $0\nu2\beta$ decay of ^{100}Mo (LUMINEU project): first tests at the Modane Underground Laboratory.* Contrib. to Proc. 37th Int. Conf. High Energy Phys. (ICHEP 2014), 00:1–7, feb 2015.

[136] Gascon, J. *Technical note of Run308 with the analysis i.* Internal note, 2015.

[137] Armengaud, E. *Analysis note on the EDELWEISS Run 308 low mass WIMP search.* Internal note, 2015.

[138] Gascon, J. *Determination of the ionization χ^2 cut for the analysis j of Run308 .* Internal note, 2015.

[139] Martineau, O.; Benoit, A.; Bergé, L.; et al. *Calibration of the EDELWEISS cryogenic heat-and-ionization germanium detectors for dark matter search.* Nucl. Instruments Methods Phys. Res. Sect. A Accel. Spectrometers, Detect. Assoc. Equip., 530(3):426–439, sep 2004. doi:10.1016/j.nima.2004.04.218.

[140] National Institute of Standards and Technology. *Composition of natural germanium.* `http://www.nist.gov/pml/`, 2016.

[141] Åström, J.; Di Stefano, P.; Pröbst, F.; et al. *Fracture processes observed with a cryogenic detector.* Phys. Lett. A, 356(4-5):262–266, aug 2006. doi:10.1016/j.physleta.2006.03.059.

[142] Cranmer, K. *Kernel estimation in high-energy physics.* Comput. Phys. Commun., 136(3):198–207, may 2001. doi:10.1016/S0010-4655(00)00243-5.

[143] Masaki Yamashita for the XMASS collaboration. *Direct Dark Matter Search with XMASS-I.* `http://arxiv.org/abs/1511.07597`, 2015.

Appendix

A. Example database document

Listing 5.1: JSON document for a SAMBA data partition.

```
{
    "_id": "run_pb28b000_000_kdatascript",
    "_rev": "12-8f91f1ecbfbbe93c229b22641858ffc0",
    "Fichier": "/Volumes/DonneesEDWh2/events/pb28b000",
    "Temperature": "0.0194926",
    "batchJob": [ ... ],
    "Source.2.calib": "absente",
    "Byte-order": "little",
    "Source.1.regen": "absente",
    "Sauvegarde.stream": "brutes",
    "proc0": {
        "transfer_method": "sftp",
        "localuname": [ ... ],
        "log": ... ,
        "stdOut": "",
        "file_size_mb": 152.9909315109253,
        "hostname": "ccage.in2p3.fr",
        "pexpect_obj": ... ,
        "processname": "ManagedSendToLyon",
        "command": "put",
        "date_unixtime": 1425119135.941757,
        "file": "/sps/edelweis/kdata/data/raw/pb28b000_000",
        "file_size": 160422619,
        "date": "2015-02-28 10:25:35.941740"
    },
    "Sauvegarde.assoc": "oui",
    "file_number": 0,
    "Trmt.altivec": "non",
    "Trigger.Type": "cable",
    "Source.2.regen": "absente",
    "Sauvegarde.regen": 100,
    "Date": {
        "year": 2015,
        "day": 28,
        "month": 2
    },
    "type": "daqdocument",
    "date_uploaded": 1425118817.712553,
    "Condition": "fond chateau ferme",
    "Trmt.evt.calage": "unique",
    "Release": "9.35.1082",
    "Trigger.actif": "oui",
    "Type": "fond",
    "Trmt.saute_evt": "non",
    "file_lastmodified": 1425118574,
```

```
    "Regeneration": "non",
    "Source.1.calib": "absente",
    "hpss_status": "done",
    "Starter": "neant",
    "Date.microsecs": 372733,
    "Duree.synchronisation": 100,
    "Detecteurs": [...],
    "hostipaddress": "134.158.176.24",
    "Calibration": "non",
    "Duree.tampon": 10000,
    "Trigger.scrpt": "script_trigger",
    "Lect.delai.mini": 1,
    "Hote": "s2",
    "Version": "9.35",
    "file": "/Volumes/DonneesANA2/RawData/Run308/pb28b000/pb28b000_000",
    "run_name": "pb28b000",
    "Voies.nb": 363,
    "Trmt.calcul": "max",
    "Date.secondes": 1425113748,
    "Run": 0,
    "author": "Samba",
    "proc1": {
        "localuname": ... ,
        "file_size_mb": 81.0650634765625,
        "hostname": "lsmmc7.in2p3.fr",
        "sftp": {
            "transfer_method": "sftp", ... ,
            "log": ... ,
            "stdOut": "",
            "file_size_mb": 81.0650634765625,
            "hostname": "ccage.in2p3.fr",
        },
        "processname": "samba2kdata",
        "file": "/sps/edelweis/kdata/data/raw/pb28b000_000.root",
        "date": "2015-02-28 10:25:47.189913"
    },
    "Echantillonage": 100,
    "hostname": "lsmmc7.in2p3.fr",
    "content": "Samba DAQ document for a particular run. Use this database entry to
        track the progress of the processing of this data",
    "Daq_dns": "lsmmc2.in2p3.fr",
    "hpss": {
        "date": "2015-03-16 14:44:54.031520",
        "file_size": 2050418691,
        "icommandOut": "",
        "file": "/edw/edw3rawdata/2015/fev15/events/pb28b000.tar.gz",
        "date_unixtime": 1426517094.031539
    },
    "Lect.taux.seuil": 100000,
    "proc2": {
        "localuname": [ ... ],
        "batchjob": 1089162,
        "file_size_mb": 12.13430404663086,
        "hostname": "ccwsge0338",
        "processname": "kdataRaw2Amp",
        "file": "/sps/edelweis/kdata/data/amp/pb28b000_000.amp.root",
        "date": "2015-03-08 07:41:44.681475"
    },
    "Sauvegarde.evt": "seul",
    "Voies": [...],
    "Heure": "09:55:40",
    "Bolo.nb": 39,
    "status": "good",
    "Trmt.sans_fltr": "non",
    "GigaStamp0": 941,
    "Trmt.datation": "maxi",
    "Trmt.pattern": "non",
    "bit-trigger": "channel",
    "Intitule": "Edelweiss3, run 308",
    "TimeStamp0": 328000000,
    "Trmt.maintenance": "oui",
    "Tubes-pulses": "arretes"
}
```

B. Additional Figures

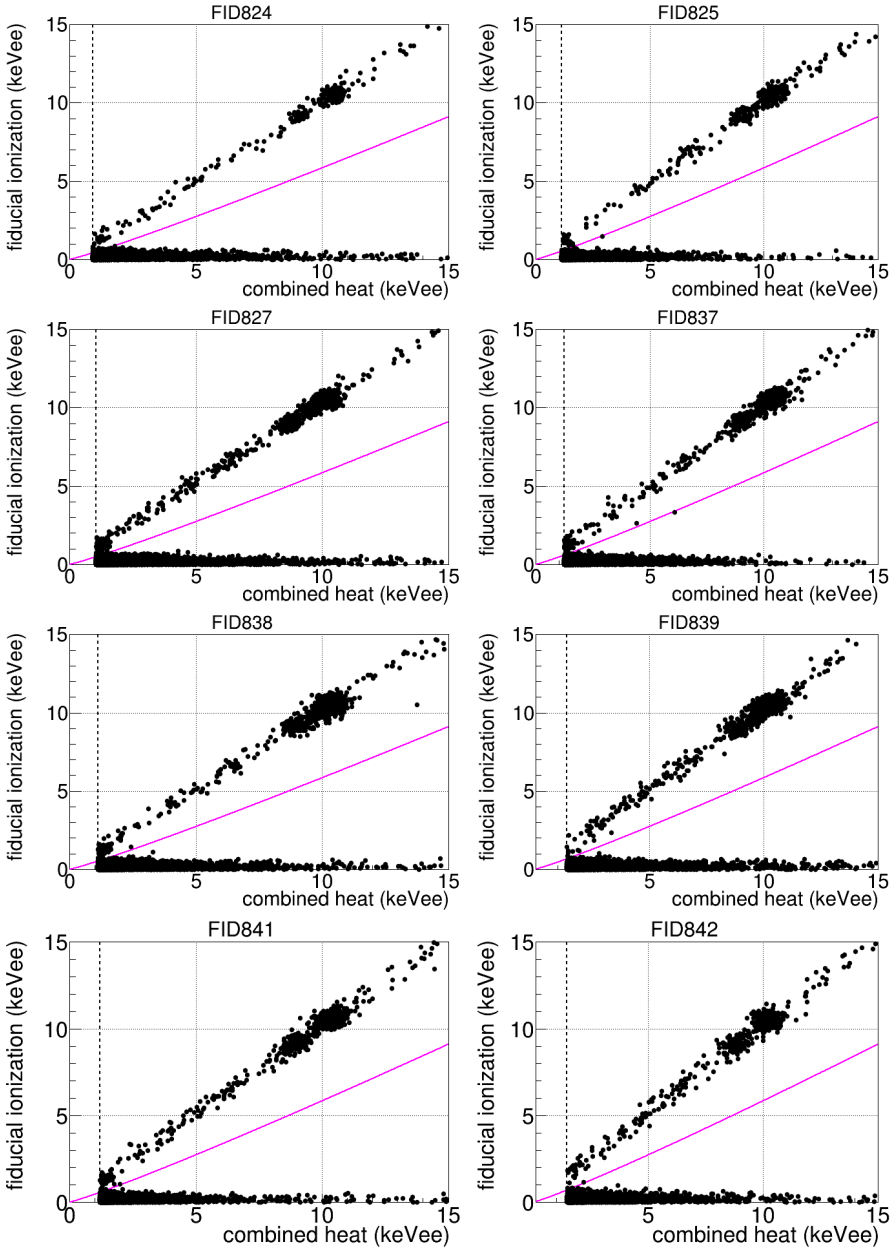

Figure B.1.: Overview of the selected data for all 8 detectors. The dashed black line indicates the analysis threshold $E_{\mathrm{c}}^{\mathrm{min}}$ which is the lower boundary of the RoI. As reference, the energy dependent ionization yield $Q_{\mathrm{NR}}\left(E_{\mathrm{r}}\right)$ for nuclear recoils from neutrons and WIMPs is shown as solid magenta line. The number of events and the value of $E_{\mathrm{c}}^{\mathrm{min}}$ are given in Tab. 4.3.

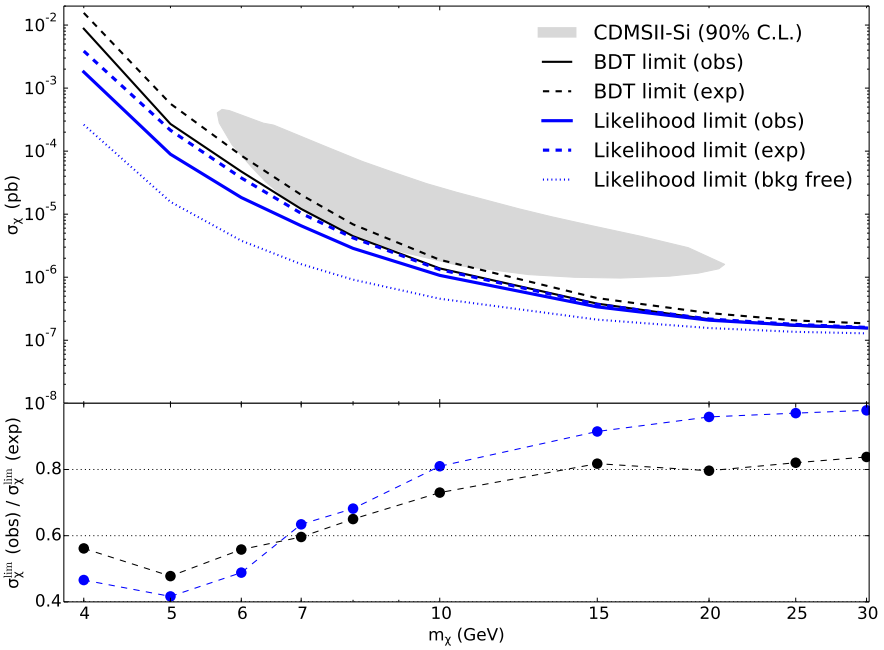

Figure B.2.: *Top*: Observed and expected exclusion limits on the WIMP-nucleon scattering cross section as a function of WIMP mass m_χ. Compared are the limits between BDT and likelihood analysis for the fit of detector FID824. Also shown for the likelihood analysis the case of $\mu_\chi^{\mathrm{lim}} = 2.35$ events (90% Poisson-limit in case of 0 observed events). *Bottom*: Ratio between observed and expected exclusion limit as a function of WIMP mass m_χ. FID824 has an underfluctuation of backgrounds and both analyses show a remarkable agreement for all WIMP masses.

C. Additional Tables

Table C.1.: Calculated parameters for rotation and slope used for the three components of the fiducial cut defined in Eq. 4.15.

Detector	r_{EIA}	s_{EIA}	r_{EIC}	s_{EIC}	r_{EDIF}	s_{EDIF}
FID824	0.0041	0.023	0.0009	0.030	0.0029	0.014
FID825	0.0058	0.034	0.0029	0.025	−0.0063	0.018
FID827	−0.0019	0.014	0.0018	0.015	−0.0020	0.013
FID837	0.0050	0.020	0.0013	0.020	0.0004	0.016
FID838	0.0028	0.020	−0.0007	0.022	−0.0009	0.014
FID839	0.0010	0.015	0.0053	0.022	−0.0052	0.013
FID841	−0.0019	0.021	0.0039	0.020	−0.0040	0.019
FID842	0.0030	0.017	0.0055	0.021	−0.0033	0.013

Table C.2.: Baseline noise FWHM values and adaptive trigger threshold averaged over all events in the RoI after cuts in units of $\mathrm{keV_{ee}}$. For a definition of the variables of the *ana* data format see Tab. 4.1.

Detector	FWC	FWF	$FWIA$	$FWIC$	KTH
FID824	0.29	0.56	0.66	0.68	0.61
FID825	0.48	0.46	0.58	0.62	0.92
FID827	0.39	0.52	0.67	0.78	0.81
FID837	0.39	0.53	0.93	0.74	0.86
FID838	0.44	0.54	0.61	0.61	0.93
FID839	0.64	0.54	0.68	0.77	1.15
FID841	0.54	0.49	0.70	0.69	1.01
FID842	0.57	0.61	0.74	0.78	1.10

Table C.3.: Correction factors for the two observables E_c and E_fid for bulk electron recoil components fitted from sideband data.

Detector	c_heat	c_ion
FID824	1.010 ± 0.002	1.019 ± 0.002
FID825	1.007 ± 0.002	1.015 ± 0.002
FID827	0.981 ± 0.001	1.013 ± 0.001
FID837	1.009 ± 0.000	1.020 ± 0.000
FID838	1.001 ± 0.001	1.018 ± 0.001
FID839	0.993 ± 0.001	1.014 ± 0.001
FID841	0.999 ± 0.001	1.020 ± 0.001
FID842	0.984 ± 0.002	1.012 ± 0.002

Table C.4.: Average baseline resolutions in E_c and E_fid and resolutions at 10.37 keV as fitted from the ^{68}Ge K-shell EC peak in the electron recoil sideband.

Detector	σ_c^0 ($\mathrm{keV_{ee}}$)	$\sigma_\mathrm{c}^{10.37}$ ($\mathrm{keV_{ee}}$)	rel. diff.	σ_fid^0 ($\mathrm{keV_{ee}}$)	$\sigma_\mathrm{fid}^{10.37}$ ($\mathrm{keV_{ee}}$)	rel. diff.
FID824	0.125	$0.220^{+0.013}_{-0.013}$	77%	0.237	$0.250^{+0.014}_{-0.014}$	5%
FID825	0.206	$0.258^{+0.011}_{-0.011}$	25%	0.194	$0.263^{+0.012}_{-0.012}$	35%
FID827	0.168	$0.238^{+0.007}_{-0.007}$	41%	0.220	$0.258^{+0.007}_{-0.007}$	17%
FID837	0.164	$0.232^{+0.012}_{-0.012}$	41%	0.224	$0.254^{+0.008}_{-0.008}$	13%
FID838	0.187	$0.278^{+0.007}_{-0.007}$	49%	0.229	$0.292^{+0.008}_{-0.008}$	27%
FID839	0.272	$0.296^{+0.010}_{-0.010}$	9%	0.229	$0.285^{+0.010}_{-0.010}$	25%
FID841	0.230	$0.282^{+0.010}_{-0.010}$	23%	0.209	$0.267^{+0.010}_{-0.010}$	28%
FID842	0.242	$0.319^{+0.014}_{-0.014}$	32%	0.258	$0.298^{+0.015}_{-0.015}$	16%

Table C.5.: Result of the 2d likelihood fit to data from the electron recoil sideband for all 8 detectors of this analysis. For each of the cosmogenic peaks from K-shell EC as well as the flat component (compton γ's plus ^3H-decay) the fitted rate is given in events with the upper and lower 1σ-error. Also listed are the fitted correction factors for the energy scale in E_{heat} and E_{ion}.

Detector	^{49}V	^{51}Cr	^{54}Mn	^{55}Fe	^{56,57,58}Co	^{56}Ni	^{65}Zn	^{68}Ga	^{68}Ge	compton	tritium
FID824	4.6 ± 3.1	0.0 ± 1.4	0.0 ± 3.0	0.0 ± 1.3	1.2 ± 2.2	0.0 ± 1.1	33.4 ± 6.2	7.7 ± 3.6	115.9 ± 11.1	78.4 ± 11.6	33.7 ± 10.9
FID825	0.7 ± 2.6	0.7 ± 2.6	0.2 ± 10.4	7.5 ± 3.8	5.9 ± 3.5	0.0 ± 1.2	48.1 ± 7.6	17.6 ± 5.4	188.9 ± 14.2	135.5 ± 15.4	33.0 ± 15.8
FID827	13.5 ± 4.8	0.0 ± 1.1	5.0 ± 3.9	16.8 ± 5.3	4.9 ± 4.0	1.1 ± 2.7	152.2 ± 12.9	79.1 ± 10.1	551.7 ± 24.0	145.7 ± 15.8	66.0 ± 17.9
FID837	4.7 ± 4.5	0.9 ± 3.4	0.0 ± 17.7	7.4 ± 4.8	0.0 ± 7.7	0.0 ± 1.1	121.4 ± 11.9	58.7 ± 8.9	408.3 ± 20.8	163.0 ± 30.0	53.7 ± 44.4
FID838	5.7 ± 3.5	0.0 ± 1.2	2.4 ± 2.9	14.7 ± 4.5	0.6 ± 2.3	0.2 ± 8.8	133.2 ± 12.2	71.5 ± 10.4	705.5 ± 27.1	114.1 ± 14.1	35.1 ± 14.7
FID839	2.2 ± 4.2	0.0 ± 2.4	3.6 ± 4.0	4.1 ± 4.2	3.3 ± 4.0	0.0 ± 1.5	100.8 ± 11.1	62.1 ± 9.9	391.4 ± 20.7	104.3 ± 13.8	108.5 ± 19.3
FID841	1.2 ± 3.3	0.0 ± 2.4	5.4 ± 4.1	6.2 ± 4.2	0.0 ± 1.2	0.0 ± 6.3	117.6 ± 11.6	19.6 ± 6.3	332.2 ± 18.9	125.0 ± 15.0	81.8 ± 17.3
FID842	2.0 ± 3.9	1.5 ± 3.6	0.7 ± 4.1	7.5 ± 4.5	0.0 ± 5.0	0.0 ± 17.7	79.3 ± 9.9	12.9 ± 5.9	208.4 ± 15.1	95.6 ± 13.3	90.1 ± 18.1

Table C.6.: Expected rate of events in the RoI for all background components except cosmogenic events from K-shell EC interactions (for those see appendix Tab. C.5)

Detector	$n_{\text{heat-only}}$	n_{neutron}	n_{tritium}	n_{compton}	n_{Zn65L}	n_{Ga68L}	n_{Ge68L}	n_{beta1}	n_{beta2}	n_{lead1}	n_{lead2}
FID824	5386.0 ± 804.4	0.2 ± 0.1	43.3 ± 14.0	41.0 ± 6.1	2.6 ± 0.5	0.6 ± 0.3	9.9 ± 1.4	3.7 ± 1.2	4.8 ± 2.0	2.8 ± 0.5	3.4 ± 0.6
FID825	5159.0 ± 518.1	0.2 ± 0.1	41.4 ± 19.8	69.6 ± 7.9	1.7 ± 0.3	0.9 ± 0.3	12.4 ± 1.5	0.8 ± 0.3	1.6 ± 0.8	1.0 ± 0.2	3.3 ± 0.5
FID827	9155.0 ± 757.2	0.2 ± 0.1	84.3 ± 22.8	75.5 ± 8.2	7.4 ± 1.0	5.0 ± 0.8	42.0 ± 4.6	2.7 ± 1.3	4.6 ± 2.2	2.7 ± 0.5	2.7 ± 0.5
FID837	4399.0 ± 311.0	0.2 ± 0.1	66.4 ± 55.0	83.1 ± 15.3	2.2 ± 0.3	2.0 ± 0.4	22.3 ± 2.5	1.3 ± 0.1	0.4 ± 0.2	2.3 ± 0.5	1.9 ± 0.3
FID838	7285.0 ± 94.4	0.2 ± 0.1	44.2 ± 18.5	58.7 ± 7.2	4.8 ± 0.6	3.7 ± 0.6	47.6 ± 5.1	0.3 ± 0.2	0.2 ± 0.1	1.7 ± 0.3	1.9 ± 0.3
FID839	6416.0 ± 447.6	0.2 ± 0.1	132.7 ± 23.6	52.5 ± 6.9	1.0 ± 0.1	1.0 ± 0.2	10.6 ± 1.2	0.1 ± 0.0	0.1 ± 0.0	2.4 ± 0.4	2.4 ± 0.4
FID841	3578.0 ± 204.0	0.2 ± 0.1	102.1 ± 21.6	64.0 ± 7.7	3.2 ± 0.5	0.8 ± 0.3	18.4 ± 2.1	0.3 ± 0.1	0.3 ± 0.1	2.0 ± 0.3	2.9 ± 0.4
FID842	2744.0 ± 53.4	0.2 ± 0.1	109.9 ± 22.1	48.0 ± 6.7	0.4 ± 0.1	0.1 ± 0.1	3.9 ± 0.5	0.0 ± 0.0	0.0 ± 0.0	1.2 ± 0.2	0.9 ± 0.2

Table C.7.: Results of a hypothesis test performed for the combination of all detectors with 3000–4000 generated Monte Carlo toy data sets for the null hypothesis. The value tested is the 90% C.L. cross-section limit $\sigma_\chi^{\mathrm{lim}}$ derived with the asymptotic approximation. For WIMP masses $m_\chi > 10\,\mathrm{GeV}/c^2$ this approximation is in good agreement with the Monte Carlo data and gives the correct coverage. For lower masses, the coverage is insufficient and the limit therefore too optimistic.

m_χ	CL_{sb}	CL_{b}	CL_{s}	q_μ^{obs}
4	0.03 ± 0.003	0.11 ± 0.007	0.23 ± 0.026	0.88
5	0.02 ± 0.002	0.11 ± 0.007	0.20 ± 0.024	1.22
6	0.05 ± 0.004	0.43 ± 0.011	0.13 ± 0.009	1.28
7	0.08 ± 0.004	0.85 ± 0.008	0.10 ± 0.005	0.98
8	0.10 ± 0.005	0.94 ± 0.005	0.10 ± 0.005	0.89
10	0.12 ± 0.005	0.98 ± 0.003	0.12 ± 0.005	0.80
15	0.10 ± 0.006	1.00 ± 0.001	0.10 ± 0.006	0.88
20	0.10 ± 0.006	1.00 ± 0.001	0.10 ± 0.006	0.86
25	0.10 ± 0.005	0.99 ± 0.002	0.10 ± 0.005	0.91
30	0.10 ± 0.006	0.99 ± 0.002	0.10 ± 0.006	0.90

Acknowledgement

First of all, I would like to thank Prof. Dr. Dr. h.c. Johannes Blümer for the possibility to perform my PhD in the EDELWEISS experiment at the Institute for Nuclear Physics at KIT. I also want to thank Prof. Dr. Wim de Boer for accepting to be my co-referee.

During my PhD I have profited from the KSETA graduate school, both financially as well as through interesting lectures and courses, I also enjoyed the various workshops.

My gratitude goes to Dr. Klaus Eitel for his support and valuable advice. The discussions with him either reassured me when I was in doubt or steered my work back into the right direction. I would like to thank Dr. Silvia Scorza, especially for working together on backgrounds and her many useful corrections. A big "thank you" also goes to Dr. Valentin Kozlov for his daily support regarding ROOT, the local cluster and his help with the exclusion plots when I was under time pressure.

There are numerous colleagues within the EDELWEISS collaboration which I would like to thank. In particular Prof. Dr. Jules Gascon from the Lyon group for answering in great detail any question about the experiment and the detectors but also asking critical questions regarding my analysis. Dr. Julien Billard for his help with the statistical interpretation of results and the many Skype calls answering my numerous questions on test statistics and limit setting. I want to thank Dr. Eric Armengaud for his analysis work from which I profitted and answering my questions.
Thank you to the whole EDELWEISS collaboration, I will especially remember the nice collaborations meetings we had at various places.

Thanks also to my former colleagues: Dr. Adam Cox, both for expanding my knowledge about programming and interesting political discussions. And to Dr. Richard Walker for courses in English but also for doing a very non-scientific diploma together. Thank you also to Marie-Christine Kauffmann for always being available and helpful. I also thank all other colleagues at the institute, either for helping me with specific questions or just because it was nice to work, talk and meet with them.

It was a great pleasure to do this thesis within the group of my fellow PhD students and for the good times we had, also outside of work. Thanks to Benjamin, with whom I gladly shared the office for these years and who helped me so often with my many questions. To Bernhard for many good times playing table football together and sharing the pain of finishing our work at the same time. To Geertje and Nadine for a lot of fun together at work and outside.

I also want to thank my family for their support at all times during my PhD.

Finally, I want to thank Cécile for her invaluable support and help until the very end. Thank you so much!